Mineralization of Biological Fiber Systems

by

Daniel J. Buss

Department of Anatomy and Cell Biology

Faculty of Medicine

McGill University, Montreal, Canada

July 2023

A thesis submitted to McGill University in partial fulfillment of the requirements of the degree
of Doctor of Philosophy in Anatomy and Cell Biology

Table of Contents

List of Figures

Introduction

Chapter 1

Chapter 4

Page

List of Abbreviations

1,25(OH)2D3	1 alpha,25-dihydroxyvitamin D3
Alpl	Alkaline phosphatase gene (mouse)
ANK	Ankylosis protein
ASARM	Acidic serine and aspartate rich motif
ATP	Adenosine triphosphate
AvBD	Avian β-defensin
BSE	Backscattered electron detector
BSE-L	Backscattered electron detector (lower)
BSE-U	Backscattered electron detector (upper)
BSP	Bone sialophosphoprotein
CAM	Chorioallantoic membrane
CF	Calcified fibrocartilage
CNN	Convolutional neural network
Col1a1	Collagen type 1, alpha chain 1 gene (mouse)
Col1a2	Collagen type 1, alpha chain 2 gene (mouse)
CREMP	Cystine-rich eggshell membrane protein
DMP1	Dentin matrix protein 1
DSPP1	Dentin sialophosphoprotein
EDS	Energy-dispersive X-ray spectroscopy
EDTA	Ethylenediaminetetraacetic acid
ENPP1	Ectonucleotide pyrophosphatase/phosphodiesterase 1
ESM	Eggshell membrane
FIB-SEM	Focused ion beam scanning electron microscopy
FGF23	Fibroblast growth factor 23
FGFR3	Fibroblast growth factor receptor 3
GAG	Glycosaminoglycan
HAADF-STEM	High-angle annular dark field scanning transmission electron microscopy
HPP	Hypophosphatasia
Hyp	Hypophosphatemic mouse model of X-linked hypophosphatemia

LCN	Lacuno-canalicular network
LOX	Lysyl oxidase
MEPE	Matrix extracellular phosphoglycoprotein
MF	Mineralized fibrocartilage
OPN	Osteopontin
OTOTO	Osmium-thiocarbohydrazide repetitive staining
PHEX	Phosphate-regulating endopeptidase homolog X-linked
PHOSPHO1	Phosphoethanolamine phosphohydrolase
POL	Periosteocytic lesion
PP_i	Pyrophosphate
PTH	Parathyroid hormone
ROI	Region of interest
SAED	Selected area electron diffraction
SCPP	Secretory calcium-binding phosphoprotein
SEM	Scanning electron microscopy
SIBLING	Small integrin-binding ligand N-linked glycoprotein family
SOX9	SRY-Box transcription factor 9
SPARC	Secreted protein acidic and rich in cystine
SSV	Serial-surface-view
TEM	Transmission electron microscopy
TNAP	Tissue-nonspecific alkaline phosphatase
TNSALP	Tissue-nonspecific alkaline phosphatase
UF	Uncalcified fibrocartilage
WT	Wildtype normal mouse
XLH	X-linked hypophosphatemia
μCT	Micro-computed tomography

This thesis is dedicated to my family, namely my parents Diane and Jim of Allentown, Pennsylvania, my brother Michael, and my partner Christiane.

Abstract

Biomineral crystal growth within extracellular fiber assemblies is regulated broadly and at fine scales by proteins and small molecules. While small-molecule and protein inhibitors broadly prevent soft and compliant tissues from mineralizing, release from this inhibition in the vertebrate skeleton occurs through local expression of enzymes that cleave these inhibitors. Mutations in these enzymes result in inhibitor accumulation leading to debilitating mineralization defects and losses of mechanical function. As an example of this in another biomineralizing fiber system, despite supersaturation of mineral ions within an avian hen's uterus which allows for an entire eggshell to mineralize in under 24 hours, mineralization of the underlying eggshell membrane fibers is restricted to outermost fibers only. This instance of broad inhibition of a fibrous network from mineralization permits splitting of the membrane fiber layers to form a membrane-enclosed air sac at the blunt-end of an egg, essential for chick respiration at hatching.

Correlative, multi-scale imaging approaches are now in common use in structural biology studies. However, this is not generally the case for hard mineralized tissues such as bone and cartilage, or eggshell – cases where the fibrous matrix is permeated with a mineral phase that renders them difficult to analyze. Mechanical properties of mineralized fibrous biocomposites originate from nanoscale relations of their constituent parts, and often propagate across several hierarchical levels in 3D. This work utilizes multi-scale imaging approaches (including FIB-SEM serial-surface-view tomography combined with deep learning-assisted segmentation) to better understand at multiple levels how mineralization develops and is refined at the interface of various fibrous, collagen-based extracellular matrices that form biocomposites having diverse properties and functions. A particular emphasis is placed on lamellar bone and enthesis fibrocartilage where we compare the 4D trajectory of mineralization in normal mice to that as observed in *Hyp* mice (a model of the disease X-linked hypophosphatemia). In XLH/*Hyp*, inactivating mutation in the PHEX enzyme results in altered FGF23 signaling causing renal phosphate wasting, and accumulation locally of the mineralization-inhibiting protein osteopontin (OPN), PHEX's physiologic substrate.

This work details a shared structural level of hierarchy across the microscale and in 3D of lamellar bone and enthesis fibrocartilage – that we have called crossfibrillar mineral tessellation. In normal bone and fibrocartilage, this type of crossfibrillar mineral unit originates via growth of small mineral foci in an otherwise unmineralized fibrous collagen matrix into close-packed

micrometer-sized tesselles, with intervening narrow organic margins. In *Hyp* mice, defective crossfibrillar mineralization leads to delays and changes in mineral tesselle packing which can account mechanistically for bone deformations and buckling (pseudofractures) found in mice and patients. This study highlights how mineral-binding proteins and potentially other factors have the capacity to influence the trajectory of mineralization (mineral focus-to-tesselle), therefore contributing to fragility in skeletal disease, or contributing to matrix-specific mechanical adaptation. Indeed, tessellation of fiber-anchored unit structures is not unique to bone or fibrocartilage. At the avian eggshell-membrane interface, organic fibers of the shell membrane course through interfacial mineral units of the calcitic shell, providing a similar developmental, reciprocal anchorage system. In this case, fibers pass through shell mineral, and shell mineral in turn anchors the fibers with mineral protrusions (so-called mineral spikes and granules). Taken together, these findings in different tissues and structures provide a fundamental 3D morphological basis for understanding attachment mechanisms between inorganic mineral and organic fiber systems.

Résumé

La croissance biominérale cristalline au sein des assemblages de fibres extracellulaires est régulée à grande et à petite échelle par des protéines et des petites molécules. Bien que l'inhibition générale de la minéralisation garantisse que les tissus mous et conciliants soient maintenus tel quel, l'arrêt de cette inhibition dans les squelettes vertébrés est assuré par l'expression spécifique cellulaire et tissulaire d'enzymes qui clivent localement ces inhibiteurs de minéralisation. Les mutations inactivatrices dans les gènes codant pour ces enzymes entraînent une accumulation d'inhibiteurs qui conduit à des défauts de minéralisation invalidants et à une perte de la fonction mécanique. En outre, malgré la sursaturation des ions minéraux dans l'utérus de la poule domestique, permettant la formation et minéralisation complète d'une coquille d'œuf en moins de 24 heures, la minéralisation des fibres de la membrane coquillière est limitée aux fibres les plus externes qui tapissent la partie intérieure de la coquille. Cet exemple d'inhibition générale de minéralisation d'un réseau fibreux permet aussi la séparation entre les couches de fibres membranaires pour former une chambre à air à l'intérieur de la membrane à l'extrémité arrondie de l'œuf, essentielle à la respiration du poussin au moment de l'éclosion. Les approches d'imagerie corrélatives multi-échelles sont maintenant couramment utilisées dans la recherche en biologie structurale.

Cependant, ce n'est généralement pas le cas pour les tissus minéralisés durs tels que l'os, le cartilage, ou la coquille d'œuf – pour lesquels la matrice extracellulaire fibreuse est imprégnée d'une phase minérale (hydroxyapatite pour l'os et le cartilage et calcite pour la coquille d'œuf) qui les rend difficiles à analyser. Les propriétés mécaniques des bio-composites fibreux minéralisés proviennent des relations de leurs composants à l'échelle nanométrique, relations qui se propagent souvent au moins à plusieurs niveaux de hiérarchie en 3D. Dans le présent travail, nous avons utilisé une variété d'approches d'imagerie à plusieurs échelles (y compris la tomographie de surface en série FIB-MEB combinée à la segmentation assistée par l'apprentissage profond) pour mieux comprendre comment la minéralisation se développe à plusieurs échelles et est affinée à l'interface (fronts de minéralisation) de diverses matrices extracellulaires fibreuses à base de collagène (dans l'os, le fibrocartilage, le tendon et la coquille d'œuf aviaire) pour former des bio-composites ayant des propriétés et fonctions diverses. Une attention particulière a été accordée à l'os lamellaire et le fibrocartilage de l'enthèse pour lesquels la trajectoire 4D de la minéralisation a été comparée chez des souris sauvages à celle observée chez des souris Hyp (étudiées comme modèle de la maladie

de l'hypophosphatémie liée à l'X chez les humains, XLH). Chez cette souris mutante et chez les patients atteints de la XLH, des mutations dans le gène *PHEX* entraînent une perte d'activité de l'enzyme PHEX, résultant en une ostéomalacie (hypo-minéralisation). Cette dernière s'accomplit par une signalisation altérée de l'hormone circulante FGF23 provoquant une perte de phosphate rénal, et par l'accumulation locale d'ostéopontine inhibitrice de la minéralisation, substrat physiologique de PHEX, dans la matrice extracellulaire.

Ce travail identifie un niveau structurel hiérarchique commun à l'échelle microscopique et en 3D de l'os lamellaire et du fibrocartilage de l'enthèse - que nous avons appelé pavage minéral inter-fibrillaire (crossfibrillar mineral tessellation). Dans l'os sain, cette structure provient de la croissance de petits foyers minéraux dans une matrice extracellulaire fibreuse et collagénique autrement non minéralisée, puis évolue en un motif de pavage tessellé micrométrique étendu et compacté, s'étendant sur trois dimensions et laissant de petits espaces entre les dites tesselles. Chez les souris Hyp déficientes en PHEX ayant une accumulation d'ostéopontine inhibitrice dans la matrice extracellulaire et une perte de phosphate rénal, la minéralisation défectueuse entraîne des retards et des changements dans le pavage tesselé minéral inter- fibrillaire, qui peuvent apporter une explication mécanique relative aux déformations osseuses molles et aux flambages (pseudo-fractures) typiquement observés chez les souris mutantes Hyp et chez les patients atteints de la XLH. Cette étude met en évidence comment les protéines de liaison minérale et potentiellement d'autres facteurs ont la capacité d'établir et d'influencer la trajectoire saine de la minéralisation (du foyer minéral à la tesselle), qui défectueux, peuvent contribuer à la perte d'intégrité osseuse et performance mécanique dans les maladies squelettiques. Le pavage tesselé des structures unitaires ancrées dans les fibres n'est pas unique à l'os dans la nature, et nous avons également identifié ce même motif à l'attachement de l'enthèse dans le fibrocartilage calcifié. À l'interface entre la membrane et la coquille de l''œuf chez les poulets domestiques, les fibres organiques de la membrane coquillère passent à travers des unités minérales interfaciales de la coquille calcitique, fournissant un système d'ancrage réciproque avec un développement similaire. Dans ce cas, les fibres traversent les minéraux de la coquille, qui ancrent à leur tour les fibres avec des protubérances minérales (appelées pics et granules minéraux). Dans l'ensemble, ces résultats dans différents tissus et structures fournissent une base morphologique fondamentale en 3D pour comprendre les mécanismes d'attachement entre les systèmes minéraux inorganiques et les fibres organiques.

Acknowledgements

- My supervisor Dr. Marc McKee was instrumental in having the foresight to support the adoption of 3D imaging technologies, including acquiring the first FIB-SEM instrument in the Facility for Electron Microscopy Research at McGill. As a result, I had the opportunity to become an expert in conducting, analyzing, and interpreting highly detailed imaging work that is included in the following thesis chapters. Marc also sought out opportunities for me to travel and collaborate with scientists internationally, including as a visiting PhD student in Israel, and at numerous international conferences and symposiums. I would like to thank Marc for fostering this exceptional educational experience I've had at McGill, and most of all for his tremendous mentorship along the PhD journey.

- My co-supervisor Dr. Natalie Reznikov provided incredible support during my PhD. She truly inspired me to think at a new level about the structural biology of mineralized tissues, and to think spatially about biological systems and develop a perspective from multiple dimensions and from the nanoscale. She was a true catalyst of my intellectual curiosity of biology early on in my PhD.

- Thanks to present and former McKee and Reznikov lab members, and specific thanks to A. Mousa, V. Nelea, B. Hoac, L. Malynowski, J. Deering, and Prof. R. Kröger (U. York) for their contributions to my training, support, and discussions.

- Dr. Monzur Murshed for certain elements of my training and helpful discussions of prior and ongoing projects.

- W. Leelapornpisit, S. Bessette, and K. Rechav, for their technical assistance in FIB-SEM serial-surface-view data acquisition.

- McGill Facility for Electron Microscopy Research staff including W. Leelapornpisit, S. Bessette, D. Liu, J. Mui, J, Ouellette, K. Sears, and A. Valdez, in providing outstanding instrument training and technical expertise.

- Local Montreal societies and organizations for their tremendous research support including the Centre de Recherche en Biologie Structurale (CRBS), Canadian Foundation for the Development of Microscopy (CFDM), Réseau de Recherche en Santé Buccodentaire et Osseuse (RSBO), and Object Research Systems/Dragonfly (in particular N. Piché, B. Provencher, and E. Yen)

Preface

This thesis is composed of four linked chapters that constitute the research of my doctoral studies. Each chapter is an original research manuscript for which I am the first author, and at the time of final submission of this thesis, has either been published or is under revision for publication in a peer-reviewed journal. This thesis addresses the broad topic of "Mineralization of Biological Fiber Systems" where the trajectory and products of this biomineralization process are revealed not only with conventional two-dimensional (2D) microscopy and analytical methods, but also with added context in three dimensions (3D). The analyses are performed across the nano- and microscale, and observations are made on fiber-mineral composite tissues having diverse underlying organic and inorganic compositions and functions. Below is a list of major new significant findings linked together in the sense that they all describe the nature and broad functional implications of mineral unit structures in several biological fiber systems:

- At the microscale, fiber systems of lamellar bone, calcified fibrocartilage, outermost eggshell membrane, and ectopic mineralization of tendon, are dominated by variations of mineral unit structures.

- Mineral units vary in their constituent fibers at the microscale in terms of size, orientation, and spacing, and at the nanoscale in terms of the occurrence and location of mineral nanocrystals within fibers.

- In mouse bone, enthesis fibrocartilage, and tendon, apatite-based mineral units are arranged in a repeating, space-filling 3D pattern called crossfibrillar mineral tessellation which occurs across multiple parallel collagen type I fibrils.

- Crossfibrillar mineral tessellation is a packing pattern for mineral where narrow organic margins remain around much of each 3D "tesselle" periphery, and with the mineral nanocrystals that constitute each tesselle penetrating into and beyond the fibers.

- In the avian eggshell, calcite mineral units present as mammillae which are penetrated by orthotropic fibers of different directions and layers, this with mineral nanocrystals penetrating distinctly into only certain fiber domains and with unique morphological signatures.

- Organic-inorganic anchorages at the membrane-eggshell interface occurring at the nano- and microscale constitute an attachment mechanism of the eggshell membrane to the calcite shell that provides an order-of-magnitude increase in the attachment surface area.

- Individual mineral tesselles in mouse tissues at sites of crossfibrillar mineral tessellation initially form from small mineral foci that subsequently enlarge and preferentially elongate along the long axis of collagen fibrils to acquire a final 3D shape geometrically approximating a prolate ellipsoid.

- Crossfibrillar mineral tessellation represents a unique level within bone's hierarchical organization with significant mechanical implications.

- From the nano- to microscale in bone, Achilles enthesis fibrocartilage, and age-related calcifying tendinopathy, near-identical deficiencies in mineral growth and formation/packing of crossfibrillar mineral tesselle units occur in osteomalacic *Hyp* mice (a model of the mineralization disease X-linked hypophosphatemia). Deviating from the normal mineralization trajectory, such a mineralization defect is consistent with a local accumulation of mineralization inhibitors that alters mineral patterning across collagen fibers in a way that results in skeletal deformities.

*<u>Note</u>: **Readers of this thesis are encouraged to additionally view the substantial movie content that supplements each manuscript and the above findings, as found online in each published journal version. Such movies are an integral part of 3D imaging data.***

Contribution of Authors

Each of the following four manuscripts presented in Chapters 1-4 contains original research results obtained by the candidate, and as the primary, first author.

Chapter 1: Crossfibrillar mineral tessellation in normal and *Hyp* mouse bone as revealed by 3D FIB-SEM microscopy

Authors: <u>Daniel J. Buss</u>, Natalie Reznikov, Marc D. McKee

Contributions:
D. J. Buss – Independently managed mouse colony including maintenance, handling, necropsy, and genotyping. Prepared specimens using conventional techniques for electron microscopy including fixation, dehydration, staining, infiltration and embedding, block trimming, and preparation/region selection for 3D FIB-SEM serial-surface-view mode. Assisted in preparation of additional samples using high-pressure freezing and freeze substitution. Independently imaged whole mice using µCT and completed volume stitching. Registered imaging data, and conducted deep-learning based feature segmentation. Conducted formal analysis of 3D µCT and FIB-SEM volumes (including using watershed transform) in Dragonfly software. Contributed to interpretation of data and conceptualization. Wrote original draft, and contributed to review/editing of the final manuscript.

N. Reznikov – Assisted in preparation of samples using high-pressure freezing and freeze substitution. Trained the first author to use advanced segmentation and analysis tools in Dragonfly software. Contributed to interpretation of data, conceptualization, and review/editing of manuscript. Provided supervision for the study duration.

M.D. McKee – Trained the first author in electron microscopy and sample preparation techniques. Assisted in preparation of samples using high-pressure freezing and freeze substitution. Contributed to interpretation of data, conceptualization, and review/editing of

manuscript. Provided supervision, project design and administration, and funding acquisition for the study duration.

Chapter 2: Hierarchical organization of bone in three dimensions: A twist of twists

Authors: <u>Daniel J. Buss</u>, Roland Kröger, Marc D. McKee, Natalie Reznikov

Contributions:

D. J. Buss – Managed mouse colony and prepared mouse tissue specimens. Contributed to investigation and analysis of μCT and FIB-SEM data in Dragonfly software. Assisted in conceptualization and wrote original draft.

Roland Kröger – Contributed to investigation and analysis of STEM tomography data. Contributed to conceptualization, review, and editing of manuscript.

Marc D. McKee – Contributed to conceptualization, review, and editing of manuscript. Provided supervision and funding acquisition.

Natalie Reznikov – Contributed to investigation and analysis of μCT, FIB-SEM and STEM tomography data using Dragonfly software. Contributed to conceptualization and led data curation. Contributed to review and editing of manuscript. Provided supervision and project administration roles.

Chapter 3: Crossfibrillar mineral tessellation trajectories in mouse enthesis fibrocartilage and in *Hyp* calcifying enthesopathy

Authors: <u>Daniel J. Buss</u>, Katya Rechav, Natalie Reznikov, Marc D. McKee

Contributions:

D. J. Buss – Performed mouse colony maintenance, handling, necropsy, and genotyping. Prepared specimens using conventional techniques for electron microscopy including fixation, dehydration, staining, infiltration and embedding, block trimming, and preparation/region selection for 3D FIB-SEM serial-surface-view mode. Independently used µCT to image enthesis fibrocartilage and Achilles tendons via critical point drying and phase contrast imaging. Independently imaged thin and bulk enthesis and tendon sections via TEM and SEM, respectively. Performed immunohistochemistry for PHEX and OPN of enthesis and tendon sections. Registered volume imaging data and performed deep-learning based feature segmentation. Conducted formal analysis and interpretation of 3D µCT and FIB-SEM volumes (including using watershed transform) in Dragonfly software. Led conceptualization and writing of original draft, and review/editing.

Katya Rechav– Performed FIB-SEM serial-surface-view setup and image stack acquisition. Reviewed the final manuscript.

Natalie Reznikov – Contributed to interpretation of data, conceptualization, review, and editing of manuscript.

Marc D. McKee – Contributed to interpretation of data, conceptualization, review, and editing of manuscript. Provided supervision, project design and administration, and funding acquisition for study duration.

Chapter 4: Attaching organic fibers to biomineral: The case of the avian eggshell
Manuscript under review

Authors: <u>Daniel J. Buss</u>, Natalie Reznikov, Marc D. McKee

Contributions:

D. J. Buss – Prepared eggshell specimens using conventional and cryo-techniques for electron microscopy including fixation, dehydration, infiltration and embedding, block trimming, and preparation/region selection for 3D FIB-SEM serial-surface view mode. Conducted independent

μCT imaging of eggshells, and imaging of thin and bulk embedded specimens via TEM (as well as S/TEM, and EDS/SAED of regions of interest), and SEM, respectively. Registered volume imaging data, and carried out deep-learning based feature segmentation. Conducted formal analysis of 3D μCT and FIB-SEM volumes using Dragonfly software. Led conceptualization and interpretation of data. Wrote original draft and contributed to review and editing.

Natalie Reznikov – Contributed preliminary μCT and SEM imaging data of eggshell membrane fibers. Contributed to interpretation of data, conceptualization, review, and editing of manuscript. Provided supervision during the project duration.

Marc D. McKee – Contributed original eggshell imaging data including immunogold labeling for OPN. Assisted in high-pressure freezing of eggshells. Contributed to study design and interpretation of data, conceptualization, review, and editing of manuscript. Provided supervision and funding acquisition during project duration.

In addition to the previous first author publications that constitute Chapters 1-4, I have also contributed as a co-author to an additional four peer-reviewed publications while a doctoral student at McGill:

M.D. McKee, **D.J. Buss**, N. Reznikov. Mineral tessellation in bone and the stenciling principle for extracellular matrix mineralization. J. Struct. Biol., 214 (1) (2022), Article 107823
DOI: 10.1016/j.jsb.2021.107823

N. Reznikov, **D.J. Buss**, B. Provencher, M.D. McKee, N. Piche. Deep learning for 3D imaging and image analysis in biomineralization research. J. Struct. Biol., 212 (2020), p. 107598
DOI: 10.1016/j.jsb.2020.107598

B. Hoac, M. Ostergaard, N.K. Wittig, T. Boukpessi, **D.J. Buss**, C. Chaussain, H. Birkedal, M. M urshed, M.D. McKee. Genetic ablation of osteopontin in osteomalacic *Hyp* mice partially rescues the deficient mineralization without correcting hypophosphatemia. J. Bone Miner.
Res., 35 (10) (2020), pp. 2032-2048
DOI: 10.1002/jbmr.4101

N. Reznikov, B. Hoac, **D.J. Buss**, W.N. Addison, N.M.T. Barros, M.D. McKee. Biological stenciling of mineralization in the skeleton: local enzymatic removal of inhibitors in the extracellular matrix. Bone, 138 (2020), Article 115447
DOI: 10.1016/j.bone.2020.115447

Biological Fiber Systems – An Introduction

Organic networks of fibers produced and assembled to constitute tissues of living organisms are widespread and are adapted for functional roles that are equally as diverse – for example in vertebrate bones and cornea, arthropod exoskeletons, and even in the cell walls of plants. Fiber systems are of critical importance to structural integrity of tissues, and may be composed of macromolecules such as fibrillar collagens, chitin, or cellulose, but must be assembled and organized appropriately to benefit from their highly anisotropic mechanical behavior. Polypeptide constituents of the fibrillar collagen proteins (the most abundant in vertebrates) are a product of various cell types whose amino acid sequence, like all other proteins, are specified by genetic code. After secretion by cells into the extracellular space, assembly and orientation of fiber constituents into larger microfibrils, fibers, and bundles may occur as dictated by their underlying chemical composition and the chemical composition of other extracellular matrix components that they associate with, including water. Remarkably, in some biological fiber systems, conditions are also afforded that favor the nucleation and growth of inorganic mineral crystals (1-7). Even more interesting is how in some fiber systems this mineral growth occurs both within and around the individual fibers, while in others it may only occur within specific fiber domains. Furthermore, to provide diverse functions in different tissues and organisms, organic fibers, other organic matrix constituents, and inorganic mineral components, are all variable in their occurrence, composition, structure, and underlying relations, and important to this work − originating from the nanoscale and in three dimensions.

In the following chapters and connecting text, the development and relationship of mineral units within several fiber systems across the microscale and into the nanoscale are revealed for the first time in three dimensions, and structure-function relationships of these different mineral units are discussed. In the first three chapters, mineralization of fibers in vertebrate tissues (this being principally collagen type I fibrils/fibers and apatite mineral) occurring as crossfibrillar mineral "tesselles" will be the topic of investigation. In the final fourth chapter, the same theme of the mineral unit of fiber systems at the microscale is extended to avian eggshells (calcite mineral), particularly concerning the initial mineralization at and around the outer surface of the chicken (*Gallus gallus domesticus*) fibrous eggshell membrane.

This introductory text aims to both familiarize the reader with the diversity of biological fiber systems found in Nature, followed by a particular emphasis on my research concerning several tissues and structures as presented in Chapters 1-4 specifically describing collagen type I fibers in the musculoskeletal system of vertebrates, and eggshell membrane fibers in the avian egg. Subsequent discussion then extends into what is already known about the process of mineralization in each system. To conclude this section, imaging methods that are used for investigation are introduced.

Literature Review

Fiber Production, Assembly, and Maintenance

Organic fiber and extracellular matrix protein constituents of biological tissues are widely produced by cells. While readily observable fibrillar proteins such as collagen dominate the extracellular matrix landscape in mass (8-10), of equal importance are nonfibrous noncollagenous components (1, 11, 12) which frequently exist in similar molar ratios and which will be discussed in the next section. Translation of protein destined for export across the cell membrane, fibrous or not, and derived from mRNA sequences that were initially transcribed from DNA inside the nucleus, occurs on ribosomes attached to rough endoplasmic reticulum. Importantly, before secretion from the cell, nascent amino acid polypeptide sequences are frequently modified chemically, and these posttranslational modifications may include addition of sugar molecules, phosphate or sulfur groups, formation of disulfide bonds, and even cleavage of specific regions that permit interactions with other proteins, among performing other functions (13, 14).

Some fibers systems are indeed not made from proteins at all (15). For example, while chitin (for example in exoskeletons of arthropods) is produced inside cells, it is actually composed of glucose-based compounds that react with different enzymes that assist in the formation of initial chains and then allow for chain elongation (16). Cellulose is a main structural component of plant cell walls and is a polysaccharide produced by glucose polymerization and assembly of microfibrils into larger fibers (17, 18). Cellulose fibers also exist in a matrix containing other complex organic polymers (pectin, hemicellulose, lignin) not associated with a protein backbone typical in vertebrate systems, such as the core proteins of proteoglycans (15, 19). Therefore, fiber

systems in Nature are frequently, but not always, produced directly from the genetic code through transcription and translation. However, biological fiber systems of all types rely on cellular production of enzymes, other proteins, and molecules to facilitate their organization.

In vertebrates, collagen type I is predominantly secreted by osteoblasts and chondrocytes, as well as tenocytes, and fibroblasts of other connective tissues, and also by odontoblasts and cementoblasts of dentin in teeth (20). In the skeleton (referring to bone and associated cartilage components), long bones develop from the embryonic stage throughout adolescence through endochondral ossification which occurs first via a cartilage model (anlagen) formed as a template for eventual mineralized bone formation (21, 22). As the naïve fibrous matrix consisting of smaller type II collagen fibrils and proteoglycans surrounding hypertrophic chondrocytes mineralizes, these cells die while at the same time allowing vascularization to import osteoprogenitor cells of mesenchymal origin (that become osteoblasts) (23) to begin the deposition of the first true collagen type I bone matrix onto cartilage, that mineralizes, and creates so-called mixed spicules. Ossification continues at the bony collar at primary and secondary centers (diaphysis and epiphysis, respectively), and continued bone remodeling allows for oppositional growth throughout adolescence (21, 22, 24). In some bones such as in the skull, intramembranous ossification occurs, this with bone formation originating directly from condensations of mesenchymal cells as opposed to be templated by a cartilage precursor.

In mature bone, while osteoblasts, osteoclasts, and bone-lining cells exist at the surfaces and at vascular canals, osteocytes that further differentiate from osteoblasts to develop long dendritic processes comprise 90-95% of all bone cells in an adult skeleton (25, 26). These osteocytes become "entombed" during the mineralization process that will be described throughout this work, but importantly as a result of this process they maintain their own lacunocanalicular network with a small margin of unmineralized organic matrix constituents and interstitial fluid remaining between the cell body or process and the mineralized matrix (27, 28). Osteocytes are critical to mention at this juncture because they are numerus within the bone collagen type I fiber system (the topic of Chapters 1 and 2). Additionally, interstitial fluid-induced strains within this network are a stimulus for mechanotransduction by osteocytes, this producing paracrine and endocrine signals targeting the aforementioned cells at the bone surface (as well as other distant cells) to remodel or model bone appropriately (28-30). A thorough description of the bone

remodeling sequence and the activity of osteoblasts and osteoclasts is beyond the scope of this writing, but it is eloquently reviewed elsewhere (31-33).

PRE-OSTEOBLAST	OSTEOBLAST	OSTEOID OSTEOCYTE	MINERALIZING OSTEOCYTE	MATURE OSTEOCYTE
Stro 1	Cbfa1	PHEX	DMP1	Sclerostin
CD29	Osterix	MEPE	CapG	FGF23
CD105	Alk Phos	E11/gp38		ORP150
CD166	Osteocalcin	Destrin		
	Casein Kinase II	Mt1-MMP		
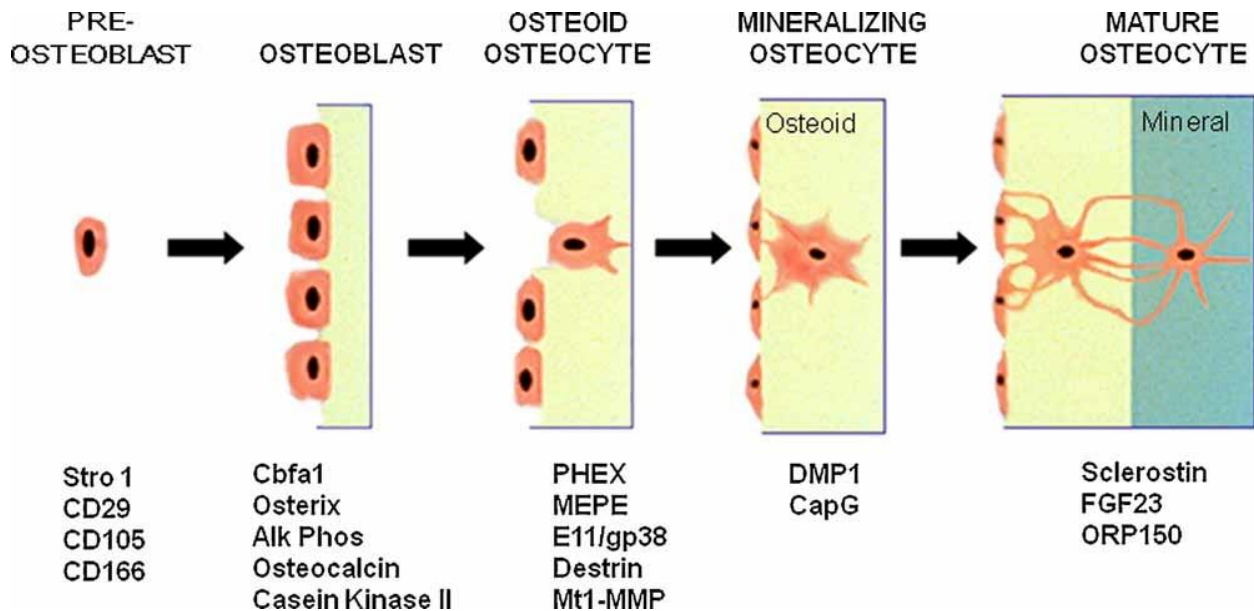
Introductory Figure 1: During endochondral and intramembranous ossification processes, osteoprogenitor cells differentiate into osteoblasts that secrete collagen type I and nonfibrous proteins essential to the mineralization process, while additionally expressing alkaline phosphatase and other biomarkers as indicated in the figure. Some osteoblasts further differentiate into osteocytes, producing proteins such as PHEX, E11/gp38, and members of the secreted integrin-binding N-liked glycoprotein (SIBLING) family such as MEPE and OPN. Osteoid osteocytes eventually become entombed in mineralized collagen matrix becoming mechanosensors within the LCN, and from there they influence mineral ion homeostasis and remodeling events which occur at the bone surface through secretion of proteins like FGF23 and sclerostin, respectively. *Figure from Bonewald et al., 2011 (34).*

Bone tissue is unique among the mineralized tissues discussed in this work in that it is widely adaptive and also may repair itself extensively after damage. Collagen type I fibrils of bone and their higher order structuring may therefore be modified over time to reflect the mechanical

loading environment to which they are subjected (35-38). Importantly, and at the same time, attachment sites of enthesis fibrocartilage that connect bone to tendons and ligaments develop from modular pools of progenitor cells (to follow elongation of the growing bone), expressing both cartilage- and tendon-specific transcription factors (39-41). Enthesis fibrocartilage also primarily contains collagen type I fibrils, with addition of some collagen type II (produced by cells called fibrochondrocytes) (42-44). Fibrocartilage does not remodel, at least certainly not to the extent of bone (45, 46). More formal details about the composition and characteristics of bone and enthesis fibrocartilage will be formally introduced below, and in Chapters 1-3.

The collagen family of proteins consists of 28 different proteins, and the biosynthesis of fibrillar collagens (types I, II, III, V, XI, XXIV, and XXVII) is complex (13). Collagen molecules are composed of three polypeptide chains containing repeat Gly-X-Y domains allowing for the formation of a right-handed helix with small Glycine amino acids located centrally, and are stabilized by hydrogen bonding. Briefly, after translation, procollagen α polypeptide chains are generated in the rough endoplasmic reticulum (47). Using a combination of α chains (produced from different collagen genes), which then also become post-translationally modified, the triple helix of procollagen molecules becomes assembled. In the case of collagen type I, a heterotrimer, there are two Col1α1 chains and one Col1α2 chain which assemble to form the procollagen triple helix (47). Transport of Col1 procollagen molecules through the Golgi apparatus is followed by secretion across the cell membrane in secretory granules (48), at which point, possibly during or after secretion, removal of steric hinderance by propeptide cleavage is facilitated by enzymes – whose cleavage also allows for the formation of intermolecular covalent crosslinks initiated by proteins of the lysyl oxidase (LOX) family (13, 48, 49). This crosslinking of end-overlapped collagen molecules occurs due to LOX-mediated deamination of N and C terminal lysine and hydroxylysine residues (telopeptide regions) to peptidyl aldehydes, allowing for condensation with adjacent residues and formation of aldimine intramolecular linkages with similarly processed Col1 molecules (50). Crosslinking of protein fibers of biological systems is absolutely essential for any resistance in tension (preventing fiber slippage) (13), and it may also vary to contribute to the diverse functionality of different tissues with fiber systems such as bone, tendon, or skin. Interestingly, further crosslinking occurring nonenzymatically after this stage through glycation and particularly associated with aging is thought to be detrimental (50), thus again highlighting the sensitivity of whole-tissue level mechanics to molecular and nano-level structural origins.

Within the extracellular matrix, and attributable to the location of molecular crosslinking at the telopeptide regions, each fibrillar type I collagen molecule (300 nm in length and 1.5 nm in width) is arranged into a staggered array with respect to adjacent molecules with a characteristic 64-67 nm overlap (8, 10, 51-53). This overlap zone creates a banded pattern that can be viewed in an electron microscope after staining, this being due to differing alternating organic densities in specific regions that result in variation in electron transmittance (contrast). Fibrils may be anywhere between tens of nanometers in diameter (naïve fibers of bone osteoid for instance) to hundreds (mature Achilles tendon), and several micrometers in length. In some tissues, further assembly into fascicles such as in tendon or ligament, or into braided, twisted, and branching bundles of collagen as seen in lamellar bone, may occur (9, 54). Finally, in some fiber systems such as in bone and cornea in vertebrates, and even in plant tissues, fibers or fiber bundles exhibit lamellar organization which are offset in their direction, but generally follow the principal direction of stress (the long axis of the tibia for example), or in the case of the cornea, allow for optical transmittance of light onto the retina (9, 15, 55, 56). In the case of the cornea, collagen fibers are arranged into ordered lamellae of different orientations creating a lattice structure to minimize the scattering of light (57, 58). Defective lamellar organization of this tissue leads to distortion of the cornea structurally, and furthermore results in a loss of visual acuity (13, 59). These examples of higher-order bundles and lamellar organization of fiber systems occur via self-assembly guided by chemical interactions between adjacent fibrils, with ordering also being thought to originate through a liquid crystalline phase (13, 15, 50, 60, 61).

After years of scrutiny, avian eggshell membrane fibers were also revealed to contain collagen (62-64), although significant complexity of these larger fibers, the lack of clear banding patterns, and their insolubility due to lysine-derived crosslinking has made it difficult to fully characterize the particular types of collagens that constitute specific fiber domains, such as the outer mantle and inner core regions of the fibers. Nevertheless, the eggshell membrane (see Introductory Figure 2) is an orthotropic network of fibers whose mantle and core constituents are produced by tubular gland cells in the hen's oviduct in the isthmus region, and which then assemble in the lumen of the oviduct as a membrane onto the egg white (formed more proximally)(65, 66). How the mantle and core regions of fibers, as well as other protein constituents, become assembled as a complete eggshell membrane remains largely unknown. One hypothesis is a gradient in expression of the proteins produced by tubular gland cells might first allow for "core" constituents

of fibers to assemble in the oviductal lumen, with mantle constituents being produced and secreted afterwards to adhere around and coat each of the cores.
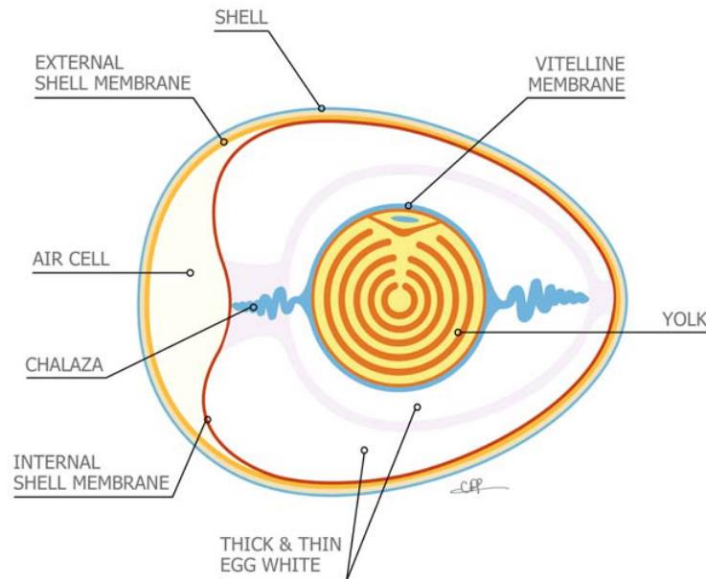
Introductory Figure 2: The interior of an avian (chicken) egg indicating major compartments and structures bounded by the shell. *Figure from Hincke et al., 2012 (66).*

Organic Extracellular Matrix Constituents

In addition to polypeptides that assemble into a variety of fiber systems, extracellular matrices consisting of fibers also contain other proteins and polysaccharides (67). These additional organic components of the extracellular matrix have a variety of functions as defined by their underlying amino acid sequence and posttranslational modifications including the ability to bind to inorganic mineral ions, provide attachment of cells to extracellular matrix, and/or attract water molecules. The organic constituents of the extracellular matrices relevant to Chapters 1-4 will be introduced now in the following paragraphs, followed by known roles of specific constituents in the mineralization process discussed in the next introductory section.

The three primary constituents of bone tissue (organics, minerals, and water) may vary slightly depending on the exact tissue location, individual age and health, and also vary at different size scales. By weight percent, collagen type I fibers constitute 90-95% of bone's organic extracellular matrix (68). Surprisingly however, in terms of molar amounts, noncollagenous proteins are as abundant as collagen (2, 11). Noncollagenous proteins in bone have additional structural roles, contribute to tissue development and remodeling, and regulate the process of mineralization. Prevalent noncollagenous proteins with diverse roles in mineralization (2, 12), bone remodeling (69), and cell-matrix interaction include osteocalcin and osteonectin (70), and other highly acidic and mineral-binding SIBLING family members, such as osteopontin (12, 71). Proteoglycans are another class of macromolecule containing a protein core that are critical to bone's mechanical performance (72). Attached to the core proteins are long chains of glycosaminoglycans (GAGs, polysaccharide) sugar molecules that have roles in mineralization and in maintaining tissue hydration (2, 15). Negatively charged sulfate and hydroxyl groups of these GAG chains bind water through electrostatic interactions (15). Other organic components within the bone collagen type I fiber system are lipids that are also thought to be important for structural integrity (73), and other small proteins and molecules such as enzymes, hormones, and growth factors (2, 21).

Contraction forces generated within muscle tissue are transmitted against rigid mineralized tissue (calcified cartilage and bone) as a means for movement in vertebrates. An important portion of this work in Chapter 3 specifically pertains to the Achilles tendon (which originates at myotendinous junctions to the lateral and medial gastrocnemius and soleus) and its insertion site into the calcaneus (74-76). The Achilles tendon is one of Nature's marvels and it is one of the thickest and longest tendons in vertebrates, although this varies based on the anatomy of particular species. Muscular contraction generates tension that is placed upon anisotropic tendon collagen type I fibers that are arranged into larger fascicles. This force enables plantarflexion of the foot which is critical for locomotion (77). Elongated tenocyte cells occupy spaces between tendon fascicles, adopting an orientation that minimizes mechanical consequence of this incorporation within this highly aligned network of collagen fibers (8, 78). These cells also secrete proteoglycans with branched glycosaminoglycan networks that help retain water, and therefore overall structural integrity (79). A small amount of elastin also plays a role in the tendon's ability to absorb and

transmit energy during movement (76). Other proteins such as matrix metalloproteinases and growth factors aid in promoting tendon remodeling and repair after damage (80).

Having a direct interface or attachment site between dissimilar organic and inorganic tissues poses mechanical challenges. This challenge occurs because of a phenomenon called stress concentration. Mineralized tissue with a higher elastic modulus will resist deformation more than adjacent unmineralized tissue with a low elastic modulus, and as a result a stress gradient having highest stress at the interface will result (81, 82). Having evolved over millions of years, enthesis fibrocartilage (also the topic of Chapter 3) is a unique tissue situated between the two tissues that have thus far been formally introduced – soft Achilles tendon (and a variety of other tendons, or ligaments), and hard mineralized bone (in this case the calcaneus), with properties of enthesis organic and inorganic constituents and their organization acting to dissipate stress along a wider gradient (83). Enthesis fibrocartilage is characterized by four zones – starting from the tendon zone, then progressing to uncalcified fibrocartilage, calcified fibrocartilage, and finally to bone. In the fibrocartilage zones, collagen type I fibrils are present along with collagen type II, and importantly large proteoglycans such as aggrecan, also having extensive branched glycosaminoglycan chains binding large amounts of water (42). Expectedly, the large proteoglycan content within this zone provides resistance to compression and contributes to enthesis viscoelasticity. In the calcified fibrocartilage zone, similar to bone, cells express enzymes that remove mineralization inhibitors (see next section). Other proteins such as those in the SIBLING family that are overwhelmingly found in bound mineral states play roles in the regulation of mineralization of this zone (84). Expression of collagen II and proteoglycans are maintained throughout this calcified fibrocartilage zone (42). In addition to the differential expression of proteins within enthesis fibrocartilage, organization over multiple length scales is a critical component ultimately contributing to the stress gradient at the insertion (83, 85). For example, in addition to the incorporation of other types of collagens, studies have indicated that fibers near the insertion change their orientation and curvature thereby promoting further distribution of forces at the nano- to microscale (74, 85).

With regard to the eggshell membrane, proteomics analysis has identified over 400 proteins, with 100 of those being highly specific to the membrane (64). Several families of proteins are present including collagens (62, 63), cysteine-rich eggshell membrane proteins (CREMPs), and AvBDs (64, 66). Other proteins include lysyl oxidase, which catalyzes the extensive

crosslinking of fibers in the membrane (in addition to widespread disulfide bonding), antimicrobial proteins such as histone proteins, ovocalyxin-36 and lysozyme (86), and a variety of glycoproteins including osteopontin (64, 66). Proteins of the ESM therefore broadly support its structure, help defend the interior of the egg against opportunistic organisms (87), and regulate where and how mineralization of the shell (originating at mammillae, otherwise known as mammillary cones or knobs) occurs (88, 89). With regard to the mantle and core regions of eggshell membrane fibers, it is largely still unknown which specific proteins constitute each region, although some immunohistochemistry work has been done for specific proteins within whole membrane fibers (62).

Mineralization

While the mineralization of fiber systems will be discussed in the following chapters, it will be first thoroughly introduced here. Biological fiber systems where mineralization occurs (through precipitation and growth of mineral crystals) become biocomposites and gain unique functional properties compared to tissue composed of only organic extracellular matrix components. Namely, mineralized fiber systems gain greatly enhanced resistance in compression. From an evolutionary perspective, this has offered advantageous functions such as protection during vulnerable developmental stages (eggshell), as well as protection of internal organs more broadly and creation of a rigid frame from which muscles can influence movement and counter gravitational forces (vertebrate skeleton).

Nanocrystal formation and local regulation

As opposed to geologic mineralization in which growth of crystals occurs unrestricted over large macroscale dimensions containing atomic order, biological mineral growth occurs within and accompanied by proteins and small molecules that also constitute the fibers and overall extracellular matrix. As a result, crystals having long range atomic order are typically very much smaller (at the nanometer scale), and minerals may be stabilized in transient, amorphous precursor phases (7, 89-91). From relatively ordinary constituent parts, variation in this crystal order, size, composition, orientation, and relation to organic constituents (and across multiple scales),

remarkably offers myriad possibilities to fine-tune mineralized fiber systems for particular functions (90, 92, 93). This is particularly true for bone where the matrix is consistently remodeled during the lifetime of an individual, roughly replacing the entire skeleton around every ten years or so, and adapting its structure based on an individual's mechanical loading history.

In bone, cartilage, and even the eggshell membrane, mineral nucleation and growth occurs at a so-called mineralization front within the fibrous matrix (94-97), then growing to eventually form mature mineralized extracellular matrix (7, 98). The mineralization front is an important site where 3D imaging at the nano- to microscales is conducted in the following studies. Indeed, this site offer a glimpse into the trajectory of mineralization therefore truly representing 4D study. Thus far, several different vertebrate collagen fiber systems have been discussed. The final portion of this introduction to the main text – which addresses the formation and structure of mature mineral units across the microscale of biological fiber systems – therefore will introduce how such biological control of mineralization is achieved. Specifically, how do cells illicit control over where and how minerals form, especially considering that there are perfectly suitable fiber systems of collagen (1, 15) for instance where mineralization would be incompatible with life, create enormous pain and discomfort (aorta, skin, tendons, and ligaments) (99-102), or in the case of the eggshell membrane – interfere with chick development and hatching.

In fiber systems of vertebrates which appeared more than 500 Ma ago, development of mineralized extracellular matrix involving collagen type I is thought to have evolved from fibrillar collagen orthologues in ancient sponges, cnidarians, and bilaterians (103). This process additionally involves numerous noncollagenous proteins and peptides, many of which are mineral-binding and have evolved from the ancient SPARC family giving rise to the small calcium-binding phosphoproteins (SCPPs) (70, 104), and some of which are included in the secreted integrin binding N-linked glycoprotein family (SIBLINGs), discussed below and in several of the main chapters. In the vertebrate systems discussed in Chapters 1-3, the mineral ions calcium and phosphorus which diffuse from the normal circulation are plentiful (2, 105, 106). Similarly, the fiber system of newly produced eggshell membrane (Chapter 4) now surrounded by oviductal uterine fluid is supersaturated with respect to calcium and carbonate ions (88). With an abundance of mineral ions generally surrounding many types of fiber systems, broad inhibition of mineralization in vertebrate fiber systems is achieved through the production of pyrophosphate (PPi), a small molecule byproduct of metabolic reactions resulting from the hydrolysis of ATP

(107). Two important regulators of PPi production are ENPP1, a pyrophosphatase, and ANK, a transmembrane protein which facilitates its transport to outside the cell (108). Other broad inhibitors that also help prevent pathological mineralization in a variety of tissues are the molecule citrate, and fetuin and matrix Gla proteins (102). PHOSPHO1 is also another phosphatase that may generate PPi by catalyzing dephosphorylation of various molecules (2, 108, 109).

Given this level of broad inhibition by PPi (110), how does physiological mineralization then occur in fiber systems like bone or cartilage? After differentiation of progenitor cell populations within fiber systems that normally mineralize, eventual expression of tissue-nonspecific alkaline phosphatase (TNAP) is the primary mechanism by which degradation of inhibitory extracellular PPi occurs (2, 107). For example, this enzyme is highly expressed by osteoblasts and osteocytes of bone, and also fibrochondrocytes within the calcified fibrocartilage zone (111). Not only does TNAP remove an inhibitory molecule from the extracellular matrix, but through cleavage of PPi it simultaneously generates local free phosphate now available for mineralization (108). Mineralization is generally thought to occur both directly through an appropriate Pi:PPi ratio created locally at sites within and around collagen type I fibers, and through vesicles released by cells into the extracellular matrix containing membrane-bound TNAP and loaded with mineral ions (108, 112). While this active pathway via cellular transport of mineral ions has been proposed for some tissues like during amelogenesis (113), it may be less energetically favorable in bone where the osteoblast and bone-lining cells do not form an epithelium and plentiful mineral ions from the circulation can simply diffuse freely between cells.

On top of broad inhibition by circulating PPi (and release from this inhibition in the normally mineralizing tissues (2, 110)), synthesis and secretion of acidic proteins – for instance ASARM (acidic serine and aspartate rich motif)-containing SIBLING family members (OPN, BSP, MEPE, DMP1, DSPP1) with polyaspartate and extensive phosphoserine residues whose phosphate groups bind tightly to minerals may act at the local level to influence mineralization. In addition to large stretches of negative aspartic acid and intrinsic disorder, extensive phosphorylation adds phosphate groups carrying net negative charge to what is normally an uncharged serine residue (12, 114). Indeed, these SIBLING proteins are typically highly expressed in tissues that do mineralize including by osteoblasts and osteocytes, chondrocytes (and fibrochondrocytes of enthesis fibrocartilage), and even in odontoblasts in dentin (12, 71). Osteopontin (OPN) is a particular SIBLING protein with highly acidic and intrinsically disordered

organization resulting in high affinity to calcium and the positively charged calcium in lattices with known localization to the mineralization front and interfaces such as the lamina limitans (delimiting the osteocyte lacunocanalicular network) (11, 71). While there is still considerable debate about the location of the earliest mineralization events within the crosslinked collagen type I matrix, outside the fibril there may be surface interactions with osteocalcin, BSP, and OPN that promote initial nucleation. Collagen amino acid stereochemistry around hole zones has also been implicated in the progression of these nucleation events of calcium and phosphate, this to proceed also in an intrafibrillar manner (115-118).

Concerning local regulation of initial mineralization at and around the organic mammillary cores, this within the uterus of a hen, sufficient availability of free calcium and carbonate mineral ions permits mineralization at these specific sites at the outer membrane fibers surface. However, what restricts eggshell membrane fiber mineralization below this point is still not entirely known, although it is thought to be broadly inhibited by several different calcium-binding proteins (66, 88, 119, 120). In addition to inhibiting mineralization at specific crystal faces (121), mineral-binding proteins such as osteopontin may additionally stabilize precursor amorphous mineral phases before their transition into a crystalline form of higher order. Indeed, the initial mineralization of avian eggshells at the outer membrane which does occur at mammillary organic cores is known to occur first through an amorphous phase that then forms calcite with the correct orientation such that further mineral growth occurs outward and then radially with respect to orthotropic eggshell membrane fibers – see Introductory Figure 3 below (89).
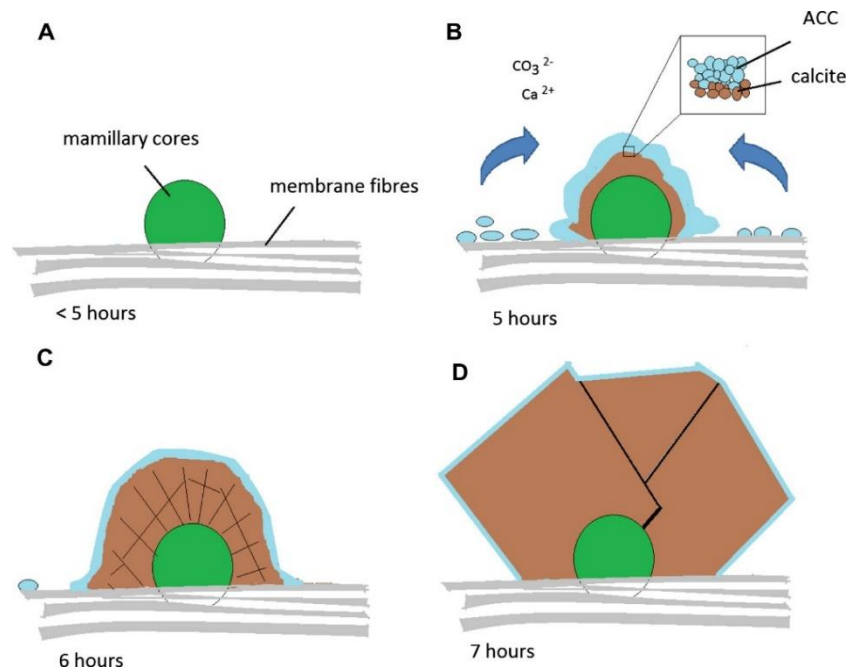
Introductory Figure 3: The time sequence of initial mineralization at the outer surface of eggshell membrane which first begins through an amorphous mineral phase which transitions into ordered crystalline calcite to form the mammillae at the base of the shell. ***Figure from Rodríguez-Navarro et al., 2015 (89).***

Mineral ion homeostasis

Diseases of hyper- and hypo-mineralization that affect vertebrate fiber systems such as bone and cartilage may therefore originate from a combination of factors including abnormal levels of mineralization inhibiting pyrophosphate molecules (107), mineral-binding proteins (122, 123), defects of the collagen fibers themselves (124-126), or also importantly from systemic factors that cause a lack of mineral ion availability (127). Extracellular circulating calcium levels are controlled by hormones and feedback mechanisms. Parathyroid hormone (PTH) is normally produced in response to low blood calcium levels sensed by PTH receptors (128). This hormone influences the activity of cells in bone, the kidneys, and intestine to mobilize and reabsorb calcium. In response to high calcium levels, another hormone called calcitonin is produced and has opposite effects to either sequester calcium (inhibit bone resorption) or inhibit its reabsorption (129).

Vitamin D that is synthesized in the skin and converted to its active form (calcitriol) is required for calcium reabsorption. Simultaneously, FGF23 is another hormone produced by osteocytes that regulates levels of serum phosphorus and indirectly influences PTH and calcitriol (130). In response to high serum phosphorus, FGF23 is produced to repress expression of NTP2 in renal proximal tubule cells that act to reabsorb phosphorus. Under low phosphorus, FGF23 production is reduced and NTP2 transporters are more highly expressed, acting to promote phosphorus reabsorption (127, 131). Interestingly, serum phosphate levels have also been linked to the release of PTH (130). FGF23 also inhibits conversion of vitamin D to its active form (132). Therefore, the interplay between PTH, FGF23, and vitamin D acts to regulate normal extracellular serum levels of calcium and phosphorus (133).

X-linked hypophosphatemia

X-linked hypophosphatemia is a rare inherited disease that will also be thoroughly discussed in this work and which manifests in patients as soft and deformed bones due to a combination of systemic renal phosphate wasting (134) and OPN accumulation locally within the extracellular matrix (123). This is one of the first mineralized tissue disorders to be assessed at the nano- to microscale with added context in 3D (here in the following chapters). The formation and structure of mineral units across the microscale in the mouse model of this disease is revealed in the following chapters, and importantly compared to normal wildtype mice. The origins of this disease, which affects about 1:20,000 individuals (12,000 individual in the United States), are inactivating mutations in the phosphate-regulating endopeptidase homolog X-linked (PHEX)(135). PHEX normally exists as a transmembrane protein with a large cytosolic domain regulating FGF23 levels by an indirect mechanism that is still not understood, and also by the binding and catalytic cleavage of its SIBLING substrate osteopontin in particular (136). Therefore, expression of PHEX by osteocytes, osteoblasts, odontoblasts, and in select other cells, influences systemic mineral ion homeostasis and local levels of mineral-binding osteopontin (123, 136). Chapters 1 and 3 investigate this combined effect of non-functional PHEX in the *Hyp* mouse model of the disease (having a truncating mutation in the *Phex* gene)(137), particularly at the mineralization front of lamellar bone and enthesis fibrocartilage where osteopontin has been shown to accumulate (11, 71, 123). Indeed, the following studies are the first to investigate a disease of mineralization deficiency with respect to its ultrastructural 3D structure. Organization at this scale of *Hyp* mouse bones and enthesis fibrocartilage is assessed with reference to the

formation of mineral units (crossfibrillar mineral tessellation) in normal mice, also characterized here for the first time in 3D.

3D Imaging of Biological Fiber Systems

By now it should be evident that functional properties of biological fiber systems originate from nanoscale relations between (for instance) individual alpha chains of collagen, that then form collagen molecules, and further associate to form fibrils, and bundles, and lamellae, that underly the structure of concentric osteons in cortical bone, to then comprise spongy trabecular bone typically found at metaphyses and epiphyses of long bones. Addition of mineral nanocrystals to this hierarchy, whose shape and form may be influenced by the collagen type I fiber network from the molecular scale and other noncollagenous proteins creates even further intricacy. Minerals may precipitate inside and outside of fibrils, crystals may adopt different sizes, or occur in different orientations within the fiber network or with respect to their intra- or extrafibrillar location. Noncollagenous mineral-binding proteins may inhibit growth of mineral crystals completely or stabilize amorphous precursor forms. The functional macroscale properties of mineralized fiber systems in Nature are heavily influenced from these nanoscale relations, and in three dimensions.

To gain an understanding of typical organization across the nano- to microscales, and to critically assess the structural relationship between inorganic mineral and organic fibers, X-ray and electron microscopy are necessary, specifically using specimen preparation protocols and microscope detectors that allow for the sensitivity required to generate contrasts that discriminate inorganic minerals from organic fibers in an image. Additionally, tomography (micro-CT and focused ion beam (FIB)-SEM in serial-surface-view mode), allow for generation of a 3D volume from 2D projections or image "slices", respectively. Dual-beam focused ion and scanning electron microscopy instruments were first used as a single system in the 1990s as a powerful tool for materials science and electronics applications. In this method, electron imaging is conducted on a blockface typically of an embedded specimen, and in sequence an ion beam (typically gallium) ablates a precise thickness of this blockface surface, typically to matching the x and y resolutions, before a next electron image of this ion-milled surface is captured. This process repeats for hundreds or thousands of slices and images to then be reconstructed into a volume. Through the

2000s this technique started to gain popularity in biological science (138) due to its ability to generate large image volumes (10s of micrometers in each direction) at unprecedented resolution (as low as 4nm isotropic voxel sizes) (139, 140). While correlative and multiscale imaging approaches are commonly used in structural biology studies, mineralized tissues are difficult to study because of the two phases which must both be assessed despite their different properties and behavior under an X-ray, electron, or gallium ion beam. Here, using repetitive osmium staining protocols (141, 142), relatively low electron beam voltages, combined with deep-learning based segmentation (143), and addition of cryopreparation protocols, this thesis represents one of the largest and most comprehensive collections of mineralized fibers systems where details of mineral units at the microscale and their functional implications are revealed in three dimensions.

Chapter 1: Crossfibrillar mineral tessellation in normal and *Hyp* mouse bone as revealed by 3D FIB-SEM microscopy

Daniel J. Buss[a], Natalie Reznikov[b], Marc D. McKee[a,c*]

[a]Department of Anatomy and Cell Biology, McGill University, 3640 University Street, Montreal, Quebec, Canada H3A 0C7

[b]Object Research Systems Inc., Object Research Systems, 760 Saint Paul West, Montreal, Quebec, Canada H3C 1M4

[c]Faculty of Dentistry, McGill University, 3640 University Street, Montreal, Quebec, Canada H3A 0C7
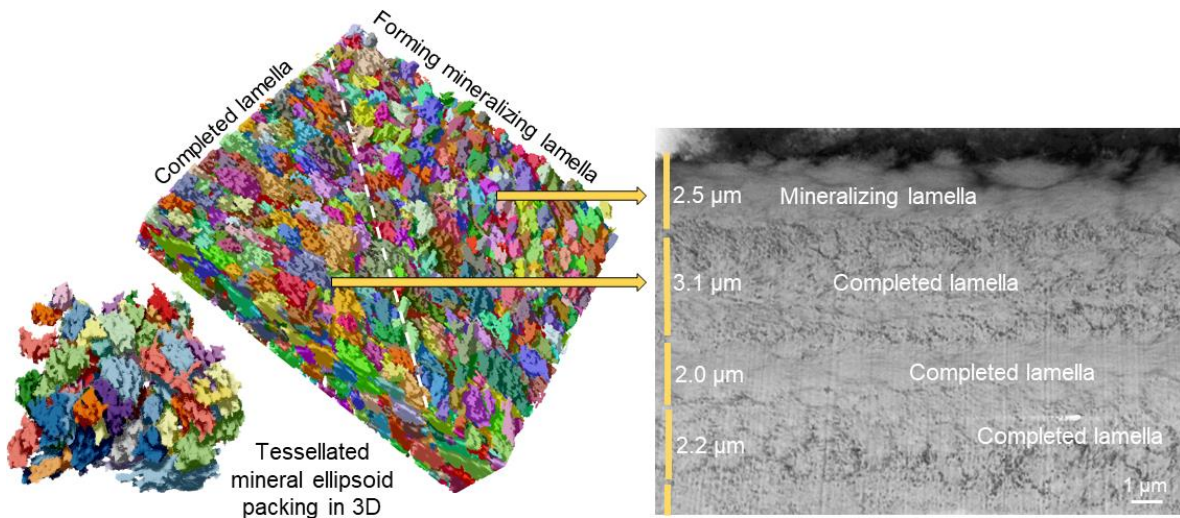
1.1 Abstract

In bone, structural components such as mineral extend across length scales to provide essential biomechanical functions. Using X-ray micro-computed tomography (μCT), and focused ion beam scanning electron microscopy (FIB-SEM) in serial-surface-view mode, together with 3D reconstruction, entire mouse skeletons and small bone tissue volumes were examined in normal wildtype (WT) and mutant *Hyp* mice (an animal model for X-linked hypophosphatemia/XLH, a disease with severe hypomineralization of bone). 3D thickness maps of the skeletons showed pronounced irregular thickening and abnormalities of many skeletal elements in *Hyp* mice compared to WT mice. At the micro- and nanoscale, near the mineralization front in WT tibial bone volumes, mineralization foci grow as expanding prolate ellipsoids (tesselles) to abut and pack against one another to form a congruent and contiguous mineral tessellation pattern within collagen bundles that contributes to lamellar periodicity. In the osteomalacic *Hyp* mouse bone, mineralization foci form and begin initial ellipsoid growth within normally organized collagen assembly, but their growth trajectory aborts. Mineralization-inhibiting events in XLH/*Hyp* (low circulating serum phosphate, and increased matrix osteopontin) combine to result in decreased mineral ellipsoid tessellation – a defective mineral-packing organization that leaves discrete mineral volumes isolated in the extracellular matrix such that ellipsoid packing/tessellation is not achieved. Such a severely altered mineralization pattern invariably leads to abnormal compliance, other aberrant biomechanical properties, and altered remodeling of bone, all of which indubitably lead to macroscopic bone deformities and anomalous mechanical performance in XLH/*Hyp*. Also, we show the relationship of osteocytes and their cell processes to this mineralization pattern.

1.2 Introduction

Extracellular matrix mineralization is a fundamental process in Nature regulated by complex, and often redundant, mechanisms. These mechanisms have evolved over time, allowing for precise control of structure and form in the biominerals found within many organisms. In healthy bone, mineralization of the extracellular matrix confers stiffness and toughness when appropriately assembled and organized, and sufficiently mineralized. In disease, mineralization

abnormalities can result in either hyper- or hypomineralized bones that are either brittle and easily fractured, or soft and deformed (with pseudofractures), respectively (144).

In bone mineralization, calcium and phosphate mineral ions combine through various precursor pathways to be deposited as crystallites of carbonate-substituted hydroxyapatite. Preventing (inhibiting) this mineralization pathway in soft tissues – where spontaneous pathologic crystal precipitation and growth would be debilitatingly destructive and often incompatible with life – are pyrophosphate molecules (PP_i) generated systemically from the hydrolysis of nucleotide triphosphates and other cellular metabolic processes (110, 145-147). With most body tissues appropriately inundated by this ubiquitous and circulating inhibitory PP_i, mineralization is generally inhibited throughout the body, thus blocking a default pathway that otherwise would permit mineralization when appropriate levels of mineral ions are present, as they generally are. Other systemic inhibitors exist, such as the circulating protein fetuin-A made in the liver (148), and great strides have been made in understanding how these biomolecules work as systemic inhibitors of mineralization. In the context of PP_i activity, selective degradation of this inhibitory molecule in bones and teeth is required for mineralization to proceed (147), and is achieved through local expression of the ectoenzyme tissue-nonspecific alkaline phosphatase (TNAP, also known as TNSALP or ALPL) in the skeleton and dentition – this enzyme hydrolyzes PP_i, (110) – as the initial step in a process recently referred to conceptually as the *Stenciling Principle* of biomineralization (149), described in more detail below.

While type I collagen is the principal structural organic component of bone matrix, and by far the most abundant in terms of mass, noncollagenous proteins and small proteoglycans collectively are present at a similar molar ratio, and expectedly, appear to have key roles in biomineralization (11, 150). The SIBLING protein family (small integrin-binding ligand N-linked glycoproteins) of the bone noncollagenous proteins have a particular importance in the mineralization process of bones and teeth because of their high negative charge and intrinsic disorder, allowing for binding to free and complexed calcium (12). One SIBLING family member – the phosphoprotein osteopontin (OPN) – functions in part to inhibit mineralization locally within the extracellular matrix of bone (151-153). OPN and other SIBLING proteins have approximately one-quarter of their amino acids as calcium-binding, negatively charged (by carboxylates) Asp and Glu, a protein net charge that can be further enhanced by post-translational phosphorylation of Ser residues (154). Dual inhibition of mineralization can be additionally achieved by the upregulation

of OPN expression by PPi, contributing to overall inhibitory activity in the tissue, and as modulated by dephosphorylation of OPN via TNAP which reduces its inhibitory function (145, 151, 155). This seemingly counterintuitive role for OPN as an inhibitor within the normally mineralizing extracellular milieu of bone argues towards a more refined function for OPN relative to PP_i through gradual (*i.e.* the extended process of protein synthesis and secretion by exocytosis, coupled with progressive enzymatic degradation) and sustained restriction of the extent of mineralization – as might occur, for example, where mineralization gradually encroaches towards cell-matrix interfaces (149, 156). Such critical interfaces for the regulation of mineralization in bone would include that between the osteocyte and its myriad cell processes interfacing with the OPN-rich *lamina limitans* (157) delimiting the lacuno-canalicular network, and that between bone-lining cells and the OPN-rich *lamina limitans* at the very surface of bone where osteoid mineralization eventually terminates (11).

In bones and teeth, an additional level of regulation of the extracellular matrix mineralization process is achieved through expression of the enzyme phosphate-regulating endopeptidase homolog X-linked (PHEX). This transmembrane enzyme functions through inactivating cleavage of its substrate – osteopontin – into small noninhibitory fragments (136), thus providing even further fine tuning of mineralization locally in the bone extracellular matrix. Taken together, these aforementioned levels of local cancellation of a more general inhibitory effect can be described as the hierarchical Stenciling Principle of the control of mineralization (149). This principle describes that there is initially a systemic prevention of default-pathway mineralization, with further downstream regulation by enzymes permitting (stenciling) mineralization by tissue-specific (bones and teeth) enzyme expression, which is then followed by local refinement (fine tuning) for optimal mineralization into forms and locations that provide for best mechanical performance.

Bone's hierarchical structure enables the merger of stiffness (the ability to withstand loading without macroscopic deformation) and toughness (the ability to dissipate impact energy without catastrophic failure) (158). These extraordinary properties – which are often mutually exclusive – originate from the scale of tens-to-hundreds of nanometers as exemplified by the intimate relationship between type I collagen fibrils and noncollagenous proteins, and the mineral with which they share more-or-less the same locale. Importantly, all these relationships occur within a hydrated environment and are facilitated by bound water (159-161). TEM investigations

by Nylen, Scott, and Mosley originally described the relationship between collagen and mineral crystals within fiber gap/hole regions in mineralizing turkey tendon (162). Around the same time, Ascenzi *et al*. reported on this process as it appeared in osteons, describing small foci of crystal inception originating in broad bands of the major collagen periods, and eventually growing in a manner which completely obscures fiber structure (7). Following this, Landis, Weiner, and Traub identified the nature of mineral precipitation and growth on arrays of organized collagen molecules – being both within and outside fibril gap/hole regions (4, 163). The confined geometries found within such an organized collagen fibril template are in fact thought to contribute towards decreasing the energy barrier for these nucleation events to occur (164), with recruitment of mineral ions facilitated by highly negatively charged and flexible noncollagenous proteins (165). This process also occurs in an extrafibrillar manner where the apatitic crystallites are often larger and somewhat curved/bent (166, 167), and where matrix vesicles may be active carrying mineral ions and the enzymatic machinery for mineralization. Additionally, extrafibrillar mineral is stabilized by noncollagenous proteins, citrate and water, all in a local environment where amorphous precursor states appear to play a large role (91, 108, 112, 168-171). Mineralization events therefore appear to occur quite heterogeneously, likely explaining the "built-in" redundancy afforded by Nature for something as vital as the vertebrate skeleton and dentition.

At the scale of microns, healthy mature lamellar bone is characterized by 3D assemblies of mineralized collagen fibrils grouped into bundles, found to be ordered into gently twisting and directional arrays with similarly aligned mineral (9). Between adjacent bundles, at the interfaces of parallel arrays of bundles (interlamellar boundaries), and near osteocytes, disordered collagen exists in a more chaotic state in which it is common to find osteocyte cell processes, and, significant amounts of proteoglycans and other noncollagenous proteins. At this micron scale, arrays of similarly ordered collagen bundles are observed as lamellae, and the osteocyte network within its vast lacuno-canalicular network is prominent. Cell bodies of osteocytes exist within the mineralized matrix in the fluid-filled lacunae in which they reside. These cells also have long processes that lie within channels called canaliculi. Within the lacuno-canalicular network, through these narrow interfacial regions around cells and processes of more compliant fluid-filled matrix, otherwise nominal strains experienced by the tissue as a whole can be amplified and sensed by the osteocyte through a variety of mechanisms (172, 173) that lead to critical signaling between bone cells (to regulate bone remodeling, for example). Development and maintenance of the nano-

and microscale dimensions of the mineralized matrix is therefore of utmost importance in not only ensuring function at any given point in time, but also in preserving key cell signaling pathways that govern the overarching homeostasis of this tissue over months and years.

Mineralization diseases with osteomalacia result from insufficient/deficient mineralization (hypomineralization) of the organic extracellular matrix, and they can be particularly severe. For example, hypophosphatasia (HPP) is an inherited genetic disorder characterized by inactivating mutations in the *ALPL* gene coding for the enzyme TNAP. With bone unable to rid itself of excess inhibitory PP_i in the absence fully functional TNAP, mineralization of the skeleton is considerably reduced, and the disease is often fatal if not treated by enzyme replacement therapy (107). In a different disorder – X-linked hypophosphatemia (XLH) – widespread osteomalacia is accompanied by a loss of fine tuning of mineralization at bone cell-matrix interfaces fails (96, 123). In this disease, inherited inactivating mutations of the *PHEX* gene result in severely hypomineralized bones and teeth (osteomalacia/odontomalacia) attributable to renal phosphate wasting (174). XLH patients, as well as the *Hyp* mouse model of this disease, present with short stature and bone deformities, with bowed legs, knock knees and atraumatic pseudofractures being common in the patients. *PHEX* is normally highly expressed by osteocytes, as well as by osteoblasts and odontoblasts. This transmembrane zinc metallo-endopeptidase regulates levels of the principal phosphatonin FGF23 and its substrate OPN (175). When PHEX activity is lost or decreased, increased levels of FGF23 result in decreased expression of class NaPi-IIa and NaPi-IIc renal transporters leading to phosphate wasting. Additionally, locally at the extracellular matrix level, in this absence or loss of PHEX activity, OPN (substrate for PHEX) accumulates at aborted/stunted mineralization foci in the osteoid, at bone interfaces such as at the mineralization front, and surrounding osteocyte lacunae and canaliculi in the lacuno-canalicular network (123). Accumulation of OPN at sites within the bone matrix correlates with hypomineralized peri-osteocytic lesions (POLs, "halos") of unmineralized bone around osteocytes (123), this likely altering the magnitude of matrix strains that these cells respond to, and perhaps causing changes in bone remodeling and even FGF23 production.

In trying to understand how mineral propagates throughout extracellular matrices of healthy mineralized tissues, and how this is dysregulated in osteomalacic diseases, here we used a combination of focused-ion beam scanning electron microscopy (FIB-SEM) operating in serial-surface-view mode and 3D reconstruction with deep learning (convolutional neural network)-

based segmentation to investigate mineral and matrix structure and relationships. More specifically we examined in detail the relationship of mineral with collagen bundles near the mineralization front in circumferential lamellar bone from normal (WT) and mutant (*Hyp*) hypomineralized mouse bone as a model for the osteomalacic disease XLH. Submicron-scale 3D analyses were also performed on osteocytes and their cell processes near the mineralization front to observe their relationship with mineral. Extending to the macroscale, and underlying bone's essential functions, we also used X-ray micro-computed tomography (µCT) to compare the full skeletons of WT and *Hyp* mice in 3D, which allowed for additional interpretation of the mechanistic basis for bone mineral hierarchical organization in health and disease.

1.3 Methods

1.3.1 Animals and sample preparation

Tibiae of normal male C57BL/6 wildtype (WT) and mutant *Hyp* mice with truncation in the *Phex* gene (aged 3.5-5 months) were dissected and trimmed to isolate the diaphysis. Initial 24 h fixation with 2% paraformaldehyde in 0.1 M Na cacodylate buffer was completed for all samples, followed by decalcification in 8% EDTA and 1% paraformaldehyde solution for select samples. All samples were stained with alcian blue for 4 h (pH 5.8) before a secondary overnight fixation in 4% glutaraldehyde.

After washing in 0.1 M Na cacodylate buffer, conductive staining was performed on all samples using repetitive exposure to osmium and thiocarbohydrazide ligand (OTOTO method). This repetitive exposure method was first used to "minimize charging within highly variable surfaces in vertebrate tissues" (176), subsequently for the staining of pollen for SEM (142), and then for the first time in decalcified bone for focused-ion beam (FIB)-SEM operating in serial-surface-view mode (see below) (9). Undecalcified samples were gradually dehydrated at room temperature to 100% acetone followed by infiltration and embedding in Epon epoxy resin. Dehydration for decalcified samples was accomplished at cryo temperatures by high-pressure freezing (Leica EM PACT2) and freeze substitution (Leica EM AFS2) followed by standard infiltration and embedding in Epon resin.

1.3.2 Focused-ion beam scanning electron microscopy (FIB-SEM) in serial-surface-view mode

Bone samples were analyzed by FIB-SEM microscopy operating in the serial-surface-view mode (also known as slice-and-view mode) using an FEI Helios Nanolab 660 DualBeam (Thermo Fisher Scientific). Embedded samples were trimmed, and light microscopy sections were used to define regions of circumferential lamellar bone near the bone surfaces of the diaphysis. The blocks were placed on a 45-degree holder and silver conductive paint was used around all nonimaging surfaces. Samples were sputter coated using a Pt target (Leica Microsystems ACE 600) to a thickness of 5 nm. FIB sectioning of each final volume was performed at a final probe current of either 2.5 or 0.79 nA, thus serially ablating 16-nm layers off the block face with sequential, iterative imaging performed with an SEM backscattered electron detector at 2 kV. A voxel size of 16 nm was used for all samples, obtaining data over volumes of 6000-9000 um³.

Dragonfly^{TM} image analysis and deep-learning software (version 4.1, Objects Research Systems Inc., Montreal, QC, Canada) was used to analyze all image data. Each of the SEM image stacks was registered with respect to similar features in adjacent slices using the "mutual info" tool. For segmentation of cell features, initial grayscale segmentation using the "range" tool was used, however, this nondiscriminatory technique is much less reliable when segmenting organic regions of interest due to its lower contrast ratio when compared to inorganic mineral within the same dataset. Even in the decalcified samples, grayscale values in UBYTE are limited, and delicate features such as cell processes and the *lamina limitans* of lacuno-canalicular network appear as similar values attributable to noncollagenous protein staining within the extracellular matrix. To most effectively deal with this issue, signal from the *lamina limitans* (as well as from other noncellular features such as cement lines/planes) were manually erased using the region-of-interest "ROI painter" brush, "smart grid", and "snap" tools on 10 pre-selected slices in each stack. Similarly, these tools were also used to add any areas of the cell body and processes that may have been originally excluded in segmentation of grayscale values. The corrected slices were then provided as training input for a convolutional neural network (CNN) using a default CNN architecture: U-Net with a depth of 5 layers and 64 convolutional filters per layer. This method of deep learning for segmentation is demonstrated as case studies in a review within this same special issue on mineralized tissues (177). The training set was partitioned into learning and validation subsets (80% and 20%) with data augmentation (1 iteration vertical and horizontal flipping). The

training parameters were the following: patch size was 32, stride-to-input ratio was 1.0, batch size was 64, and the number of epochs was 50. Following an initial segmentation using this trained deep-learning model, another 10 slices were manually corrected and used for further training of the same CNN for an additional 50 epochs with the same parameters. Small disconnected noise of less than 100 nm³ was excluded from the final segmentation using the "multi ROI analysis" operation. Subsequently, the final ROI was converted into a "mesh" with one round of smoothing, with spherical kernel size 3.

Mineral segmentation in undecalcified (mineralized) bone stacks was accomplished through global grayscale thresholding. Using the Boolean operation of subtraction, any remaining cell features that were distinguished via deep learning above were removed. Volume thickness heatmaps were then constructed using the "volume thickness map" operation. To create these maps, each mineral segmentation was simplified using the "smooth" operation, using k=3 for 5 rounds. Slight smoothing was necessary because of the heavy computational nature of this method. Construction of the volume thickness heatmap involves inscribing spheres of maximal possible diameters within the 3D foreground features. The range of the spheres' diameters is then color-coded between blue (smallest) to red (largest) using the "jet" look-up table. For the analysis of full mice (see below), this look-up table was modified across all samples to ramp nonlinearly in order to highlight all skeletal features (both normal and pathologic).

For analysis of the mineral tessellation pattern seen throughout the stacks of undecalcified WT bone, a small subset of 3 out of 1272 slices was corrected from the mineral segmentations. Despite these tessellations being apparent upon visual inspection of the raw data, simple grayscale segmentation was not robust enough to distinguish the small variations in grayscale values where tessellations abut. To generate an ROI of the actual tessellations, a CNN with the same architecture described previously was trained using the corrected subset. The training set was partitioned into learning and validation subsets (80% and 20%) with data augmentation (2 iterations of vertical and horizontal flipping). The training parameters were the following: patch size was 64, stride to input ratio was 0.5 (50% overlap of adjacent patches), and the number of epochs was 100.

The next task was to label each prolate ellipsoid as a unique object. Thus far an ROI was created from the prior deep-learning segmentation, however, many adjacent ellipsoids, although discrete, still made contact at several points. Keeping those volumes intact while labeling each tessellation as unique would allow the opportunity to quantify their individual size, orientation,

and location with respect to each other, and to other features in the bone such as collagen bundles. To perform this task, a "watershed transform" operation was performed. The ROI was inverted and a "distance heatmap" was created. From this map, cores or origins of each ellipsoid were selected using local thresholding. In the "watershed transform" operation, both the original segmentation and selected origins/seeds are used as input. Each individual label was expanded in 3 dimensions from the defined origin until it reached the boundary with an adjoining tessellated ellipsoid. Shadowing effects were used to highlight the texture and orientation of these 3D tessellations in certain figures.

Analysis of the sublamellar organization of collagen through each stack was completed using the Image J (Fiji) directionality plugin. Reznikov *et al*. 2013 originally used this method to describe the appearance of repeating sublamellar collagen domains – ordered and disordered motifs (9). This automated directionality analysis was based on gradient change of recognizable elements of similar thicknesses – the collagen fibrils. Output from this analysis was the average angular directionality of the fibrils in each slice, and their dispersion. High-dispersion values indicate a lack of fibril organization within any one slice.

1.3.3 X-ray micro-computed tomography (µCT)

In addition to the bone sample analyses described above, 3 whole WT and 3 whole *Hyp* mice were euthanized and whole mice were placed in 50 mL conical tubes with pre-drilled holes to allow for penetration and exchange of a solution of 4% paraformaldehyde and 1% glutaraldehyde in 0.1 M Na cacodylate, within a 1 L beaker in which they were suspended under agitation for 14 days. Mice were transferred to new dry tubes after 14 days and imaged by X-ray micro-computed tomography using an Xradia Versa 520 (Carl Zeiss Gmbh, Oberkochen, Germany). Scanning was performed with a 0.4x objective lens, 40 kV source voltage, LE1 filter, and exposure of 1 seconds per projection. Detector and source distances were optimized to create a voxel side length of between 30 and 35 µm for each mouse, with no binning. This small difference in pixel size, along with automated vertical stitching, was necessary to fit the larger full WT mouse projections onto the detector. Segmentation of whole bone (mineralized and unmineralized) was completed using Dragonfly™ software and a combination of global grayscale thresholding, "range tool", elimination of background noise via "multi ROI analysis", and elimination of noise from the conical tube (manually using the "shape" tool and "remove from

ROI" option).   Five rounds of object smoothing were used across each segmentation, with spherical kernel size 3.   This is the minimum smoothing option, lowering the computational expense of generating the aforementioned volume thickness heatmaps for each mouse.

1.4 Results

1.4.1 Characterization of the *Hyp* skeletal phenotype in 3D

Fig. 1A and Movies SM1A-WT and SM1A-*Hyp* (Supp. Material) shows WT and *Hyp* mouse whole skeletons at different ages as observed in 3D by µCT.   Segmented skeletons obtained from the reconstructed X-ray tomograms image stack are portrayed using a color-coded heatmap for bone thickness.   Prominent general features of the mutant *Hyp* mice include smaller overall stature and a substantial degree of thoracic kyphosis.   More specific abnormalities readily observed from the thickness maps include lower limb deformities presenting as shorter and thicker limb bones.   Enlarging the hindlimb (Fig. 1B upper panels, and Supp. Material Movies SM1B-LowerLimb-WT and SM1B-LowerLimb-*Hyp*) and thoracic/forelimb skeletal elements (Fig. 1B lower panels, and Supp. Material Movies SM1B-Thorax-WT and SM1B-Thorax-*Hyp*) revealed extensive flaring and thickening of the metaphyses in *Hyp* mice, as frequently found in severe cases of XLH and being most evident in the tibia.   In the forelimb/thorax region, a similar thickening of both the proximal and distal ulna and radius was evident in *Hyp* mice as compared to WT mice.   Another deformity frequently observed clinically in both hereditary and vitamin D-deficient forms of rickets – the so-called rachitic rosary of the rib (178) – has to date only been poorly documented in the *Hyp* mouse (179), but is clearly evident here when rendered in 3D, and it was observed in all three of the mice examined (Fig. 1A right panel).

1.4.2 3D nanostructure of the mineralization front in the tibial diaphysis of normal WT and mutant *Hyp* bone

1.4.2.1 Mineral foci and mineral ellipsoids in WT and Hyp bone

As correlated with conventional light microscope histology of von Kossa (for mineral)- and toluidine blue (for counterstaining)-stained undecalcified tibial diaphysis (Fig. 2A and B), regions of WT and *Hyp* bone with a readily identifiable mineralization front (active bone formation

site) were selected from these survey sections and were imaged in the FIB-SEM serial slice and view mode. After alignment of SEM image slices, the morphological landscape near the mineralization front in the WT bone (Fig. 2C, E and G) appeared well organized and with a well-established osteoblast layer, osteoid, a few forming mineral foci, and a packed, irregular ellipsoidal-shaped pattern of contiguous but discrete elements emerging at the mineralization front. Movie SM2E (Supp. Material) shows in 3D – moving in an *en face* trajectory from the outermost osteoblast surface, through the osteoid and then mineralization front, and finally into the interior of fully mineralized bone. From this perspective, the mineralization pattern (bright areas) emerges gradually as small mineralization foci related to the organized collagen fibril bundles that then enlarge into ellipsoidal structures that coalesce at the mineralization front but retain their discrete boundaries deeper into the bone lamellae. This mineralization landscape is dramatically altered in *Hyp* mouse bone viewed the same way by examining the whole FIB-SEM stack (Fig. 2D, F and H, and Supp. Material Movie SM2F). In this state of hypomineralization in *Hyp* tibia where there is substantially more unmineralized matrix (osteoid), there was a striking large number of isolated mineral foci and mineral ellipsoids, that unlike in normal WT bone, showed a significant delay in coalescence and failed to form a distinct, coherent mineralization front. Eventually, deeper in the bone, substantial but irregular coalescence was achieved. Additionally, in Movie SM2F (Supp. Material), an osteocyte residing in its lacunae appeared near the end of the image stack. In both WT and *Hyp* bone, packed mineral ellipsoids (tesselles) retained discrete visible boundaries. Segmentation of mineral only (Fig. 2G and H) reveals the relative extent and depth of the aborted mineral ellipsoid landscape in the extracellular matrix in the mutant *Hyp* bone volume as compared to the normal WT bone volume (also see Supp. Material Movies SM2G and SM2H).

Using the thickness-mapping feature of the reconstruction software in which a progression of sphere-size fitting is used to establish relative thicknesses (here describing mineral volumes), mapped throughout the mineral segmentation, there was a median size of around 0.9 µm for the mineral ellipsoids in WT mouse bone (Fig. 3 left panel). In the *Hyp* bone sample, where progression (enlargement) of mineral volumes is impaired, the dispersion of the mineral component was again highly visible within the depth/thickness of the sample, and the median size of the spheres was approximately 0.4 µm, roughly half that of normal WT bone, and with few larger than 2 µm (Fig. 3 right panel). This *Hyp* sample thickness heatmap also reveals the presence

of many aborted small mineral foci having measurements of only a few hundred nanometers (as also seen in Fig. 2D, F and H, and Supp. Material Movie SM2F).

1.4.2.2 Mineral ellipsoids mature into crossfibrillar mineral tessellations

In normal WT tibia, mineral foci clearly show a progression into packed prolate ellipsoids (Fig. 2C, E and G, and Fig. 4A, C and E). Maturing ellipsoids in these images (white arrows) join a growing/coalescing mineralization front yet they remain slightly but distinctly discrete as abutting tessellation (ellipsoid packing) starts to occur. While many of these tessellations can readily be seen as distinct structures without any tagging/labeling or pseudocoloring, a CNN was trained to differentiate tessellations from the boundaries where lower grayscale values appeared. Following this, a watershed transform operation was applied to label each tessellation as a distinct region. The coloring scheme in Fig. 4 shows the results of this CNN segmentation, revealing distinct boundaries for all tessellations in normal WT bone (left panels), and the impairment that occurs in reaching a similar level of tessellation in the *Hyp* bone (right panels). The relation of mineral ellipsoids to collagen bundles can be seen in Fig. 5. Bundles of around 1.5-2.5 μm at the mineralization front are described in Fig. 5A-D, with 5-10 mineral tessellations present in cross-section, or many tessellations along the length of a bundle. Tessellations and bundles having different orientation are shown through multiple lamellae in Fig. 5E and F. The lamellar period in which there is an observable change in this orientation appears as 2-3 μm (Fig. 5F).

1.4.2.3 Observations on the osteocyte network

Additional tibial volumes slightly deeper (near or beyond the mineralization front) were obtained to study osteocytes in 3D in normal and osteomalacic *Hyp* bone. Since sample charging often occurs in the dual-beam microscope during FIB-SEM serial surface viewing, these samples were decalcified after conventional fixation to allow for better penetration of conductive osmium staining to reach osteocytes deeper in the bone. Fig. 6, along with Movies SM6A-WT and SM6A-*Hyp* (Supp. Material) shows the results from these analyses. Deep learning-based segmentation was used to discriminate osteocyte cell body and cell processes (labeled in blue); in the WT sample, cement lines/planes, and *lamina limitans* lining the lacuno-canicular network, stained similarly and strongly with osmium (likely from the known accumulation of OPN at this site (11), and this imaging signal made segmentation difficult, so a deep-learning approach was applied

(177). In both the WT and *Hyp* bone, cell processes radiated with an overall directionality towards bone surfaces. The WT osteocyte shown here (Fig. 6A-C left panels, and Supp. Material Movie SM6A-WT) had existed fully encased within mineralized matrix of its lacuno-canalicular location just beyond the mineralization front. For the *Hyp* osteocyte shown here (Fig. 6A-C right panels, and Supp. Material Movie SM6A-*Hyp*), although at approximately the same depth into the bone as its WT counterpart, the cell existed in the zone where only a diffuse mineralization front was present on account of the typical *Hyp* osteomalacia, and thus there is no well-defined outline of a lacuna and canaliculi. Remarkably visible in this EDTA-decalcified *Hyp* bone volume is the bright osmium staining dispersed throughout the matrix evidently arising from the original close association and co-localization of noncollagenous proteins with mineral and thus demarcating the mineral's previous locations (180) – this sometimes being referred to as a "crystal ghost" pattern (181). In Fig. 6B, the volume thickness heatmap operation (*i.e.* sphere fitting) of the software was applied as described previously to the cell processes (excluding the cell body) for each segmentation. From this analysis for these two cells – one each from normal WT and mutant *Hyp* bone − there was a clear difference in the size of the osteocyte processes, where the WT cell-process diameters were generally under 150 nm (except for a few converging nodal connections), whereas the *Hyp* cell-process diameters approached 400-500 nm in several cases, with most processes being over 200 nm. Selected images from the FIB-SEM stack are shown for both samples in Fig. 6C.

1.5 Discussion

Skeletal structure in vertebrates is a product of both inorganic and organic material constructed and shaped in response to biomechanical demands placed by evolutionary pressure. These demands have largely resulted in there being a balance between sufficient mechanical performance, with the energy cost of maintaining this biological infrastructure (158). Under normal physiological circumstances, precipitation, growth, and refinement of inorganic calcium phosphate as apatitic mineral deposited throughout bone's organic collagen matrix, together with considerable amounts of noncollagenous protein and water, allow for a stiff tissue that also displays considerable toughness. It is the arrangement and structure of these individual material

54

components in the bone tissue that permit the diverse mechanical capabilities of the skeleton as a whole, and those of individual skeletal elements at different anatomical locations.

Diseases affecting bone in which there are alterations in the inorganic to organic material ratio, *i.e.* hyper- and hypomineralized bone, typically result in decreased mechanical performance. In osteogenesis imperfecta (so-called brittle bone disease) – a group of disorders characterized predominantly by collagen defects – there is impaired bone toughness and the brittle bone tissue frequently fractures under minimal mechanical loading (126). Hypermineralized bone has also been found in cases of osteoporosis, contributing to fracture risk in states of poor bone mass where toughness is already impaired (182). Conversely, hypomineralized osteomalacic bone fails because of excessive deformation and creep attributable to insufficient stiffness. In cases of rickets, abnormal levels of constituent mineral ions result in hypomineralization and growth plate abnormalities, with patients commonly having short stature and often bone deformities including *genu varum* (bowing of the legs) or *genu valgum* (knock knees) caused by plastic deformation of bones that are soft; other symptoms include, atraumatic pseudofractures, rachitic rosary of the ribs, and dental complications (183, 184).

With an inactivating truncation of the *Phex* gene (137), the skeletal phenotype of the *Hyp* mouse model phenocopies the osteomalacic inherited rickets disease X-linked hypophosphatemia (XLH). In examining the whole skeletons of these mutant mice by μCT and comparing them to normal WT mouse skeletons, and similar to what is seen in XLH patients, we show the expected smaller stature of these *Hyp* mice compared to their WT counterparts. Spinal abnormalities are a relatively common occurrence in XLH patients, and these likewise can be observed in *Hyp* mice (179). Here, in 3D from X-ray tomography, we corroborate the prominent kyphosis in these mice. Although this deformity appears to be poorly investigated in the context of rachitic disease, it may well occur from the thickening and/or fusion of vertebral bodies, as well as through enthesopathy at vertebral ligaments. Closer examination of individual bone anomalies in 3D, and using thickness maps for skeletal elements as generated by an application of the software we used, we were able to observe the full extent of skeletal deformities across the whole *Hyp* skeleton. This included the prominent, XLH-characteristic "rachitic rosary" showing a flaring/thickening of the ribs at their costochondral joints. Increased and thickened bone was also seen at long bone metaphyses and joints, this generally being thought to be a compensatory feature that resists bending and torsional forces in a mineral-deficient state (185). In general, these various bone

deformities in the *Hyp* mouse (and in XLH patients) may also be partly explained by disruptions in osteocyte-mediated mechanosensing arising from the well-documented peri-osteocytic lesions (POLs) where defective (hypo) mineralization increases matrix pliancy as sensed by osteocytes, and changes the degree to which strains are amplified into cues for bone remodeling (28).

This study was also undertaken to advance our understanding of the mechanistic basis by which mineral achieves its hierarchical organization in bone to provide it with its unique, resilient functional properties. Using the high-resolving power of FIB-SEM microscopy operating in serial-surface-view mode, we were able to reconstruct at the nano- and microscale mineral organization in 3D and in relation to collagen fibril bundles at the mineralization front in normal WT and mutant *Hyp* mouse bone. Physiologically, the growth of initial crystallites into mineral foci ranging from tens-to-hundreds of nanometers in size both within fibrils (these remain very small) and in the extrafibrillar space (these are larger) where specifically the negatively charged SIBLING family members (particularly OPN), have been precisely located (181, 186). Here, we build upon these 2D descriptions derived from conventional TEM micrographs to show in 3D how small nanoscale mineral foci enlarge to grow inside collagen bundles forming bone lamellae, to transform into micrometer-sized, packed and tessellated mineral ellipsoids (tesselles). While early crystallite growth is known to exceed the confines of the gap zone/D-spacing and the lateral dimensions of typical collagen fibrils in bone (7, 187), much less is known about what happens thereafter in terms of foci growth. Here we describe how small, initially nano-sized mineral foci, being roughly spherulitic (at least in the interfibrillar compartment) transform to enlarge along one axis – in this case we observe elongation of the polar *c*-radius with respect to the equatorial *a*-radius – as prolate ellipsoids towards the mineralization front. The subsequent steps of this ellipsoid growth process are described as tessellation, and the details for this are given below in Section 4.1.

Mineralization foci growth is clearly regulated by OPN, where over many years we have used high-resolution colloidal-gold immunolabeling to document the intimate relationship of OPN to these foci (69). This early work has been supported by numerous *in vitro* and *in vivo* studies from our group and from others (notably from the Boskey, Hunter and Goldberg, Gower and Millan groups) showing the importance of OPN and its peptides in regulating the mineralization process, including work done in human patients (123). Of particular importance, OPN and its bioactive fragments have been shown to be physiologically relevant substrates for the PHEX enzyme produced by osteoblasts and osteocytes (136). PHEX enzyme essentially completely

degrades OPN, gradually removing (inactivating) this mineralization inhibitor from the extracellular milieu allowing mineral growth to be carefully regulated, just as most intracellular pathways are carefully regulated. More specifically in this regard, where PHEX activity is absent or decreased (*Hyp*/XLH), OPN accumulates at aborted early mineralization foci, at the mineralization front, in the lacuno-canalicular network, and within peri-osteocytic lesions (123, 136). A similar pattern for OPN localization at the mineralization front is seen in osteomalacic *Fgf23*-knockout mice having highly elevated OPN (153).

While osteomalacia in *Hyp* mice is widely known to result in part from poor systemic phosphate availability (and thus bone tissue phosphate availability) because of renal phosphate wasting caused by elevated circulating FGF23 produced by osteocytes, much less known is the role of OPN in inhibiting mineralization locally within the extracellular matrix (149). Here, it would be expected that such an accumulation of this inhibitory protein could affect mineral foci growth. In the present study we show in 3D the combined actions of low phosphate availability (low circulating serum phosphate) and inhibitory OPN accumulation on mineral foci that would otherwise (in normal bone) transform into packed irregular ellipsoids of mineral that ultimately tightly tessellate within the collagen bundles of lamellar bone. In *Hyp* bone, this tessellation transformation is apparently stunted by both the low serum phosphate and by the increased OPN, to the extent that incomplete tessellation takes place, and peri-osteocytic hypomineralized lesions occur. Indeed, in XLH patients given oral phosphate supplementation as a component of standard treatment, this combined effect might be enhanced by the known induction of OPN by phosphate (188, 189). Morphologically, related to altered mineral foci growth in hypophosphatemia, these findings advance earlier SEM work in which it was noted that "the mineralizing fronts of the bone from patients with hypophosphatemic rickets typically showed an unusually wide range of orientation of the unjoined mineral particle clusters" (96). In the present work we show, both quantitatively and visually in 3D, the extent of this impaired trajectory for mineral foci development in *Hyp* bone that results in incomplete mineral ellipsoid tessellation at the altered mineralization front landscape characteristic of *Hyp*/XLH.

1.5.1 Crossfibrillar tessellation as a mineralization outcome of the packing of irregular mature prolate ellipsoids

As introduced above, the obvious disruption of mineral foci and ellipsoid growth and packing in *Hyp* mouse bone – attributable to low phosphate levels and increased inhibitory OPN – led us to further investigate this process of growth and fusion of mineral volumes under normal physiological circumstances. After looking at many samples of normal WT tibiae having smoothly milled (FIB) surfaces, a pattern was recognized near the mineralization front that extended into the bone across multiple lamellae. Mineral foci that had developed into mature ellipsoids and had joined the mineralization front appeared to remain slightly discrete with no complete fusion against adjacent abutting ellipsoids. This organization of abutting mineral volumes (irregular ellipsoids / tesselles) visible by eye in the microscope, formed the basis of what we now refer to as crossfibrillar tessellation. Using our 3D reconstruction deep-learning software, this pattern was recognized by a trained convolutional neural network (CNN) and was segmented over the full 3D analysis volume selected for the mineralization front. After applying watershed transformation for segmentation of these abutting tessellations, each were individually tagged (here shown with differing colors in our figures, but they can be readily seen even without coloring). Upon applying this same segmentation and labeling method to *Hyp* tibial bone, it was evident that there was much more spacing between the aborted mineral foci and the isolated mineral ellipsoids, as can even be observed by light microscopy. While some larger solid mineral volumes did appear, there was no *coherent* tessellation pattern visible within the analyzed volumes.

In surveying the literature, we were able to find some previously reported evidence (electron micrographs) of this crossfibrillar mineral tessellation. Using SEM, Bertazzo *et al*. noted similar "agglomerates of mineral plaques" in deproteinated rat femur and calvarial bone (190). Midura *et al*. likewise by SEM described "calcospherulites" in rat bone of similar appearance and size, being 0.5-1 μm in diameter (94, 191). More recently, Grandfield *et al*. reported on mineral "rosettes" in human femur where FIB sections viewed by HAADF-STEM seemed to match the appearance and size of the tessellations we describe when viewed perpendicular to the long bone axis (192). Finally, using SEM, Shah *et al*. reported on micrometer-sized, "marquise"-shaped motifs of bone apatite in rat calvaria (193). A similar pattern has also been noted previously for the distribution of organics (extracellular matrix) in decalcified bone that to some degree reflects the mineral pattern that we describe as tessellations. Following from early reports of "mineral

ghosts" (181) comprised of noncollagenous protein electron-dense staining in TEM corresponding to the general location, size and morphology of developing mineral foci, Reznikov *et al*. observed a differential intense staining "hour glass-like" pattern by FIB-SEM (194), again of similar dimensions to the crossfibrillar mineral tessellation pattern we report on here. Taken together, this evidence supports the notion that noncollagenous proteins (such as OPN enriched at these sites) regulate the formation of these μm-sized tesselles that have been reported by several groups in one way or another. Furthermore, dysregulation of this process in disease, for example by decreased phosphate availability and increased mineralization-inhibiting OPN (as in XLH/*Hyp*), would be expected to result in grossly inhibited mineral growth and organization (as we have documented here) leading to bone deformation and pseudofractures in osteomalacia. In Fig. 7, we summarize our understanding of the trajectory of mineralization events in WT and *Hyp* mice. Further, we describe the expected mechanical consequences of the final products of mineralization, with resistance to compression and bending at tessellated interfaces in normal WT bone, but slip or creep attributable to the irregular, aborted, mineral volumes in mutant *Hyp* bone.

At this point it seems noteworthy to underscore that the microscale subunit product of these mineralization events – tesselles – guided in their growth by mineral ion availability and noncollagenous proteins, exist not as a solid block-phase of mineral, but rather as discrete abutting entities tessellating throughout bone lamellae. Importantly, this tessellation first arises at the mineralization front from the moment when mature, irregular prolate ellipsoids derived originally from small mineral foci are large and finally abut against one another, while at the same time remaining discrete. Implicit in this growth trajectory is that the tesselles encompass (incorporate in a crossfibrillar manner) the collagen fibrils in the collagen bundles within which they grow and mature. While there is indeed some variation in size, particularly near the mineralization front, they generally appear as prolate ellipsoids approximately 0.5-1 μm in diameter when viewed in their shorter dimension, and 2-2.5 μm in length. Of note, these similar dimensions were described in the recent analysis of the "marquise-shaped motifs" found in bone (193). The tessellations are found in all the lamellae we examined, and they appear to occupy only the collagen bundles in which they form, and they do not cross bundle boundaries. When examined by electron microscopy, the tessellations are best viewed by backscattered electron imaging using a smooth, FIB-milled surface near the mineralization front.

1.5.2 Osteocyte morphology and peri-cellular (peri-lacunar) matrix pliancy

To examine osteocytes, some of our bone samples were preserved under cryo-conditions (high-pressure freezing followed by freeze substitution) to minimize cell shrinkage and other artifacts associated with conventional fixation and embedding protocols. From these samples, additional FIB-SEM volumes were obtained, and deep learning-based segmentation of osteocytes was performed, particularly to discriminate (for segmentation) between cellular and matrix osmium-stained structure. Using this approach, osteocyte processes were observed to extend primarily towards the endosteal and periosteal surfaces similarly in both normal WT and mutant *Hyp* bone. However, alterations in the dendritic cell process morphology became evident between the two samples when local thickness heatmaps were produced, with *Hyp* osteocyte cell processes appearing much thicker. Moreover, in these decalcified samples near the mineralization front where the WT osteocyte existed within fully mineralized matrix (before the decalcification procedure) in its lacuno-canalicular environment, the *Hyp* osteocyte existed in a zone of incompletely mineralized bone replete with its collagen but with noticeably abundant noncollagenous protein matrix (in part excess OPN) in this hypomineralized region of the *Hyp* sample.

This knowledge of osteocyte relations with a surrounding hypomineralized bone matrix in XLH/*Hyp* allows for conjecture about how osteocyte cell signaling might be affected in this disease state. Our work is supported by previous studies showing the well-documented peri-osteocytic lesions (POLs) where unmineralized matrix surrounds entire osteocytes. Steendijk and Boyde noted frequent circumlacunar lesions or unmineralized "lids" of lacunae in the bone of hypophosphatemia rickets patients that appeared together with a disrupted mineralization front, correctly hypothesizing about osteocyte control over mineralization given the minimal evidence at the time (96). Not only do we now know that changes in osteocyte signaling result in profound mineralization defects both locally at peri-lacunar sites in the matrix and in bone as a whole through its role as an endocrine cell pertaining to FGF23 and likely other factors (195), but we are also starting to understand the role that alterations of the peri-lacunar environment (such as in XLH/*Hyp* bone) plays on biomechanics (196). Moreover, osteocytes are central to mechanosensing and bone homeostasis programs, events clearly dysregulated given the altered osteocyte cell geometries within a hypomineralized matrix that we have shown. More generally and unrelated to any pathology, these data also speak to the heterogeneity of the osteocyte cell

population. In previous FIB-SEM investigations on osteocytes in normal bone, Hasegawa *et al*. noted thicker, "stout" processes with what could be considered as "distribution hubs" near the mineralization front (the samples were also decalcified) (197). We see evidence of this here as well, particularly in the *Hyp* bone sample residing in the more-pliant, unmineralized matrix. It remains entirely possible, and even likely, that subsets of osteocytes exist before (osteoid osteocytes), at, and beyond the mineralization front where cell morphology and interactions with matrix and mineral contribute to their gene expression and signaling programs (26). Further investigation using volume-based microscopy methods sensitive enough to discern nanoscale cell geometries such as delicate/thin cell processes, with the sharing of more streamlined protocols between researchers, and using deep-learning approaches for refined analyses, will be key to advancing this topic further.

1.5.3 A new paradigm for lamellar organization and mineral packing in bone

Given the observations we have made for mineral form and packing at the microscale in bone, we propose to expand the current comprehensive view of the hierarchical organization of normal bone to now include the presence of micrometer-sized crossfibrillar mineral tessellations. It could be considered that evidence for such tessellations might be construed by finer scale observations on the organization of bone mineral such as by descriptions of mineral rosettes by TEM (192) and mineral aggregates by STEM (54). However, beyond this, here we demonstrate in normal bone an extensive and pervasive packing pattern for mineral (true tessellation) at both the nano- and microscale, with discrete, interface-rich packing of mature prolate ellipsoids (tesselles) within ordered collagen arrays. This periodic structuring paradigm for mineral organization differs from the former hypothetical view that mineralization of the extracellular matrix in bone is both generally solid and continuous over the many dimensions beyond the well-characterized mineralization events related to the collagen D-spacing structure (gap/overlap zones).

Collagen fibrils within lamellae are organized into distinct bundles – although merging and splitting – which range between 2-3 µm in cross-sectional diameter (194, 198). These three-dimensional collagen bundles co-aligned within one lamella contain a patchwork of tessellated and staggered, packed prolate ellipsoids of slightly differing sizes and irregularity: 3-4 ellipsoids roughly span the transverse dimension of each collagen bundle. The co-existence of the bundles of the collagen phase and the smaller-scale mineral tessellations that populate the bundles is

schematically depicted in Fig. 5D. Within each bundle, the longer axes of prolate ellipsoids are co-aligned with their bundle axis. Any layer of ordered collagen bundles (that are populated by abutting tessellated mineral ellipsoids) and an adjacent layer of ordered collagen bundles (populated by their own set of mineral ellipsoids) are identical except for having different orientations. Although the periodicity of bone lamellae – as canonically inferred from polarized light microscopy or electron microscopy observations – results from pairs of adjacent layers of bundles combined being 4-6 µm thick (7, 198, 199), we now demonstrate that every such pair consists of angularly offset, nearly identical sublayers, each being 2-3 µm. The assembly of angularly offset layers of parallel bundles that contain submicrometer-sized tessellated ellipsoids is shown in Fig. 5D.

1.5.4 Comparisons with other mineral tessellations in biology

Tessellation is a common theme in Nature, particularly in the field of biomineralization where stiffness and toughness are routinely required. For example, tessellated cartilage or "tesserae" of "abutting, mineralized, hexagonal blocks, are prominent features at the scale of millimeters in the skeleton of elasmobranchs (200). Some members of this family – such as myliobatid stingrays – crush hard mineralized structures in their prey using tessellated "pavement-like tooth plates" (201). In turtles, the carapace of its shell use hierarchically organized, interlocking, alternating rigid and flexible elements to achieve stiffness, strength, and toughness at a low weight (202). Similarly, the armadillo carapace uses tessellated mineral tiles connected by collagen fibers – this proving advantageous for thwarting the keratin-based claws of predators (203). There are many other examples of biological tessellation, and this theme has been used in bioinspired materials design. The "tablet sliding" principle of mineral tessellation as seen in mollusk-shell nacre was used to design a superior impact-resistant glass through internal laser etching (204). Tessellated assemblies with minimal stagger are more adapted for flexibility and toughness, while those with extensive stagger are stiffer (205). In support of this, increases in the mineral content of staggered composites are responsible for larger changes in elastic modulus, as modeled by Bar-On and Wagner (206).

1.6 Conclusions

This study describes a trajectory and a product of mineral growth in bone from the nano- to the microscale. It also provides for additional understanding of the hierarchical organization of bone at the level of mineral integration with collagen fibril bundles and their organization into lamellae. We also present a new understanding of the periodicity of bone lamellae based on the tessellation feature we describe – an alternative model describing a lamellar periodicity of only 2-3 µm. Additionally we discuss the importance of appropriate development and maintenance of tessellated interfaces, much of which occurs through the inhibitory actions of noncollagenous proteins (such as OPN) and the enzymes that remove them (such as PHEX); as such, we highlight the Stenciling Principle of biomineralization in which the interplay between inhibitory molecules/proteins and tissue-specific enzyme expression (for which the inhibitory molecules are the substrates) promotes and refines mineralization. Further 3D investigations into the nature of tessellated inorganic-organic arrangements in other normal mineralized tissues will be critical in establishing this as a universal strengthening mechanism. Finally, we describe defective mineral foci and ellipsoid growth in XLH/*Hyp* as interfering with the normal mineral tessellation program such that a mechanistic view of the weakened mechanical properties of osteomalacic bone can be explained. We additionally describe in *Hyp* mice the altered relationship between abnormal early osteocyte morphology and mineral distribution in the osteomalacic extracellular matrix of bone – a circumstance that likely leads to dysregulation of cell signaling important to the homeostasis of healthy bone.

1.7 Declaration of Competing Interest

Natalie Reznikov discloses that she consults for Object Research Systems Inc. in Montreal, but has no financial stake in the company.

1.8 Acknowledgements

Fig. 1. **Volume thickness heatmaps of normal WT and mutant *Hyp* skeletons imaged by μCT**. Complete skeletons (A) and regional bones (B) of normal WT and mutant *Hyp* mice at different ages, as indicated, revealing the extent of the *Hyp* phenotype in terms of stature, deformities and thickness changes. Compared to WT mice, *Hyp* mouse skeletons are smaller,

show prominent spinal kyphosis, have many long bones that are deformed and thickened with flaring metaphyses, including an obvious "rachitic rosary" of the ribs. See also Supp. Material Movies SM1A-WT, SM1A-*Hyp*, SM1B-HindLimb-WT, SM1B-HindLimb-*Hyp*, SM1B-Thorax-WT, and SM1B-Thorax-*Hyp*.
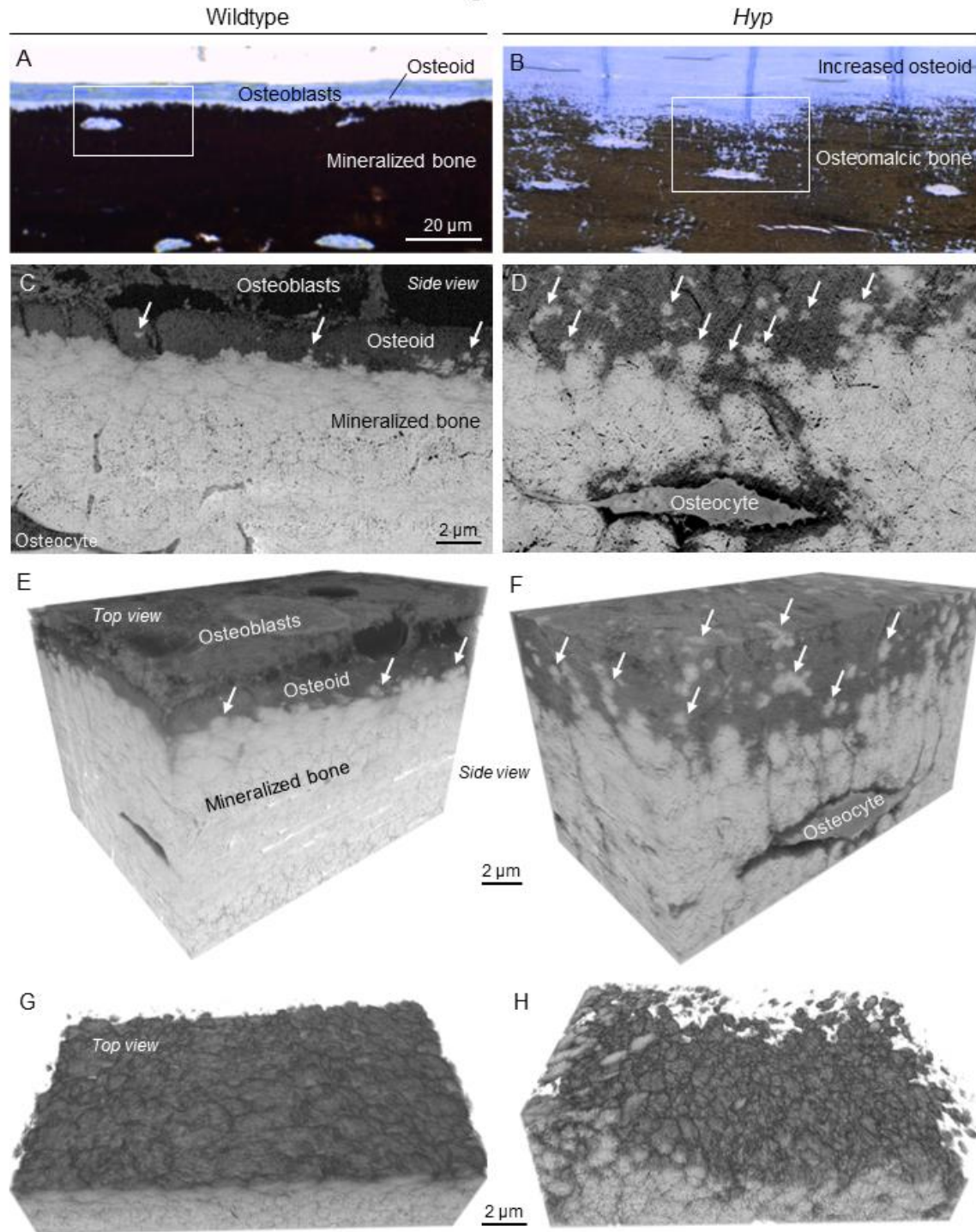
Fig. 2. **2D and 3D imaging of the mineralization landscape near the mineralization front at the tibial diaphysis in undecalcified normal WT and mutant *Hyp* adult mouse bone**. (A,B) Light microscopy of von Kossa- and toluidine blue-stained sections, and FIB-SEM (C,D) selected SEM images and (E-H) 3D reconstructions showing mineral ellipsoids (arrows) growing from

mineral foci in the extracellular matrix near the mineralization front. Reconstructions G and H of mineral are after segmentation to exclude unmineralized matrix and cells from the dataset excluded (from the same datasets shown in C-F). Note the increased number of aborted and smaller mineral foci/ellipsoids in the osteomalacic (hypomineralized) *Hyp* mouse bone. See also Supp. Material Movies SM2E, SM2F, SM2G and SM2H.
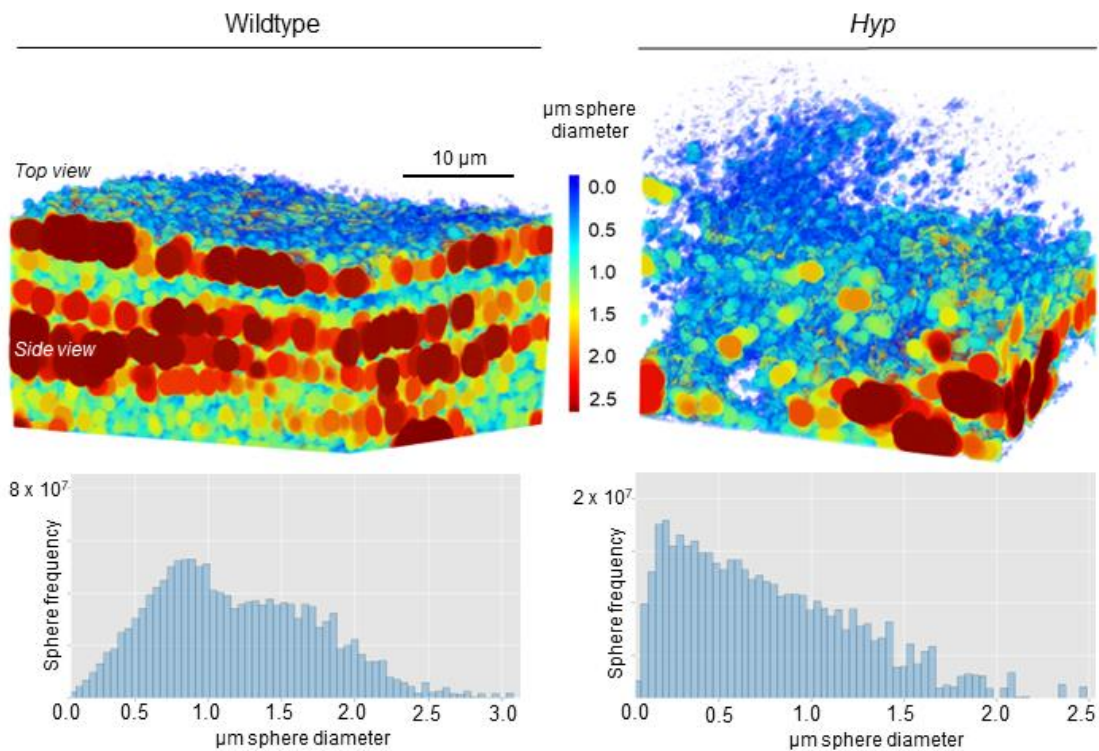
Fig. 3. **Volume thickness heatmaps and plots of mineral ellipsoids near the mineralization front of bone in the tibial diaphysis of normal WT and mutant *Hyp* mice**. Computational sphere fitting is applied by expanding spheres at random points in the dataset until a boundary is reached, at which time the sphere diameters are recorded and color heatmapping is produced to describe the overall trajectory of mineral foci and mineral ellipsoid distribution and growth. Note the increased number of smaller ellipsoids in the *Hyp* mouse bone
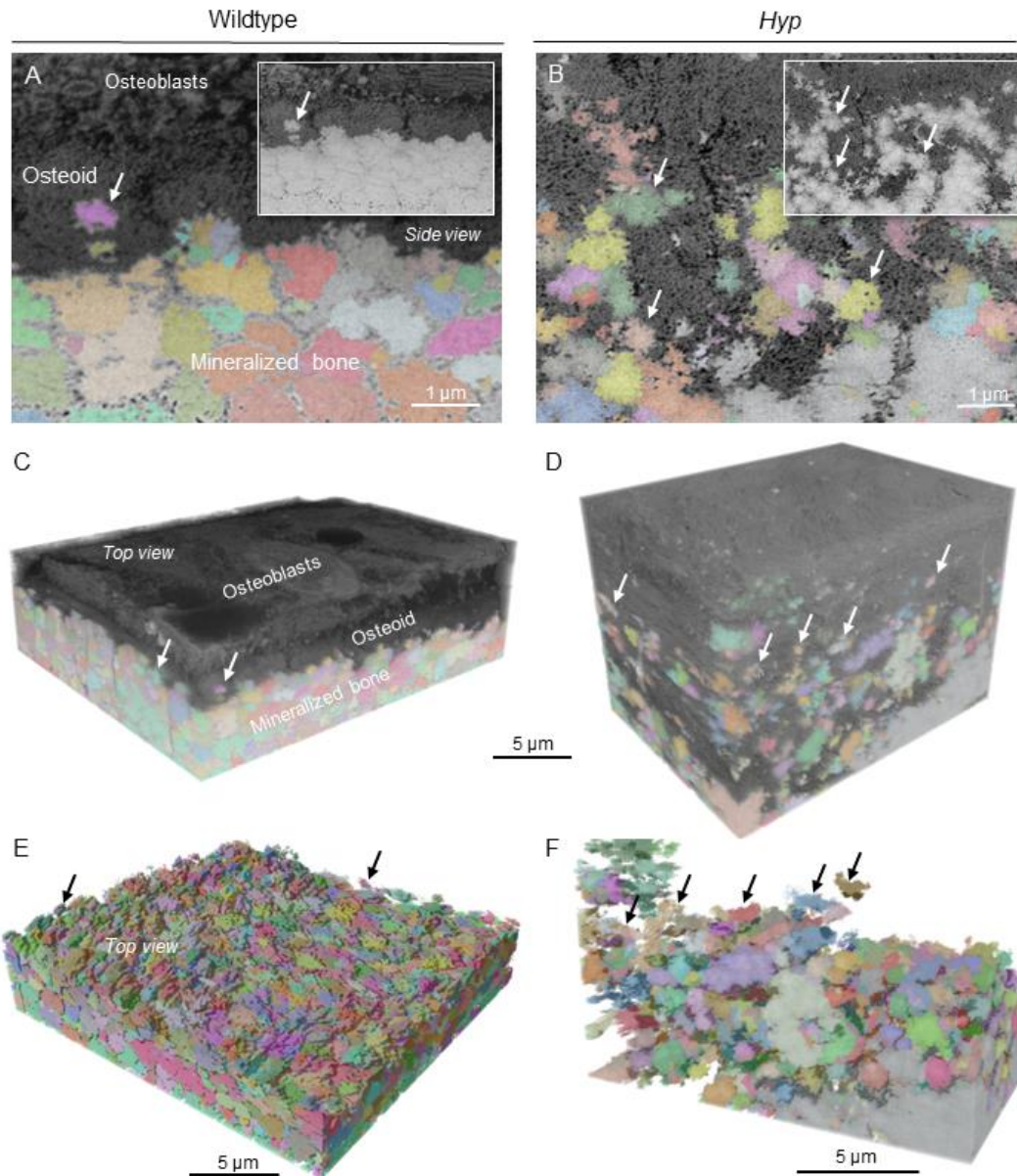
Fig. 4. **FIB-SEM reconstruction, segmentation, and labeling (coloring) of discrete and abutting mineral prolate ellipsoid volumes in undecalcified samples near and beyond the mineralization front in normal WT and mutant *Hyp* adult mice**. (A,C,E) In WT bone, mineral ellipsoids (arrows) deriving from mineral foci grow into irregular crossfibrillar tessellations (tesselles) whose packing can be observed across the entirety of the mineralization front volume. (B,D,F) In osteomalacic *Hyp* bone, there is defective growth, organization and packing of the mineral ellipsoids (arrows) with no contiguous mineral tessellation pattern occurring at this tissue depth within the tibia. Reconstructions E and F of mineral are after segmentation to exclude unmineralized matrix and cells from the dataset (from the same datasets shown in C and D).

69
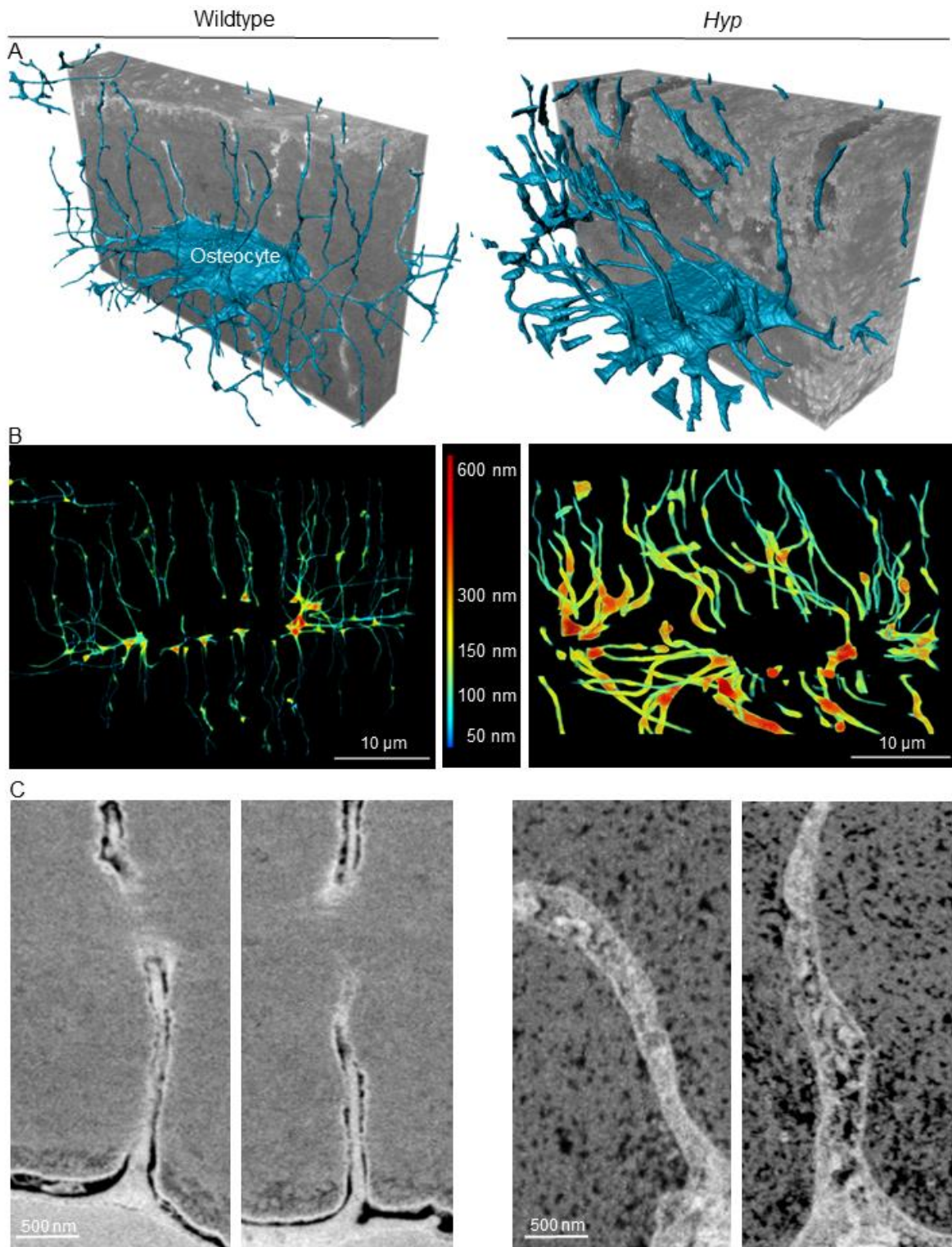
Fig. 5. Incorporation of crossfibrillar mineral tessellation within the lamellar structure of normal WT bone. (A,B) Assessment of collagen bundle thickness and spacing by intensity profiling after FIB-SEM. See also Supp. Material Movie SM5A. (C) Single FIB-SEM image

showing the relationship between collagen bundles in cross-section and the pseudo-colored mineral tessellations that occupy their volume in mineralized bone. (D) Schematic diagram of the prolate mineral ellipsoid packing that provides crossfibrillar mineral tessellations occupying collagen bundles (here the collagen bundle volume dimensions are depicted as voids) that results in an adjacent lamellar offset by an indefinite angle. (E) Full segmentation and labeling/coloring of tessellations at the mineralization front within two lamellae, and a portion of this at higher magnification in the lower left corner. See also Supp. Material Movie SM5E. (F) Single SEM stack image of several bone lamellae from the side view near the mineralization front (osteoid towards top of the figure) where packed prolate ellipsoids/mineral tessellations can be readily seen either longitudinally or more-or-less in cross-section depending on the lamellar angle with respect to the imaging surface. Insets show top views likewise depicting prolate ellipsoids of mineral with their long axes aligned parallel to each other and to the long axis of the collagen fiber bundle within which they are situated; as mineralization proceeds, the ellipsoid growth trajectory packing progresses towards crossfibrillar tessellation. Dashed lines demarcate clearly distinguishable, well-developed mineral ellipsoids. All samples are undecalcified to show both mineral and collagen relationships.
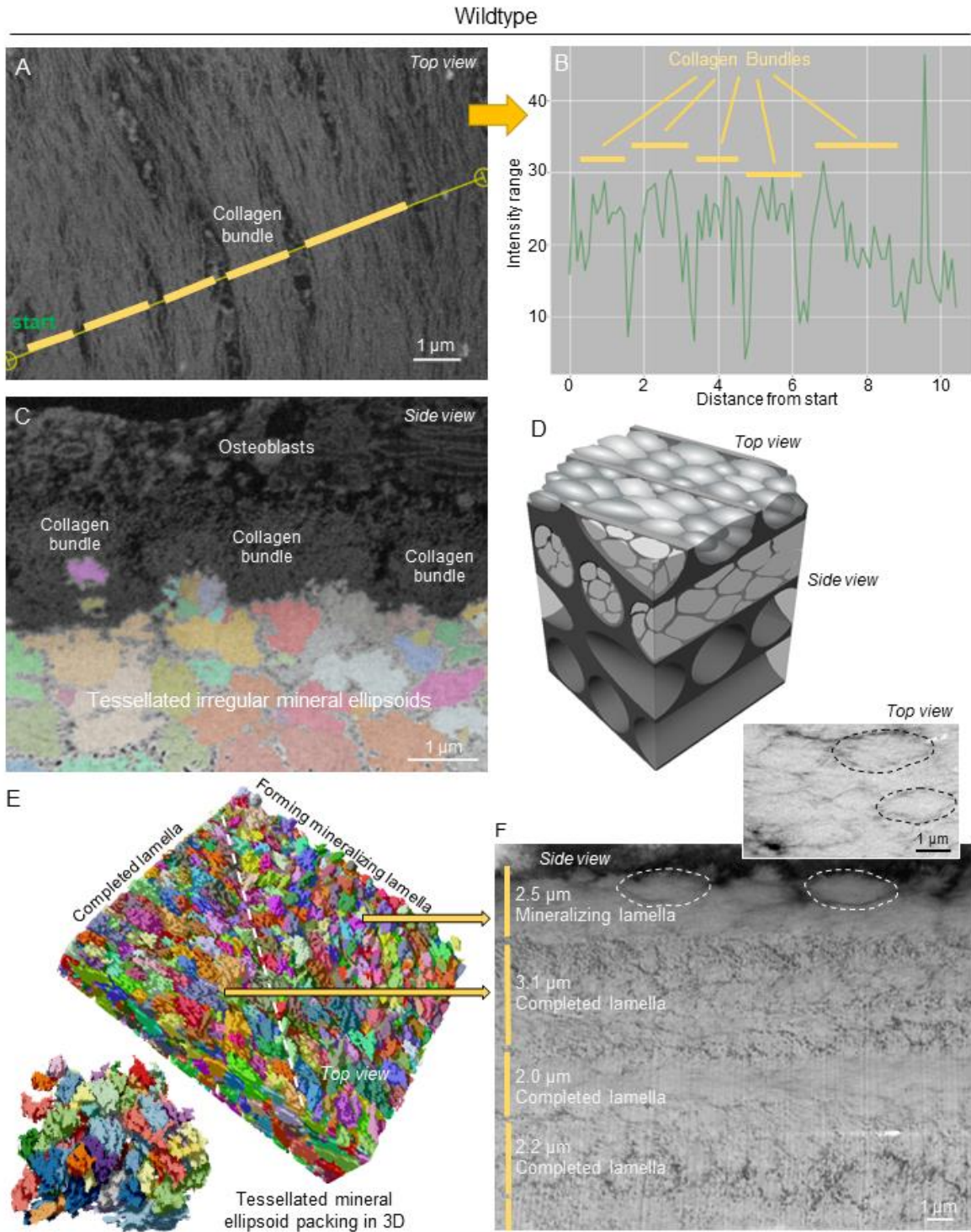
Fig. 6. **FIB-SEM reconstruction of the osteocyte network in the tibial diaphysis of normal WT and mutant *Hyp* adult mice**. (A,B) Deep learning-based segmentation of osteocytes and their cell processes (blue). Note the thickened cell processes in the *Hyp* osteocyte. Brighter regions

are from osmium staining of noncollagenous protein accumulation in association with the defective mineralization landscape in these samples of decalcified *Hyp* bone, and the lacuno-canalicular system is not well-established in this region near the mineralization front, this differing significantly from the WT scenario. In WT decalcified bone, the brightest osmium-containing areas correspond to the *lamina limitans* layer delimiting the lacunar and canalicular walls, and a cement line/plane in the upper left corner. See also Supp. Material Movies SM6A-WT and SM6A-*Hyp*. (B) Volume thickness heatmaps of cell processes only after deep-learning segmentation showing thicker osteocyte cell processes in the *Hyp* bone sample. (C) Selected single SEM images of cell processes from normal WT and *Hyp* mice, again illustrating the increased thickness of the processes in the *Hyp* mice.
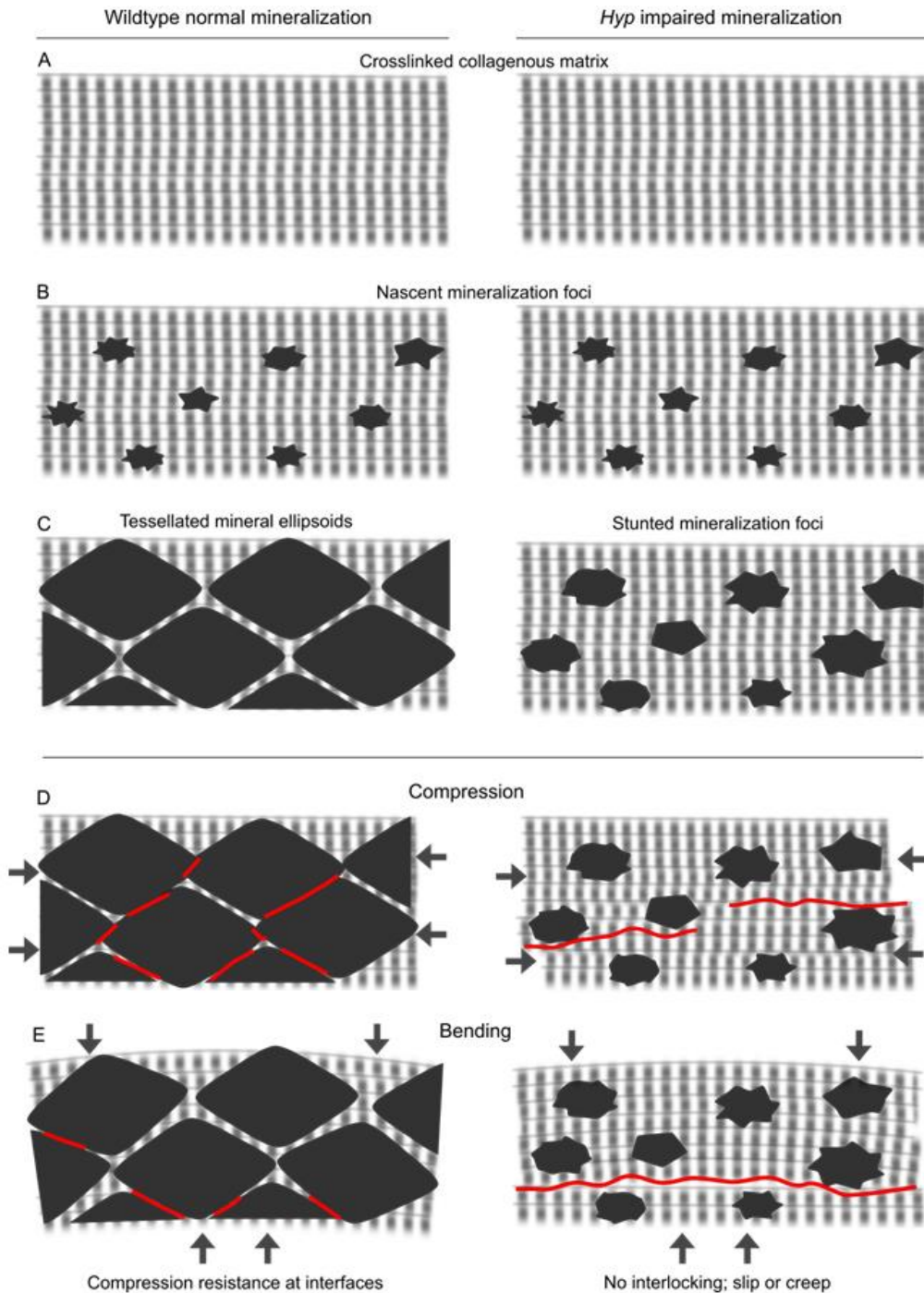
Fig. 7. Mechanistic effect of normal crossfibrillar mineral tessellation and the lack thereof in *Hyp* mice. (A-C) Schematic diagram of the trajectory of mineral nucleation, and mineral foci and mineral ellipsoid growth, in WT and *Hyp* bone. (D,E) Anticipated mechanical behavior of normal and *Hyp* bone under compression and bending stresses. Red boundaries indicate the sites of maximal strain.
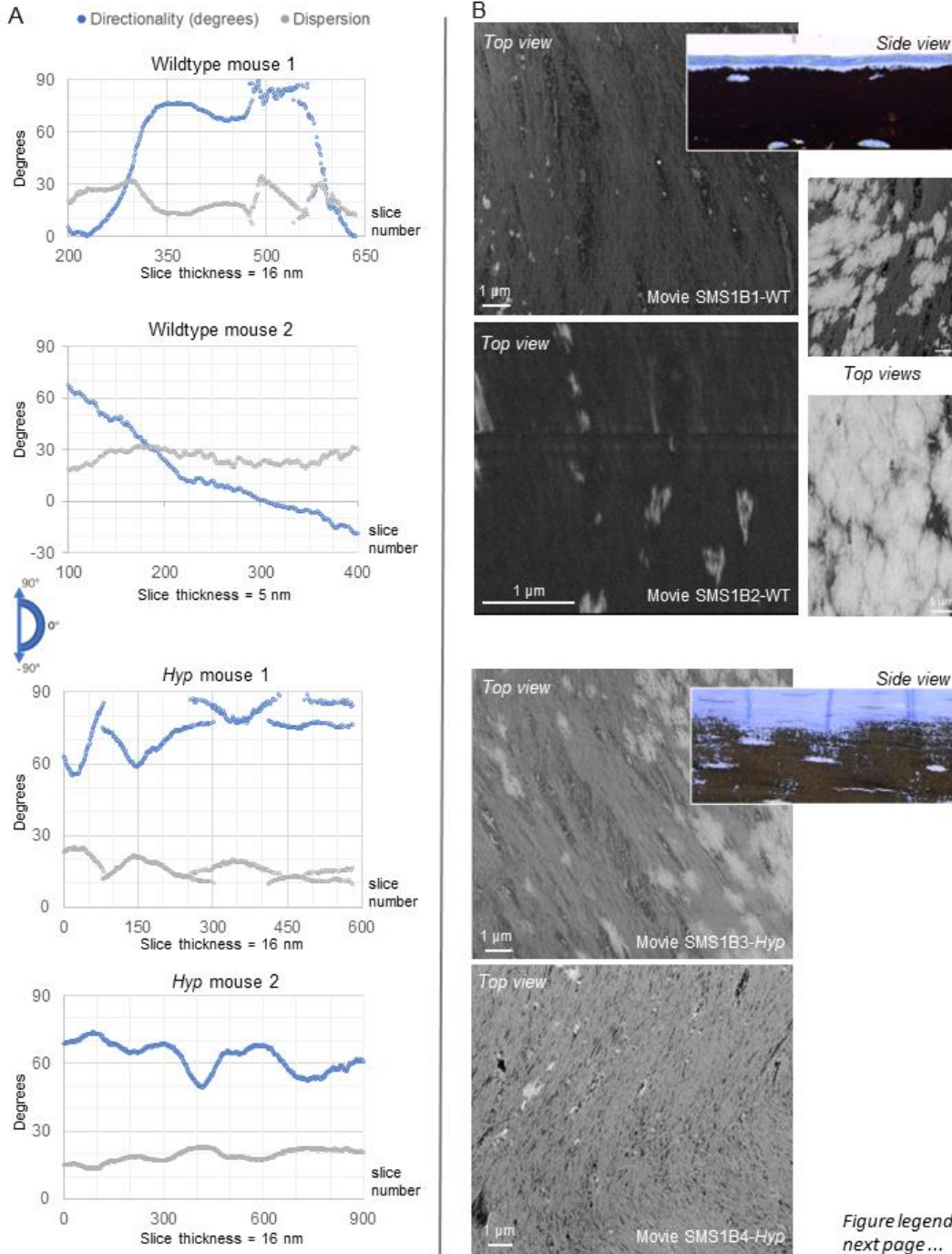
Supplemental Fig. S1. (A) FIB-SEM slice-by-slice directionality and dispersion analysis using ImageJ (Fiji) of collagen bundle sublamellar packing at the tibial diaphysis in four FIB-SEM stacks from WT and *Hyp* mouse bone (B). Analyses begin in the osteoid and progress *en face* (top-to-bottom) towards and into the mineralized matrix. All four volumes analyzed display characteristic

ordered motifs (Reznikov et al., 2013) with low slice-to-slice dispersion indicating the presence of co-aligned collagen packing throughout each stack. The two smaller-panel electron micrographs to the right, from the image stacks of normal WT mice, show the prolate ellipsoids of mineral beginning to appear in the collagen bundles, and then enlarging to fill the field and pack against one another. These two micrographs also show that the long axis of the prolate ellipsoids aligns with the long axis of the collagen bundle. See also Supp. Material Movies SMS1B1-WT, SMS1B2-WT, SMS1B3-*Hyp*, and SMS1B4-*Hyp*, and SM5E1 and SM5E2.

Supplemental Figure S2

Mineral ellipsoid aspect ratio in two adjacent bone lamellae at the mineralization front
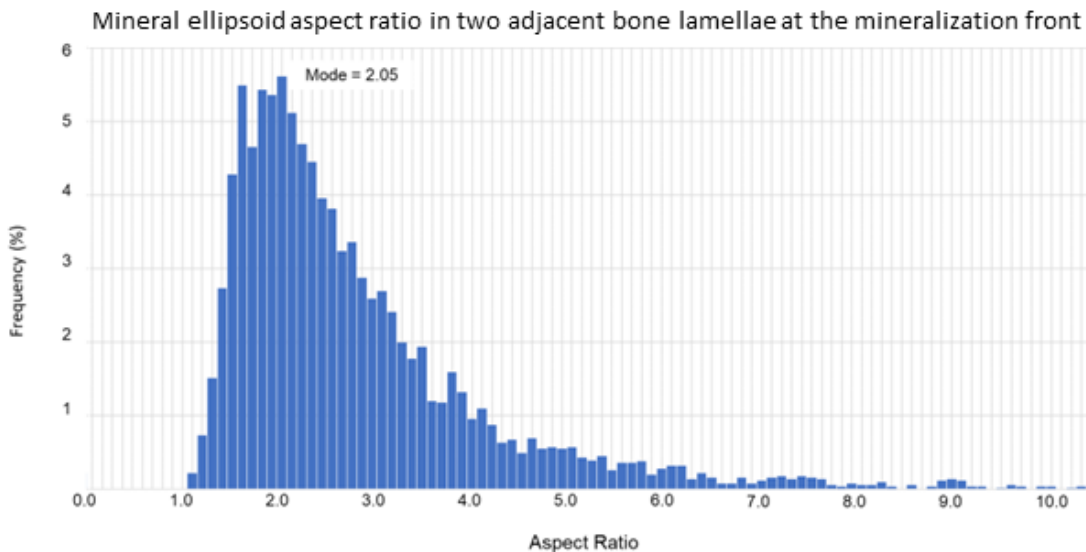
Supplemental Fig. S2: Histogram of the aspect ratio distribution of mineral ellipsoids as measured from a FIB-SEM wildtype mouse tibial bone volume containing a forming lamella with a mineralization front, and the immediately underlying, completely formed lamella. Data are from 5,132 watershed transform-segmented prolate mineral ellipsoids, giving a mode aspect ratio of 2.05.

Introduction to Chapter 2

      In addition to the relationship between bone's primary constituent parts – organic collagen fibrils and inorganic carbonate-substituted hydroxyapatite crystals – a critical determinant of bone toughness and overall mechanical performance is its hierarchical organization across scales. In Chapter 1 it was revealed that tessellation of micrometer-sized crossfibrillar mineral unit "tesselles" occurs in normal bone as a mineral-packing pattern originating from foci at the mineralization front . In Chapter 2, further original data is presented in the form of a graphical review highlighting the prevalence of spiraling, twisting, and curved motifs across each of bone's hierarchical levels, starting from the nanoscale (to also include crossfibrillar mineral tesselles), and with respect to organic fibrillar and inorganic mineral phases which are extremely difficult to image simultaneously. Indeed, here with additional 3D context between the organic and inorganic phases, mineral tesselles are found to adopt a slight twist mimicking the well-documented twist of collagen bundles at the broader hierarchical level which they occupy. This "twist of twist" is presented with historical context to exceptional early structural biologists – Pettigrew, and Thompson (207, 208), who were the first to describe the ubiquity of spiraling, twisted, curved, and braided motifs in Nature. Here, this idea is expanded upon in modern day, using 3D imaging and deep learning-based segmentation, starting at the finest scales with S/TEM tomography, then FIB-SEM serial-surface-view through the nano- and microscales, and finally using micro-CT all the way up to the level of whole bones and full mouse skeletons. Twisting of hierarchical elements of bone is proposed to contribute to its overall mechanical resilience. Using newly acquired 3D data we present a discussion and up-to-date visualizations that support this notion.

Chapter 2: Hierarchical Organization of Bone in Three Dimensions: A Twist of Twists

Daniel J. Buss[a], Roland Kröger[b], Marc D. McKee[a, c], Natalie Reznikov[d]

[a]Department of Anatomy and Cell Biology, McGill University, 3640 University Street, Montreal, Quebec, Canada H3A 0C7

[b]Department of Physics, University of York, Heslington, York, United Kingdom, YO10 5DD

[c]Faculty of Dentistry, McGill University, 3640 University Street, Montreal, Quebec, Canada H3A 0C7

[d]Department of Bioengineering, McGill University, 3480 University Street, Montreal, Quebec, Canada H3A 0E9
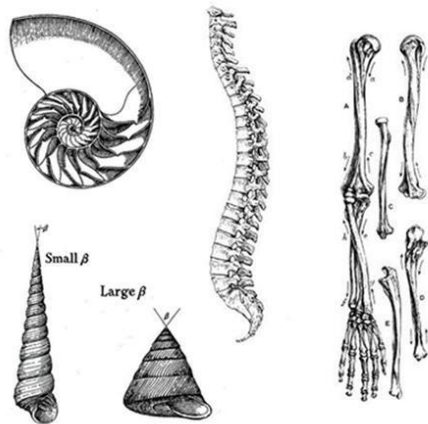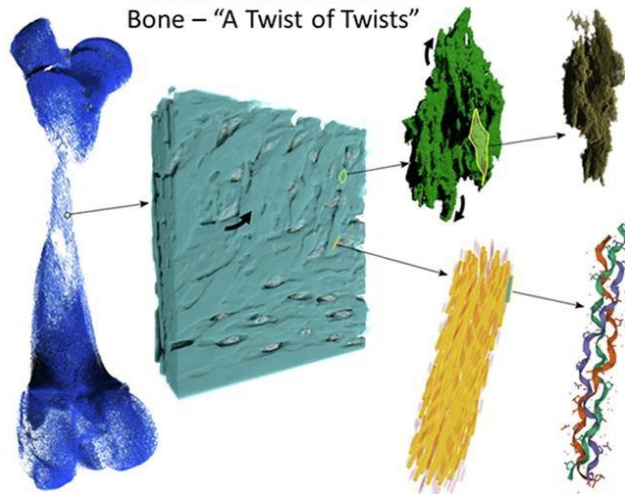
2.1 Abstract

Structural hierarchy of bone – observed across multiple scales and in three dimensions (3D) – is essential to its mechanical performance. While the mineralized extracellular matrix of bone consists predominantly of carbonate-substituted hydroxyapatite, type I collagen fibrils, water, and noncollagenous organic constituents (mainly proteins and small proteoglycans), it is largely the 3D arrangement of these inorganic and organic constituents at each length scale that endow bone with its exceptional mechanical properties. Focusing on recent volumetric imaging studies of bone at each of these scales – from the level of individual mineralized collagen fibrils to that of whole bones – this graphical review builds upon and re-emphasizes the original work of James Bell Pettigrew and D'Arcy Thompson who first described the ubiquity of spiral structure in Nature. Here we illustrate and discuss the omnipresence of twisted, curved, sinusoidal, coiled, spiraling, and braided motifs in bone in at least nine of its twelve hierarchical levels – a visualization undertaking that has not been possible until recently with advances in 3D imaging technologies (previous 2D imaging does not provide this information). From this perspective, we hypothesize that the twisting motif occurring across each hierarchical level of bone is directly linked to enhancement of function, rather than being simply an energetically favorable way to assemble mineralized matrix components. We propose that attentive consideration of twists in bone and the skeleton at different scales will likely develop, and will enhance our understanding of structure-function relationships in bone.

2.2 Main Text

Ingenious structural arrangements found at every scale throughout Nature permit the wide range of functions that organisms rely on for movement, feeding, protection, and reproduction. In the vertebrate skeleton, hierarchical organization of the primary organic (type I collagen) and inorganic mineral (carbonate-substituted hydroxyapatite) constituents determines a balance between the stiffness and toughness of this lightweight framework. This allows vertebrates to move against gravitational forces, and provides protection against mechanical impacts, all at a reasonable metabolic cost. Following from over a century of structural studies on bone, and now supported by recent investigations aided by the development of 3D volume electron microscopy

and deep learning-aided segmentation methods, this graphical review highlights the presence of twisted, curved, sinusoidal, coiled, spiraling and braided motifs in at least nine of the hierarchical levels in bone (out of about twelve known to date). Having been inspired by the spiraling of fibers found in his original dissections of heart tissue, James Bell Pettigrew emphasized the ubiquity of the spiral in Nature and hypothesized its relation to function(208, 209). His colleague D'Arcy Thompson comprehensively described the importance of spirals in biological objects(210). He emphasized that the spiral is a common and generic shape used in many instances of biology, with just graded change in the radius of curvature resulting in geometric differences ranging between (for example) the subtly arced horns of the Oryx to the coiling tendrils of creeping plants. From these observations, we extend Pettigrew's and Thompson's thinking on spirals and twists to various additional hierarchical arrangements of structure in the vertebrate skeleton enabled by new visualization methods.

From the speedy cheetah that coils and uncoils her entire body in each stride, to the tiny hovering hummingbird that sketches a distinct "figure 8" shape with every wing stroke(211), macroscopic twisting and curving of skeletal assemblies are key to function. Although these are kinematic observations, even in a static view obvious curvatures can be commonly seen in vertebrates, for example, along the length of the spine. Expectedly, given the fact that most quadrupedal animals share the same body plan, a similar curvature can be found in many spines (as shown in the mouse skeleton in Fig. 1A, B). At the level of individual bones, twisting may be observed when one dimension exceeds another. Our ribs follow a screw trajectory around the body axis, and our clavicles are twisted around their own axes(212). In short bones, such as vertebrae or metacarpals, it is naturally difficult to observe overt twisting at this level. While a gentle curvature and twist typically can be seen in most long bones (Fig. 1C and 1D), in some species such as squirrels this twist is quite pronounced (Fig. 1E). In fact, the degree of twisting in humeri among ancient fossil mammals appears to be indicative of overall preferred posture attributed to a particular species(213), therefore reflecting the biomechanical environment of an organism.

At a higher magnification level (millimeter scale), where cortical bone can be distinguished from trabecular bone, twisting may not be immediately apparent. The epiphyses and distal metaphyses of long bones are characterized by a 3D network of plate and rod-like trabeculae within a cortical shell. Nearing the transition from metaphysis to diaphysis, trabeculae form fine and then

coarse struts that fuse into larger buttresses. However, observation of this transition from the axial aspect (Fig. 2) reveals a twisting staircase-like structure as trabecular struts seem to spiral around the bone's central axis. Interestingly, this twisting appears to be more pronounced at the proximal metaphyses of the femur and humerus, where the range of movement is broadest. This level is the last one at which an overall curvature, or spiral, or twist, can be observed by an unaided eye – for the higher magnification levels, digital image analysis methods are employed.

The next level of spiraling is that of the osteons which surround the osteonal (Haversian) canal system in the cortical bone of large animals. It is technically challenging to visualize osteonal canals in 3D (usually done with micro-computed tomography, μCT) over an entire bone specimen. In small animals like laboratory rodents, there is minimal osteonal remodeling (therefore, scarce osteonal canals to image). In large animals like pig or sheep, who do undergo osteonal remodeling, the larger bone sizes typically prohibit imaging with resolution high enough to resolve the canals of 40-50 μm in diameter, unless scanning of a long bone is done in portions that are digitally "stitched" together. Incomplete osteons, in which concentric lamellae are in the process of being deposited, have a wider lumen, up to a few hundred micrometers. Figure 3A shows the resorption canals and incomplete osteons in the femur of a juvenile sheep where these cavities are about 100 micrometers wide and therefore can be imaged with micro-computed tomography and then segmented over the entire specimen. Figure 3B shows the far less numerous resorption canals and incompletely filled osteons in a mature sheep femur. From this, spiraling is indeed observed around the shaft axis with a pitch of about 5-15°. This corroborates the work by Hert et al.(214), although their study was not in 3D (Fig. 3C), in which ground sections of human bone dyed with India ink were found to have a similar low-pitch twist, with symmetry between right and left limbs. Functionally, the helicoid trajectory of the capillary-containing canals along a bone shaft likely mitigates the stress-raising effect of local discontinuities that are present in bone at many structural levels(215, 216).

The next hierarchical level in bone architecture is the wrapping of concentric lamellar layers around the osteonal canals. Wagermaier *et al*. in 2006 using micro-beam wide-angle X-ray scattering showed that the pitch of multiple lamellar layers of the same osteon varies cyclically between having a low angle and a high angle(217) (Fig. 3D). Of interest, they observed that the angle was never 0° nor 90°, and that the handedness of lamellar layers was the same, except for a few outermost lamellar layers. Thus, an osteon can be viewed as an assembly of concentric nested

springs/coils that provide for better mechanical resilience: "Helicoidal structures have certain advantages in resisting mechanical loads compared to orthogonal plywood structures since the twisted orientation enables a higher extensibility in tension and compression"(217). However, already a hundred years prior, Gebhardt(218) in his seminal work on osteonal structure explained the importance of alternating pitch and alternating handedness to resist torsional deformation and buckling (Fig. 3E). It is of interest to note that circumferential lamellar layers display a similar range of pitch angles with respect to the long bone axis(219).

To properly resolve and assess structures beyond the aforementioned levels, covering now the micro- and nanoscales, electron microscopy is typically employed. One particular method which has provided for significant advances in understanding bone's hierarchical organization over the past ten years or so has been serial-surface-view (also called slice-and-view) imaging using the focused-ion beam scanning electron microscope (FIB-SEM). This method uses sequential electron imaging and ion beam milling (typically gallium ions) to produce a stack of 2D images that are reconstructed into a 3D volume of nanometer-scale voxel resolution. Using this approach, the Weiner lab was the first to comprehensively characterize the 3D sub-lamellar organization of collagen in decalcified lamellar bone(194, 219-221). They showed that lamellar alignment is also never strictly along or across the osteonal axis, with the winding angle varying between 15 and 80 degrees. They also illustrated a previously unidentified level of hierarchical organization, these being "order" and "disorder" as repeating components of the lamellar sequence. The lacuno-canalicular network – housing osteocyte cells and their dendritic cell processes – is contained entirely within the disordered collagen array(194, 219). The canaliculi with their resident cell processes meander across repetitive lamellar layers, at the same time displaying a screw-like twist (Fig. 4B), which is in accord with the biomechanical incentive to minimize the stress-concentrating factor(216). It remains to be seen if there is a discernable twist of the actual osteocyte dendrites on a larger scale(27, 197) – indeed undoubtedly an elusive question to answer, given the need for such high resolution over a large volume of interest. An additional observation at this level of hierarchy is that the layers of ordered collagen matrix are not discontinuous entities; they form bundles of 1-3 micrometers in diameter that are quasi-cylindrical in shape, splitting and merging continuously, and twisting around their own axes(194, 220). Collectively, these 3D FIB-SEM tomography works confirmed earlier SEM observations of collagen bundles by Boyde and Hobdell (198) (Fig. 4 C, D). Segmentation of twisted and braided bundles of collagen in 3D

reconstructions as shown in hierarchical Level 7, which comprise the ordered collagen array, was then made possible a few years later with the arrival of deep learning applied to this type of bioimaging(222).

More recent studies using serial-surface-view FIB-SEM imaging on mineralized (not demineralized) bone specimens has revealed a subtle twisting that takes place at the next hierarchical level, at the level of crossfibrillar mineral tessellation (97, 223, 224). These micron-sized mineral "tesselles" are generally observed as abutting polycrystalline mineral aggregates that form prolate ellipsoids whose longer axis generally follows the direction of collagen fibrils. Thus, across the microscale, this tessellated arrangement of mineral that traverses and bridges collagen fibrils in a crossfibrillar manner presumably acts as a toughening mechanism, resisting compression, and perhaps acting as a sublamellar mechanism for crack deflection. Figure 5A shows ordered arrays of segmented collagen bundles at the micrometer level, merging and twisting (demineralized for visibility) and size-wise what would be a matching field-of-view of undemineralized bone (Fig. 5B) showing the interlocking, abutting mineral tessellations within mature mineralized lamellar bone. The space-filling assembly of rigid abutting tesselles within a continuous viscous collagenous matrix, so that the many narrow 3D interfaces remain unfused, may contribute to reconciling the conflicting properties of stiffness and toughness in bone.(223) A single tesselle from a human femur (Fig. 5 C) is rendered in 3D (Fig. 5 D): note the spindle-shape and twist at this structural level which mimics and contributes to the larger overall twist at the collagen bundle level where many tesselles pack together. This particular tesselle was imaged at the near-limit of FIB-SEM resolution using a voxel size 4 nm, and it was labeled using deep learning-based segmentation (Dragonfly[TM], Object Research Systems Inc., Montreal).

At finer size scales, the organization of collagen itself has been extensively documented (using a variety of methods) as twisted super-helical arrays, all the way down to the level of amino acids of individual alpha chains, to the coiling of these chains into the triple helix of collagen molecules, and even to the slight twisting of molecules within the fibril itself(225-230) (Fig. 5 E-I). The intercalation of hydroxyapatite crystals into the collagen fibrils strongly depends on the internal organization of the collagen triple helices(227). Charvolin and Sadoc have suggested a phyllotactic assembly pattern of the collagen triple helices with the in-plane distribution resulting in a sunflower seed type of arrangement(231, 232). Assuming that crystal growth occurs along the path of most adjacent gaps in a fibril, and considering the reported superhelical tilt of the

collagen molecules with respect to the fibril axis of about 5° (233), a gently twisted and bent crystal geometry would be in agreement with the experimentally observed crystal morphology in bone(234-237). Mineral structure has recently been visualized by scanning transmission electron microscopy (STEM) tomography which has allowed for 3D reconstructions of mineral organization at the nanoscale level – within the tesselle and at the level of individual mineralized collagen fibrils. This method reveals confluent aggregates of crystallites where it is difficult to state whether they are needles or platelets, intrafibrillar or extrafibrillar, and where one crystallite ends and another one starts(234). It is known that in pristine bone, mineral crystallites would be flexible(237). Specifically for this graphic review, we processed previously acquired STEM data(234) using deep learning-assisted segmentation and applied a watershed transform operation to digitally separate confluent mineral aggregates. Figure 6 shows the full tomogram with the crystallites volume-rendered and color-coded according to their computationally separable boundaries (which don't necessarily coincide with the elusive true boundaries). Panel B in Fig. 6 shows a few selected aggregates with the modal size varying between $10^5 \, nm^3$ to $10^6 \, nm^3$. This range of volumes would correspond to roughly about 10 to 100 canonically described irregular mineral platelets 10 x 25 x 50 nm(238). In Fig. 6 C, 20 selected individual grains/aggregates are shown with orientation different from that *in situ*, ordered from the largest to the smallest. Despite the remarkable variety of these shapes, the clear common features are that each aggregate (even the smallest one) is a hierarchical assembly on its own (needles fusing into platelets, and platelets stacking into "decks"), and that they are gently curved, resembling fan blades, consistent with prior studies(236, 237), while yet displaying crystalline order at the scale of individual needles (Fig. 7). Interestingly, the larger labels in Fig. 6 C appear to recapitulate the curvature that is seen at the edge of a larger tesselle, of which they are indeed a component. Perhaps we should hesitate using comfortable and simplistic depictions of bone's apatite crystallites as being parallelepipeds – they are anything but parallelepipeds – because this description is as accurate as depicting trees like neat cylinders.

In summary, the twisting motif can be found in the skeleton at essentially every magnification level (239), see also Fig. 8. Although twisted elements of some bones are not always obvious to the unaided eye or through 2D imaging, recent 3D investigations demonstrate how twisting across the nano- and microscales, distinctly among both inorganic and organic constituents, is largely conserved in lamellar bone – whether macroscopically arranged into short,

flat, or long bones. At each individual level, twisting within bone's hierarchy appears to enhance bone's overall resistance to biomechanical challenges. This could occur through the twisting of braided collagen fibril bundles into lamellae that then twist around each osteonal canal, or through the fusion of slightly curved confluent crystal aggregates into spiraling, closely packed mineral tesselles, or through spiraling of trabecular elements at the proximal metaphyses. Maybe this motif occurs for a biomechanical reason – as if the system is thought of as a whole, where springs coil into springs that are coiled into larger springs (and so on) throughout bone's complete hierarchy – in principle, such an assembly could be very resilient indeed(217). Comprehensive simulation studies would be of great value to rule out whether the multiscale "twist of twists" could be a spandrel – being just "the way things are"(240) – or rather (more likely) be there for a reason. Perhaps, twisting might be a truly intrinsic and wide-ranging design principle for hierarchy in Nature's structures (as it appears to be in bone). While exceptions might exist to these notions, it remains an unresolved question as to say why a flamingo's or a stilt's legs are so impeccably straight – at least macroscopically!

2.3 Declaration of Competing Interest

The authors declare that they have no competing financial interests or personal relationships that could appear to have influenced the work reported in this paper.

2.4 Acknowledgements

Figure 1. Hierarchical levels of the full skeleton and of whole bones. (A,B) A mouse skeleton imaged using microcomputed tomography (μCT). The same structural plan can be observed in the skeletons of mammals: here, the murine spine shows the same principle curves as the human spine – cervical and lumbar lordosis (convexity oriented forwards) and thoracic kyphosis (concavity oriented forwards). (C,D, E) Individual bones (imaged by μCT) scaled to the same figure height: sheep femur (C) with its shallow c-shaped curvature, partridge humerus (D) with an s-shaped curvature, and squirrel humerus (E) showing a screw-shape geometry.

Level 3: Cortical and trabecular bone
A. Proximal femur, sheep
C. Proximal humerus, squirrel
10 mm
1 mm
B. Distal femur, sheep
D. Distal humerus, squirrel
10 mm
1 mm
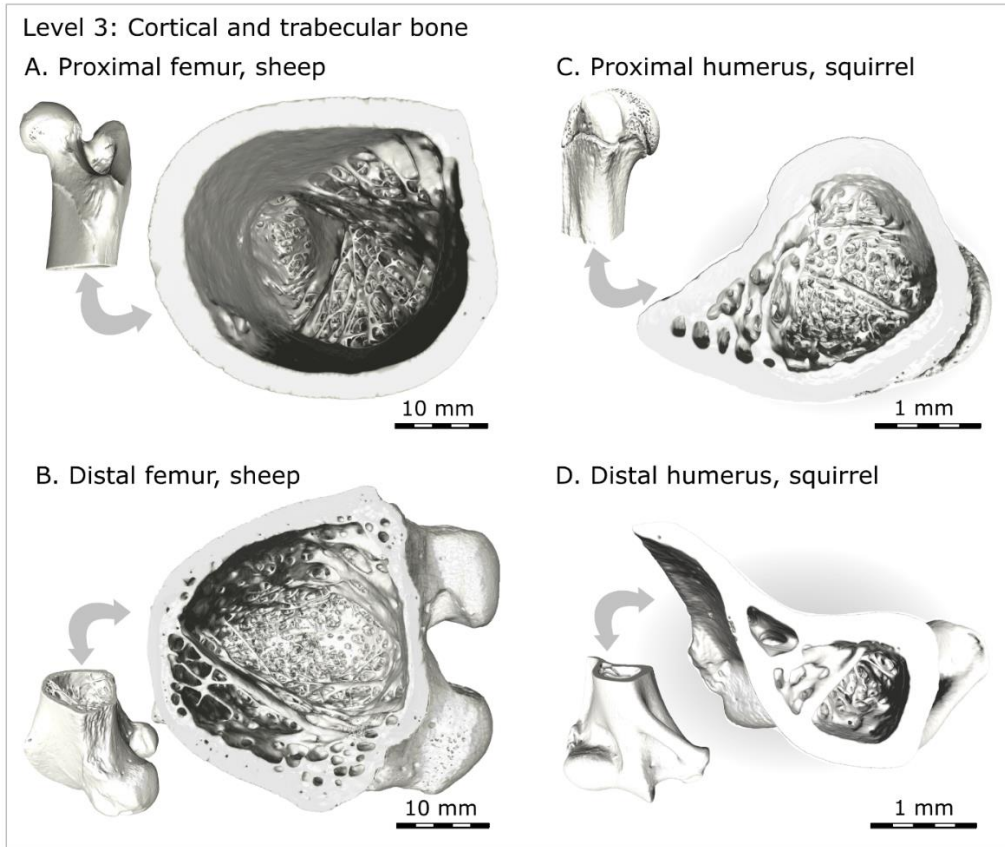
Figure 2. Cortical-to-trabecular bone transition (hierarchical Level 3) in the metaphyses of the sheep femur (A, B) and the squirrel humerus (C, D). Note that both proximal metaphyses show geometric "vorticity" of trabecular buttresses (A, C), but this is not that obvious in the distal metaphyses (B, D).
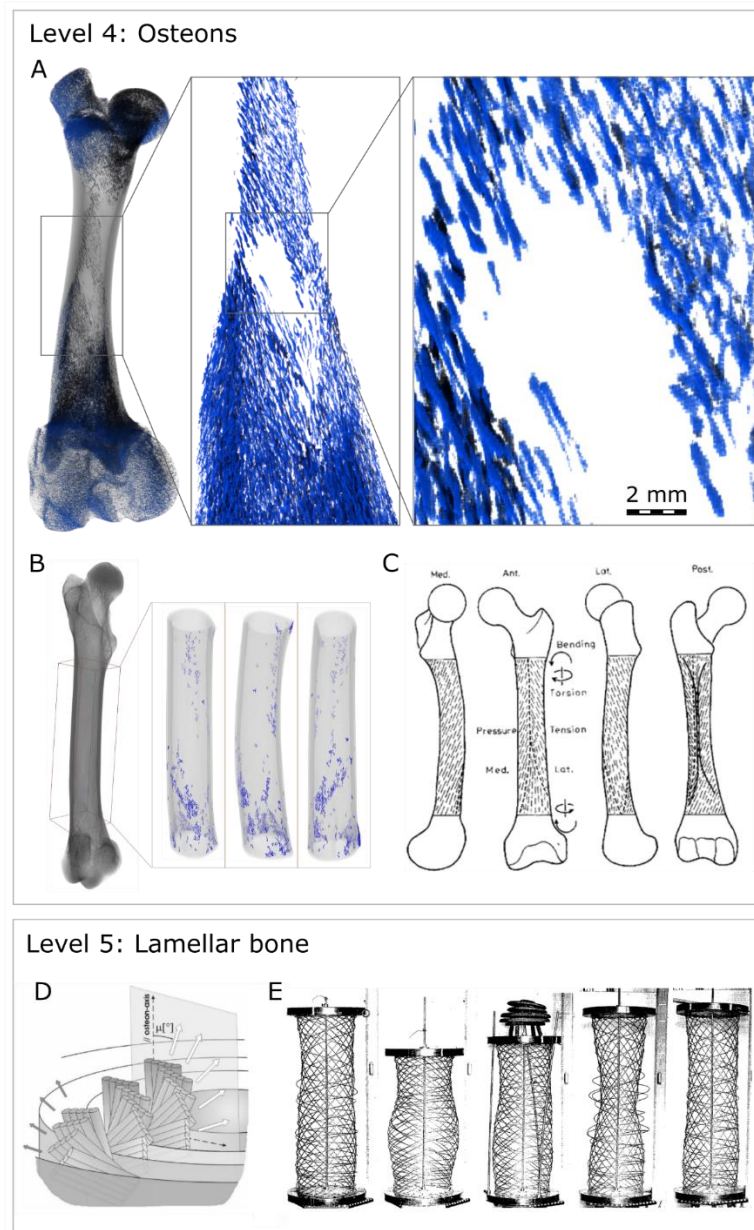
Figure 3. Vascular canals in a sheep femur (hierarchical Level 4), and winding of lamellar layers around the canals (osteons, hierarchical Level 5). (A) Resorption cavities and incomplete osteons within a juvenile sheep. (B) Less-abundant resorption canals and incomplete osteons in a mature sheep femur. Note the similarity between B and the "hatching" of osteonal canals in the human femur (from Hert et al. (214) , with permission). (D) Spiral winding of co-oriented mineralized collagen fibrils around the central capillary of an osteon, from Wagermaier et al.(217), with permission. The lamellar assembly in the whole osteon can be viewed as a series of concentric

nested coils. Note the switch in handedness in the outermost layer. (E) Preceding work by Gebhardt (218) in 1906, who empirically illustrated the stiffening effect of multi-layered coiling assemblies with varying pitch and handedness: either in tension, compression or torsion, there will always be a subset of lamellae that resist such deformation axially.
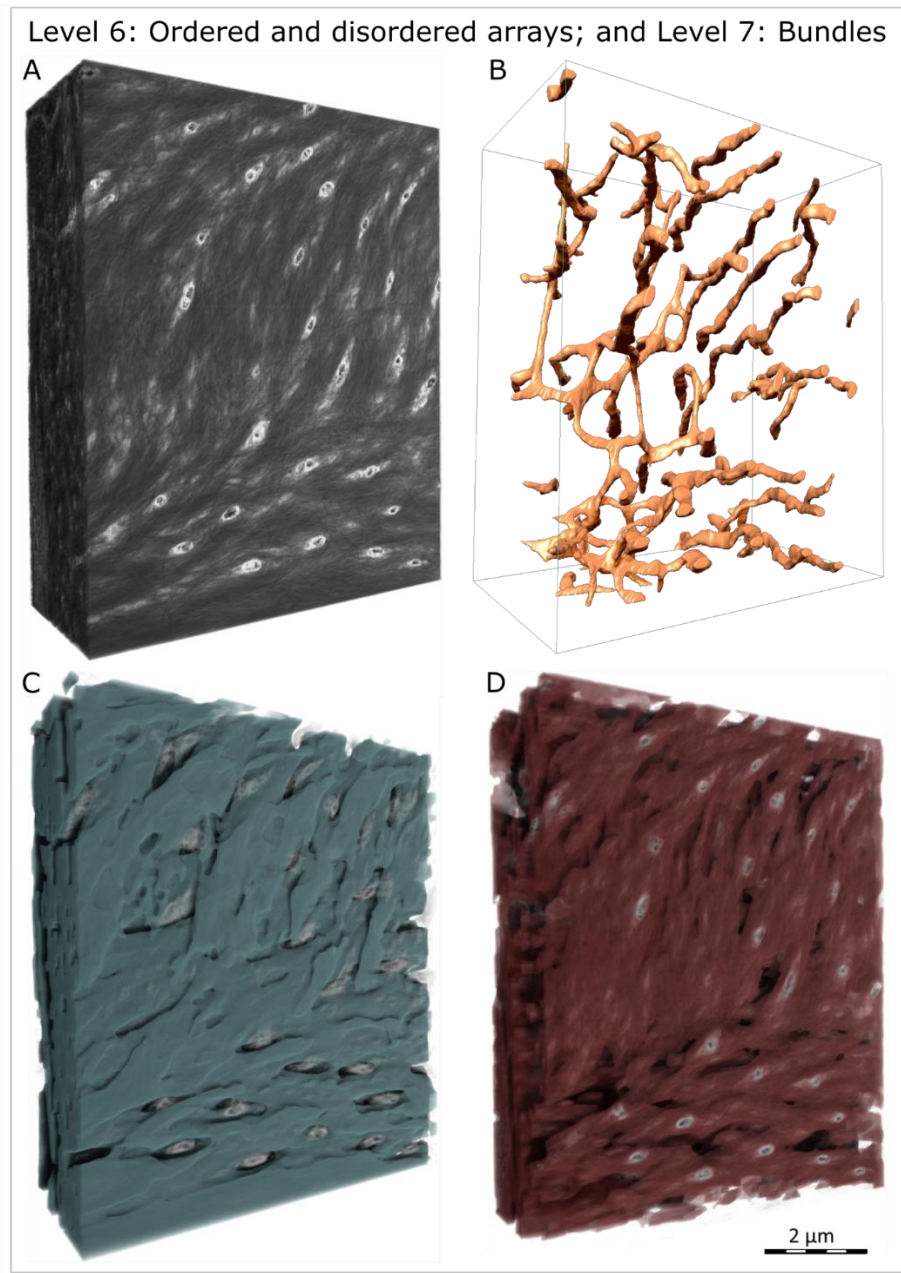
Figure 4. Hierarchical Level 6 (ordered and disordered repeats in the lamellar structure), and Level 7 (packing of co-aligned collagen fibrils into quasi-cylindrical bundles). These images were acquired using the FIB-SEM slice-and-view method on demineralized and stained lamellar bone. (A) Grey-scale 3D volume in which collagen fibrils appear dark grey, interfibrillar ground matter appears light grey, the *lamina limitans* lining canaliculi is white, and osteocyte processes are also white. (B) The same canaliculi as in A, surface-rendered and shaded to illustrate their meandering course across the ordered bundles, and their screw-shaped axial twist. (C) Segmentation of the ordered arrays of collagen, 3D rendered and superimposed on a semi-transparent grey-scale

volume (same sample and same orientation as in A). Note the braided and gently twisted appearance of splitting and merging bundles of collagen fibrils. (D) Disordered collagen fibrils alternate with the ordered bundles and house the cellular processes. Here, the disordered phase has been segmented using deep learning-aided segmentation, and its content is about 30% with respect to the total volume of the extracellular matrix (original nonquantitative work by Reznikov *et al*.(219) underestimated the proportion of the disordered array by volume).
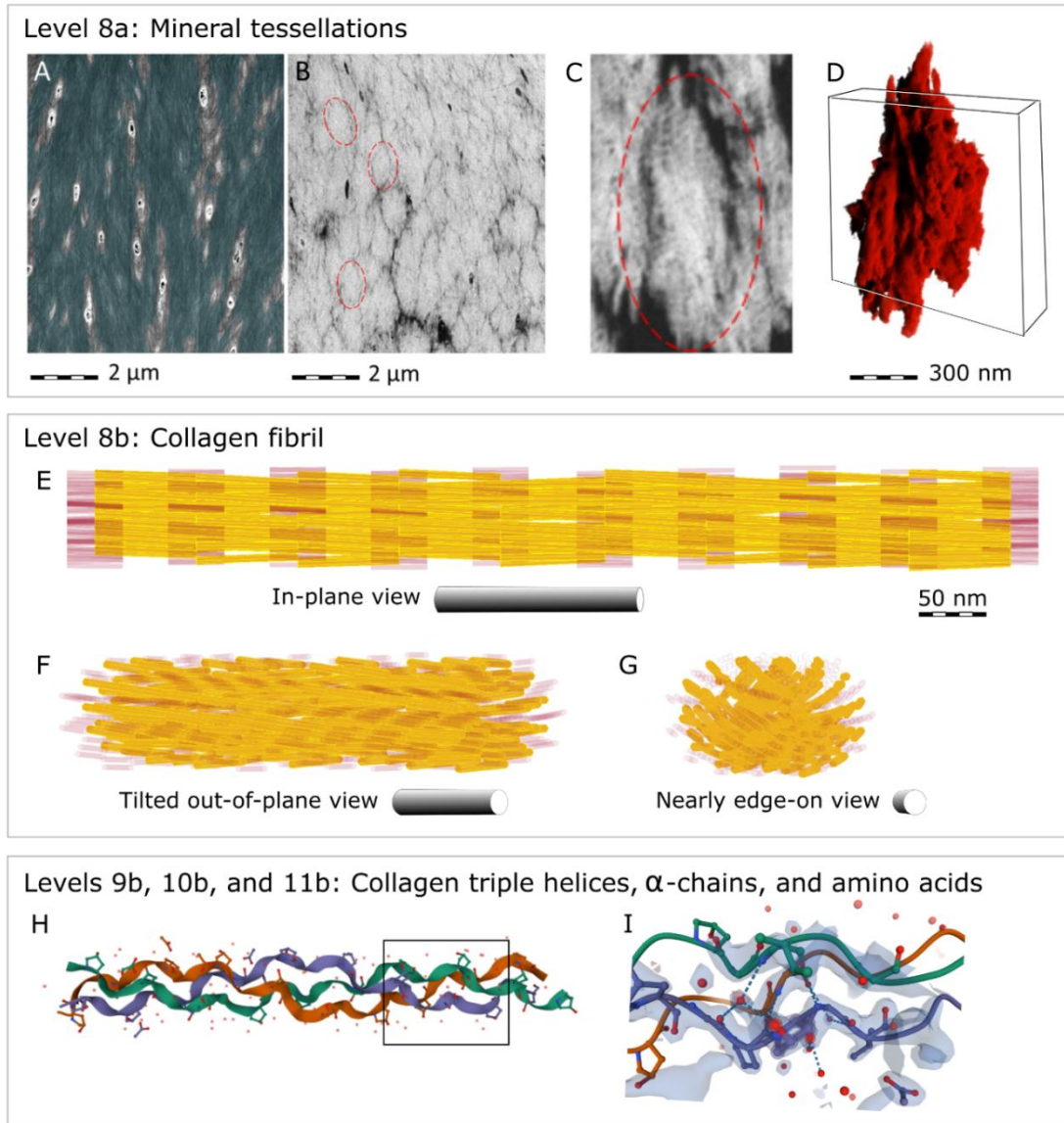
Figure 5. Hierarchical Level 8a – prolate ellipsoidal mineral tessellations that populate bundles of ordered collagen fibrils in lamellar bone. (A) A 2D view from Figure 4A and 4C. (B) An orientation- and magnification-matched 2D view of undemineralized bone from Buss *et al.*(223). (C) A further magnified 2D image of a typical mineral aggregate – a "tesselle". (D) A 3D rendering of a typical single tesselle, as outlined by dashed red ellipses in panels B and C (the tesselle in panel C is one 2D cross-sectional view of its subsequent 3D volume shown in panel D). The rectangular box in panel C roughly corresponds to the complete volume of interest presented in the following Figure 6. (E) Hierarchical Level 8b showing a supertwisted model of a mineralized collagen fibril with a characteristic stagger of triple helices and a 5° molecular tilt with respect to the fibril axis, inspired by the seed arrangement in the sunflower as suggested by Charvolin and

Sadoc (231, 232). Gap regions between collagen triple helices are depicted in transparent red with the hydroxyapatite crystals represented in yellow. (F,G) The same 3D supertwisted collagen model rotated around the vertical axis ("yaw") to accentuate the resultant spiraling alignment of the gaps and the mineral crystallites that would be confined to the gap zones. Panels H and I show the hierarchical structure of collagen only at the levels of triple helices, α-chains and amino acids (images adapted from the RCSB Protein Data Bank (229, 241), DOI:10.2210/pdb1CAG/pdb). The corresponding organizational levels for bone mineral are shown in Figures 6 and 7.
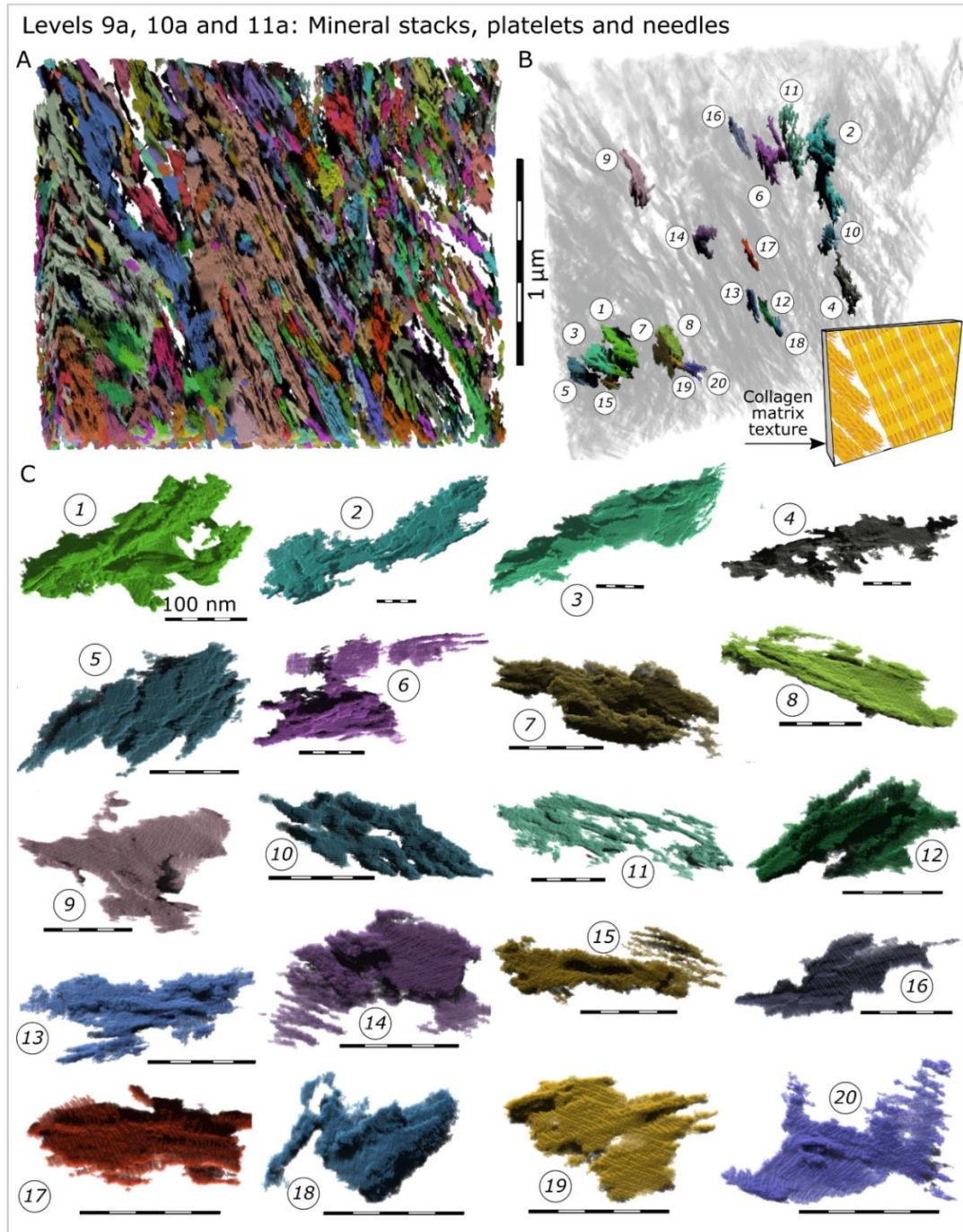
Figure 6. Hierarchical Levels 9, 10 and 11 of bone mineral organization: stacks, plates and needles. (A) STEM tomography of a FIB-milled foil of lamellar bone. The contrast originates from the crystallites' electron density, and all the crystallites are segmented (using a deep neural network), volume-rendered, and color-coded following a watershed transformation. (B) Twenty digitally separable crystallite aggregates are shown *in situ* (in unmodified orientations) within the

same STEM tomographic volume as in A. The remaining tomogram volume is rendered transparent. The yellow inset in the bottom right corner of B schematically illustrates the orientation of collagen fibrils within the tomogram rendered in A and B. (C) A gallery of 20 individual crystallites ranging in size between 10^6 nm^3 and 10^5 nm^3 (in a descending order). Individual crystals are intentionally shown in re-orientations different from those orientations observed *in situ*.
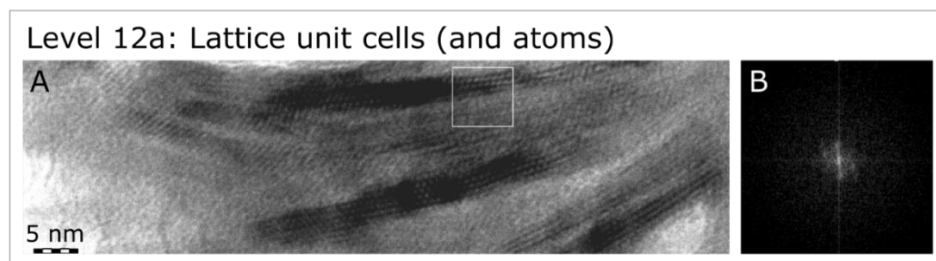
Figure 7. Hierarchical Level 12, here pertaining only to the mineral component of bone, is represented by the unit cells and atoms themselves comprising bone mineral crystallites (A). Panel B shows a Fourier transform of the area outlined in (A), white square.
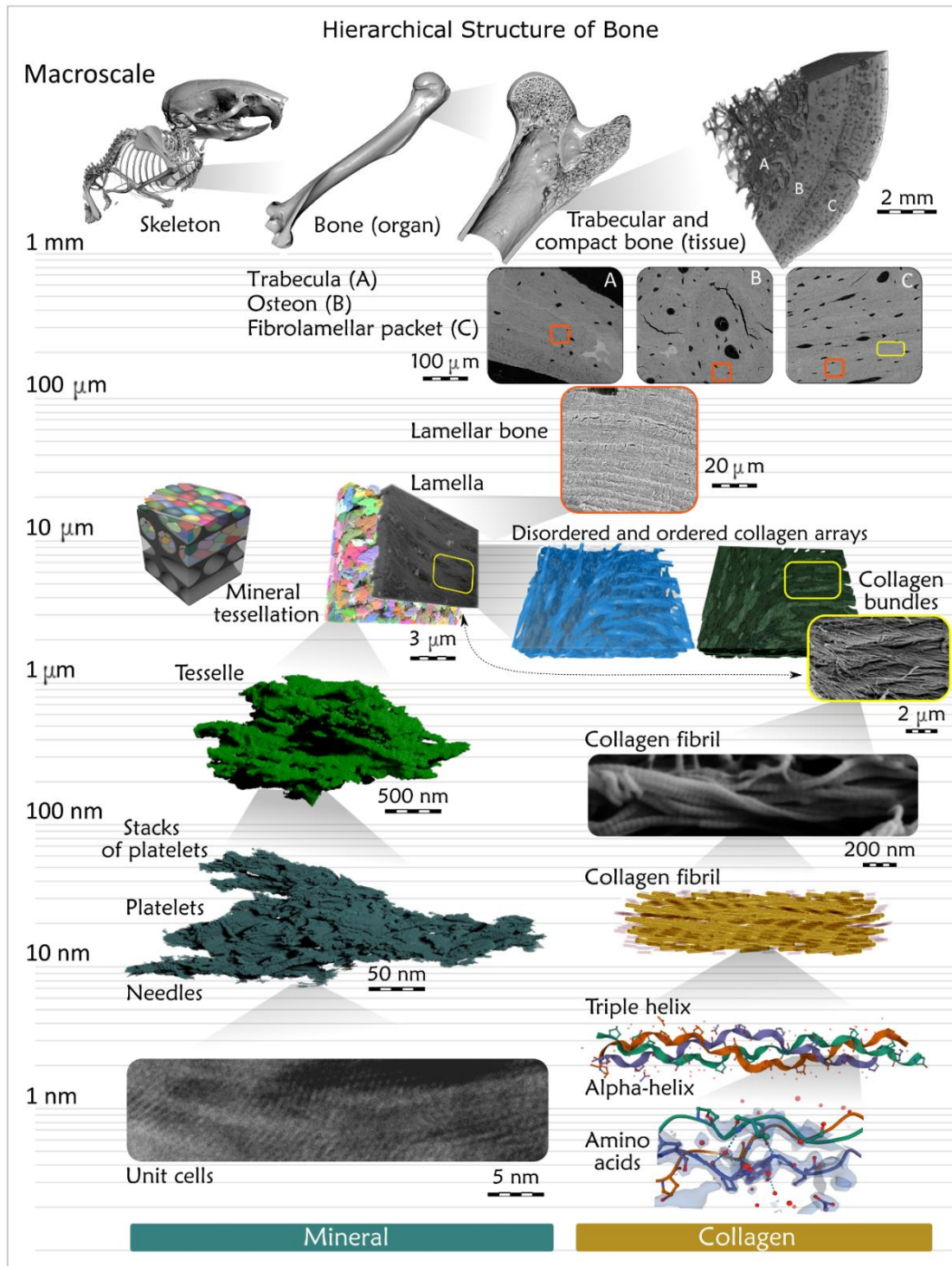
Figure 8. Contemporary understanding of the hierarchical structure of bone. According to the recent inventory, there are approximately twelve levels: 1) skeletons, made of 2) bones, made of

3) cortical and trabecular tissue, made of 4) cortical osteons, fibrolamellar bone packets, and trabecular lamellar packets, all of which contain 5) lamellar bone, made of 6) lamellae, made of 7) ordered collagen motifs that form 8) bundles, surrounded by the disordered collagen motif. The bundles are made of 9) collagen fibrils, made of 10) triple helices, made of 11) alpha-helices, made of 12) amino acids. The mineral organization in 3D shows its own hierarchical organization starting at level 8) of mineralized collagen bundles, that contain 9) tessellated prolate ellipsoids of mineral, made of 10) mineral platelets, made of 11) laterally merging acicular crystals, made of 12) unit cells. Because the cascade of hierarchical levels splits at the micrometer level for organic and inorganic matter, and because same-level mineral and collagen units have different shapes and even scale (for example, the tesselles, and the collagen fibrils, which are both level 9), and also for visual flow and continuity between levels, we intentionally did not number the levels in the figure.

An Introduction to Chapter 3

Attachment sites between zones of unmineralized and mineralized tissue are particularly prone to degeneration and failure due to the concentration of stress that occurs between these overall dissimilar materials. This effect is pronounced at tendon and ligament insertion sites where loading must be repeatedly transmitted across organic and inorganic phases of the collagen fiber extracellular matrix where there is a twofold stiffness differential. Enthesis fibrocartilage has evolved to contain a gradient of tissue properties to reduce stress concentration directly at sites where soft tendons and ligaments attach to highly mineralized bony eminences (74, 81, 242). Due to the mechanical challenges at this site, and limited capability for repair and regeneration after disease or dysfunction, it is not only critical to understand potential gradients in collagen or mineral content or orientation within the enthesis, but also, importantly, to further understand the spatial relationship from the nanoscale and in 3-dimensions of the organic collagen fiber phase and the inorganic mineral phase in the calcified fibrocartilage zone – this in relation to crossfibrillar mineral tessellation that we characterized in lamellar bone. In the following chapter we highlight how mineral unit tesselles are found in other collagen fiber systems in vertebrates – here in mouse Achilles enthesis fibrocartilage and in ectopically mineralizing mouse Achilles midsubstance tendon. By comparing normal WT mice of various ages to *Hyp* mice at this site (XLH patients paradoxically frequently develop calcifying enthesophytes), we now reveal how patterning of crossfibrillar mineral units occurs in various instances of normal and ectopic mineralization events. We do this in 4D and originating at mineralization fronts, and provide novel discussion concerning structure-function relationships at this site and molecular determinants of both physiologic and pathologic instances of mineralization.

Chapter 3: Mineral tessellation in mouse enthesis fibrocartilage, Achilles tendon, and *Hyp* calcifying enthesopathy: A shared 3D mineralization pattern

Daniel J. Buss[1], Katya Rechav[2], Natalie Reznikov[1,3,4] and Marc D. McKee[1,4]

[1]Department of Anatomy and Cell Biology, School of Biomedical Sciences, Faculty of Medicine and Health Sciences, McGill University, Montreal, Quebec, Canada

[2]Electron Microscopy Unit, Weizmann Institute of Science, Rehovot, Israel

[3]Department of Bioengineering, Faculty of Engineering, McGill University, Montreal, Quebec, Canada

[4]Faculty of Dental Medicine and Oral Health Sciences, McGill University, Montreal, Quebec, Canada

3D multi-scale imaging of enthesis
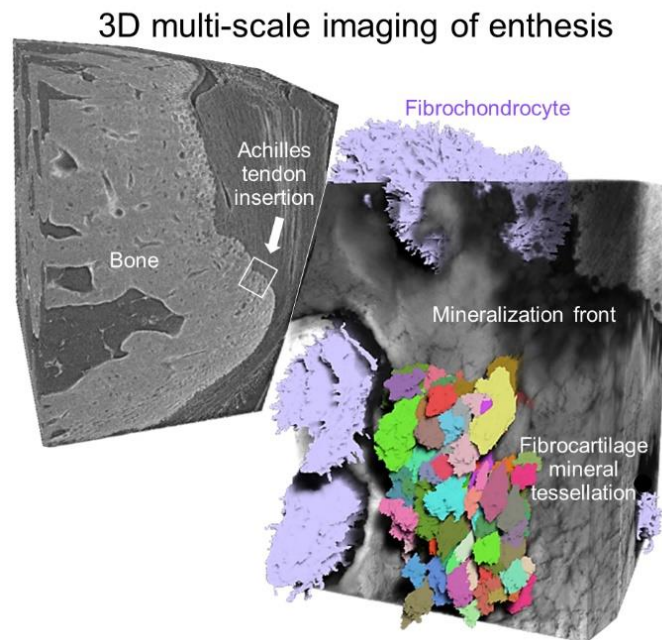
3.1 Abstract

The hallmark of enthesis architecture is the 3D compositional and structural gradient encompassing four tissue zones – tendon/ligament, uncalcified fibrocartilage, calcified fibrocartilage and bone. This functional gradient accommodates the large stiffness differential between calcified bone and uncalcified tendon/ligament. Here we analyze in 3D the organization of the mouse Achilles enthesis and mineralizing Achilles tendon in comparison to lamellar bone. We use correlative, multiscale high-resolution volume imaging methods including μCT with submicrometer resolution and FIB-SEM tomography (both with deep learning-based image segmentation), and TEM and SEM imaging, to describe ultrastructural features of physiologic, age-related and aberrant mineral patterning. We applied these approaches to murine wildtype (WT) Achilles enthesis tissues to describe in normal calcifying fibrocartilage a crossfibrillar mineral tessellation pattern similar to that observed in lamellar bone, but with greater variance in mineral tesselle morphology and size. We also examined Achilles enthesis structure in Hyp mice, a murine model for the inherited osteomalacic disease X-linked hypophosphatemia (XLH) with calcifying enthesopathy. In Achilles enthesis fibrocartilage of Hyp mice, we show defective crossfibrillar mineral tessellation similar to that which occurs in Hyp lamellar bone. At the cellular level in fibrocartilage, unlike in bone where enlarged osteocyte mineral lacunae are found as peri-osteocytic lesions, mineral lacunar volumes for fibrochondrocytes did not differ between WT and Hyp mice. While both WT and Hyp aged mice demonstrate Achilles tendon midsubstance ectopic mineralization, a consistently defective mineralization pattern was observed in Hyp mice. Strong immunostaining for osteopontin was observed at all mineralization sites examined in both WT and Hyp mice. Taken together, this new 3D ultrastructural information describes details of common mineralization trajectories for enthesis, tendon and bone, which in Hyp/XLH are defective.

3.2 Introduction

This mouse study was designed to investigate normal Achilles tendon enthesis structure and mineralization in three dimensions (3D) using multi-scale X-ray and electron microscopy tomographic methods, with a comparison to enthesis structure found in the osteomalacic X-linked hypophosphatemia (XLH) *Hyp* mouse model. More specifically, our analysis focused on using

101

high-resolution (<1 µm) micro-computed tomography (µCT) and focused ion beam-scanning electron tomography (FIB-SEM, Serial-Surface-View mode) to understand how pliant collagenous extracellular matrix interfaces with mineral at the enthesis. We describe the 3D trajectory of mineralization (in mice of different ages) whereby small foci of mineralization within uncalcified fibrocartilage of the Achilles enthesis matures to form calcified fibrocartilage. We also describe and similarly characterize a newly identified prevalent calcifying tendinopathy mineralization pattern in the Achilles tendon mid-substance region in aged mice.

Entheses are remarkably adapted – like no other tissue in the body – in that they have evolved to address the extreme mechanical challenges that arise when loading must be repeatedly transmitted across tissues with a roughly two-orders-of-magnitude stiffness differential. Vertebrates use force generated from muscle contraction against a rigid bony skeleton to facilitate movement . These forces are transmitted to, and between, bony elements by tendons and ligaments, respectively. While tendons and ligaments are compliant and therefore store energy, mature mineralized cartilage and bone tissue – being permeated with carbonate-substituted hydroxyapatite – differ substantially with respect to their overall material properties (81, 242). At insertion sites of tendons and ligaments into bones, particularly at the epiphyses of long bones and at bony eminences, a transitional tissue – enthesis fibrocartilage – provides a gradient in extracellular matrix properties that acts to minimize stress concentration (42, 85, 243).

The unique stiffness gradient found across the enthesis, which remarkably span as little as only hundreds of micrometers in the mature enthesis of mice, develops as a result of complex gene expression patterns during development (40, 244). In turn, these developmental cues result in defined zones of tissue with varying extracellular matrix composition and organization, and with distinct mineralization and hydration status, this as determined by resident cell activity and matrix conditioning. The mature fibrocartilage enthesis attachment is classically described as having four zones defined by the resident cell type and by the proteins that they produce (42, 243).

The first two zones starting from the tendon/ligament side normally do not involve mineralization (calcification) events in the extracellular matrix. In the tendon zone, aligned type I collagen fibrils are highly aligned (anisotropic), closely packed, and crosslinked, and with neighboring fibrils forming larger fibril bundles/fibers, all of which resist tensile forces. Positioned between the type I collagen fibrils are flattened, highly elongated tenocytes aligned along the collagen's long axis, with thin cytoplasmic extensions that extend out into the

extracellular matrix (245, 246). In the next contiguous zone, uncalcified enthesis fibrocartilage (UF) is present as broadly characterized by the combination of type I collagen matrix predominantly with type II collagen and proteoglycan, the latter with its glycosaminoglycan content binding large amounts of water, a hydration feature that enhances resistance to compression (247). This zone also has changes in fiber orientation (85). As opposed to the elongated tenocytes of the tendon zone, uncalcified fibrocartilage is populated by more rounded fibrochondrocyte cells, decorated by abundant and regularly spaced filipodial extensions (246, 248).

Extracellular matrix mineralization occurs in the next two zones, providing a rigid, robust anchoring mechanism to attach tendon/ligament to bone. In terms of mineralization-regulating molecules, this third calcified fibrocartilage zone (CF) includes incorporation of type X collagen (42) and osteopontin (OPN) to the extracellular matrix (84), as well as differential expression of enzymes known to favor mineralization such as tissue-nonspecific alkaline phosphatase (TNAP) which degrades small-molecule inhibitors of mineralization such as pyrophosphate (PPi) (107, 111, 249). The variation in mineral content in this zone, together with its organization (250), provide a gradient from less-mineralized to more-mineralized extracellular matrix towards the heavily mineralized bone tissue (251, 252), potentially further acting to reduce stress concentration at this interfacial region. In addition to these broader features imparted by mineralization, it has been suggested that at the scale of tens to hundreds of micrometers, mineralization events might eventually culminate structurally with an irregular mineralization front in the fibrocartilage, thus additionally acting as a toughening mechanism, increasing attachment area over a three-dimensional interface (253). Fibrochondrocytes in the calcified fibrocartilage zone become either partially or fully surrounded by mineral (to form mineral lacunae) depending upon their proximity to the mineralization front. An interdigitated transition at the cement line (presumably also as a stress dissipation architectural arrangement (85, 254)) demarcates the transition to the final enthesis zone, mineralized bone proper.

As a result of the stiffness mismatch between tendon and bone, and the complex structuring of the matrix and mineral of the fibrocartilage that act to minimize the mechanical consequences of this mismatch, repair after injury or degeneration (either related to disease or aging) is particularly difficult (243, 255). In the osteomalacic (and odontomalacic) inherited disease X-linked hypophosphatemia (XLH), and in the *Hyp* mouse model of this disease studied here, bones

and teeth are hypomineralized (27, 123, 256, 257). The skeleton deforms commonly through bending, buckling, and fracturing of individual bones, and calcifying enthesopathy is a common occurrence (258-260). These manifestations are associated with debilitating pain and loss of mobility for patients.

In XLH, inactivating mutations of the *PHEX* gene (that encodes transmembrane endopeptidase PHEX enzyme normally expressed by osteocytes, osteoblasts, and odontoblasts) results in elevated levels of systemic circulating FGF23 causing renal phosphate wasting (127), and an accumulation of mineralization-inhibiting osteopontin locally in the extracellular matrix (123). In particular, as related to the present study on enthesis, paradoxical ectopic calcification (calcifying enthesopathy) occurs as expansion of the calcified fibrocartilage of the enthesis – a frequent occurrence at a variety of tendon and ligament insertion sites, and at a relatively early age of adulthood for many patients, leading to further loss of mobility and pain (249, 258-261).

To date, for normal enthesis, beyond conventional radiography and some micro-computed tomography and histology studies, less is known about the nano- to micro-scale 3D structure of the insertion site in terms of its ultrastructural trajectory and culmination of mineralization events, more specifically in reference to the micro-scale mineral packing we have recently described in lamellar bone as "crossfibrillar mineral tessellation" (27, 262, 263). Similarly, beyond just a few studies attempting to address XLH enthesopathy in the commonly used *Hyp* mouse model (having truncating mutations in the *Phex* gene) (111, 249, 261, 264, 265), there exists no information on the ultrastructure of XLH/*Hyp* enthesis. Here we provide new comparative 3D multi-scale information of mineralization in normal (wildtype, WT) and osteomalacic (*Hyp*) Achilles enthesis insertion and Achilles mid-substance tendon (and therefore in the various instances of normal and ectopic mineralization events), in mice of different postnatal ages. Several recent original research articles and reviews have detailed the necessity of assessing mineralized tissues in a correlative fashion, with added context being provided from analysis of nano-scale dimensions (and in 3D), and through to the micro-scale, together providing the origin of macroscale mechanical properties (266-270). In addition to the new ultrastructural findings observed in normal and *Hyp* mice, we also provide a discussion of the molecular mechanisms which may influence the trajectory of mineralization in physiologic and pathologic circumstances.

3.3 Material and Methods

3.3.1) Rationale for a multi-scale 3D imaging approach to study enthesis mineralization

Correlative imaging approaches are commonly used now in structural biology studies investigating both cell cultures and tissues. However, this is not generally the case for extracellular matrix studies on mineralized tissues, where the matrix is permeated with a hard mineral phase that renders them difficult to analyze. Given the nano-scale structure of apatite crystallites within collagenous extracellular matrices in bones and teeth, together with their micro-scale crossfibrillar tessellation (27) – a packing pattern that contributes to bone's well-known mechanical properties – it has become imperative to assess mineralized tissue matrix and cells in a correlative and contextual 3D manner to understand cell, matrix and mineral relationships in these tissues. Here, we use a variety of multi-scale imaging approaches previously used for normal (wildtype) and osteomalacic (*Hyp*) bone (27) to characterize in 3D, and at the electron microscope level, enthesis structure. These correlative approaches include light microscopy, transmission electron microscopy, and micro/nano-computed X-ray tomography and FIB-SEM electron tomography, the latter two with the additional implementation of feature segmentation aided through the use of deep-learning algorithms and image analysis protocols.

3.3.2) Animal models and tissue harvesting

Hindlimbs, including the feet and Achilles tendon, were obtained from normal male C57BL/6 wildtype (WT) and mutant *Hyp* mice (B6.Cg-*Phex^{Hyp}*/J) mice of different ages (The Jackson Laboratory, Bar Harbor, ME, USA). *Hyp* mice have a loss-of-function truncation in the *Phex* gene (135, 137) and are a commonly used mouse model for X-linked hypophosphatemia. To date, at the ultrastructural level at which we are looking by electron microscopy for changes between normal WT and *Hyp* mouse mineralized tissues, we have not detected differences in respective mineralization patterns between the sexes. For the *Hyp* mice used here, although both males and females lack a functional *Phex* gene and show osteomalacia, mild gene-dosage effects have been noted between heterozygous and homozygous females (271). Located on the X chromosome, the *PHEX*/*Phex* gene is under the control of dosage compensation by random X chromosome inactivation (272) – half the cells in the heterozygous females express normal *PHEX*/*Phex* allele, and the other half express mutant allele. To avoid confounding gene dosage

effects, and to ensure that we can compare findings appropriately to the published literature, only male mice were used in this study. After mouse sacrifice (ages of mice for each experiment are indicated below), hindlimbs were quickly dissected and gently trimmed to isolate the calcaneus and a sufficient length of the attached Achilles tendon and plantar fascia ligament, and immediately placed in the chemical fixatives mentioned below. All animal procedures were reviewed and approved by the McGill University Institutional Animal Care and Use Committee, and they followed the guidelines of the Canadian Council on Animal Care.

3.3.3) X-ray imaging

3.3.3.1) *Sample preparation and imaging*

Hindlimbs from WT and *Hyp* mice at 3.5, 7, 10.5 and 14 months of age were used for µCT X-ray imaging after fixation of the tissues in 4% paraformaldehyde (Thermo Fisher Scientific, Waltham, MA, USA) and 1% glutaraldehyde (Electron Microscopy Sciences, Hatfield, PA, USA) in 0.1 M sodium cacodylate buffer (Electron Microscopy Sciences), pH 7.3. Specimens were fixed at room temperature for 2 hours on a rotator followed by a 48 h fixation period at 4°C. After several washes in 0.1 M sodium cacodylate buffer, the specimens were gradient-dehydrated over several hours into 100% ethanol. A Leica EM CPD300 instrument (Leica, Wetzlar, Germany) was precooled to 10°C in which specimens were critical-point dried through liquid CO_2 replacement of ethanol over several purging cycles, followed by heating to reach the critical point for converting CO_2 liquid to gas.

Critical-point dried samples of each genotype from each time point were imaged on the Zeiss Xradia Versa 520 (Carl Zeiss, Oberkochen, Germany) X-ray microscope (µCT). Samples were immobilized within the narrowing walls of plastic 100 µL micropipette tips. µCT analysis of the Achilles tendon insertion site into the calcaneus was performed using a 4x objective lens, an 80 kV source voltage, and an exposure time of 5 s per projection. Source-sample and sample-detector distances were optimized for phase contrast and for resolutions of about 1 µm/pixel with no binning. An additional scan of the Achilles tendon insertion was done for the 3.5-month and 14-month time points at 0.5 µm/pixel. Micro-CT of the mid-substance region more proximally in the Achilles tendons of 7-month-old WT and *Hyp* mice was completed using similar settings. Because of the size of the calcifying sites observed in the mid-substance tendon, two vertical scans were completed in sequence and digitally stitched together for the specimens, allowing for high

resolution to be maintained over twice the volume size. Additional conventional radiography was performed on the mid-substance Achilles tendon using a Kubtec Xpert 80 (KUB Technologies, Stratford, CT, USA) operating at 21 kV and at 4x magnification (Figure S1).

3.3.3.2) *µCT analysis (X-ray microscopy, high resolution)*

Structural analysis of fibrocartilage and cells of the Achilles enthesis was completed by cropping to small volumes that included only the calcified fibrocartilage (CF) zone (above the bone cement line, and below the lower grayscale uncalcified fibrocartilage (UF). For each cropped specimen volume, the Otsu algorithm (273) was applied to obtain a multi-region of interest (multi-ROI) using Dragonfly software (Object Research Systems Inc, Montreal, QC, Canada). Each distinct, nonconnected region was then assessed by volume/surface area ratio to eliminate the wider "noise" from each bi-modal distribution that was clearly not of the morphology of an individual lacunae or several connected lacunae. A watershed transform operation was then completed to label individual lacunae (of fibrochondrocytes, each lacuna presumably having their own single cell) that were indeed connected. An example of the importance of this labeling may be best explained using the example from higher magnification SEM images such as in Figure 6B – *Hyp*, rightmost green box, where two cells of two lacunae are connected, yet, for analysis purposes, each lacuna should in fact obviously be labeled distinctly. Next, edge volumes (partial lacunae) were removed using the box tool and "keep intersected" operation in the Dragonfly software. A round of manual assessment through labels of each specimen was completed to eliminate only a few lacunae that were mislabeled. Finally, segmented lacunae of the CF zone (150-250 for each specimen) were labeled and color-coded for visualization and quantification.

3.3.4 FIB-SEM serial-surface-view (slice-and-view) imaging

3.3.4.1) *Sample preparation and imaging*

Additional hindlimb specimens of WT and *Hyp* mice at 2 months, 3.5 month and 8 months of age were dissected as previously described and fixed in 2% paraformaldehyde in a solution of 0.1 M sodium cacodylate buffer (pH 7.3) for 2 h at room temperature under constant rotation, then overnight at 4°C. Specimens were stained with alcian blue (Sigma Aldrich, St. Louis, MO, USA) at pH 5.8 for 4 h before a secondary overnight fixation in 4% glutaraldehyde. After several washes in sodium cacodylate buffer, the undecalcified specimens were stained by repetitive exposures to

osmium tetroxide (Electron Microscopy Sciences, Hatfield, PA, USA) and thiocarbohydrazide (Sigma Aldrich) ligand, as termed the OTOTO method (9, 142). Subsequently, specimens were gradually dehydrated over several hours into 100% acetone, followed by epoxy resin infiltration over several days using decreasing acetone:Epon (Electron Microscopy Sciences) ratios, with final embedding in pure Epon polymerized over 2 d at 60°C. Cured Epon blocks were manually trimmed, sectioned on a microtome, and sections were stained on glass slides using silver nitrate (von Kossa staining) for mineral staining and toluidine blue counterstaining for light microscopy. Regions of interest from these light microscopy survey sections were selected from appropriate sagittal sectioning at the Achilles tendon insertion site. Corresponding blockfaces were further trimmed and sputter-coated with platinum to provide a conductive 5 nm film on the specimen for additional viewing by SEM (see below Section 2.5) for FIB-SEM region of interest selection.

Tomography at the nano-scale of the Achilles enthesis was performed using backscattered electron (BSE) imaging in a dual-beam Zeiss Crossbeam FIB-SEM electron microscope, operating in its serial-surface-view mode at a probe current of 700 pA and at 2 kV imaging voltage after blockface milling in the microscope using a focused ion beam of gallium. Each region of interest for FIB-SEM characterization was chosen such that it included regions of both calcified fibrocartilage (CF) and uncalcified fibrocartilage (UF), this ensuring capture of early mineralization events at the mineralization front, as well as including surrounding neighboring soft tissue and cells. Volumes of the enthesis from both WT and *Hyp* mice were obtained at an isotropic voxel size of either 17 nm (15,000-18,000 µm³) or 5 nm (250-500 µm³) isotropic voxel size. For the ectopic calcification of the mid-substance region of the Achilles tendon proper (Figure 11), imaging was performed using an FEI Helios Nanolab 660 DualBeam FIB-SEM (Thermo Fisher Scientific) microscope operating under similar conditions (2 kV imaging voltage, 0.79 nA milling current) and at 16 nm voxel size. Nano-tomography of additional lamellar bone volumes (Figure 2B) was carried out as previously described in Buss *et al*., 2020 (27) also using the FEI Helios FIB-SEM microscope using equivalent conditions (at 16 nm and 4 nm voxel size volumes), and likewise using BSE detection.

3.3.4.2) *Deep learning-assisted feature segmentation and analysis*

Mineralized regions and structures were segmented using the deep-learning features in Dragonfly software (Object Research Systems Inc). When segmentation of close-packed

108

individual mineral volumes was desired (to visualize crossfibrillar mineral tessellation (27)), extreme care was taken to manually remove the thin margins of lower grayscale boundaries from selected "ground truth" slices of cropped volumes. Using a convolutional neural network (CNN) with U-net architecture having a depth of 5 layers with 64 convolutional filters in the first layer (doubled in subsequent layers), manual inputs were partitioned into learning and validation subsets (80% and 20%) with 2 iterations of vertical and horizontal data augmentation (143). The training parameters used were patch size of 32, S:I ratio of 0.5 or 1.0, batch size of 64, and 50 epochs, or until training improvement had not been demonstrated for 10 consecutive epochs. Corrections were made to a wider range of slices again particularly around mineral tesselle boundaries. Because of the propensity of mineralized tissue samples to charge under the electron beam, extreme care was needed to not only train the network to recognize thin margins of lower grayscale values, but also to identify morphologies and orientations of lower grayscale features that were indicative of charging artifacts (so as not to include these in the resulting segmented ROI/region of interest). A second round of training was completed for each network for each volume. Using additional CNNs, a similar strategy was used to segment fibrochondrocytes. To easily create a robust inventory of training examples for fibrochondrocytes, the "snap" tool was used in combination with some manual ROI painter brush corrections in Dragonfly. To assess the bulk of mineralization, volume thickness heatmaps were constructed. Each segmentation of the bulk CF region was smoothed slightly and to the same degree (Kernel 3 for 5 rounds) to reduce computational time. The thickness heat-mapping approach of the software for imaging and quantification inscribes spheres of maximal possible diameters at every point within the 3D foreground features of the segmentation. Sphere diameters were color coded using the more perceptually uniform "linear" color map (274).

3.3.4.3) *Mineral tesselle labeling and analysis*

To label individual, roughly prolate ellipsoidal mineral tesselles in 3D, we used a watershed transform operation in Dragonfly on smaller cropped volumes. First, the meticulous segmentations of CF from the previous section were copied and inverted. This inverted ROI was then converted to a distance map which, similar to a volume-thickness heatmap, logs maximal expansion diameters at every point within the 3D foreground of the segmentation. Using the range tool, so called "seeds" were then carefully defined based on distance map intensities that would

roughly appear within each tesselle (roughly towards the center of each tesselle where their thickness is greatest). Inputs for the watershed transform were a multi-ROI created from the ROI of seeds, the distance map itself with values inverted, and the original segmentation ROI. Several iterations of labeling were done to find the best threshold that would reduce the exclusion of lowest-intensity seeds while also not allowing for more intense seeds to intersect. Tesselles were color-coded randomly using 64 discrete colors look-up table and multi-ROI quantitative analysis was conducted for volume, aspect ratio, and Feret diameters.

3.3.4.4) *Mineral foci analysis*

From the 5 nm voxel size Achilles tendon insertion and lamellar bone volumes (250-500 µm³), mineral was segmented as described previously using deep learning in Dragonfly. Next, a multi-ROI was created, and from this a new ROI was established to then only include mineral volumes (diffuse foci and maturing ellipsoids) that were separated from the bulk of the mineral. A distance map was then created which maps nearest neighbor distances at each point within the labeled foreground features (and thus represents a digital expansion of each focus in one direction). The distribution of these nearest neighbor distances was then plotted. A watershed transform was then completed for each volume based on the distance maps. This operation creates multi-colored labels for each digitally expanded foci that now abut their digitally expanded neighbors.

3.3.5 SEM blockface and TEM imaging

Hindlimbs from older (12-14 months) WT and *Hyp* mice were dissected and fixed as described previously in Section 2.3. In this case, undecalcified specimens were washed and stained in 4% potassium ferrocyanide-reduced osmium tetroxide. Graded dehydration to 100% acetone and infiltration and embedding into Epon resin was completed as previously described above. Following microtoming and staining for light microscopy for region selection as above, blocks were coated with 5 nm Pt and imaged by BSE detection using an FEI Quanta 450 FE-SEM microscope operating at an accelerating voltage of 10 kV. Blocks were then further trimmed, and 80-nm-thick sections were produced on an ultramicrotome, placed on TEM mesh copper grids, and conventionally stained with uranyl acetate and lead citrate. TEM imaging was performed using a Talos F200X S/TEM microscope (Thermo Fisher Scientific) equipped with a 4k x 4k Ceta 16M CMOS camera and operating at 200 kV with an inserted 40 µm objective aperture.

3.3.6 Immunohistochemistry

Hindlimbs from WT and *Hyp* mice at 3.5 (for enthesis) and 12 (for tendon) months of age were dissected and fixed as previously described above in Section 2.3, but using a lower 0.1% glutaraldehyde concentration in the fixative solution. Specimens were then demineralized in 8% EDTA containing 0.1% glutaraldehyde for approximately 4 weeks at 4°C in a large beaker under gentle stirring (solution was changed once at 2 weeks). Specimens were embedded in paraffin and sectioned onto glass slides with a microtome, and the sections were then deparaffinized with xylene and rehydrated to water through a graded ethanol series. Endogenous peroxidase activity was quenched using a 3% H_2O_2 solution. Immunohistochemical staining was carried out with an avidin-biotinylated peroxidase enzyme complex-based kit (Vectastain® Universal Elite ABC Kit; Vector Laboratories, Newark, CA, USA) and 3-amino-9-ethylcarbazole substrate (ImmPACT™ AEC Peroxidase Substrate; Vector Laboratories). Anti-PHEX labeling was conducted using a polyclonal antiserum as described in Ecarot and Desbarats (1999) as "a polyclonal antiserum raised in rabbits against a synthetic peptide (CGG)PRNSTMNRGADS corresponding to residues 734-745 of the carboxy-terminal sequence of Phex" (dilution 1:200 in blocking buffer) (275). Goat anti-mouse OPN (AF808; R&D Systems, Minneapolis, MN, USA) was used as a primary antibody for labeling of similarly cut sections, also diluted 1:200 in blocking buffer. Negative controls consisted of the same procedures while omitting the primary antibody. Hematoxylin counterstaining was applied followed by coverslipping in DAKO Ultramount (reagents from Agilent Technologies, Santa Clara, CA, USA).

3.4 Results

Here we extend our original report on crossfibrillar mineral tessellation in lamellar bone of WT and *Hyp* mice (27) now to a comparative 3D analysis of Achilles enthesis structure at the micro- and nano-scale in these two mouse strains, again using X-ray and electron tomography methods. Given the distinctive nature of enthesis fibrochondrocytes that mature to produce layered zones of fibrocartilaginous extracellular matrix that does, or does not, calcify (*i.e.* uncalcified fibrocartilage [UF] and calcified fibrocartilage [CF]), we examined this mineralization pattern in

relation to the well-known calcifying enthesopathy that is frequently found at the Achilles insertion in XLH patients.

3.4.1 Crossfibrillar mineral tessellation in normal (WT) mouse Achilles enthesis calcified fibrocartilage

3.4.1.1 *Normal enthesis mineral tessellation in comparison to that of normal lamellar bone*

Nano- and micro-scale structural relationships between minerals and the organic extracellular matrix of mineralized tissues and structures in biology underlie their mechanical performance across larger scales. To examine such structural patterns arising from cumulative mineralization events occurring across multiple scales, we used multi-scale imaging methods (light microscopy, high-resolution X-ray micro-computed tomography [X-ray microscopy], FIB-SEM serial-surface-view tomography, blockface SEM in BSE detection mode, and TEM) to provide correlative 2D and 3D structural information on the Achilles enthesis fibrocartilage insertion site (Figure 1A-D). In general, a similar analytical approach was used as we applied previously to examine mineralization trajectories and mineral patterning in lamellar bone (27). In particular, this approach allows for a new 3D understanding (with quantitation) of mineralized tissues using the high-resolution capabilities of electron microscopy at the nano- and micro-scales.

Using reconstruction of image volumes coupled with the deep-learning based segmentation functions of the Dragonfly software, mineral segmentation after FIB-SEM tomography of small volumes of the Achilles tendon enthesis at the mineralization front enabled the 3D organization of mineral to be revealed within the calcified fibrocartilage of the Achilles tendon insertion site (Figure 1B and Supp. Movie SM1A-WT; light grey – raw data, blue – segmentation, and multicolored – watershed labeling) [*We respectfully request that the editors and the reviewers take the time to examine our supplemental movies which are an important part of the data in this type of 3D imaging work*]. Starting at the mineralization front where uncalcified fibrocartilage (UF) transitions into calcified fibrocartilage (CF) across a mineralization front (MF)(Figure 1B,C) and then continuing throughout the CF, there exists a very similar, collagen fibril-spanning mineral packing pattern as we observed previously in bone (27) and termed crossfibrillar mineral tessellation. This mineralization pattern for both lamellar bone and the enthesis CF examined here generally consists of close-packed mineral tesselles (geometrically approaching prolate ellipsoids) having discrete margins that delineate intervening narrow zones (interphase boundaries) that are

112

generally mineral-free yet filled with the organic components of the extracellular matrix. These peripheral organic-rich mineral gaps between the mineral tesselles range in thickness from tens to hundreds of nanometers.

3.4.1.2 *Tesselle size and expansion from small mineral foci*

Comparing measurements from two FIB-SEM serial-surface-view volumes (Figure 1D) – one from under the mineralization front of lamellar bone (segmentation shown in Figure 2B), and one from under the mineralization front of the CF (Figures 1B,C and 2B, and Supp. Movie SM2A-C) – a similar distribution of tesselle aspect ratios was observed (Figure 1D). In both cases, starting at or near the mineralization front as viewed by SEM-BSE or FIB-SEM tomography, small foci of mineralization within otherwise uncalcified fibrocartilage or bone osteoid expand to form tessellating larger prolate ellipsoids/tesselles of closely packed mineral (Figure 2A,B and Supp. Movie SM1A-WT). Using the watershed labeling function of the software applied to full tesselles (Figure 2B, incomplete tesselles not fully contained within the volume were removed from the analysis), we computed the overall distribution of tesselle widths at their smallest dimension (calculated as the minimum Feret diameter) that generally aligns perpendicular to the long axes of both the tesselles and the collagen fibrils. Taken together, these 3D FIB-SEM tomography data (Figure 2B) over small volumes of fibrocartilage, coupled with SEM backscattered imaging over much larger 2D block faces (Figure 2A), indicate a greater size variation of tesselles and heterogeneity in tesselle spacing/packing in fibrocartilage as compared to that found in mouse periosteal lamellar bone.

We next considered whether the larger and more heterogeneously sized and spaced mineral tesselles in fibrocartilage (in comparison to bone) originate primarily from discrete, individual small nanometer-sized mineral foci, or alternatively, whether fusion of mineral volumes at or near the mineralization front contribute to tesselle dimensions. To investigate this question, we calculated the distribution of nearest neighbor distances of segmented mineral foci near the mineralization fronts of fibrocartilage and bone using higher-resolution FIB-SEM volumes acquired at 5 nm voxel sizes or less (thus resolving even the smallest mineral foci). For lamellar bone, the distance distribution was unimodal and centered around 0.35 µm (Figure 2C). This distance represents the average minimum at which another expanded mineral focus would be met in a Voronoi pattern; therefore, the complete average minimum width of each digitally expanded

foci would be 0.70 µm for bone. This 0.70 µm value approximates that which we have observed as the minor axis (minimum Feret diameter) after physiologic tesselle growth (Figure 2B), and moreover, it suggests that individual mineral foci are indeed primarily "seeds" that through growth and expansion define mineral tesselles. In Achilles enthesis CF, a similar effect was observed, although with a wider distribution of sizes in both the distribution of mineral foci nearest-neighbor distances and the minor *a*-axis of mature tesselles. This indicates that a greater heterogeneity of initial foci formation is a determinant of mature tesselle morphology heterogeneity as we observed in the data shown in Figure 2B.

3.4.1.3 *Observations on tesselle abutment and their boundaries*

To assess the packing pattern of mineral tessellation at finer scales, and thus the relationship of mineral nano-crystals within and between collagen fibrils at the level of the periphery of individual tesselles found in the enthesis fibrocartilage, we completed a manual segmentation from a 5 nm voxel resolution volume (Figure 3A,B). At each tesselle periphery/boundary there existed a less electron-opaque (a less mineralized) interphase region ranging in thickness from tens to hundreds of nanometers.   This was a consistent feature over all samples and in mice of all ages, indicating these interfacial boundary zones are maintained over time in fibrocartilaginous mineralized tissue (that is not remodeled, in contrast to bone). As viewed in FIB-SEM images, within the tesselles, mineral textures showed clear evidence of integrating with the underlying banding structure of collagen fibrils (Figure 3A,B, and left panel in C). In other samples imaged by TEM (Figure 3C, right panel), a similar pattern was observed where mineral crystals aligned with the gap/overlap molecular spacing of the collagen fibrils observed as the well-known characteristic 67 nm repeat pattern (Figure 3D).

3.4.2 Crossfibrillar mineral tessellation in Achilles enthesis calcified fibrocartilage in the *Hyp* mouse model of XLH

Based on the frequency in XLH of calcifying enthesopathy, here we also aimed to gain a greater understanding of Achilles enthesis structure in *Hyp* mice. First, like for WT mice as described above, we imaged *Hyp* Achilles enthesis insertions at different mouse ages using X-ray micro-computed tomography (µCT, X-ray microscopy). Compared to normal WT mice, *Hyp* mice presented with substantially decreased mineralized bone and increased bone porosity in the

calcaneus in the vicinity of the Achilles tendon insertion site, readily evident in *Hyp* mice at all the ages we examined (from 3.5 months to 14 months, Figure 4A and Supp. Movies SM4A,B, SM5A). Although occasionally some small calcaneal enthesophytes were observed at the Achilles enthesis, enthesophytes were not consistently noted at this site (even in older mice), but sometimes they were more pronounced on the plantar fascia side of the calcaneus, but only slightly so (Supp. Movie SM4B provides a good example).

Given that hallmark peri-osteocytic lesions (POLs, halos) in bone are a characteristic feature of XLH/*Hyp* – where osteocyte mineral lacunar volumes are enlarged – we investigated whether this might likewise occur related to fibrochondrocyte mineral lacunar volumes in the calcified fibrocartilage. To assess this, 3D full-volume fibrochondrocyte mineral lacunae were segmented at the insertion site from WT and *Hyp* mice using watershed transform labeling (Figure 4B). Using this methodology of assessment, no significant changes in lacunar volumes were observed either within WT or *Hyp* mice of different ages, or between WT and *Hyp* age-matched mice ranging from 3.5 months to 14 months (Figure 4B,C).

For further analysis of enthesis sites, SEM backscattered electron (BSE) imaging – that highlights mineral – was performed on calcaneal Achilles enthesis and plantar fascia enthesis on the block faces of Epon-embedded and microtomed samples (Figure 5A). Using this imaging method, additional details on mineral distribution were observed, for example, in WT mice, the highly interdigitated interface of the calcified fibrocartilage was observed with the underlying calcaneal bone, and fibrochondrocyte mineral lacunae and distribution were readily apparent. This broad survey method of the blockface among samples was useful for comparisons to show the less organized distribution of cells/mineral lacunae in the *Hyp* mice versus the WT mice. It also revealed thin "rings" of mineral surrounding cells in the *Hyp* mice on the plantar fascia side of the calcaneus, perhaps an early mineralization event (Figure 5A, arrows). Such observations were placed in broader context when localized at a larger scale using 3D reconstructions from μCT analyses of both entheses of the calcaneus that were examined in both mouse phenotypes (Figure 5B). 3D-rendered surface features shown in μCT movies (Supp. Movie SM5A) reveal morphological differences between the insertion sites of WT and *Hyp* in 10.5-month-old mice, with the mineralized *Hyp* enthesis and bone surfaces showing increased surface texture/roughness.

3.4.3 3D nano- and micro-structure of the mineralization front of Achilles enthesis calcified fibrocartilage in WT and *Hyp* mice

3.4.3.1 *Hyp mice display defective calcified enthesis fibrocartilage structure as early as 2 months of age*

Previously we described in 3D that *Hyp* mice have defective nano- and micro-structural organization of mineral within hypomineralized lamellar bone; in particular, *Hyp* mice have bone with incomplete crossfibrillar mineral tessellation near the mineralization front that presumably at least partly contributes to the *Hyp* macroscopic bone deformities (27). This type of mineralization defect at the nano- and micro-scale is unrecognizable by conventional light microscopy and μCT methods, but requires the resolution of electron microscopy tomography methods (as we have applied here). To investigate whether the pathogenesis of XLH/*Hyp* involves similar structural malformations of mineral at entheses, we examined in detail and in 3D — with electron microscope resolution — the mineralization front of the Achilles insertion into the CF zone. We assessed multiple FIB-SEM volumes of various ages from WT and *Hyp* mice, starting with a matched pair at 2 months of age (Figure 6 and Supp. Movies SM6A,B). Enthesophytes were not evident in these 2-month-old mouse samples.

While WT mice displayed a characteristic trajectory of mineralization from small mineral foci tens to hundreds of nanometers in length which then elongated aligned with the long axis of collagen fibrils and enlarged across collagen fibril arrays to pack and tessellate with neighboring tesselles, *Hyp* specimens lacked such a mineralization trajectory to produce coherent crossfibrillar mineral tessellation (Supp. Movies SM6A,B). Below the mineralization front, this was readily observed in 3D as generally smaller and more irregular and isolated mineral volumes that did not abut against one another and instead had larger separating organic unmineralized spaces between them and their neighboring mineral volumes (Figure 6A-C). Also presented here are segmentations to show the comparative ultrastructure of fibrochondrocytes directly adjacent to the mineralization front, with *Hyp* fibrochondrocytes having less cell-surface membrane ruffling (Figure 6D).

3.4.3.2 *Hyp mice exhibit an aborted and irregular mineral foci growth trajectory*

FIB-SEM reconstruction of fibrocartilage volumes at 2-, 3.5- and 8.5-month mouse ages demonstrated smaller and more diffuse mineral tesselles in *Hyp* mice, and incomplete mineral

tessellation (Figure 6 and Supp. Movies SM6A,B). Specimens of fibrocartilage from 2-month-old WT and *Hyp* mice were additionally compared to other sampled volumes from older mice by FIB-SEM electron tomography. To quantify the observations depicted in Figure 6, we applied thickness heatmapping to general segmentations of mineralized volumes (foci/tesselles) from each volume (Figure 7A,B). Using the software's sphere-fitting algorithm to ascribe and map the maximum thickness of each labeled/segmented voxel, when compared to WT mice, *Hyp* mice had an accumulation of smaller thickness measurements in the zone of calcified fibrocartilage for the segmented mineral volumes (Figure 7A). Next, we then segmented all of the small mineral volumes that were not connected to the mineralization front (*i.e.* growing smaller mineral foci), and approximating the mineralization front of the larger attachment site as a 2D cross-sectional planar area, we calculated that from this perspective that there are more than double the number of disconnected mineral foci volumes in the *Hyp* (7.6 per 10 µm²) as compared to the WT (3.1 per 10 µm²) mouse fibrocartilage (Figure 7C and Supp. Movie SM7A), this being attributed to the occurrence of immature mineral volumes for a larger depth (versus WT where small mineral volumes were only observed immediately above the mineralization front). We used area to normalize this measurement because if we had used volume it would skew the data given that in WT mineralization there are normally no foci that persist below the mineralization front (this is because at that point there is confluent, space-filling tessellated packing of geometrically approximating prolate ellipsoidal mineral tesselles). In *Hyp* mice, untessellated mineral foci and ellipsoids persist throughout the volume and there is no clear mineralization front for an extended distance (see Supp. Movie SM7A) – similar to what we have shown in lamellar bone (27).

3.4.4 PHEX and osteopontin localization at the Achilles enthesis insertion of WT and *Hyp* mice

To gain insight into which proteins may contribute to these divergent trajectories of fibrocartilage mineralization, we assessed the presence and location of PHEX and OPN by immunohistochemical staining of WT and *Hyp* enthesis insertion sites (Figure 8). As has been shown for most mineralized tissues (262), staining for OPN was found to be closely associated with the mineral in the CF of both WT and *Hyp* mice (Figure 8A,B). The PHEX antibody clearly showed the well-known staining pattern for osteoblasts and osteocytes (and their cell processes) in WT bone (in this case tibial bone located proximally within the same sections), but there was

no staining related to WT enthesis fibrochondrocytes (Figure 8C), this compared to our control incubations (Figure S2). In *Hyp* mice, there was no staining for PHEX observed in either tibial bone or enthesis fibrocartilage (Figure 8D), as would be expected as a result of their inactivating truncating mutation in PHEX.

3.4.5 Age-related ectopic calcifying tendinopathy in WT and *Hyp* mice: 3D ultrastructural aspects and crossfibrillar mineral tessellation

During the course of this study, we observed in the μCT scans of the lower hindlimb — dissected to contain the full length of the Achilles tendon — that both older WT and *Hyp* mice consistently had large discrete regions of electron opaque mineral within their tendon mid-substance, occurring well proximal of, and not connected to, the enthesis or enthesophytes (Figure 9). Given this observation in a highly aligned, collagen fibril-dominated extracellular matrix, we considered whether this age-related instance (given occurrence in WT) of ectopic mineralization might have a mineral tessellation trajectory similar to what was observed in WT and *Hyp* entheses and lamellar bone. In mice over 7 months of age, calcifying Achilles tendinopathy was prominent in every WT and *Hyp* mouse we observed (Figure 9A-C, Supp. Fig. S1), bilaterally, and in mice of both CD1 and C57BL/6 strain backgrounds. We are unaware of any study that has recognized this frequent occurrence in older mice, and we describe it in detail below. In Achilles mid-substance tendon sections from 12-month-old WT mice, strong osteopontin immunostaining was associated with the ectopic mineralized regions (here decalcified for paraffin embedding and sectioning) of the mid-substance tendon (Figure 9D,E). By electron microscopy of polished sample block faces imaged by SEM-BSE, a surprising resemblance occurred for the ultrastructural patterning of WT mineral foci and mineral tessellation seen in bone and calcifying fibrocartilage versus the defective patterning and defective tessellation seen in these mineralized tissues *Hyp* mice (Figure 9F,G and Supp. Movies SM9A). In *Hyp* mice there were large regions of diffuse and isolated foci together with an overall aberrant structure of ectopically calcifying regions (Figure 9G and Supp. Movie SM9A) as compared to the more organized WT tendon mid-substance calcification pattern having well-organized regions such as clear zones of unmineralized collagen, a mineralization front, and a heavily mineralized tessellated zone (Figure 9F and Supp. Movie SM9A).

In conventionally stained TEM sections of the WT calcifying Achilles tendon mid-substance site, extensive mineralization occurred in a tessellation packing pattern immediately adjacent to tenocytes and farther from these cells (Figure 10). Mineralization was observed both between and within the tendon collagen fibrils, with mineral banding patterns being observed (Figure 10A,C,E). In TEM sections of the *Hyp* calcifying Achilles tendon mid-substance site, mineralization foci (rather than interlocking tesselles) were prominent, with much of the mineralization occurring between the collagen fibrils (Figure 10B,D,F).

To assess the 3D nano- to micro-structure of this ectopic mineralization in normal WT mice, and in a correlative approach, we used the same block from Figure 9D and coated the surface first for SEM-BSE blockface imaging (Figure 11A-C) followed by subsequent small region preparation for FIB-SEM serial-surface-view imaging (Figure 11D-F). Here we found that ellipsoidal mineral tesselles were quite larger in length (up to and exceeding 5 µm). Similar to bone and enthesis fibrocartilage, we observed discrete lower grayscale organic interfaces around much of each tesselle periphery, partly defining their boundaries. Four tesselles were segmented in 3-dimensions in Figure 11D (also shown in Supp. Movie SM11A-WT), with corresponding images in different views shown in Figure 11E,F. Despite the larger tesselle size, close-packing tessellation was achieved as observed in both 2D and 3D imaging (Supp. Movie SM11A-WT).

3.5 Discussion

Here we extend our original report on crossfibrillar mineral tessellation in lamellar bone of WT and *Hyp* mice (27) to a comparative 3D analysis of Achilles enthesis structure at the micro- and nano-scale in these two mouse strains, again using X-ray and electron microscopy and electron tomography methods. Given the distinctive nature of enthesis fibrochondrocytes that produce zones of fibrocartilaginous extracellular matrix that does not, or does, calcify (*i.e.* commonly called uncalcified fibrocartilage and calcified fibrocartilage), we examined this mineralization pattern in WT mice and compared it to that found in *Hyp* mice which have long served as a commonly used model for X-linked hypophosphatemia (XLH). More specifically, we describe 3D features of fibrocartilage mineral at both the micro-scale and ultrastructural levels in *Hyp* mice having similar calcifying enthesopathy characteristic of the Achilles enthesis in XLH patients (111, 249, 258,

259, 261, 264, 265). Furthermore, we identify and characterize an Achilles tendon mid-substance calcifying tendinopathy in both WT and *Hyp* mice.

Enthesis fibrocartilage has evolved with unique properties to minimize stress concentration at a juncture where there are large applied forces on juxtaposed tissues having a large discrepancy in their elastic moduli. The fibrocartilage enthesis has four zones with distinct compositional and structural properties starting from the tendon or ligament, then to uncalcified fibrocartilage, then across the mineralization front into calcified fibrocartilage, and finally continuing across to a mineralized cement line/plane interfacing with underlying bone. Even within this continuum of different unmineralized or mineralized extracellular matrices, finer gradients of properties and adaptations within each individual zone have been identified that act to prevent stress singularities, contributed to by features such as collagen fiber orientation, tissue interdigitation, and mineral gradation (74, 83, 85, 251-253, 276-278). It is well-known that matrix-mineral (organic-inorganic) relationships as generally found in mineralized tissues are critical determinants underlying macro-level performance (279-281). Therefore, we undertook this multi-scale mouse enthesis study with a specific focus on the 3D micro- to nano-scale structure of Achilles enthesis calcified fibrocartilage, using particularly X-ray and FIB-SEM tomography methods coupled with advanced quantitative image analysis using deep learning-assisted segmentation of features of interest (particularly mineral).

3.5.1 Progression of calcifying enthesopathy in the osteomalacic *Hyp* mouse model of XLH

As a result of inherited inactivating mutations in the *PHEX* gene, XLH patients and *Hyp* mice have soft, hypomineralized bones and teeth (27, 123, 256, 257). This is attributable to both an increase in systemic circulating FGF23 levels causing hypophosphatemia through renal phosphate wasting coupled with abnormally low-to-normal $1,25(OH)_2D_3$ (127), and an accumulation of mineralization-inhibiting osteopontin (OPN) protein locally in the extracellular matrix (as a result of decreased PHEX enzyme activity, OPN is a substrate for PHEX (136)). These changes manifest clinically in bone as rickets, osteomalacia and peri-osteocytic lesions (123), and in teeth as odontomalacia (123, 174). We have previously used FIB-SEM tomography to identify in *Hyp* mouse bone a delayed and defective mineralization trajectory/patterning different from the normal trajectory called crossfibrillar mineral tessellation in lamellar bone. Mineral patterning (tessellation) at the micro- and nano-scale in normal bone has generally been overlooked until

recently because it is not resolved by light microscopy or µCT. This space-filling, tessellated close-mineral-packing pattern observed at the micro-scale in bone has just been revealed from the recent application of FIB-SEM tomographic imaging and 3D reconstruction methods at the high-resolution scale of electron microscopy (27, 262, 282). In addition to having aberrant crossfibrillar mineral tessellation, bone deformities and frequent fractures/pseudofractures, XLH patients and *Hyp* mice commonly have expansion of the calcified fibrocartilage zone at the Achilles tendon insertion site (enthesis) leading to calcifying enthesopathy causing additional debilitating pain and loss of mobility for patients (258-260). Several studies have addressed the underlying molecular mechanisms of calcifying enthesopathy using the *Hyp* mouse model of XLH (111, 249, 261, 264, 265).

XLH patients (and to some degree *Hyp* mice) commonly have expansion of the calcified fibrocartilage zone at the Achilles tendon enthesis leading to calcifying enthesopathy. Beyond the differentiation of progenitor cell populations into differentiated cells in the mineralized tissues of the skeleton and dentition, an important factor in permitting bulk mineralization of extracellular matrices is the broad release from inhibition imposed by the small molecule pyrophosphate (PPi). This release from inhibition (inhibiting an inhibitor) occurs through the enzymatic activity of TNAP (tissue-nonspecific alkaline phosphatase, also abbreviated TNSALP and ALPL; gene *ALPL*) which degrades inhibitory PPi (107) allowing mineralization to proceed according to the *Stenciling Principle* (2, 262). This principle refers to the double-negative paradigm of inhibiting an inhibitor, as originally described by Jacob and Monod (repressing a repressor) for the genetic regulation of enzyme expression in bacteria (283). For mineralized tissues, several enzyme-substrate pairs following this principle have been identified in mineralized tissues that include the pairs TNAP-PPi and PHEX-OPN (2, 262).

In Achilles enthesis fibrocartilage, Liang *et al* (249) observed an expansion of TNAP-producing cells in female *Hyp* mice as compared to WT mice. This cellular expansion of TNAP production (*Alpl* expression) occurs in conjunction with an expansion of fibrocartilage extracellular matrix markers such as collagen type 2 and an egression/advancement of the mineralization front into the uncalcified fibrocartilage zone (249). At this site, Karaplis *et al* (111) reported expansion of TNAP-producing cells at the Achilles insertion of transgenic mice overexpressing *Fgf23*, with PHEX retaining its functionality (111). Both of the aforementioned studies discuss the fact that tenocytes and fibrochondrocytes express *Fgfr3* and *Klotho*, this having

the implication that heightened levels of FGF23 may be involved in the pathogenesis of XLH/*Hyp* enthesopathy. Additional studies by Liu et al (265) in *Hyp* mice identified *Scx-* and *Sox9-* expressing progenitor cells at the Achilles enthesis as was originally described by the Zelzer group for normal mice (40, 41). Of note, Liu *et al* (265) showed that early treatment (before 2 weeks of age) of *Hyp* mice with 1,25(OH)$_2$D$_3$, or with anti-FGF23, antibody appear to reduce Achilles enthesopathy despite 1,25(OH)$_2$D$_3$ increasing circulating FGF23. These findings challenged the prior notion of increased circulating FGF23 as being the primary driver of enthesopathy whether in FGF23 transgenic mice, in *Hyp* mice and XLH patients, or in DMP1-deficient mice where enthesopathy also occurs in a state of elevated circulating FGF23 (284). Furthermore, Liu *et al* (265) propose that the lapse in 1,25(OH)$_2$D$_3$ increases expression of *Bmp* and *Ihh* target genes, this underlying the subsequent expansion of TNAP expression to additional mature fibrochondrocytes. Indeed, hedgehog signaling is a well-documented essential pathway which underlies enthesis development and mineralization (244).

In parallel with these descriptions of aberrant molecular pathways present in *Hyp*/XLH, altered mechanics as a result of defective mineralization in the bone-calcified fibrocartilage complex of entheses has also been implicated in the pathogenesis of calcifying enthesopathy in XLH/*Hyp* (264). Over the course of Achilles enthesis development in XLH/*Hyp*, it is expected that the forces experienced by Achilles insertion fibrocartilage directly attached to a softer-than-usual, more pliant osteomalacic bony anchor would be far different from that in normally developed entheses (in humans, mice and otherwise). Based on the known role of mechanical stimulation in development of the "enthesis organ" (243, 285, 286), this alone would be expected to alter developmental, structural and functional aspects of the insertion itself as compared to a normal unaffected enthesis.

Particularly in the context of defective mineralization in *Hyp*/XLH, our results provide new 3D context into calcifying enthesopathy in *Hyp* mice linking the mineralization trajectory in fibrocartilage with micro- and nano-scale 3D structure at the enthesis insertion site. As part of this analysis, using μCT and the higher resolution of sample block face SEM-BSE, we found it was not trivial to discriminate overt calcifying enthesophytes in *Hyp* mice compared to what has been reported in the literature about the prevalence of this phenotype in human patients (as assessed by conventional radiography). As shown in the 7-, 10.5-, and 14-month mouse ages we examined, as compared to normal WT mice, there appears to be some minor protrusion of the calcified

fibrocartilage in *Hyp* mice mainly at the plantar fascia ligament insertion into the inferior calcaneal tubercle, with only minor widening of mineralization occasionally at the superior Achilles insertion. The noticeable expansion of calcified fibrocartilage into the plantar fascia uncalcified fibrocartilage shown in some *Hyp* mice seems to start as a thin rim of mineralization immediately surrounding the lacunae of fibrochondrocytes within the uncalcified fibrocartilage zone, expanding from there to become more confluent to form the more apparent mineral protrusions. We note in the 2D X-ray projections from *Hyp* mice in Faraji-Bellée *et al* (261) that it was likewise the expansion of calcified fibrocartilage within the plantar fascia that was most evident, this compared to the more prominent calcified spurs in human patients occurring at both the superior and inferior calcaneal tubercles. Also, in this same report, and as we noted in our study, calcifying enthesophytes were not consistently observed (261).

Differences in the prevalence of calcifying enthesophytes between mice and humans could be explained by the different loading conditions of locomotion and ambulatory gait between species. Ground reaction forces from locomotion influence the loading environment for any long bone, where the orientation and magnitude of the forces partly determine the strain and bending moments experienced by the bone (287). It would indeed then seem quite reasonable to consider that in species such as mice — where the metatarsals are lengthened and the calcaneus does not normally contact the walking surface during gait — the mechanical forces applied to the calcaneal entheses would be very different from those found in humans, and likely even more so for conditions such as the osteomalacias having defective mineralization.

In addition to this difference in prevalence and appearance of calcifying enthesophytes between XLH patients and *Hyp* mice, also observed was extensive and consistent age-related calcifying tendinopathy in the mid-substance region of the Achilles tendon proper, in both normal WT and *Hyp* mice, and starting at 7 months of age. While this was a consistent finding in the sampled aged mouse groups, this is a rare occurrence in older human adults (288, 289). Distinct differences in the occurrence of ectopic calcifications between human and mouse, and in other species, support the broader notion of how anatomical and lifestyle differences predispose connective tissues distinctly to ectopic calcifications, and those which originate from both disease and age-related degeneration. Taken together, our findings generally reinforce our understanding of the importance of altered mechanics in the pathogenesis of XLH/*Hyp* calcifying enthesopathy. These may act in addition to the aforementioned influences from high circulating FGF23 and/or

low-to-normal 1,25(OH)$_2$D$_3$ on fibrochondrocyte maturation and function, all of which influence mineralization trajectories in the mineralized tissues of entheses. Below we discuss our multi-scale 3D findings of mineralization trajectories in the fibrocartilaginous zones of calcaneal entheses in WT and *Hyp* mice.

3.5.2 Nano- to micro-scale (crossfibrillar mineral tessellation) trajectories of mineralization in WT and *Hyp* mouse Achilles enthesis

The inherent trade-off between resolution and broader field-of-view context traditionally complicates our ability to provide seamless, integrated understanding between magnification scales for characterizing tissue, cell and molecule structural biology. Mineralization of tissues, notably in extracellular matrices, adds yet another dimension to be analyzed and integrated into our understanding — in this case an inorganic phase of calcium-phosphate mineral. However, significant advances in our knowledge of these tissues have been afforded by microscopy methods cutting across different magnification scales. Here, for the study of Achilles enthesis structure, we have used predominantly X-ray microscopy (µCT with resolution less than 1 µm) for broader-context information at the micro-scale, and FIBSEM 3D tomography and SEM and TEM for finer-scale information at the nanometer-to-micrometer scale, as we have done previously for lamellar bone (27, 266-268). Here we provide an integrated, correlative, 3D description of the structural relationships in Achilles enthesis where both organic and inorganic constutients contribute greatly to macro-level function of the enthesis. For mouse Achilles enthesis, we examined this in both normal fibrocartilaginous tissue (WT) and in osteomalacic fibrocartilaginous tissue (*Hyp*).

Mineralization lies at the core of mechanically anchoring tendons and ligaments to bone. Recent progress in our understanding of mineralization mechanisms working at the nano-scale, and mineral structuring/patterning occurring at the micro-scale, has partly stemmed from our more fully understanding the role of enzymes such as TNAP and PHEX in removing mineralization inhibitors such as PPi and OPN, respectively (1, 2, 107, 136, 262). In addition to the previously mentioned broad release of inhibition of mineralization by degradation of inhibitory PPi that occurs through the enzymatic actions of TNAP, we have hypothesized that another substrate-enzyme pair — OPN and PHEX — acts to refine mineralization at the nano- and micro-scales. Unlike rapid small-molecule (PPi) degradation via TNAP enzymatic activity, refinement of mineralization patterning is proposed to occur through the more extended process of

124

mineralization-inhibiting phosphoprotein synthesis and secretion (*e.g.* OPN) and subsequent degradation over time into small inactive peptides via PHEX enzymatic activity (2, 262). This notion is supported by *in vivo* genetic evidence of aberrant mineralization phenotypes in many transgenic (including compound mutants) and spontaneous-mutation mouse models, by immunohistochemical localization of these proteins, and by *in vitro* assays of their enzymatic activities.

Building upon previous work done originally in bone (27, 97), here we add a multi-scale 3D analysis of two more distinct mineralizing collagenous extracellular matrices — calcified enthesis fibrocartilage, and ectopic age-related mineralization of the mid-substance Achilles tendon — and provide evidence in mice of structural alterations in mineral packing that relate to the pathobiology of calcifying enthesopathy observed in *Hyp*/XLH. In normal WT lamellar bone and in calcified fibrocartilage, at or near the mineralization front, fields of small nanometer-sized mineral foci (whose exact origins remain unknown) enlarge and close-pack into abutting prolate ellipsoids (geometric approximation) of mineral to form the micro-scale pattern of crossfibrillar mineral tessellation. As part of this close mineral packing of "tesselles", narrow organic (without overt mineral) interphase zones are formed as discrete boundaries of tens to hundreds of nanometers in their thickness dimension, and they remain largely intact throughout the tissues. We have proposed that this type of tessellation patterning over three dimensions — a regular occurrence in different bones of different species (27, 78, 190, 192, 262, 282, 290-292) — provides resistance to compressive and bending forces. Mineral tessellation has recently been classified as a regular component of bone's hierarchal organization (263). Here in this study, we have identified this same feature (with some differences) in enthesis calcified fibrocartilage, suggesting that crossfibrillar mineral tessellation has evolved to be modular, where tesselle spacing and size (and potentially even other unknown nano-scale properties associated with each tesselle) may simply vary between different mineralized tissues within a species. It is also possible that these parameters of mineral tessellation may vary amongst different vertebrate species as an adaptation to functional demands. Equally important to the mineral tesselles may be the nature and properties of the intervening organic interphase network bounding and remaining at the tesselle boundaries.

Specifically concerning crossfibrillar mineral tessellation at the Achilles enthesis, we provide structural evidence which supports its contribution to the gradient of properties from the bone, through the enthesis fibrocartilage, and into Achilles tendon proper. We suggest that there

exists an intermediate range of sizes and spacings of crossfibrillar mineral tessellation in the calcified fibrocartilage as compared to the underlying calcaneal bone, this acting to reduce the overall stiffness of the enthesis compared to bone, and thus perhaps improving the tissue's elastic response. This likely represents another structural mechanism for reducing stress between soft tendon and hard bone proper. This notion is supported by work indicating that failure at the insertion site frequently occurs through bony avulsion, and not within the fibrocartilage zones of the enthesis (83). Additional FIB-SEM work is needed to determine whether differences in progressive tesselle packing near the mineralization front (as we observe to a degree in lamellar bone) versus beyond (deeper into the tissue towards the bone) form the basis of a "mineral gradient" across the enthesis tissues (251, 252).

In hypomineralized/osteomalacic *Hyp* bone, crossfibrillar mineral tessellation is delayed and incomplete (27). In the present study comparing WT mineral structural features in Achilles enthesis calcified fibrocartilage to those observed in *Hyp* mice, to our surprise, mineral tessellation in *Hyp* bone, fibrocartilage and mid-substance tendon had nearly identical deficiencies (as compared to WT) in the trajectory of mineralization within each unique matrix type. Mineralization of fibrocartilage and mid-substance tendon in *Hyp* mice showed delayed growth from their foci-of-origin, and incomplete tessellation, just as in *Hyp* bone. Since PHEX activity is absent in *Hyp* mice, and mineralization-inhibiting OPN thus accumulates at sites where it is expressed and secreted as we have shown here by immunohistochemistry in the calcified fibrocartilage zone of the *Hyp* enthesis, this accumulation likely contributes to the mineralization defect in conjunction with the hypophosphatemia. While OPN was readily detectable and abundant by immunohistochemistry in both WT and *Hyp* calcified fibrocartilage, PHEX was not detected in the WT enthesis. This lack of PHEX immunostaining in the WT enthesis fibrocartilage represents either epitope masking of some sort in this particular tissue compared to bone (where there was indeed an expected positive reaction), or that the fibrochondrocytes do not express PHEX. The consistency of strong OPN immunostaining at all mineralization sites examined here (bone, enthesis calcified cartilage, and calcified mid-substance tendon) in both WT and *Hyp* mice provides indirect evidence that matrix OPN levels are regulated (and may become dysregulated) in mineralized tissues to influence mineralization trajectories, consistent with abundant literature on OPN acting in this mineralization-inhibiting regulatory capacity for physiologic and ectopic calcification (2, 262, 293, 294). In fact, as shown for healthy WT bone, in addition to OPN being

degraded/inactivated by PHEX enzymatic activity (136, 175), there are also other factors that may influence the expression of OPN, such as Pi, PPi, FGF23 (145, 188, 295), and vitamin D levels.

Amongst likely others, two possible explanations (as suggested largely from previous work on bone) for the altered mineralization trajectory occurring at the Achilles enthesis of the *Hyp* mouse are *i*) altered regulation of an as-yet-unknown enthesis mineralization-associated protein, peptide, or molecule (including additional unknown regulatory substrate-enzyme pairings (2, 123, 174, 262), and/or *ii*) inadequate free phosphate available for mineralization. At the Achilles entheses in *Hyp* mice, the expansion of calcifying fibrochondrocytes producing TNAP (expressing *Alpl*) to remove mineralization-inhibiting PPi broadly supports the expansion of mineralization and gradual encroachment of the mineralization front further and further into what would normally be uncalcified fibrocartilage — this potentially proceeding to the formation of overt enthesophytes. However, broad accumulation of inhibitory PPi has also been shown to occur in the tissues of *Hyp* mice (295, 296), also near the mineralization front, and this also potentially acts to upregulate OPN (145).

In reconciling the similar aberrant trajectories of mineralization between bone, the enthesis, and that occurring ectopically in the more proximal mid-substance Achilles tendon, it seems reasonable to consider that directly adjacent to fibrochondrocytes, at or slightly beyond the mineralization front within the uncalcified fibrocartilage, TNAP activity could act to increase the Pi:PPi ratio to the point of permitting mineralization initially in the matrix immediately surrounding the fibrochondrocyte lacunae. This could also potentially occur related to tenocytes when calcification occurs in tendon ectopically adjacent to those cells. Therefore, during ectopic mineralization expanding into the uncalcified fibrocartilage zone of *Hyp* entheses and occurring in mid-substance Achilles tendon, mineralization occurs initially preferentially circumscribing fibrochondrocyte cells, or diffusely initially nearby tenocytes, respectively. The mineralization then becomes more confluent at a time when constitutive expression of *Alpl*/TNAP by many cells might reach a level sufficient to create a matrix environment that more broadly has a Pi:PPi ratio conducive to mineralization.

3.5.3 Calcifying tendinopathy in the Achilles tendon proper (mid-substance)

In the Achilles mid-substance tendon we documented consistent age-related mineralization (calcifying tendinopathy) in both WT and *Hyp* mice. Moreover, using 2D and 3D electron

microscopy methods to examine the nano- and micro-scale features of this ectopic calcification, we show in WT mice that like in bone and in enthesis fibrocartilage, the mineralization similarly follows a crossfibrillar mineral tessellation pattern. This pattern in fibrocartilage again arises from a mineralization trajectory that starts with small mineral foci in the collagenous extracellular matrix that then expand into abutting tesselles. In *Hyp* mice, again similar to bone and fibrocartilage, an ultrastructural mineralization deficiency was observed that likewise leads to altered mineral tessellation, with mineral foci nucleation favored over mineral foci growth, thus leaving abundant small foci and tesselles as compared to the WT mid-substance calcification. Like for the other mineralized tissues examined in this study, OPN was abundant at this calcifying site. Additional studies on this newly found, consistently present, ectopic tendon calcification site in aged mice are required to examine other factors involved in this ectopic mineralization. Moreover, this site offers a readily available *in vivo* mouse calcification model for examining apatitic mineralization events in a highly anisotropic collagen fibril extracellular matrix assembly, such being the intrinsic nature of muscle- and bone-spanning tendons and ligaments.

3.5.4 Concluding comments

Prior to the availability of methods for 3D ultrastructural research as is the topic of this investigation, John Currey — when writing on the heterogeneity of bone — postulated that "The ideal situation would seem to have bone filled with coherent, reasonably strong interfaces, which will behave elastically, but which open up if a dangerous crack nears them, and which lie in such an orientation that the crack growth is impeded" (297). Now, with the advent of new sample processing methods, 3D imaging instrumentation and advanced software algorithms for deep learning-based segmentation and analysis tools (143), new coherent and continuous organic-inorganic interfaces and structure have been revealed in mineralized tissues, and these persist into old age. As part of crossfibrillar mineral tessellation in these tissues, differing degrees of tesselle size, spacing, and fusion exist depending on the tissue, and on the location within a given tissue (292, 298, 299). Indeed, 2D and 3D space-filling mineral tessellation with repeating units of alternating soft and stiff elements appears to be a strategy widely present in biology to provide combined strength and toughness (200-202, 205, 281).

The recent ability to now correlatively link together the previously inherent trade-off between distinctly unique resolution and broader field-of-view context is resulting in connected

structural imaging data that is providing new functional mechanistic insight into biological structures characterized in three dimensions over multiple magnification scales. At the high-resolution end of the spectrum of scale, these methods include at the ultrastructural, molecular and atomic scales, amongst others, electron microscopy, atomic force microscopy, and atomic probe tomography methods. Here, as applied to mineralized tissues, we were able to characterize in 3D at multiple scales, including at the ultrastructural scale, normal enthesis structure and dysregulated mineralization in the Achilles enthesis and tendon of *Hyp* mice; this including alterations in the appearance and dimensions of crossfibrillar mineral tessellation and their nano-interfaces. Looking beyond osteomalacia, it is indeed possible that in other musculoskeletal diseases where mineral-binding proteins, peptides, or small molecules are dysregulated, or where mineral ion homeostasis involving phosphate and/or calcium metabolism is altered, defective mineral tessellation trajectories may now be identified. These may contribute to the integrity and fragility of mineralized tissues beyond what is routinely reported via conventional radiography and μCT.

3.6 Disclosures

Disclosures: The authors have no disclosures to make.

3.7 Acknowledgements

Figure 1. Wildtype mouse Achilles enthesis insertion and crossfibrillar mineral tessellation of calcified fibrocartilage at the mineralization front. (**A**) MicroCT segmentation (top panel) and 2D sagittal projection (bottom panel) of mouse Achilles tendon and plantar fascia ligament insertion sites at the superior and inferior calcaneal tuberosities, respectively. The enthesis has zones of uncalcified fibrocartilage (UF) and calcified fibrocartilage (CF). (**B,C**) Electron microscopy (FIB-SEM Serial-Surface-View) tomographic 3D reconstruction, segmentation, and watershed labeling reveals micrometer-sized, close-packed, space-filling mineral tesselles commencing at the mineralization front of normal mouse Achilles enthesis fibrocartilage. Panel

C shows labeled (colored) mineral tesselles in relation to a fibrochondrocyte positioned at the mineralization front (unmineralized collagen digitally removed). (**D**) Distribution of mineral tesselle sizes generated from watershed labeling in Achilles enthesis fibrocartilage (and, for comparison, in lamellar bone likewise near the mineralization front) obtained from FIB-SEM mineralized tissue volumes. An example of a typical tesselle from each volume, representing their general morphological characteristics (as geometrically approximating prolate ellipsoids) are shown to the right (in turquoise). A, 7-month-old WT; B-D, 2-month-old WT.
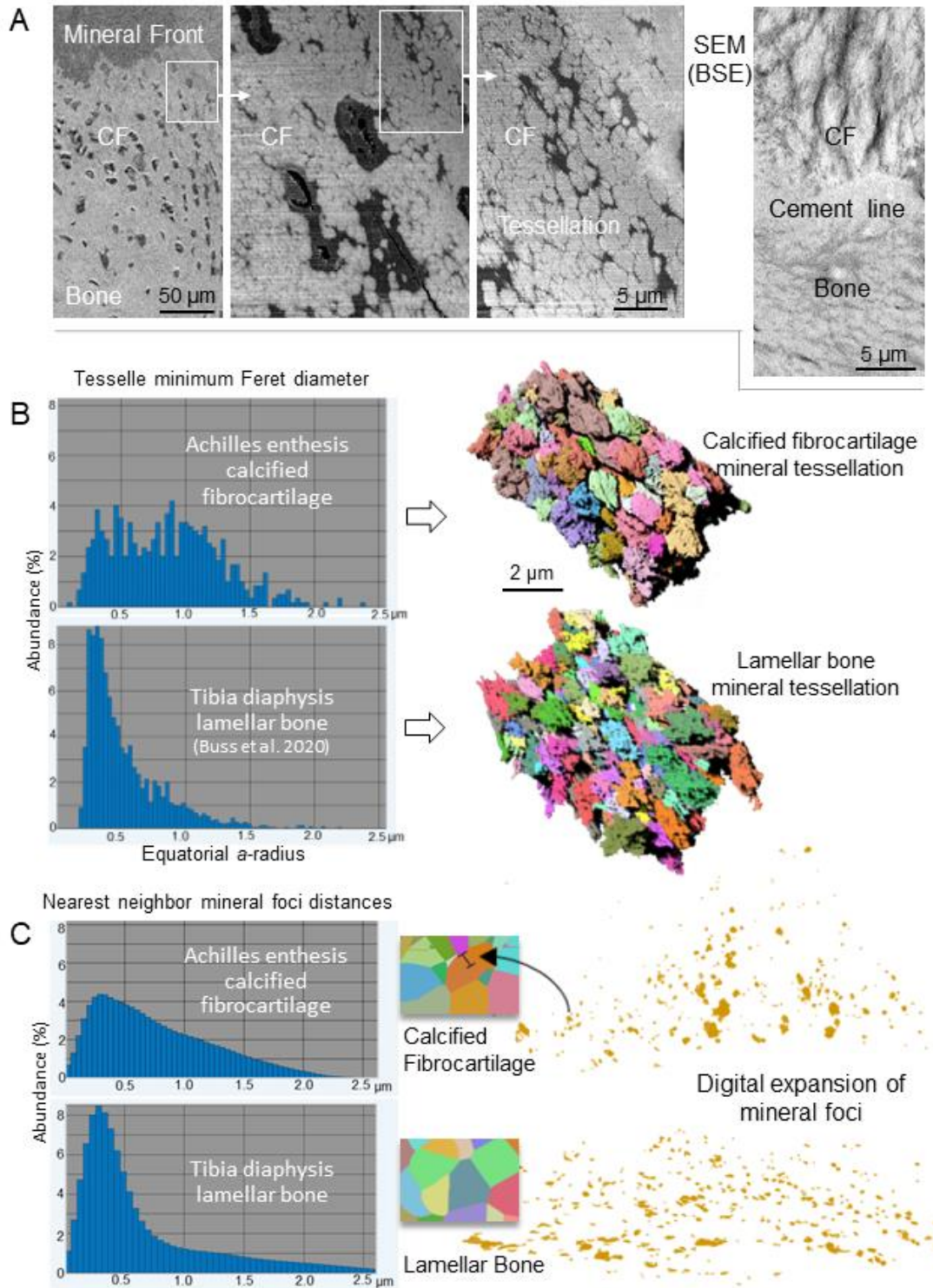
Figure 2. Wildtype mouse crossfibrillar mineral tessellation in fibrocartilage compared to bone. (**A**) An increasing magnification series of polished block faces containing the Achilles enthesis calcified fibrocartilage (CF) zone as viewed by SEM backscattered electron imaging

(SEM-BSE) to highlight mineral shows the distribution of mineral tesselles in 2D that continue to the cement line interfacing with bone. Note the larger size of the mineral tesselles in fibrocartilage compared to bone. (**B**) Distribution of minimum equatorial diameters of watershed-labeled tesselles (left panels) as measured from 3D FIB-SEM segmented volumes (right panels) of mineral-tessellated calcified fibrocartilage and lamellar bone (for comparison). (**C**) Distribution of nearest-neighbor distances (indicated by bracket for one mineral focus), then plotted for all foci in the corresponding histogram of immature mineral foci from above the mineralization front as labeled/segmented from FIB-SEM volumes. These distances represent a digital, simulated expansion of mineral foci (represented by the bracket in the associated Voronoi partition). A, 2-month-old WT; B, 2-month-old (calcified fibrocartilage) and 3.5-month-old (bone); C, 2-month-old calcified fibrocartilage and bone.
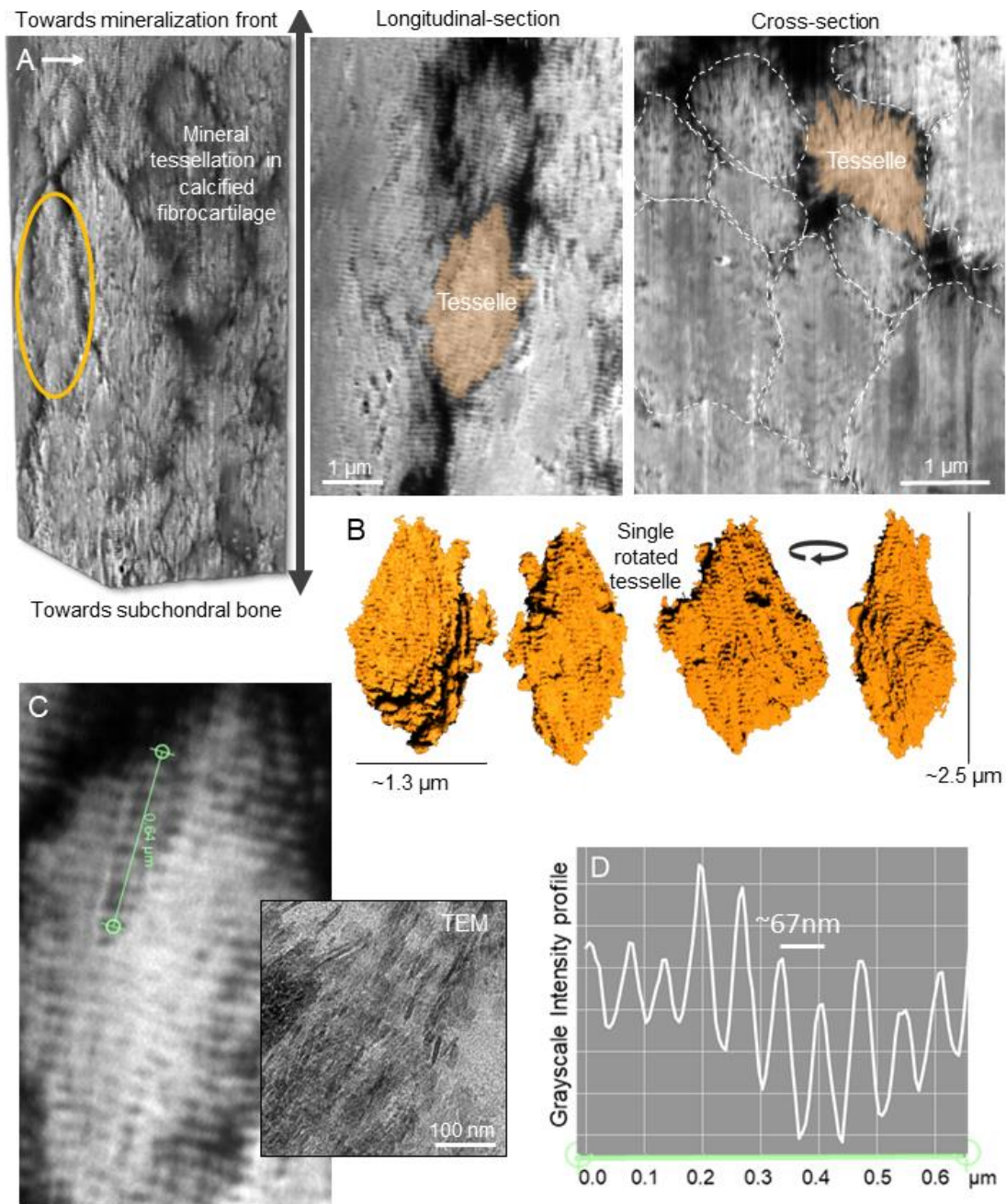
Figure 3. **High-resolution imaging of crossfibrillar mineral tessellation in WT mouse Achilles enthesis calcified fibrocartilage**. High-resolution rotation images of an individual tesselle (orange) from within 10 µm below the mineralization front. (**A**) A region from a FIB-SEM stack showing how tesselles interface with one another leaving nanoscale intervening gaps of unmineralized organic matrix at their boundaries. Different projections of the same tesselle are shown in the three panels showing longitudinal and cross-sectional views. Dashed lines demarcate

neighboring individual tesselles. (**B**) The same segmented tesselle (as in the A panels) in rotation with surrounding tissue digitally removed. Underlying collagen fibril molecular striation patterns (banding pattern) are reflected in the mineral segmentations. (**C**) Single 2D image slice from the sampled volume of the same tesselle showing preferential mineralization along the collagen molecular spacing, likewise imaged by TEM (from a different tesselle) showing how this pattern originates from the distribution of individual nanocrystals related to the collagen fibril. (**D**) Intensity profile of the grayscale values along the green line indicated in panel C shows 10 crests and troughs. Samples from 8.5-month-old mice except TEM image from a 12-month-old mouse.
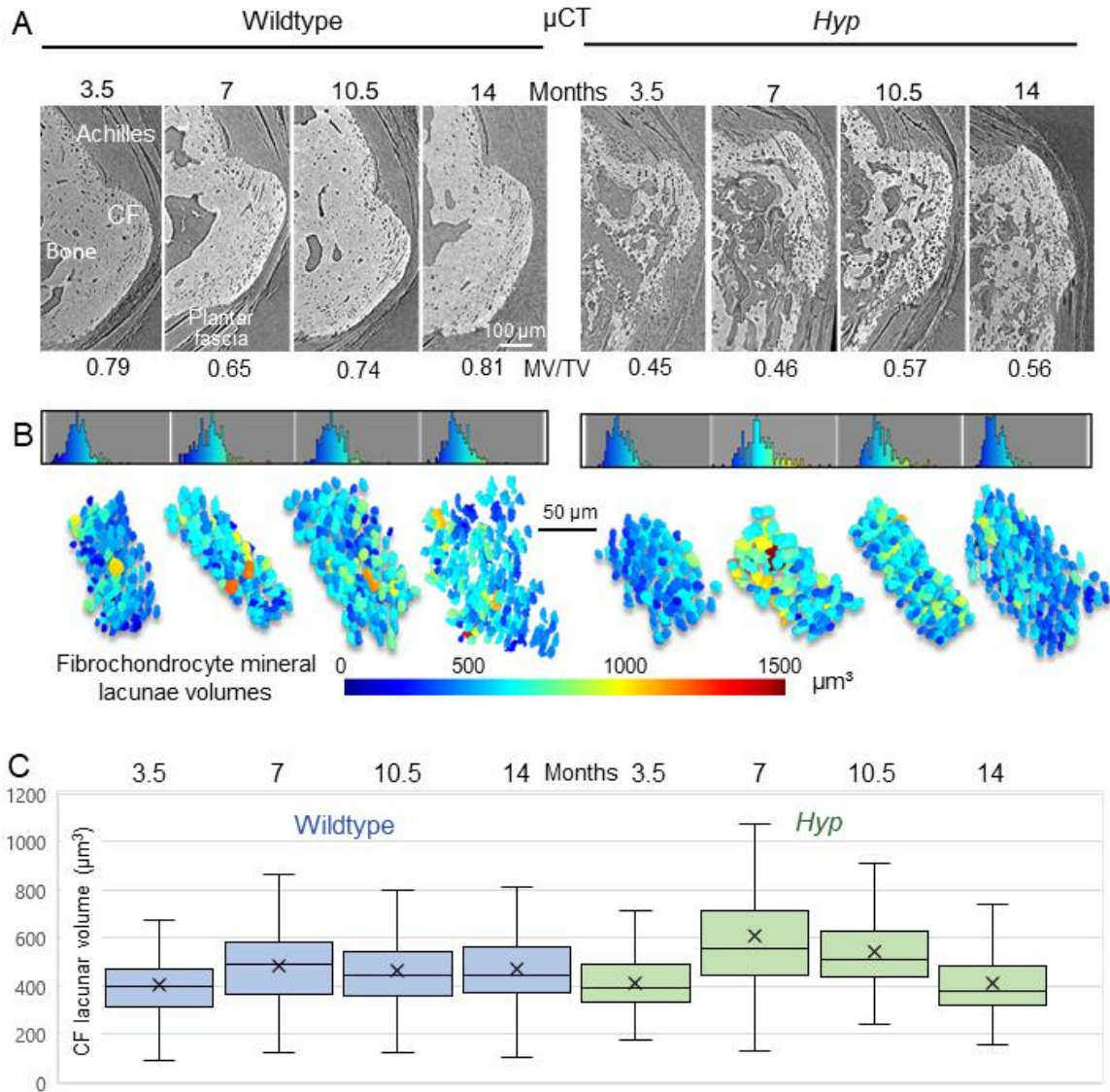
Figure 4. MicroCT of Achilles and plantar fascia insertion sites in WT and *Hyp* mice. (**A**) MicroCT sagittal single 2D projections from mice of various ages as indicated. CF indicates calcified fibrocartilage. *Hyp* calcaneal bone and calcified fibrocartilage show extensive hypomineralization showing as decreased mineralized tissue volume fraction (MV/TV) at this level of magnification across each age. Enthesophytes are not prominent in the sampled entheses. (**B,C**) Fibrochondrocyte mineral lacunae volume analysis in Achilles enthesis calcified fibrocartilage obtained through watershed transform labeling, color-coded heat-mapping of their distribution, and plotting and comparison of lacunar volumes. No differences in lacunar volumes were determined within and between the mouse ages and the phenotypes. For each plotted box,

the central line of the box represents the median, the "x" the mean, the bottom and top lines of the box the median of the first and third quartiles, and the whisker arms extend to the overall maximum and minimum values. MV, mineralized tissue volume; TV, total tissue volume.
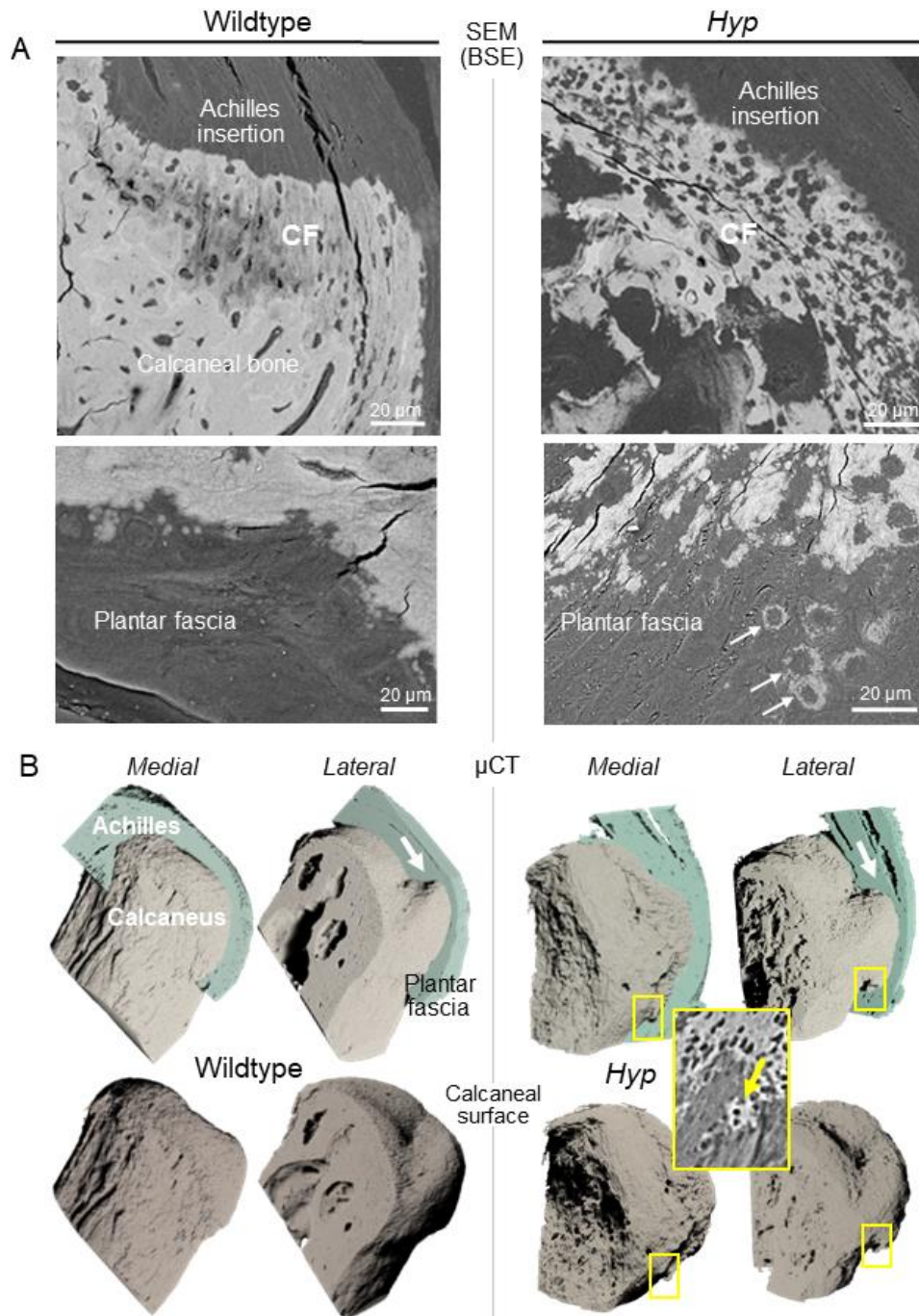
Figure 5. Achilles and plantar fascia entheses in WT and *Hyp* mice. Correlation of insertion-site structure using electron (SEM) and X-ray (µCT) imaging. (**A**) SEM-backscattered electron imaging (SEM-BSE) of embedded-sample block faces from WT and *Hyp* 12-month-old mice showing evidence of irregular morphology and deficient mineralization at insertion sites in the *Hyp* mice. Arrows indicate unusual circular/spherical mineral deposition around

fibrochondrocytes in the deeper regions of the uncalcified cartilage zone, perhaps the beginning of an enthesophyte. (**B**) MicroCT segmentations from different mice of nearly the same age (here 10.5 months old) show an expansion of calcified fibrocartilage within the plantar fascia insertion (yellow frames). The top panels show an Achilles tendon segmentation (green) at a partial cut-away plane, and the bottom panels show mineralized tissue only (bone/calcified fibrocartilage
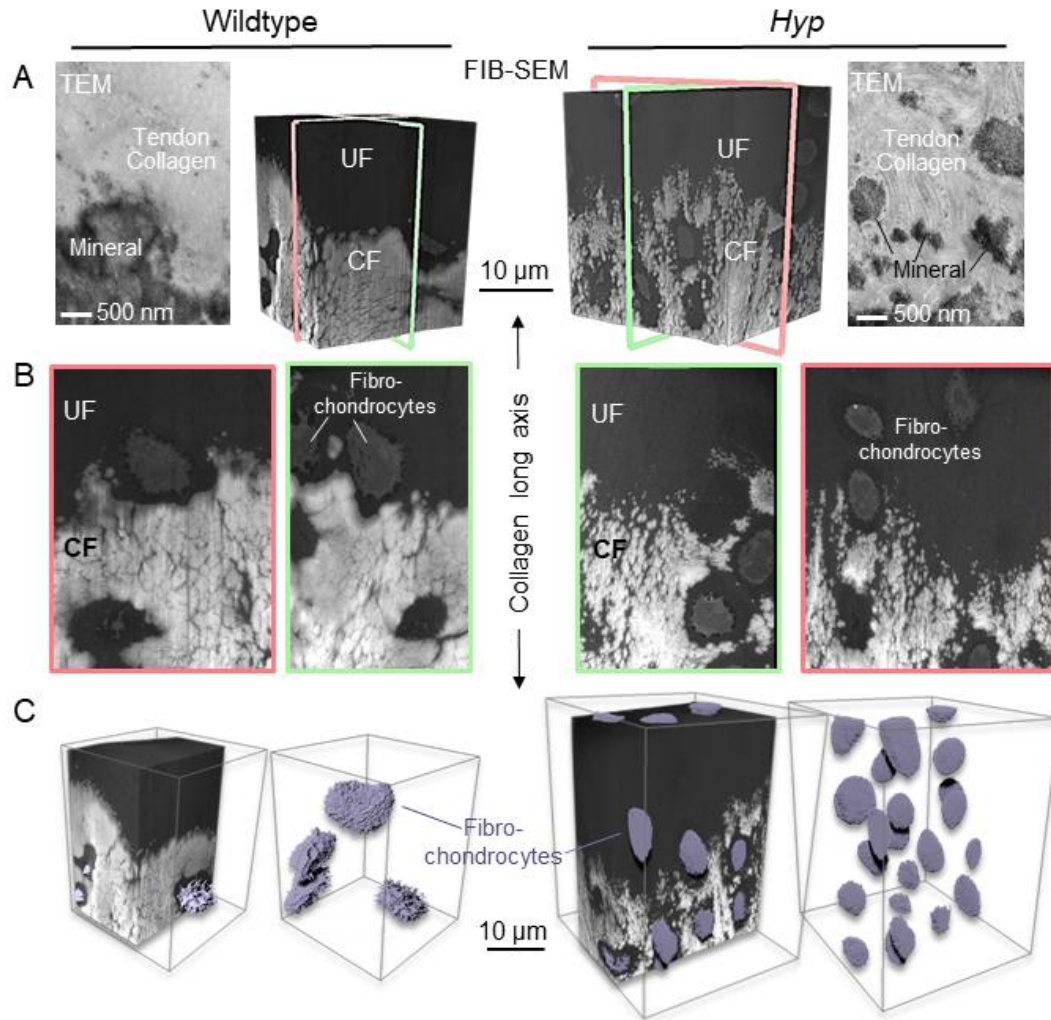
Figure 6. FIB-SEM tomography 3D reconstructions of 2-month-old WT and *Hyp* mouse Achilles enthesis. (**A**) 3D FIB-SEM volumes and higher-resolution TEM of mineralization events directly adjacent to the mineralization front. (**B**) 2D projections from the inner panels of A showing the extent of mineral packing in normal and *Hyp* mice. (**C**) Additional 3D views showing the location of fibrochondrocytes near the mineralization front (fibrochondrocyte cells only are shown in the right panels, with surrounding tissue being digitally removed). All from mice aged 2-months-old except TEM images (from 12-month-old).
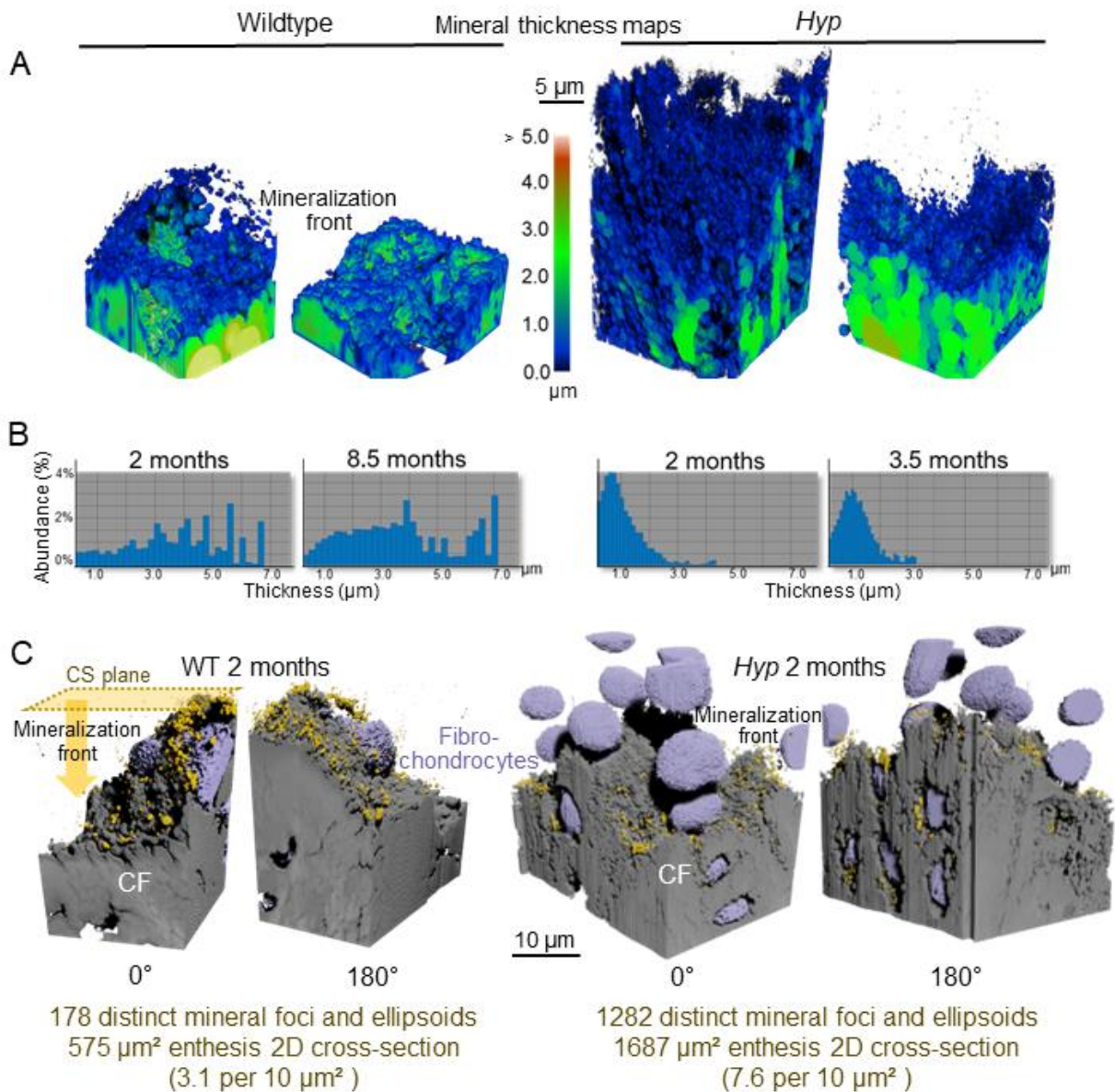
Figure 7. Comparison of the calcified fibrocartilage mineralization front 3D landscape between WT and *Hyp* mouse Achilles insertion as analyzed by FIB-SEM tomography. (**A,B**) Local volume thickness mapping (A) and thickness abundance of mineral foci and tesselles (B) throughout 17 nm-voxel FIB-SEM volumes showing a narrower range of foci/tesselle size, and smaller size, in *Hyp* mice as compared to WT mice. (**C**) From the 2-month-old age-matched pair, analysis of isolated mineral foci (gold color) above the mineralization front assessed by number in relation to the cross-sectional (CS) area of the mineralization front, illustrates that *Hyp* mice have more scattered, numerous smaller mineral volumes (foci and immature tesselles) than in WT mice, and that a distinct mineralization front is difficult to identify/outline.

142
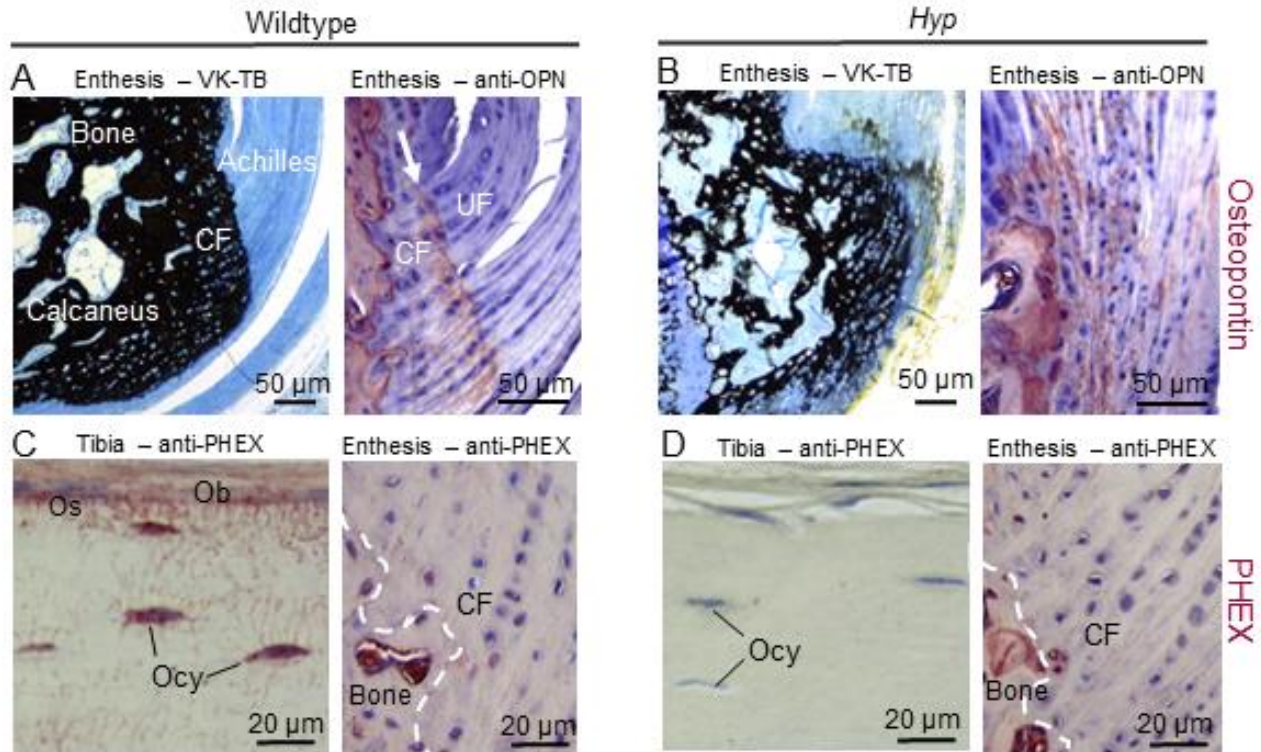
Figure 8. **Light microscopy histology and immunostaining for OPN and PHEX at the Achilles insertion in WT and *Hyp* mice**. (**A,B**) Staining for mineral (black) using the Von Kossa method (VK) with counterstaining from toluidine blue (TB) on epoxy sections, and immunostaining for osteopontin/OPN (red) on paraffin sections of EDTA-decalcified samples. In WT enthesis, OPN is prominent in the bone and calcified fibrocartilage, and particularly at the mineralization front (arrow) between uncalcified fibrocartilage (UF) and calcified fibrocartilage (CF). In *Hyp* enthesis, the OPN immunostaining pattern is diffuse in the fibrocartilage, reflecting the scattered mineralization pattern that occurs there in *Hyp* mice, with the mineralization front not being well defined. (**C,D**) Comparison of immunohistochemical staining for the PHEX enzyme in decalcified paraffin sections of WT and *Hyp* lamellar bone versus Achilles enthesis calcified fibrocartilage. Whereas WT bone tissue shows prominent immunolabeling for PHEX in osteoblasts (Ob) and osteocytes (Ocy), and in their cell processes (C), *Hyp* mouse bone (lacking the PHEX enzyme) shows the expected lack of immunostaining in the absence of PHEX, as does the *Hyp* enthesis (D). No PHEX immunostaining is observed in the examined entheses of WT mice. VK/TB-stained 2-month-old; Osteopontin and PHEX immunostaining 3.5-month-old. Os, osteoid.
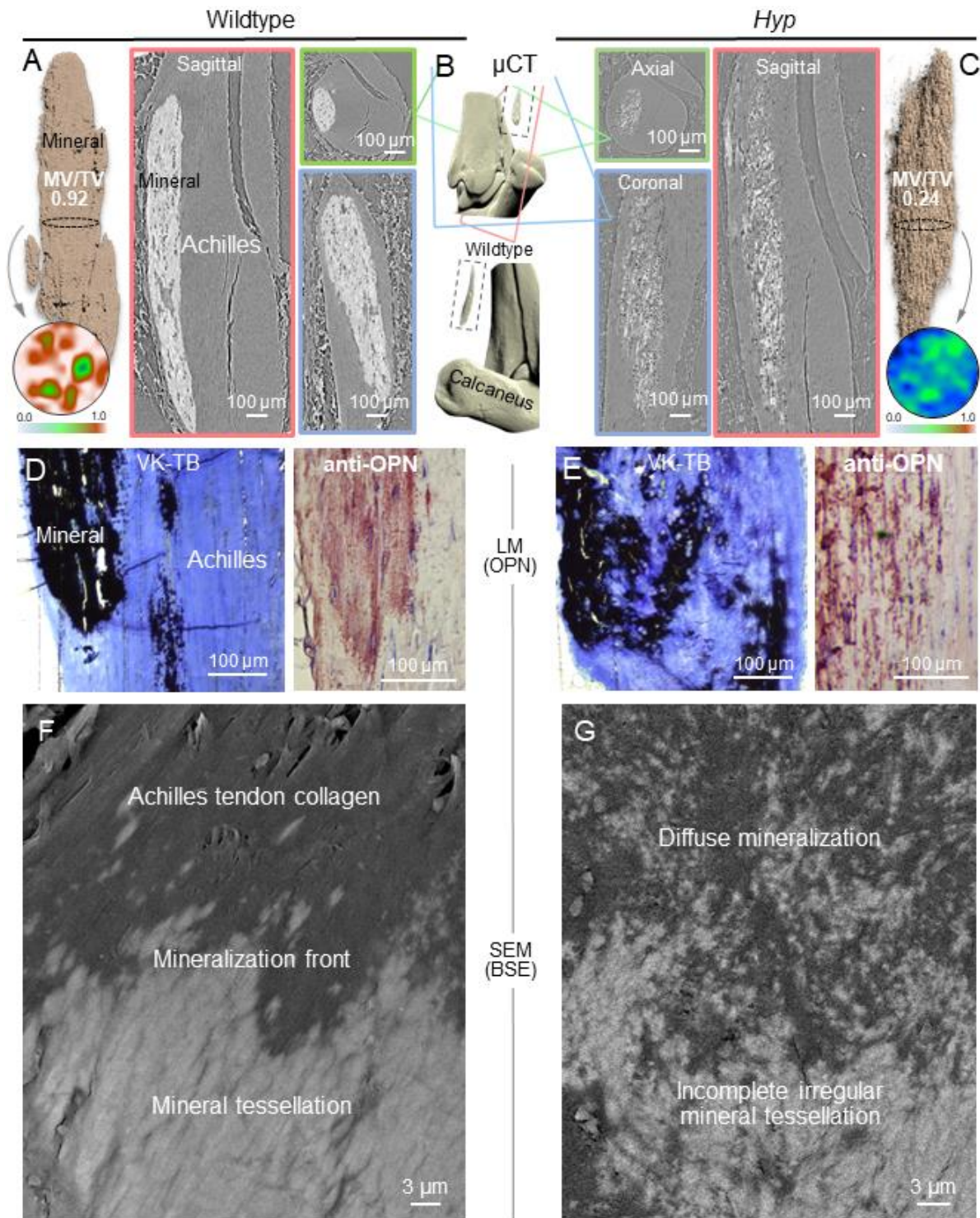
Figure 9. Multiscale analysis of Achilles tendon midsubstance calcifying tendinopathy in both WT and *Hyp* mice. (**A,C**) Vertically stitched high-resolution µCT projections and 3D segmentation of complete calcifying lesions from the midsubstance Achilles tendon of 7-month-old WT and *Hyp* mice, with a substantially less MV/TV in *Hyp* compared to WT within each

calcifying lesion volume (cross-sectional mineral volume fraction maps are shown in circular profile). (**B**) Lower magnification example from a WT mouse showing the general location of midsubstance calcifications (dashed boxes). (**D,E**) Von Kossa (black)/Toluidine Blue staining of mineralized regions, and OPN immunostaining of the midsubstance calcification tissue (here from a similar region from 12-month-old WT and *Hyp* mice). (**F,G**) SEM-backscattered electron imaging (SEM-BSE) of block faces of the midsubstance calcification region in 12-month-old mice, with clear crossfibrillar mineral tessellation in the WT tendon, but with scattered, spotty mineralization in the *Hyp* tendon, observations consistent with *Hyp* bone described previously and here, and with calcifying fibrocartilage at enthesis sites as described in this present study. MV, mineralized tissue volume; TV, total tissue volume.
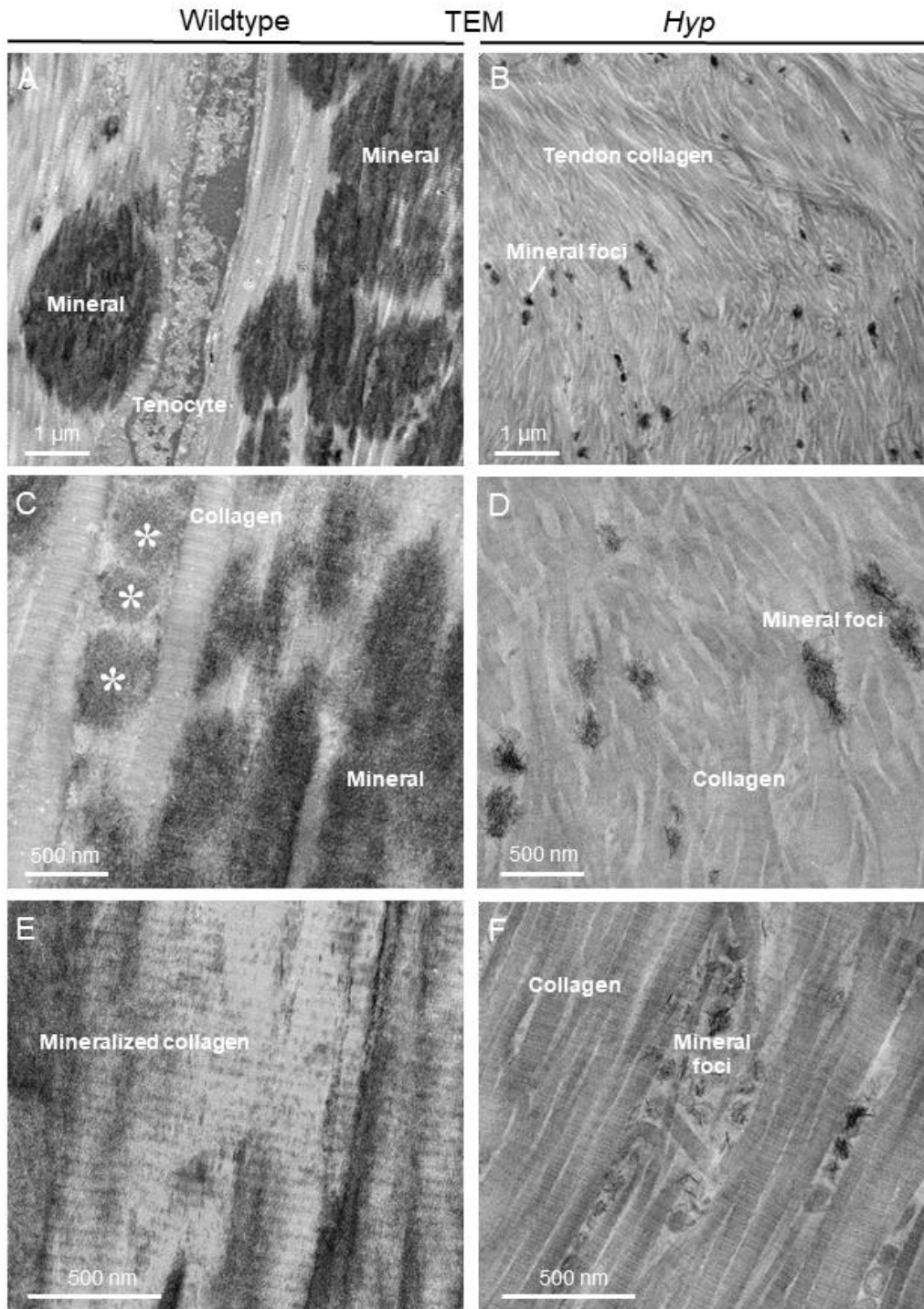
Figure 10. TEM of Achilles calcifying tendinopathy in WT and *Hyp*. (A,C,E) Crossfibrillar mineral tessellation in Achilles tendon in WT mice. Mineralization of the Achilles tendon, beginning as smaller mineral foci, enlarge along the collagen trajectory and across collagen fibrils to become abutting crossfibrillar mineral tesselles. Their long axis aligns with the long axis of collagen (A). More spherulitic deposits of mineral (asterisks) are often found between the collagen

fibrils (C), and mineral crystals register with the collagen banding pattern (E). (**B,D,F**) Lack of distinct crossfibrillar mineral tessellation in Achilles tendon of *Hyp* mice. Unlike the mineral tessellation that occurs in WT tendon, *Hyp* tendon shows predominantly scattered calcification as numerous widely scattered small foci, again with many nucleation sites seemingly between collagen fibrils. Despite the defect in mineral tessellation in *Hyp* mice, the accumulation of many small foci in different areas still lead to large swaths of mineralized tendon (see previous Figures 9C,E,G). All images from 12-month-old mice.
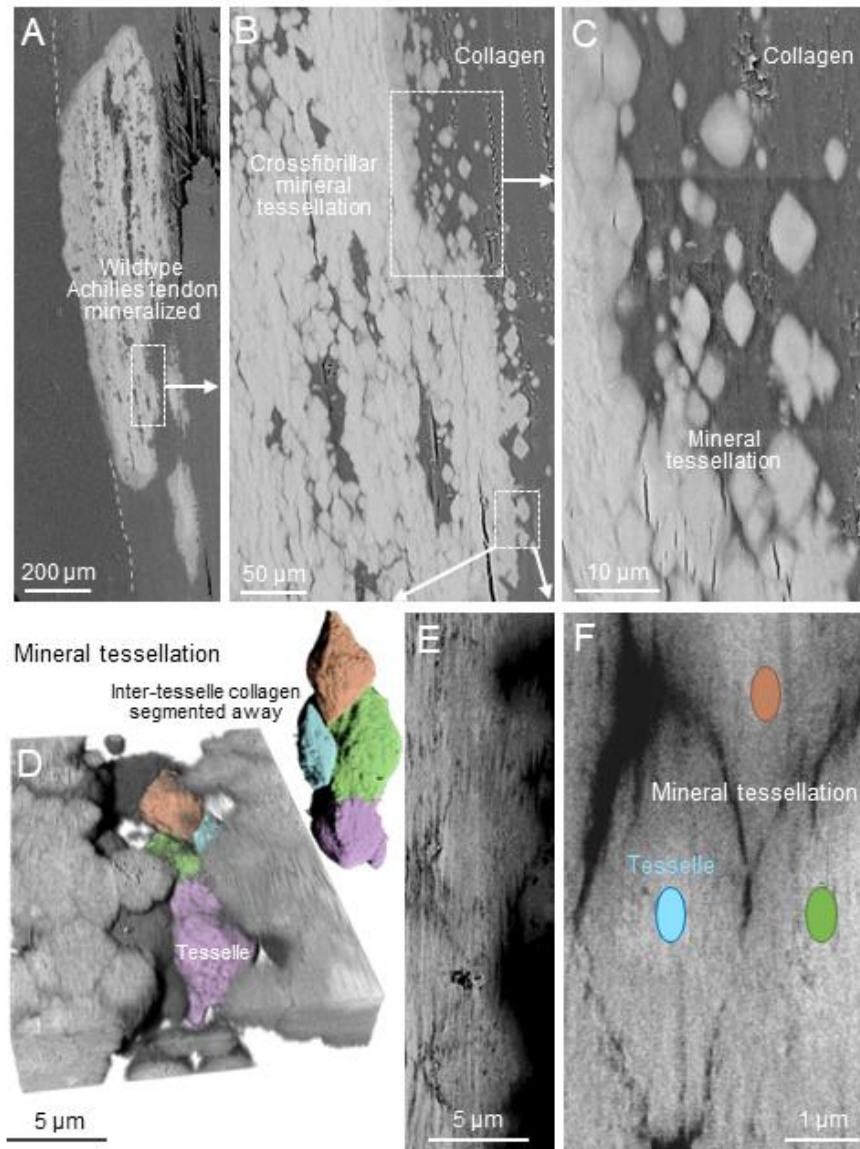
Figure 11. Wildtype mouse Achilles midsubstance tendon and crossfibrillar mineral tessellation. FIB-SEM region-of-interest selection and serial-surface-view volume correlation from the same block as shown in Figure 9D. (**A-C**) Block face SEM-BSE images at the periphery of the calcifying tendinopathy in the WT Achilles tendon show somewhat more "faceted" edges of the tesselles than observed in bone and fibrocartilage, but which similarly closely pack into a tessellation pattern, with some tesselles being as large as 5 µm in their long axis. (**D**) FIB-SEM 3D reconstruction from the white boxed region in panel B, and segmentation of a cluster of tesselles from the mineralized tendon interior. (**E, F**) 2D FIB-SEM slices showing interlocking and jagged-edged abutting of tesselles, with persistent boundaries. Colored ovals labeling tesselles in panel F correspond to the colors used in panel D. All images from 12-month-old mice.
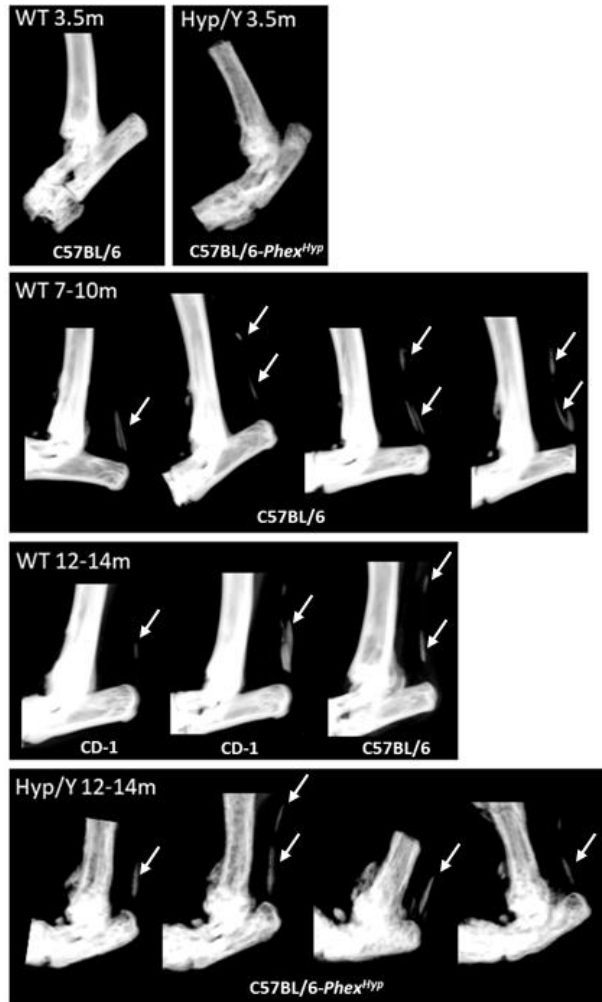
Supp. Figure S1. A collection of conventional radiographs from normal WT mice (of C57BL/6 and CD-1 backgrounds) and *Hyp* mice (on C57BL/6 background) documenting the locations and degree of Achilles calcifying tendinopathy in the midsubstance region (arrows) at 7 months of age, compared to 3.5-month-old mice (top two panels) where no ectopic calcifications were observable at this magnification.

Immunohistochemistry of enthesis and bone negative controls

WT Tibia anti-PHEX (-control)

WT Enthesis anti-PHEX (-control)

Hyp Tibia anti-PHEX (-control)

Hyp Enthesis anti-PHEX (-control)
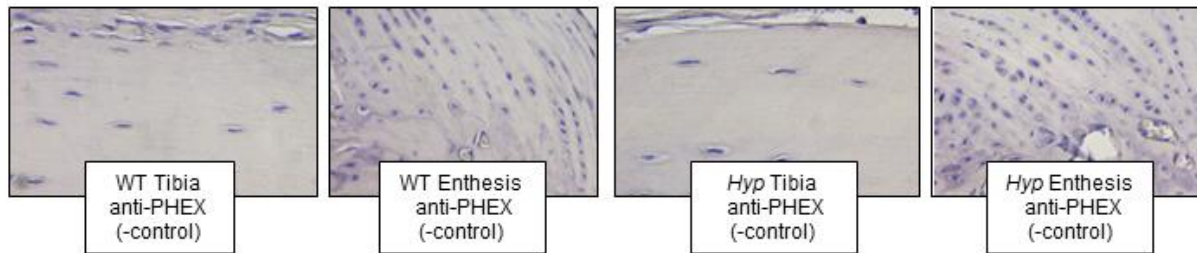
Immunohistochemistry of Achilles tendon negative controls

WT tendon anti-OPN (-control)

Hyp tendon anti-OPN (-control)
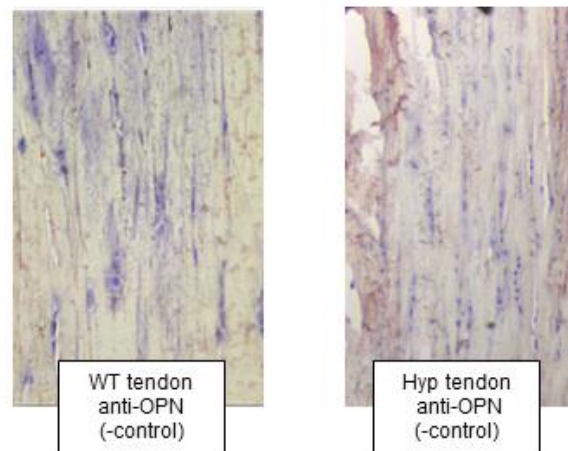
Supp. Figure S2. Negative controls (as indicated) for immunohistochemical staining for PHEX in normal WT and Hyp bone and enthesis fibrocartilage. In each case, the primary antibody was omitted, with all other processing steps remaining the same. All samples are from mice 12 months of age.

An Introduction to Chapter 4

The preceding chapters have thus far provided a comprehensive quantitative analysis of a repeating crossfibrillar microscale mineral unit (mineral tesselles) occurring in normal lamellar bone, enthesis fibrocartilage, and ectopic tendon calcification in vertebrates. In addition, through the assessment of *Hyp* mouse tissue from this scale, the preceding work has highlighted the sensitivity of this mineral patterning to the combined effects of adequate removal of local inhibitors from the extracellular matrix and sufficient availability of mineral ions. Interestingly, this structural theme of numerous organic fibrils occupying repeating inorganic mineral units extends beyond vertebrate calcium phosphate-based fiber systems of bone and fibrocartilage. Developing in the isthmus region of the avian hen oviduct (65), eggshell membrane fiber production by tubular gland cells and their subsequent assembly as a membrane forms the fibrous substrate for initial mineral nucleation and calcitic mineral growth. Once formed, the interface between these two dissimilar materials (organic fibrous membrane and calcitic shell) is an important attachment site critical to chick development and hatching. This is at odds however with the trajectory of the initial mineralization events occurring from quasiperiodic cone-shaped mammillae (89, 119, 300), and the requirement for thousands of eggshell pores around avian eggs which originate from these prominent gaps between mammillae along the interface. In the final chapter, eggshell samples with the attached underlying membrane are prepared for X-ray and electron microscopy (again assessed with various segmentation and analysis techniques) to understand how anchorage of organic membrane fibers to calcitic mammillae is achieved given such a discontinuous interface. Once again, we assess the critical relationships between an organic fibrous phase and an inorganic mineral phase, in 3-dimensions. To address the difficulty of imaging organic and inorganic phases simultaneously and enhance our understanding of this particular site, here we also use a combination of conventionally prepared and stained specimens, cryo-prepared (301) and unstained specimens, and simultaneous acquisition of distinct populations of backscattered electrons.

Chapter 4: Attaching organic fibers to mineral: The case of the avian eggshell

Daniel J. Buss[1], Natalie Reznikov[1,2,3] and Marc D. McKee[1,3,*]

[1]Department of Anatomy and Cell Biology, School of Biomedical Sciences, Faculty of Medicine and Health Sciences, McGill University, Montreal, Quebec, Canada.

[2]Department of Bioengineering, Faculty of Engineering, McGill University, Montreal, Quebec, Canada.

[3]Faculty of Dental Medicine and Oral Health Sciences, McGill University, Montreal, Quebec, Canada.

At the time of thesis submission the manuscript comprising this chapter was submitted to a journal awaiting peer review.
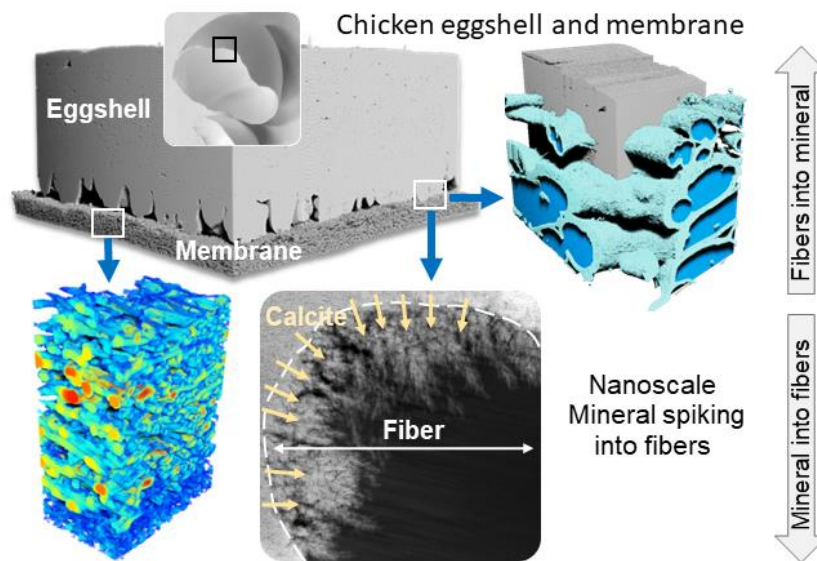
4.1 **Abstract**

Bird eggs possess a hard (mineralized) eggshell with a soft underlying fibrous membrane. These two dissimilar material layers successfully evolved a structural attachment to each other as a conserved avian reproduction strategy. In the fertilized avian egg, this attachment is essential to avian embryonic development, growth and hatching of the chick (302, 303). To understand how organic membrane fibers attach to shell mineral (calcite) we used 3D multiscale imaging including X-ray and electron tomography coupled with deep learning-based feature segmentation of conventionally and cryo-prepared chicken eggshells. Here we show how membrane fibers are organized and anchored into shell mineral. Whole fibers are embedded within mineral across the microscale, while fine mineral projections (spikes) insert into fiber surfaces at the nanoscale to provide considerable anchorage. With about 100 mineral spikes protruding into every square micrometer of fiber mantle surface, this increases the attachment surface by almost an order of magnitude. Taken together, this large, multiscale organic-inorganic interfacial contact area between membrane fibers and shell – being approximately 560 cm^2 per egg – is much greater than the outer surface area of the egg itself (70 cm^2). Such a reciprocal anchorage system occurring at two different length scales between organic fibers and inorganic mineral provides a secure attachment mechanism for avian eggshell integrity required for chick embryonic growth.

4.2 Main text

Avian eggshell formation is one of the fastest biomineralization processes known, where a fully formed highly organized calcified structure (with traversing pores for gas and water vapor exchange (302-304)) arises within 20 hours from a template of organic fibers (66). Mineralized eggshell formation occurs in the shell gland segment (uterus) of the hen's oviduct but is preceded by the assembly of an organic eggshell membrane at the surface of the egg "white" as the egg transits through the oviduct (65, 66). The membrane – which eventually becomes attached to the innermost portion of the shell – is formed predominantly of an interconnected and branching meshwork of fibers (300, 305-307). Compositionally, the membrane consists of approximately 250 proteins including various collagens (62, 63, 308-310), cystine-rich eggshell membrane proteins (CREMPs), and other proteins and biomolecules including those with known

antimicrobial function, such as lysozyme (64, 311) (86, 88, 312). Nucleation of the shell's calcium carbonate mineral originates on the outermost membrane fibers, beginning as an amorphous phase, and then growing and maturing towards calcite, (89, 119, 312). This mineralization trajectory starts with the formation of quasiperiodic mineral aggregates on the outer membrane. Growing outwards from the incipient aggregates, so-called mammillae are formed, altogether constituting the innermost mammillary layer of the shell (66, 89, 300, 307, 313, 314). Rapid, confluent columnar calcite growth then proceeds further outwards from each mammilla as densely packed calcite columns, resulting in a contiguous array that also contains radial pores (66, 88, 302, 304). This process occurring in the shell gland of the oviduct produces close to 5 grams of calcite (119) to reach a final shell thickness of approximately 300 µm.

After a fertilized egg is laid, secure attachment of the outer membrane fibers to the mammillae is essential for successful development of the chick. With egg incubation, by embryonic day 15, a fully developed, cellular and vascularized chorioallantoic membrane (CAM) lying immediately beneath the membrane (306, 315) mediates significant dissolution of the shell to mobilize calcium from mammillary calcite for the growing chick skeleton through acidification mechanisms acting across the membrane (316, 317). Secure attachment of the membrane to the shell is therefore required to approximate the underlying CAM close to the shell to facilitate shell dissolution and calcium release (315-317). Towards the end of CAM-mediated shell dissolution, the outer eggshell membrane partially detaches from the shell (315, 316, 318), potentially contributing to shell weakening for emergence of the chick (pipping). Related to this, an intact eggshell membrane attachment has been implicated as a contributor to shell mechanical strength (319, 320).

While the congruent, trilaminar structure of the CAM, the membrane, and the shell constitutes the typical egg "wall", at the blunt end of the egg, something substantially different occurs (66). In the blunt region, the membrane splits to form the air sac – this occurring after the egg is laid and begins to cool, drawing in air through the pores of that region (302-304). Once formed, the air sac provides a reservoir to meet the developing chick's growing oxygen demand before and at the time of hatching (302, 303).

For unfertilized and unincubated "table eggs" stored in a variety of conditions and used as a major food source across most populations, food safety is of concern (321). The intact membrane is a major physical and antimicrobial defense barrier for the egg contents (64), and detachment of

the membrane from the shell in eggs may render them more susceptible to contamination from opportunistic microorganisms (321, 322). The present study was undertaken to provide a better fundamental understanding of how such an important and robust attachment is achieved at this interface between overall strikingly dissimilar materials − organic fibers and biomineral.

4.2.1 3D multiscale imaging of chicken eggshell membrane structure

To date, avian membrane structure has primarily been studied using light microscopy, scanning electron microscopy (SEM), and transmission electron microscopy (TEM) of conventionally prepared specimens (critical-point dried, aldehyde-fixed) (300, 305, 306). Here, we expand upon this largely 2D information to a 3D multiscale assessment of the chicken (*Gallus gallus domesticus*) membrane and its interface with the shell (Fig. 1, 2, Movies SM1, SM2 [*Note added by authors: Reviewers, please examine our supplemental movies which are an important part of the data in this type of 3D imaging work - thank you*]).

The organic fibrous membrane attaches to mammillae of the calcitic shell (Fig. 1A,C, Movies SM1, SM2). Using deep learning-based segmentation and thickness mapping of membrane fibers from submicrometer microcomputed tomography (μCT) volumes, small inner membrane fibers and large outer membrane fibers were differentiated (Fig. 1B, *n=5,* representative areas shown). For higher-resolution examination of the membrane fibers, precise focused-ion beam (FIB) milling in conjunction with SEM imaging (particularly using backscattered electron imaging in the serial-surface-view [SSV] mode) has recently provided enhanced understanding of 3D nano- to microscale relationships in a variety of mineralized fibrous biocomposites (27, 78). Using serial gallium-FIB milling tangential to the membrane, and imaging using backscattered electron detection, we assessed the 3D structure of a complete thickness of the membrane. Using fiber thickness mapping at this scale (Fig. 1D, Movies SM3, SM4), the outer and inner membrane layers were visualized in detail with an abrupt shift to thin fibers within the approximate inner 15 μm of the membrane (towards the egg albumen). Directionality mapping of fibers through the membrane (Fig. 1E) revealed orthotropic, mat-like fiber orientation.

An important morphological feature of eggshell membrane fibers when imaged using an electron microscope (and typically stained), are inner core and outer mantle regions of each fiber (305) (Fig. 2A, Movie SM5). From several 3D volumes, we were able to reveal oblique projections at both the micro- (Fig. 2C) and nanoscales (Fig. 2D) that document a previously uncommunicated

propensity of chicken eggshell membrane fibers to form bundles (some up to 50 µm in width and several up to 100 µm in length), with a shared mantle region and discrete core regions (Fig. 2 C and D). Segmentation of core and mantle fiber regions through the membrane thickness suggests that the inner membrane, with smaller overall fiber diameters, indeed has a reduced proportion of core organic constituents compared to that of larger outer membrane fibers, whereas the mantle thickness is rather similar in both thin and thick fibers (Fig. 2B, Movie SM5).

4.2.2 Attaching organic fibers to biomineral at the eggshell-membrane interface

Having obtained a broader understanding of overall membrane fiber morphologies (including mantle and core regions) and orientation, we addressed unresolved questions regarding the morphology of fiber incorporation (of both embedded fibers and interdigitated fibers) in the mammillary calcite (300, 313, 314). Collectively, compelling evidence is provided for a self-affine, reciprocal anchorage of organic fibers at both the micro- and nanoscale. First, at the microscale, about 10 fibers are anchored into each mammilla (Fig. 3A,B, Movie SM6). Deep learning-assisted segmentation of these fibers within mammillae calcite (Fig. 3B,C) revealed that all mammillae in the field of view (between 200 to 300 mammillae per 1 mm² area of shell (323)) contained anchored fibers (Fig. 3C).

At higher resolution (FIB-SEM reconstructions), using 3D segmentation of a portion of a mammilla (from the same volume as Fig. 1), multiple fiber tracks (about ten per mammilla) can be revealed by digitally removing the fibers (Fig. 3D, Movie SM7). Two additional volumes at even higher resolutions (Fig. 3E,F, Movie SM8) show the difference of the mantle texture around embedded and interdigitated fibers – namely uniformly thin mantles having a rough irregular texture when embedded, compared to the thicker mantles of the interdigitated fibers. In addition, a different 3D structure of the fiber mantle regions was observed (Fig. 3E rightmost image, Fig. 4D, Movie SM8). Segmentation and thickness mapping of embedded and interdigitated mantle regions reveals that the mantle area contains numerous occluded mineral extensions into the fiber, the back-scattered signal intensity of which is consistent with the shell mammillary calcite (Fig. 3F, Fig. 4A). Indeed, these embedded fibers, including where they stretch between adjacent mammillae, remain attached after manually peeling off the membrane (Fig. 3G).

Sections of interdigitated fibers cut using a microtome and imaged under TEM brightfield conditions previously indicated (based on electron density and shape), that a mineral phase within

fiber mantles is likely responsible for these radial inhomogeneities in the mantle (300). Still, the suggested mineral polymorph and 3D morphology of anchored fiber mantles has not been assessed in the context of membrane-shell attachment – this likely being attributable to the extreme difficulty and lack of precision of cutting hard and brittle shells with a microtome. To address this, FIB milling of a conventionally fixed and osmium stained electron-transparent section (lamella) of a mammilla with its embedded fibers was conducted for further observations by STEM (scanning transmission electron microscopy). Using selected-area diffraction (SAED) (Fig. 4F), we observed only diffuse reflections of the mineral penetrating into the fiber mantle, this in contrast to mammillary mineral showing regular bright spot reflections indicative of single-crystal calcite. This observation of poorly crystalline mineral penetrating into the mantle was supported by similarly prepared specimens imaged using angle-selective (BSE-L) and energy-selective (BSE-U) detectors from our high-resolution FIB-SEM volumes in which isolated bright electron-dense spots were observed within the mantle voids (Fig. 4D).

Given the high surface-to-volume ratio of the fine mineral extensions, and the known solubility of certain precursor phases of calcium carbonate in water, we next FIB-milled an electron-transparent section through a mammilla region with embedded fibers from a cryo-fixed specimen. Cryo-preparation of samples (high-pressure freezing followed by freeze-substitution) results in better preservation of hydrated mineral phases, including unstable amorphous mineral precursor phases (301). SAED patterns collected from the now cryo-prepared fiber mantle (Fig. 4G) instead revealed an arching diffraction pattern indicative of polycrystalline calcite texture. This finding was corroborated by STEM high-angle annular dark field imaging (Fig. 4B,C,E). With the preservation enabled by cryo-processing and ultrafine ion-beam milling, two unique mantle mineral morphologies were captured – polycrystalline "granules" in the embedded fiber mantles (Fig. 4C) and "spikes" in the interdigitated fiber mantles (Fig. 4E). Energy-disperse spectroscopy (EDS) spectra confirmed the presence of calcium (Fig. 4H) and oxygen (Fig. 4I) within these mammilla-anchored fiber mantles (compared to fiber core regions where there was little calcium or oxygen signal), and where there was a similar intensity as mammilla calcite itself (Fig. 4H,I, at the top of each map). These analytical data show that mantle "voids" in conventionally prepared specimens (Fig. 4D, Movie SM8) are indeed decalcified proxy spaces occupied in their entirety in native eggshell by polycrystalline mineral spikes or granules (Fig. 4E). In addition, by taking together results from the FIB-SEM high-resolution 3D segmentation, the

osmium-stained conventionally prepared lamella, and the cryo-prepared lamella, we now have shown how mineral "spikes" (of up to 100 nm in thickness) indeed penetrate into the mantle radially and extend partially into even the inner core of membrane fibers (Fig. 4J, Fig. 5, Movie SM9).

To estimate the extent of the anchorage of the membrane fibers to the shell mammillae, a coarse-grained calculation can be applied as follows. The surface area of an average-sized chicken egg is approximately 7,000 mm^2 (70 cm^2) consistent with reported surface area from Narushin and Paganelli (324, 325)). Next, the number of mammillae per square millimeter varies between 180 to 300 (being more numerous in younger hens (323)), which gives a conservative estimate of about 1.3 million mammillae per egg. The diameter of a typical mammilla at the level of the membrane anchorage is usually slightly exceeding 100 µm^2. With an average of approximately 10 fibers being anchored to each mammilla covering about 50 µm in length (not all fibers necessarily traverse the mammilla over the entire mammilla diameter), this calculates to collectively 0.5 mm of anchored fiber length. Approximating fiber geometry to a cylinder being 3 µm in diameter, the surface area of the anchored fibers adds up to 5,000 µm^2 (0.005 mm^2). Therefore, the total contact area between the anchored fibers' surface and mammillary calcite is, by a conservative estimate, about 6,500 mm^2, which is very close to the total area of the egg. This appears natural – indeed, the membrane and the shell collectively bound the egg – but it must be kept in mind that at the microscale the orthotropic fibers are aligned with the egg surface, whereas the calcitic mammillae are oriented radially with respect to the egg surface. While the two layers of the shell-membrane complex are parallel/congruent, the structural units of each layer are perpendicular to each other which makes their connection nontrivial. Should the mammillary apices only touch the membrane without 3D embedding/interdigitating, the area of contact would vary between only 10-40% of the total egg surface, depending on the bluntness of the mammillary apices. Moreover, the area of contact between the fibers and the mammillary calcite is further amplified by the fine protrusions of calcite into the fiber mantles in the form of spikes or granules. Since one mineral spike extends into the mantle by about 500 nm, having a typical diameter of 50 nm, then the surface of one spike would be 78,500 nm^2 (0.08 µm^2). With about 100 spikes protruding into every square micrometer of a hypothetically cylindrical fiber mantle surface, the total spikes area is 8 µm^2, which is an increase of surface area of almost an order of magnitude. In other words, the reciprocal anchorage

system of fibers within calcite at the microscale, and of calcite within fibers at the nanoscale, ensures a total organic-inorganic interface area of at least 560 cm^2 per egg.

4.2.3 Discussion

Functional properties of biomineralized tissues and structures are defined by intricate relationships between organic and inorganic constituents, originating from nanometer length scales and in three dimensions (263, 326, 327) – the avian eggshell being no exception. In eggshells, an organic fibrous membrane located between the hard mineralized shell and the soft egg albumen forms an important physical and antimicrobial barrier, while also serving as a substratum for shell formation (66, 89, 119). Importantly, unknown features of the membrane determine the spatial distribution of incipient mineral nucleation sites (323) (related to organic cores that attached to the membrane fibers, and become the calcitic mammillae of the shell (89)) that dictate the extent of attachment and the initial trajectory of mineralization. Membrane fibers are oriented orthotropically, like a multilayered mat, in which each fiber roughly follows the curvature of the egg surface. Conversely, the calcitic shell forms from discrete quasiperiodic sites (which will become mammillary apices) scattered over the outer layer of the membrane. Mineral growth then extends radially, forming mammillary bodies and then palisade columnar layer (66). The orthotropic membrane fibers and the radial crystal domains are essentially perpendicular to each other, which renders surface congruency intuitively impossible. And yet, following these events in shell formation, not only reliable attachment is enabled, but also protein occlusion into calcite ensures adequate dissolution kinetics (317). Here we described detailed aspects of the eggshell membrane in 3D using submicrometer-resolution μCT and FIB-SEM serial-surface-view electron tomography. Our use of deep learning-assisted segmentation of fibers that differentiates thicknesses across relatively large μCT volumes of up to 1 mm³ presents a method to assess broadly, and in detail, the intricacy of the membrane fiber and shell mammilla "contact". This turns out to be a reciprocal hierarchical assembly on its own account, endowing the natural incubator chamber – the egg – with marvelous functionalities as being *i*) protective against pathogens and yet permeable for gas exchange, *ii*) strong from the outside yet penetrable from the inside (hatching), and *iii*) ensuring calcium flux from the hen to the shell to the chick skeleton (328, 329).

With very high calcium levels in the hen's oviductal fluid, it remains unknown what limits mineralization to the outermost portion of the eggshell membrane yet restricts mineralization elsewhere in the membrane. While the concept of broad default inhibition of mineralization in soft tissues by small biomolecules and proteins in organic fiber systems has been noted, and conversely the promotion of mineralization through enzymatic degradation of these inhibitors (release from inhibition) – as summarized by the *Stenciling Principle* of mineralization (2, 262) – there is no clear explanation yet for how the majority of the membrane fibers remain unmineralized. Evidence best supporting the notion of inhibition of fiber mineralization in the avian egg is by *in vitro* biomimetic studies describing great difficulty in prompting intrafibrillar biomimetic mineralization of shell membrane fibers (120). Recently, this difficulty was overcome through the use of polycarboxylic acid analogues bioinspired by similar protein chemistries operating at the level of mineralization regulation in a variety of marine and terrestrial organisms, and in various *in vitro* model systems (120). These and other negatively charged proteins and peptides associate with metastable amorphous mineral phases (89) to form transient liquid-like precursors (330), and their degradation by enzymes likely facilitates mineralization; such enzymes may be largely absent in the milieu of the eggshell membrane.

Here we show using a combination of cryogenic specimen preparation methods and electron imaging, diffraction, and spectral mapping, that mineralization of eggshell membrane fiber mantle and core regions does occur naturally in the specific instances where fibers interdigitate with, or are embedded within, shell mammilla mineral. In building upon early work done by Dennis et al. (300), we describe in three dimensions and at the nanoscale, the spatial extent of this membrane fiber mineralization which forms the morphological basis of the eggshell attachment zone, spatially and specifically delineated by a unique thin membrane (Supp. Fig. S1) whose outermost fibers are embedded within shell mineral, and where in turn shell mineral reciprocally penetrates into the fibers as mineral spikes and granules. Such a "pinning/nailing" mechanism at the nanoscale likely provides firm attachment strength by anchoring and preventing untimely detachment of the fibers, thus preventing membrane separation from the shell.

In conclusion, and in broader terms, in biological systems where there is a limited inventory of available materials, attachment between highly dissimilar substances such as unmineralized and mineralized fiber systems requires unique structural adaptations to mitigate accumulation of critical stresses at and near the interface (81). With this in mind, biological structure (as it

originates from atoms through the nanoscale, and in three dimensions), is often vastly more complex than engineered materials, especially for organisms that incorporate mineralized tissues where water, proteins, and minerals (and of course many other constituents) interact over time to achieve different phases and morphologies (90, 331). This self-affine, reciprocal anchorage system of having organic fibers penetrating bulk mineral at the microscale, and with mineral spikes penetrating organic fibers at the nanoscale (fibers-into-mineral and mineral-into-fibers) provides a morphological basis for understanding the membrane-shell attachment mechanism important to avian eggshell integrity and chick embryonic growth.

4.3 Declaration of Competing Interest

All the authors declare that they have no competing interests.

4.4 Acknowledgments

We thank the staff of the Facility for Electron Microscopy Research for assistance with this work, particularly K. Sears, W. Leelapornpisit, D. Liu, and S. Bessette, we thank the staff of the Integrated Quantitative Biology Initiative, and we thank J. Deering for helpful discussions. N.R. and M.D.M. are members of the Québec FRQ-S Centre de Recherche en Biologie Structurale, the Québec FRQ-S Réseau de Recherche en Santé Buccodentaire et Osseuse, and the McGill Institute for Advanced Materials. We also thank Objects Research Systems Inc. (Montreal) for the free-of-charge academic license for the Dragonfly software.

4.5 Supplemental Materials – Materials and Methods

X-ray micro-computed tomography (µCT)

Fresh unfertilized and unincubated chicken eggs were carefully opened from above the equatorial region (near the pointed end of the egg) and the inner contents were drained. The

remaining shell and attached membrane were gently and quickly rinsed from the inside with several rounds of tap water (with gentle swirling motion) for about 2 minutes to remove any remaining inner egg contents. Small pieces of shell (approximately 5 mm x 5 mm) were cut from the equatorial region using a sharp dissecting scissor, and the best-cut pieces were chosen for μCT imaging. After drying overnight, intact shell and attached membrane pieces were imaged using an X-ray microcomputed tomography scanner Xradia Versa 520 (Carl Zeiss, Oberkochen, Germany) having submicrometer resolution. "Scout" lower-resolution warmup scans were performed with a 0.4x objective lens to ensure that final high-resolution scans would be located centrally within each specimen ("Scout and Zoom" method, Carl Zeiss, Oberkochen, Germany). High-resolution scans were performed with a 4x objective lens, 60kV source voltage, and an exposure of 5s per projection. Detector and source distances were optimized to create a voxel size of 500 nm with no binning. 3000+ projections were obtained for each high resolution scan. Additional separate specimens from the equatorial region were subject to mechanical removal of the membrane by hand, this after the rinsing step and while still hydrated. The membrane was confirmed to be removed by a dissecting light microscope, this as compared to specimens with the membrane left intact.

For 3D imaging of the membrane split to form the air sac at the blunt end of the egg, a similar workflow for specimen dissection was employed. The air sac and membrane split are visible under a dissecting microscope and by eye. After careful washing, and then removal of shell above the split, the site of the physiologic membrane split could be preserved. A significant portion of the shell above and below the split was left intact so as not to disturb the split site of interest (Supp. Fig. S2). To secure the inner membrane during scanning, a very small drop of strong adhesive was painted onto the topmost portion of the shell fragment (significantly outside the volume to be scanned), and the free end of the inner membrane "flap" was then gently secured at this position (Supp. Fig. S2). These specimens were also left to dry overnight and imaged with the same conditions as above. Since the inner membrane is only 10-15 μm thick, the "Scout and Zoom" method was critical to finding the exact coordinates of the split, then allowing for high-resolution imaging at this precise location (Supp. Fig. S2).

Focused ion beam scanning electron microscopy (FIB-SEM) in serial-surface-view mode

Four FIB-SEM serial-surface-view volumes were obtained at different resolutions to characterize the eggshell membrane and its attachment to the calcite shell mammillae. Eggs were drained and rinsed with tap water in the same manner as above, and then chemically fixed with 4% paraformaldehyde (Thermo Fisher Scientific) and 1% glutaraldehyde (Electron Microscopy Sciences, Hatfield, PA, USA) in 0.1 M sodium cacodylate buffer (pH 7.3, Electron Microscopy Sciences, Hatfield, PA, USA) for 1 hour. After washing in additional 0.1 M sodium cacodylate buffer, specimens were stained with 4% potassium ferrocyanide-reduced osmium tetroxide. Graded dehydration to 100% pure acetone was then followed by gradual infiltration with Epon resin over several days. Final polymerization in pure Epon was achieved over 2 days at 60°C. Cured Epon blocks were manually trimmed to a suitable plane within the embedded eggshell, and then the blockfaces were polished using a Struers LaboSystem polisher. Semi-manual polishing was done without using the LaboSystem head. A series of polishing steps was applied for approximately 5-10 minutes of polishing per stage. Each mat was rinsed with water and dampened before addition of slurry and lubricant. The specimen was briefly rinsed in a sonicator between each polishing step. After polishing, the block was attached to a metallic stub, coated with a 5-nm layer of Pt on the polished face, and imaged initially using SEM-BSE to define a suitable region of interest. FIB-SEM serial-surface-view imaging was conducted using an FEI Helios Nanolab 660 (first 2 volumes), and a Hitachi Ethos NX5000 (2 other volumes, and lamella preparation as explained below). Volumes 1 (Supp. Fig. 1) and 2 (Figs. 1D,E, Figs. 2C,D, Figs. 3D, SM3,4,5,7) were collected with conditions of 2 kV imaging voltage and 0.79 nA milling current with slice thicknesses of 41 nm and 70 nm, respectively, achieving isotropic voxel resolutions over total volumes of 36,132 µm³ (approximately 64 x 43 x 13 µm) and 328,530 µm³ (approximately 111 x 73 x 41 µm). To achieve such a large volume in Volume 2, the length of the eggshell membrane was oriented parallel to the direction of the ion beam (Supp. Fig. S2). Electron imaging on the opposite face was conducted within a few µm's of the ledge as to avoid heavy curtaining artifacts. Volumes 3 (Figs. 3E,F, Fig. 4A, SM8) and 4 (Fig. 3E right-most image, Figs. 4D,J [except for cryo-prep image]) were collected on the Hitachi Ethos NX5000 using a 2 kV source voltage 1.5 nA milling current, with image formation occurring separately from both upper and lower backscattered electron populations simultaneously (BSE-U and BSE-L detectors, see Figs. 4A,D). Slice thicknesses of these volumes were both 14 nm, with volume 3 x/y resolution at 12.5 nm, and

Volume 4 continuing for some additional time with x/y resolution 6 nm, to achieve final volumes of 2,739 µm³ (approximately 16 x 14 x 13 µm) and 48 µm³ (approximately 6 x 6 x 1.3 µm), respectively. Each stack of images was registered and aligned in Dragonfly using the slice registration toolkit "mutual info" algorithm.

Segmentation and image analysis

Dragonfly image analysis software with deep learning capabilities (Object Research Systems Inc., Montreal, QC, Canada) was used to analyze all image data. To assess overall morphological differences between inner and outer membrane fibers of Micro-CT data, and to segment the calcite shell in these acquired volumes of nearly 1 mm³ at a resolution of 500 nm/voxel, deep learning-based segmentation was employed. From several projections of the *en face* view of the membrane (derived as a new dataset into the image plane), segmentation of "ground truth" slices was carried out using the range and ROI painter tools. Additional separate "ground truth" examples were taken of embedded fiber tracts (also of lower overall grayscale values than the surrounding calcite). A mask ROI was created to label each slice that was manually segmented. For each region (normal membrane fibers and embedded fiber tracts), a separate convolutional neural network (CNN) was generated with an architecture having a depth of 5 layers and 64 convolutional filters per layer (and with inputs being partitioned into learning [80%] and validation [20%] subsets). Training parameters were patch size of 64, the S:I ratio was 0.5, and the batch size was 64. Training continued until no improvement was made for 10 epochs. After initial segmentation, corrections were made on different slices, and the models were further refined in an additional round of training. This approach was demonstrated recently in a review with case studies with special emphasis on mineralized tissues (including eggshell) (50). Both normal fibers and fiber tract segmentation labels were combined into one, thus labeling all of the membrane fibers including those interfacing with and within shell mammillae calcite. For select volumes, only the fiber tracts (embedded and interfacing fibers) are shown. For other select volumes thickness heatmapping was applied using Dragonfly software after 3 rounds of smoothing (k=3) to reduce computational expense.

To segment stained fibers, fiber mantle and core regions, and calcite mammillae of FIB-SEM volumes, a similar deep learning-based approach to the Micro-CT data was utilized. Briefly, 1-2% of total image slices from each FIB-SEM stack were manually segmented using Dragonfly

ROI painter tools. Corrected slices were provided as training input for a convolutional neural network (CNN), again using default architecture (depth of 5 layers and 64 convolutional filter per layer). Training parameters were the same as above, except for batch and patch sizes of 32. Training stopped after 10 consecutive epochs with no improvement in learning (based on the training/validation loss convergence. Different semantic segmentation models were trained for each target class – ex. fiber mantle vs. core vs mammillae. The model for the largest volume of the membrane in full cross-section was trained to recognized and ignore minor bright curtaining artifacts towards the far edge of the volume. Three rounds of object smoothing were applied to each segmentation output (kernel = 3). This is a minimum smoothing step and is designed to reduce computational expense for subsequent analyses. Volume thickness maps were also created of select FIB-SEM segmentations and cropped regions from these segmentations using the "volume thickness map" operation. This operation computes maximum possible diameters within 3D foreground features. Sphere diameters are the color coded and also displayed as histogram distributions for appropriate panels. Shadowing effects are used to highlight texture and orientations of FIB-SEM 3D segmentations. Directionality mapping was completed with the Dragonfly software Bone Analysis plugin using a surface normal algorithm and segmentation input of the full membrane in cross-section.

To approximate what the surface area of a theoretical "nonspiked" mantle would be (as it would interface directly to mammilla calcite), a cylinder was created in Dragonfly and modified to have its curved dimension approximating the overall true spiked fiber mantle curvature (shown in Fig. 4J). While the cylinder was selected, the view mode was changed to a nonplanar view. From this view, multislice painting with the smallest brush was used to label this curvature as a thin plane approximating an equivalent smooth mantle curvature. The surface area of mantle spikes/voids from Figure 4J was then compared to the surface aera of the theoretical nonspiked thin plane to determine the magnitude difference in the inorganic-organic attachment area provided by the mineral spikes in native eggshell.

Scanning Transmission Electron Microscopy (S/TEM) and Transmission Electron Microscopy (TEM)

Sample Preparation

- Lamella 1 – Conventional preparation:

    From the same block as FIB-SEM Volume 3, front and back trenches were progressively milled into the blockface at the tip of a different selected mammilla to create a thin lamella where several mammilla-embedded and interfacial fibers were visible. A standard lift-out technique using the Hitachi Ethos NX5000 FIB-SEM was used to trim the lamella to a final thickness of around 250 nm (Gallium milling at 30 keV, 1.5 nA; 30 keV, 280 pA; 15 keV, 100 pA; and 10keV, 50pA; with each step being applied to both faces of the lamella). Sequential reduction in current and voltage was applied to decrease contamination and an amorphous gallium layer in the lamella. A final step of 210 s of Argon (each face receiving half this duration) at 2 keV was applied to eliminate any residual gallium.

- Lamella 2 – Cryo-preparation:

    Different chicken eggshells were rinsed and briefly washed in the same manner as mentioned in the sections for X-ray and FIB-SEM specimens. Exactly following this, eggshell pieces (with membrane) were placed in a dish with cryoprotectant (hexadecane), and placed in a vacuum for 30 minutes. Within 2 hours, all eggshell pieces were cryo-fixed using a Leica EM ICE (Leica, Wetzlar, Germany), and samples were subsequently dehydrated into pure acetone by freeze substitution in a Leica ASF2. Standard infiltration and embedding in Epon resin, and block preparation were conducted as outlined in the FIB-SEM section above. Lamella preparation of this cryo-prepared specimen was carried out similar to Lamella 1 above using the Hitachi Ethos NX5000 FIB-SEM.

- Decalcified sections and immunogold labeling for osteopontin:

    Equatorial-region eggshell samples with attached eggshell membrane were chemically fixed with 4% paraformaldehyde (Thermo Fisher Scientific) and 1% glutaraldehyde (Electron Microscopy Sciences, Hatfield, PA, USA) in 0.1 M sodium cacodylate buffer (pH 7.3, Electron Microscopy Sciences, Hatfield, PA, USA) for 1 hour. After washing briefly in additional 0.1 M sodium cacodylate buffer, specimens were decalcified in 8% EDTA, and then gradient-dehydrated to 100% pure ethanol, and then gradually infiltrated and embedded in LR White acrylic resin (Electron Microscopy Sciences, Hatfield, PA, USA). Final polymerization in pure LR White was achieved over

2 days at 60°C. Cured resin blocks were manually trimmed to a suitable plane within the embedded eggshell, and microtomed with a diamond knife for light microscopy at 0.5-µm-thickness, or at 80-nm-thickness for TEM using a Leica Ultracut E ultramicrotome. For immunogold labeling and TEM, grid-mounted sections were incubated with anti-chicken polyclonal osteopontin antibody (courtesy of Dr. Louis Gerstenfeld) followed by protein A-gold conjugate (14 nm gold particle size, from G. Posthumus, University of Utrecht, The Netherlands). Labeled grids were then conventionally stained with uranyl acetate and lead citrate.

Imaging

Transmission (TEM) and scanning transmission electron (S/TEM) microscopy were performed on conventional and cryo-prepared specimens. TEM imaging was conducted using a Talos F200X S/TEM microscope (Thermo Fisher Scientific) equipped with a 4k x 4k Ceta 16M CMOS camera and operating at 200 kV, and using a 40 µm objective aperture. Diffraction patterns were collected after removing the objective aperture, changing the camera mode to HDR with a camera length of 330 mm, and inserting a selected area aperture (270 nm). For EDS mapping, a unique STEM field emission gun register was utilized (changing the gun length to 3, and spot size 6), and camera length was set to 98 mm with no apertures inserted. A spectrum image area containing features typical of mammilla, mantle, and core (of the cryo-prepared lamella) was created alongside a separate smaller drift area. Spectra intensities were recorded for 15 minutes as maps for Ca, O, and C. High-resolution STEM imaging (gun length = 5, spot size 9) of mineralized fiber morphology was also conducted on the Talos F200X using a high-angle annular dark-field (HAADF) detector (collecting only electrons scattered to 58-200 mrad).
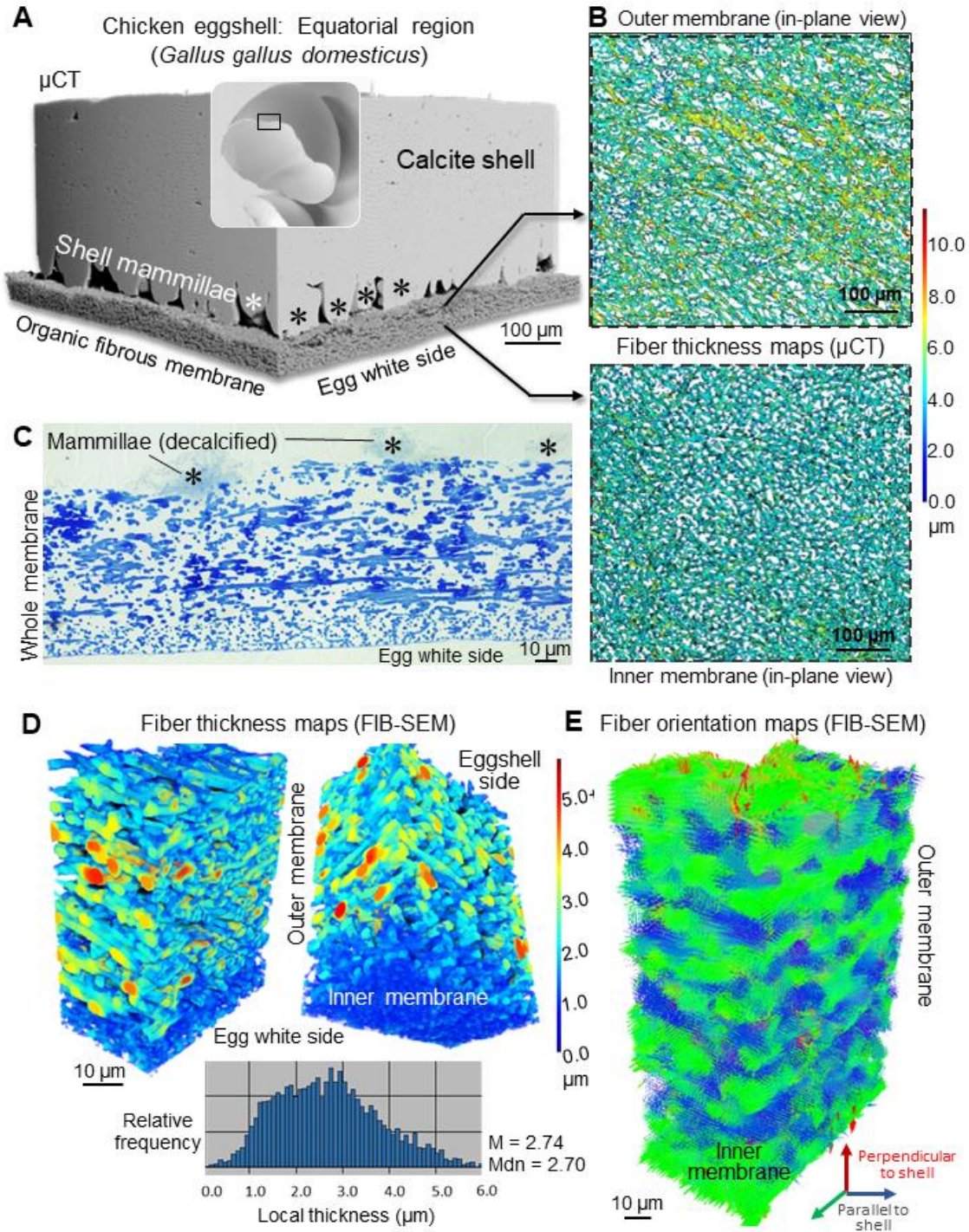
Fig 1. Chicken eggshell membrane fibers by submicrometer µCT and FIB-SEM microscopy.
(**A**) µCT and segmentation of a complete shell and eggshell membrane cross-section from the equatorial region of an egg. Shell mammillae (*****) form from initial mineral nucleation and growth at the outer membrane surface (see Movies SM1 and SM2). (**B**) Thickness heatmapping of digitally

prepared sections of outer and inner membrane fibers showing fiber size differences over large fields of view. (**C**) Light micrograph of a toluidine blue-stained section of full-thickness eggshell membrane. Mammilla (here decalcified, no mineral) are denoted by asterisks. (**D**) Thickness heatmapping of a gallium FIB-SEM serial-surface-view reconstruction of a full-thickness eggshell membrane, with the corresponding distribution of fiber thicknesses. A portion of an adjacent calcitic mammilla was segmented and digitally removed, but can be seen in Movies SM3 (registered slices), SM4 (thickness map), and SM7 (mammilla detailed). (**E**) Mapping of local fiber directionality showing orthotropic assembly through the same full eggshell membrane 3D cross-section.
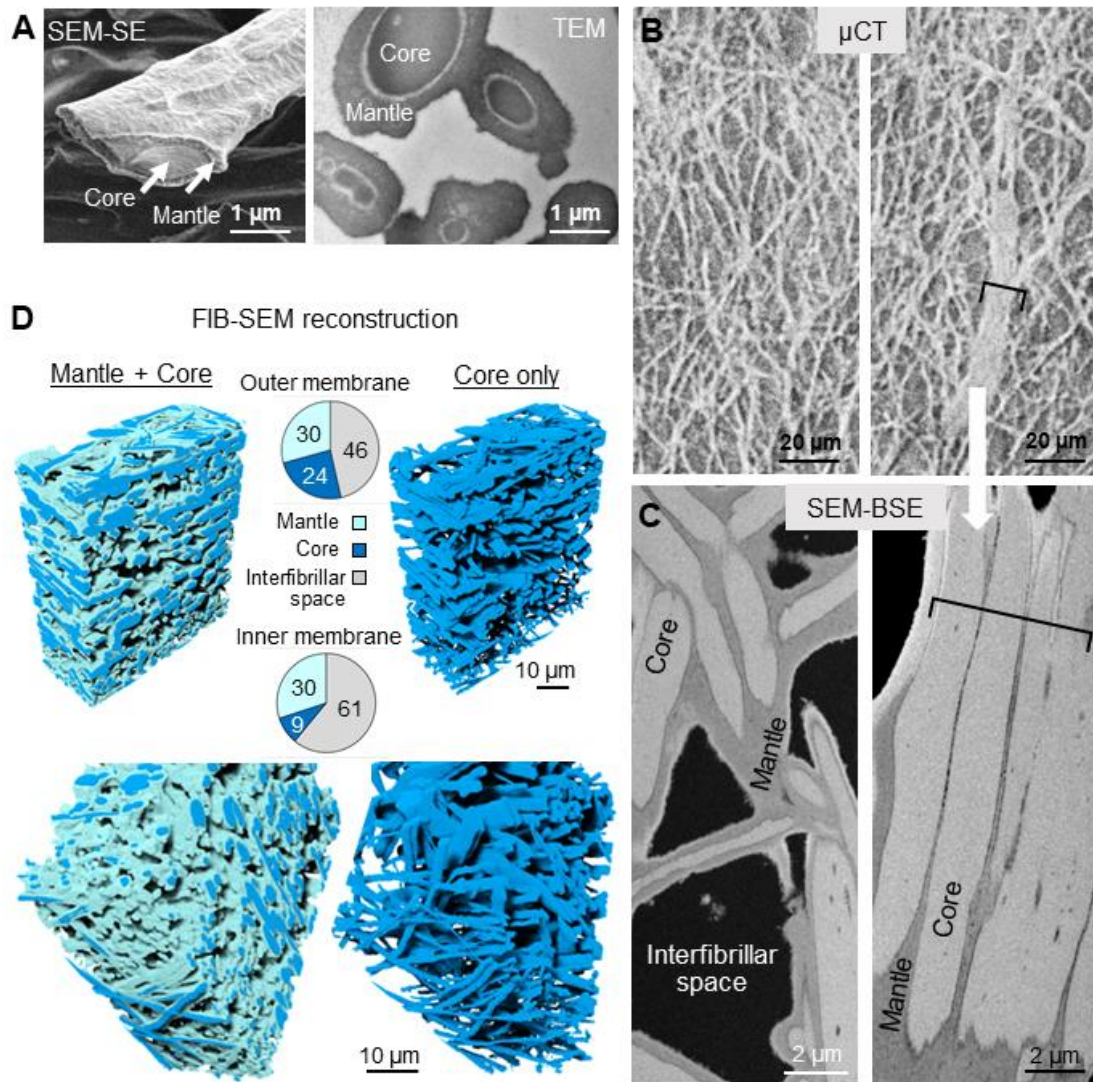
Fig 2. **Fiber mantle and core morphologies assessed correlatively and in 3D.** (**A**) SEM and TEM electron microscopy images showing distinctions typical of mantle and core eggshell membrane fiber regions in topographical and stained section micrographs. (**B,C**) Correlation of oblique projections of outer membrane fibers from μCT (B) and SEM-BSE (C) showing regions of both isotropic fibers and also large fiber bundles (brackets) with significant similar directionality and size within the outer membrane. Fiber bundles exist as arrays of sandwiched mantle and core constituents. (**D**) FIB-SEM serial-surface-view deep learning-based segmentation of fiber mantle (turqoise) and core (blue) through a near full-thickness membrane (Movie SM5). While mantle volume fractions are the same in outer and inner membrane, core volume fraction within the inner membrane is reduced.
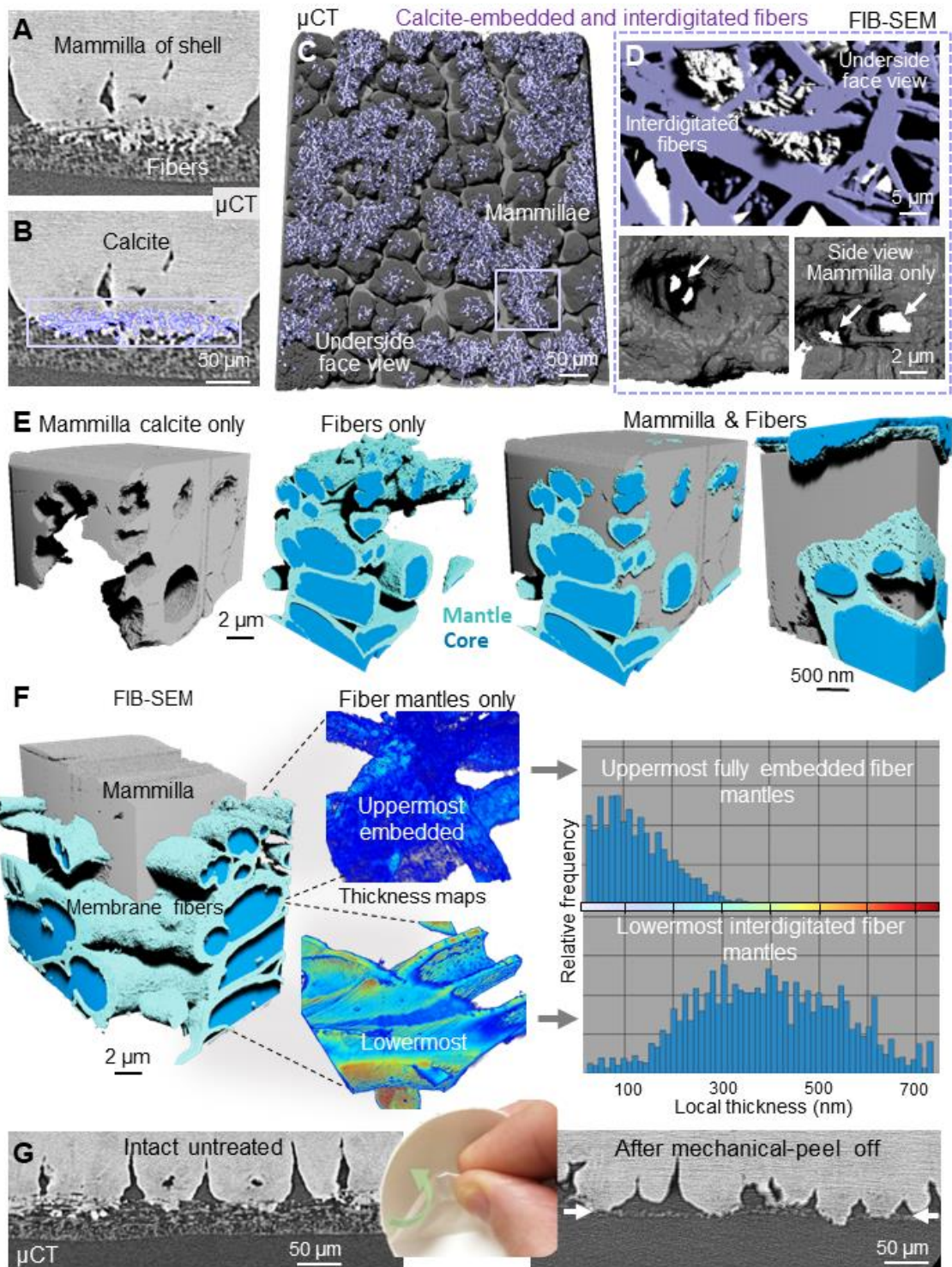
Fig 3. **Attachment of interdigitated eggshell membrane fibers to the shell across the micro-scale: Ubiquitous and progressive embedding of fibers within calcitic shell mammillae.** (A) During initial mineralization to form the eggshell, outermost membrane fibers become embedded

within calcitic mammillae. (**B**) Deep learning was used to segment only mammilla-anchored fibers (purple) that are either completely embedded or interdigitated with mammilla calcite. (**C**) Multiple fibers are anchored to all mammillae, thus attaching the membrane to the shell. (**D**) FIB-SEM serial-surface-view and segmentation of calcite mineral (gray) and fibers (purple) reveals tracts where fibers are anchored to the mammilla (Movie SM7). (**E**) At higher resolution in different reconstructed FIB-SEM volumes, both embedded and interdigitated fibers are observed, showing distinct morphologic features. (**F**) The mantles of the completely embedded uppermost fibers are thin and uniform, whereas the mantles of the interdigitated fibers show nonuniform and higher thicknesses. (**G**) μCT projections reveal that after manual peeling of the membrane from the shell, mineral-embedded fibers remain (arrows), even in areas where they stretch between mammillae.
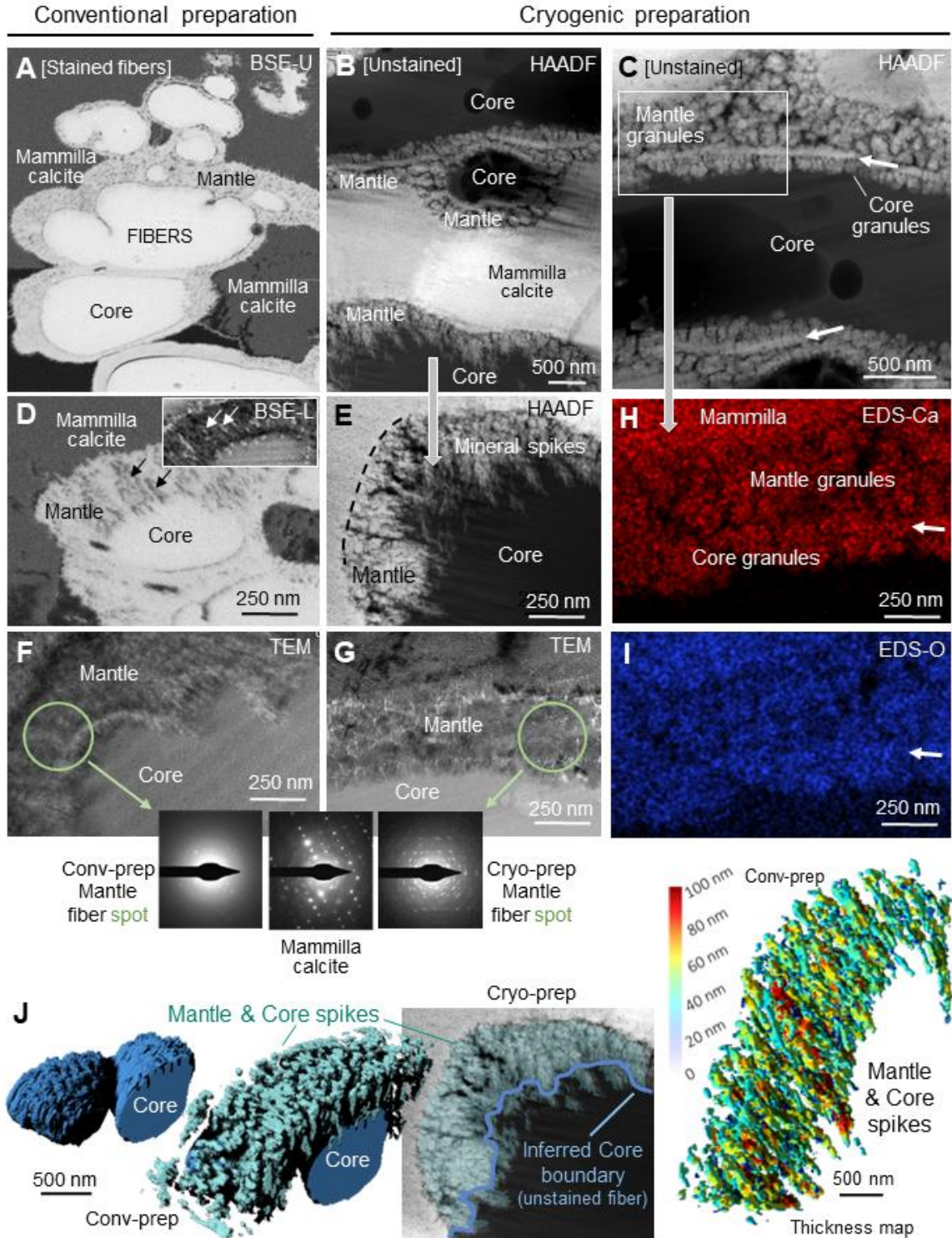
Fig 4. Attachment of eggshell membrane fibers to the shell at the nanoscale: Multiscale assessment of fiber mineral granules and spikes. Transient amorphous mineral phases at fine dimensions are sensitive to aqueous-based conventional sample-preparation techniques (301). After acquiring several FIB-SEM volumes that were conventionally processed and stained (**A**),

BSE differences in contrast suggested that within fiber mantles that adopt the more porous "void-like" morphology (**D,** black arrows, also see Movie SM8), there was in fact propagation of small mineral spots/streaks (**D,** white arrows in inset). Diffuse electron diffraction reflections after SAED of fiber mantle from a FIB-prepared lamella of the same sample corroborated that these were voids with little mineral (**F**). For better characterization of the mammilla-embedded and interdigitated fiber mantle "voids" that shows some evidence of mineral, an additional lamella (**B, C, E, G, H, I**) was prepared using cryo-conditions to preserve mineral, namely high-pressure freezing and freeze substitution. STEM/HAADF imaging of this lamella revealed two previously unrecognized mineral morphologies (**B**) – mineral "granules" present in embedded fiber mantles (**C**), and mineral "spikes" of interdigitated fiber mantles (**E**). Electron diffraction of fiber mantle mineral from this cryo-prepared specimen was indicative of polycrystalline calcite (**G**), with much stronger reflections than that after conventional aqueous preparation, but distinct from single-crystal calcite of the mammillae. These data were further corroborated by EDS showing abundant Ca and O within the mantle (**H, I**). Stained conventionally prepared samples consistently show fiber voids also extending into the core region of the fibers (**D, F,** Movie SM8), and a gap between mantle and core regions (**D,F**). Taking both preparations together, these results indicate that fiber voids (**D, J**) from conventionally prepared specimens (up to 100 nm in thickness) are filled with mineral spikes in native eggshell (**E, J**), and further suggest that spikes extend through the mantle and slightly into the core region (**D, F, J**), as indicated by conventional preparation staining patterns and void morphology within the core region (**D, F,** Movie SM9). Additionally, a uniform band of mineral appears to intervene between mantle and core granules (**C,H,I** arrows).
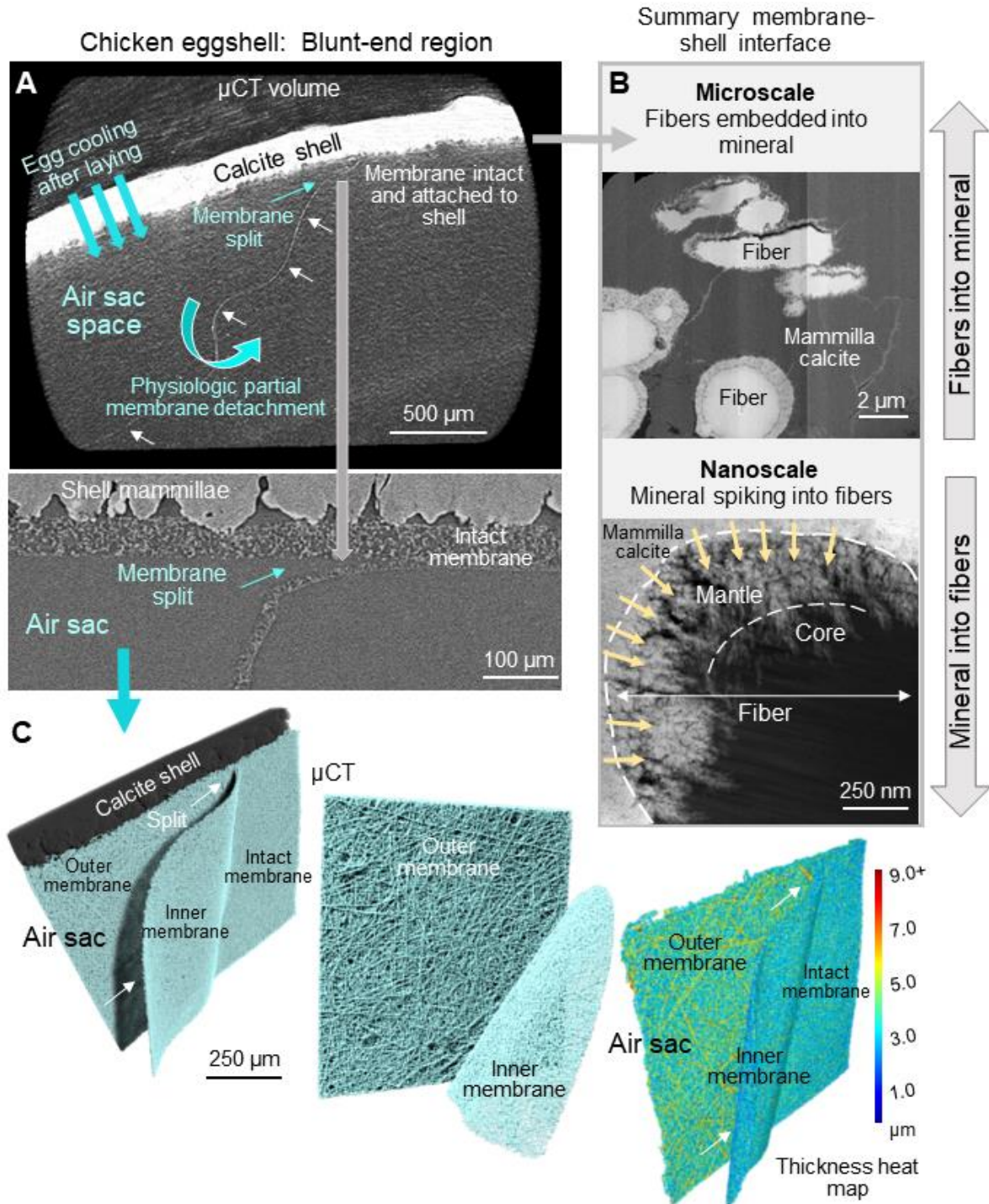
Fig 5. **Summary describing multi-scale, self-affine and reciprocal attachment of organic fibers to eggshell mineral: A morphological basis for membrane fiber anchorage underlying air sac formation.** (**A,B**) Summary depiction of chicken eggshell-membrane relationships forming the structural basis for fiber attachment to the avian calcitic shell. During transit in the hen's oviduct (prior to laying), eggshell membrane fibers become anchored into mineral, and

mineral penetrates into fiber mantles, collectively securing a strong reciprocal attachment. After an egg is laid, cooling from loss of internal body warmth from the hen results in air ingress through shell pores into the egg to form an air sac which continues to increase in volume over time, and provides oxygen to the developing chick. Using a low-resolution scout µCT scan, the exact coordinates of the membrane split were found (**A,** Supp. Fig. 2) and used to image this location at high resolution (**C,** also see Movie SM10). The split occurs exactly at the interface between inner (thinner) and outer (thicker) membrane fiber layers, shown here in 2D and 3D, where the outer and inner membrane fibers detach from each other, with an intact (yet to be split) portion of membrane still clearly visible adjacent to the shell (**A, C**). Splitting of the membrane in thickness at the blunt end of eggs, rather than complete detachment from the mammillae, is ensured by anchorage of outer membrane fibers to the shell (**A**, left side lower panel and Movie SM10, see remaining fiber anchorage to the mammillae). The present study provides a morphological basis for understanding how robust attachment is achieved between organic fibers and mineral over multiple length scales, critical not only for air sac formation, but also for association of the underlying chorioallantoic membrane to facilitate eventual shell dissolution, and for overall shell strength. In panel B, brightness variations result from changes in acquisition settings to adjust for sample charging.
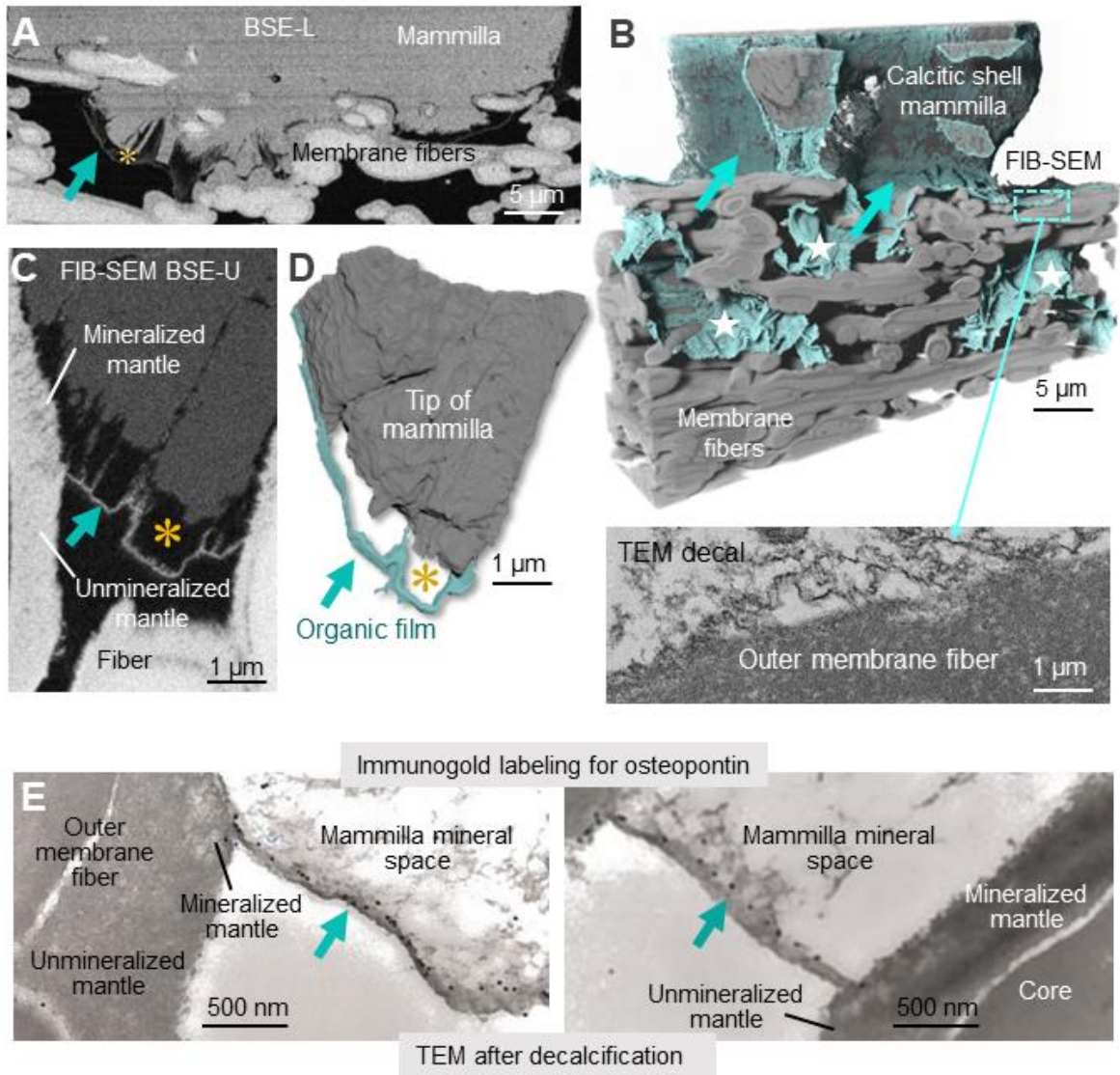
Fig. S1. **A distinct thin organic membrane containing mineral-binding osteopontin delimits mineralization sites of eggshell membrane fibers.** An osteopontin-containing (labeled with gold particles), nanometers-thick membrane delineates the base of calcitic mammillae where mineral is exposed/interposed between interdigitating outer membrane fibers, and continues as extended sheets draping into the eggshell membrane (turquoise segmentations and turquoise arrows). (**A**) The thin membrane drapes down from the edges of each calcite mammilla, and at some point contacts and adheres to outer membrane fibers (**A, B, C**). (**B**) In 3D by FIB-SEM reconstruction, this thin membrane is continuous around each mammilla, and extends down further into the outer membrane where it splits and makes many contacts with deeper fibers – but only to a limited depth

177

of about 10 µm into the outer membrane. (**C,D**) Application of conventional aqueous-based fixation and washing procedures results in mineral dissolution in the outermost exposed regions of the mammillae, leaving behind large voids (gold asterisks). (**E**) Immunogold labeling for osteopontin (small black dots) is associated with the thin mammilla-delineating membrane. [Note: Osteopontin is a prominent interfacial and surface protein in many mineralized tissues, particularly where it accumulates in bone at cement line interfaces and at the surfaces of mineralized bone as a thin (nms) lamina limitans (reviewed in McKee M and Nanci A, Microscopy Research and Technique, 33:141-164, 1996).
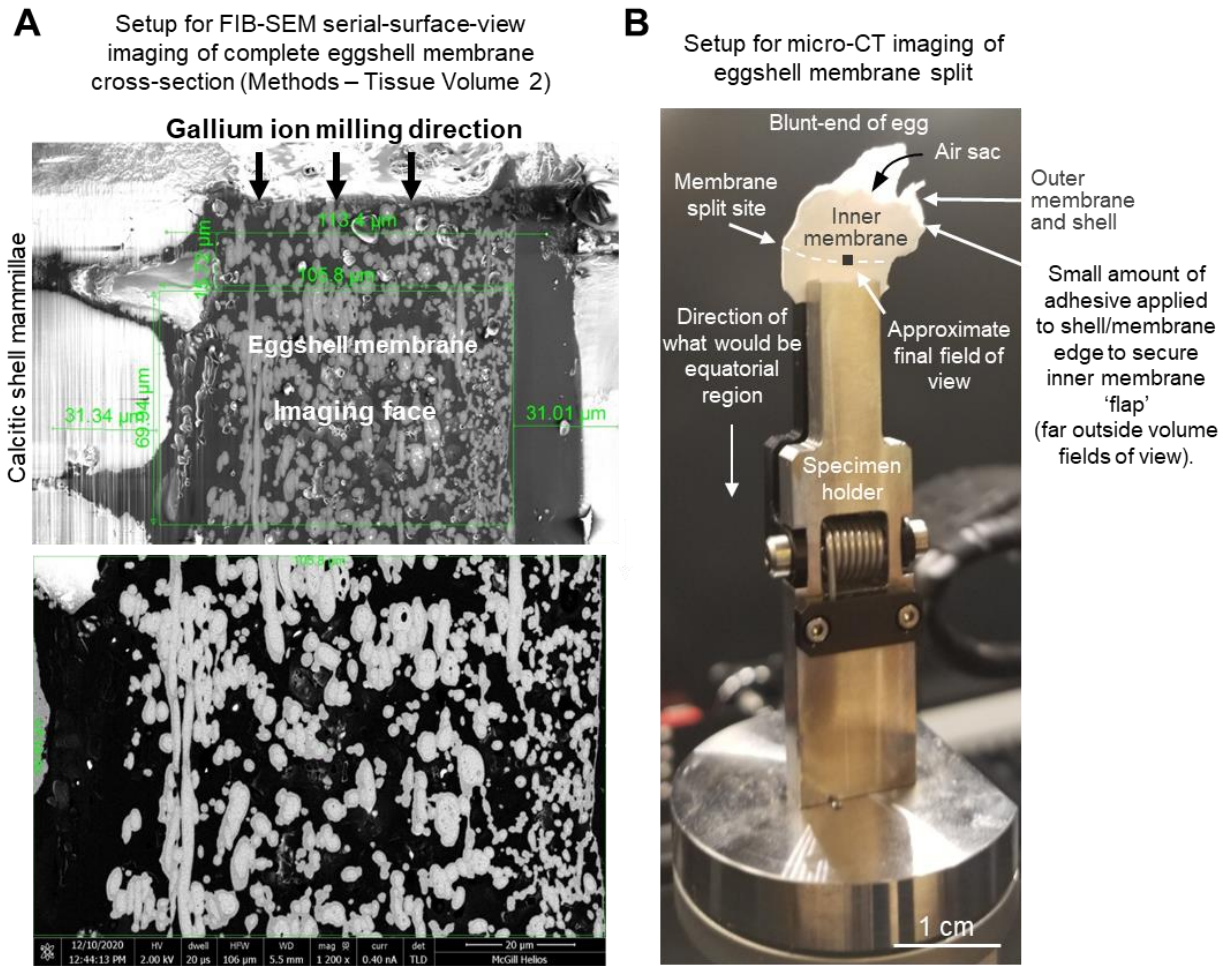
Fig. S2. **Imaging setup for Gallium FIB-SEM of entire eggshell membrane cross-section and Micro-CT of eggshell membrane blunt-end split.** (**A**) Gallium ion milling direction (arrows) was conducted parallel to the eggshell membrane long axis to reduce curtaining artifacts within the acquired image slices. A mammilla that was just appearing within the blockface was chosen to center the imaging area, and is shown at the extreme left of the bottom image which was the first image taken during FIB-SEM acquisition. (**B**) Micro-CT approach for imaging the membrane split. Gentle preparation of a region of shell from the blunt end of a chicken egg (outlined in methods section) was followed by securing the inner membrane flap with adhesive to the edge of the top piece of shell (outside of field of view -see box approximate volume). The other shell side (also outside of final field of view) was secured using a clamp style Zeiss Xradia Versa specimen holder, and then placed inside the instrument for imaging using the "Scout and Zoom" method.

General Discussion and Future Work

The topic of repeating, 3D-tessellated or quasi-periodic mineral units as presented in this work, that form within biological fiber systems, result from complex biomineralization processes evolved over hundreds of millions of years (104). Nano- to microscale relationships within and between the fibrous organic phase and the mineral units, occurring over three dimensions, underly whole-tissue mechanical properties – with two examples being presented here, namely crossfibrillar mineral tessellation in bone, and multi-scale reciprocal attachment in the mammillae of the eggshell. These are two different biological systems − one with permeating apatitic Ca-P mineral tesselles into collagen fibrils and fibers having a repeating layered structure, and the other with calcitic Ca-carbonate mineral mammillae protrusions integrating into only a portion of outermost eggshell membrane fibers that are less-well characterized − yet each share features of an integrated organic-inorganic interface. The biomineralization process to produce these mineral unit assemblies interfacing with and intercalated into an organic fiber network requires a sufficient quantity of mineral ions and regulatory molecules produced by cells. Often this occurs through selective expression and/or removal of a variety of small inhibitory molecules (107, 110), inhibitory mineral-binding proteins (136, 332), and enzymes to degrade these inhibitors (2, 136, 262).

Key Definitions

Biological tessellation

A geometric array consisting of uniform or nonuniform, space-filling close-packed units, traversing a surface or a volume. Units may interdigitate and are also frequently observed with soft and stiff elements in series filling a continuous surface or volume (201).

Semantic segmentation

All objects of a given class/category. Ex. "people" as a category, without distinguishing individuals. In this thesis the tesselles are firstly collectively labelled as a semantic class.

Instance segmentation

Identification of each instance within the class as a unique object. Ex. "persons" within the semantic category of "people". In this thesis, each individually colored tesselle is an instance, and collectively multiple tesselles comprise a semantic class. Instance segmentation permits statistical/comparative analysis of the objects comprising the semantic category/class.

Ground truth

Representative image subsets (selected 2D slices or small 3D subvolumes) that are expertly segmented by the operator as training examples for a deep learning segmentation model. "An expected or exact output to allow a neural network to construct the most effective path from raw input to interpretable output" (143).

Distance mapping

A computational tool used to map distance values from any voxel in an image to a user-defined pattern (an object, or a background/foreground interface). The distance values are mapped as voxel intensity (high-to-low, or low-to-high). Using a distance map, the approximate "centroid" of each tesselle can be labeled (in this case, based on the distance between every voxel of the tesselle interior and the interface of the tesselles and the background). Such distance threshold-based labelling of discrete tesselle centroids generates a set of tesselle "seeds" – the seeds, as opposed to the tesselles themselves – do not "touch" each other in the image, and serve as points of origin for the watershed transform and for digital separation of confluent objects.

In vertebrate mineralized tissues where inhibitors are widely present to prevent mineralization that is not compatible with life, a system of double-negative "inhibition of inhibitors" by enzymes is employed to facilitate mineralization (2). At the organismal level, an initial first level of inhibition of mineralization is achieved by the small molecule pyrophosphate (PPi) that is generated in metabolic processes and exported from cells (2, 107, 110). At the next level, synthesis and secretion of negatively charged mineral-binding proteins − for example the ASARM (acidic serine and aspartate rich motifs)-containing SIBLING proteins (OPN, BSP, MEPE, DMP1, DSPP1) rich in calcium-binding aspartic and glutamic acid amino acids together with abundant serine residues that are phosphorylated − regulate the extracellular matrix mineralization process (2, 12, 262, 333). In the eggshell membrane fiber system, mineralization is also inhibited broadly throughout most of the fibrous membrane during its transit through the

hen's oviduct, except for within and around specific regions of the outermost fibers, where mineralization events form mineral units known as the shell mammillae (89, 119, 300). Nucleation and growth of mineral is permitted within these fiber systems presumably when an appropriate ratio of promoters (mineral ions and enzymes that cleave inhibitors) to inhibitors (small molecules and proteins) are present at local domains both within and around fibers (2, 108).

Here, using a variety of volume imaging methods including 3D X-ray and electron tomography, cryo-processing techniques, and deep learning-based segmentation and analyses, we report on detailed high-resolution aspects of several extracellular matrix fiber systems (bone, enthesis fibrocartilage, Achilles tendon, eggshell membrane). This thesis includes quantitative high resolution (nanometers to tens of nanometers resolution) 3D imaging data (FIB-SEM serial surface view imaging), specifically from 6 volumes of lamellar bone at the mineralization front, 10 volumes of enthesis fibrocartilage at the mineralization front, 1 volume of Achilles tendon at the mineralization front of ectopically forming mineral, and 5 volumes from eggshell-shell membrane interface. Amid myriad potential *in vivo* mineralization determinants present in different tissues, we observed a consistent formation of repeating, tessellated, or quasiperiodic mineral units across the microscale, and that these integrate with organic fibers. Studying this further for bone in a mouse model (*Hyp*) of the osteomalacic human disease X-linked hypophosphatemia (XLH), we show that the combined effect of inhibitory OPN (122) (153, 334) accumulation in the extracellular matrix, together with reduced circulating serum phosphorus, affects the microscale and ultrastructural integrity of these mineral units across three dimensions, severely affecting mineral patterning in bone. The described changes are well beyond what has been known from lower-resolution light microscopy and X-ray studies, and these defects likely explain exacerbated bone and calcified fibrocartilage defects in mice and humans that are not addressed by correcting serum phosphate levels through the currently used FGF23-antibody therapy for XLH patients (335). Also provided in this work is evidence that the ultrastructural integrity of mineral unit tesselles, and their heterogeneity of sizes, is dictated from as early as the mineral foci stage near the mineralization front in bone matrix, a stage where OPN and other acidic proteins are also known to be constitutively active through binding to calcium and mineral phases.

Taking together, and building upon prior studies, this work has contributed to the development of something we have named as the *Stenciling Principle* for extracellular matrix mineralization, where enzyme-substrate (promoter-inhibitor) pairings allow for double-negative

regulation of mineralization (inhibiting the inhibitors) (2, 262, 283). This occurs initially and broadly through the TNAP/PPi axis, and then more specifically to refine mineral-unit (tesselle) packing through the PHEX/OPN axis. These pathways, likely along with other similar substrate-enzyme pairings yet to be determined, allow for physiologic growth and packing of mineral units as crossfibrillar mineral tessellation as inhibitory molecules and proteins are enzymatically cleared from the extracellular matrix. Aligned with this notion is that tessellation of repeating "stiff" and "soft" elements appears to be a strategy widely employed in Nature as a toughening mechanism (201). While the effect of bone's lamellar organization and lacunocanalicular network has been well documented with regards to crack propagation (336-338), crossfibrillar mineral tessellation, with its repeating mineral unit tesselles and organic gaps, likely represents a sublamellar mechanism for dissipation of critical stresses, possibly through sacrificial bonds (201, 339, 340) of mineral-bound peptides bridging between tesselles.

The chapters of this thesis were the first to show mineral unit structures in a number of fibrous tissues using high-resolution 3D imaging with deep learning-aided segmentation (143) across the micro scale. Overall, mineral units simply consist of varying degrees of whole-fiber incorporation within mineral, and reciprocally, variation of nanoscale mineral incorporation within fibers themselves. At the microscale in mouse lamellar bone, calcified enthesis fibrocartilage, and Achilles ectopic calcifying tendinopathy, a shared crossfibrillar mineral tessellation pattern is observed (27, 262), although with slight variations in mineral "tesselle" size in each respective matrix (though with similar aspect ratios) (341). In crossfibrillar mineral tessellation, small mineral foci grow within an otherwise unmineralized collagen zone (osteoid of bone, uncalcified fibrocartilage, tendon) near the mineralization front to become elongated into approximately a mineral ellipsoid shape aligned with respect to the long axis of collagen fibrils (27, 341). Although mineral "rosettes" or "spherulites" were previously described from 2D views of tesselles (94, 190, 192, 198, 292), the first chapter of this thesis was the first to show their full three-dimensional shape, their 3D relation to other constituents of bone and cartilage hierarchy including the lacunocanalicular network, collagen fibrils, bundles, and lamellae, and cells, and using precedents from other tessellated materials, a terminology was applied that reflects the functional implications of this structure (mineral "tesselles"). This relation was revealed using watershed transform segmentation to segment thousands of bone tesselles (27, 341), and in multiple lamellae in bone

(27), and thus providing reliable quantitative values that previously could have only been postulated.

Watershed Transform

Definition

Watershed transform is a computational method used to separate distinct neighboring objects that are confluent, abutting, or continuous across 2D or 3D space. Operationally, a distance map is used to first define, and then expand, the centroids of all the objects ("seeds") until digitally expanding boundaries of neighbouring objects abut, and the semantic category can be discretized into individually ID-ed objects (instances).

Limitations

The primary limitation of watershed transform is the possibility of under-separating neighboring objects (after too conservative labelling of the seeds – too few seeds for the number of confluent objects), or over-separating of some objects into smaller fragments (after too inclusive labelling of the seeds – too many seeds for the number of confluent objects). Careful examination of the selected seeds to ensure that roughly each object in the class contains one and only one seed, is sufficient to ensure accurate digital separation of the confluent objects, and a successful transformation of the semantic class into a population of individually labelled instances comprising that class.

It is unknown what restricts mineralization at the majority of the tesselle periphery to result in organic gaps typically of tens of nanometers. Restriction of mineralization at these gaps appears to occur both within and in spaces between fibrils (341). Fusion of tesselles around a minor portion of their periphery has been noted (292, 299), however, in old bone and deep into calcified fibrocartilage near the cement line we observe maintenance of the tessellation pattern, suggesting that the role of time (organismal age) may not always influence this pattern. OPN and other mineral-binding proteins may become sequestered in these organic gaps, still bound to mineral tesselles, and acting to restrict full tesselle fusion during their initial packing at the mineralization front, and then beyond. Another possibility is that this could be combined with depletion of mineral ion availability at a certain level locally beyond the mineralization front. Importantly,

within these tesselle mineral units of vertebrate fiber systems, the nanoscale mineral phase completely penetrates fibrils and extrafibrillar space. This occurrence of apatite nanocrystals within and between collagen fibrils (within each tesselle) is well known to bone researchers, however, it surprisingly stands in contrast to that which occurs in another mineral unit – calcite mammillae of the eggshell membrane fiber system. In this latter system (here assessed using avian chicken eggs from commercially available North American layers), organic fibers also penetrate the mineral unit mammillae, but in this case occurring from all directions instead of being highly aligned with collagen type I fibrils of bone or cartilage. Remarkably, unlike in bone or cartilage, and at the nanoscale, organic fibers of the eggshell membrane that penetrate mineral unit mammillae are not completely consumed by mineral crystals, but instead are selectively penetrated by polycrystalline granules or spikes.

For mineralized tissues, the study of attachments between soft (organic) and hard (inorganic) tissue is of critical importance to handle stress concentration variation at these sites during loading. Complex spatial gradients and clever structural arrangements (40, 42, 83, 92, 251, 252) have evolved over hundreds of millions of years (104, 280) to reduce stress concentration between soft and hard tissues. Biological systems are well-adapted in their advanced ability to produce structures that address stiffness differentials at inorganic-organic interfaces starting from the nanoscale and continuing hierarchically, with this ability often being afforded through molecular interactions between small acidic proteins and peptides that bind calcium and crystal lattice calcium (12, 92, 104). Here, a new perspective is given for structure-function relationships at soft/hard attachment sites, showing in particular the influence of close-packed mineral units (341). In Achilles calcified enthesis fibrocartilage, mineral unit tesselles are widespread across this zone and evidence is provided that their structure (being slightly larger and more heterogeneous, and often with larger organic gaps) contributes to the overall gradient enthesis properties between unmineralized tendon and mineralized lamellar bone (having smaller and close-packing tesselles).

Similarly but separately, mineral unit mammillae in the avian eggshell provide initial sites for radial mineral growth of the eggshell (66, 89). As opposed to growth like occurs at the mineralization fronts of bone or cartilage, such radial growth from mammillae achieves two goals. First, growth in the radial direction allows for the formation of eggshell pores that are critical for nutrient and gaseous exchange for the developing chick (303). Second, despite these required

pores, distinct radial single crystal calcite growth originating from mammillae occurring around the entire shell creates boundaries which act to strengthen the eggshell. Here, it is shown that despite this radial growth process whereby the necessity of quasiperiodic mammillae to form calcitic columns but with collectively a substantial amount of space between mammillae near the membrane attachment site seemingly (from previous lower-resolution studies and in 2D (323)) reduces the membrane-shell attachment area, this in fact is not the case. It is shown here that 3D microscale and nanoscale structural refinement at this mineralization interface and within each mineral unit mammillae indeed completely mitigates this "decreased attachment problem" by a mineralization solution that conservatively reaches a surface area of attachment that is actually ten times greater than the surface area of the egg itself. This order-of-magnitude surface area increase, despite the large gaps between mineral unit mammillae, is approximately equivalent to the increase in area from a normal-sized playing card (3.5 x 2.5 inches) to a standard 11 x 8.5-inch sheet of paper.

Not only are mineral units a fundamental structural product of mineralization of biological fiber systems across the microscale, and with their composition being critical to functions of mineralized tissues and at attachment sites, deficiencies in mineral units in the diseased state are also fundamental in causing tissue malfunction. In fiber systems of *Hyp* mice (lamellar bone, Achilles enthesis fibrocartilage, and midsubstance tendon), we provide the first-known example as shown in 3D of deficient formation of mineral units, in this case defective and incomplete crossfibrillar mineral tessellation (27, 341). Like in the eggshell membrane where the initial number and spacing of quasiperiodic mineral unit mammillae influence the ultimate mechanical integrity of an egg, we provide the first extrapolation of this idea in vertebrate mineralized tissues where we suggest the distance between early nascent mineral foci indeed predict the heterogeneity of final mineral tesselle spacing during mineral patterning (341). In disease, where levels of mineral-binding small molecules or proteins such as PPi and OPN, or lack of mineral ion availability, may occur, slight changes in the spacing of initial foci precipitation or their growth could conceivably affect the packing of mature tesselles over the broader scale. Although the extracellular matrix would appear to be adequately mineralized, heterogeneity (297) in tesselle sizes and spacings could severely alter the crack initiation process and weaken a bone's mechanical properties. For example, this could be explained hypothetically by the case of a rogue tesselle say twenty times the "normal" size where diffuse loading damage with energies that might normally

be dissipated at organic gaps now abnormally propagate to reach more critical dimensions. Repeated damage in a mineralized matrix of this defective quality could be more susceptible to the development of larger cracks of critical size being potentially catastrophic. Therefore, more heterogeneous tesselle packing even in an extracellular matrix with otherwise equal overall mineral density could affect the damage initiation process of lamellar bone where stress concentrations originate initially through local incongruities where tesselle sizing and spacing deviate from normal. Physical and/or computational modeling approaches using both homogeneous "steps" in tesselle size and spacing (with elastic modulus of two components approximating that of mineralized collagen and unmineralized collagen), and also with heterogeneous packing, would allow for a greater understanding of the effect of tesselle close-packing on mechanical properties of mineralized tissues. Mechanical testing of physical models might be achieved through 3D printing of tessellated beams from two different materials with properties approximating those of matrix (softer) and mineral (harder).

Overall, future correlative imaging studies that include 2D blockface imaging with selected area 3D FIB-SEM sampling would be of great benefit in understanding, for example, whether tesselle sizing and spacing has evolved to contribute to the gradient of mineralization in calcified fibrocartilage itself, or whether a similar mineral tessellation pattern is observed in woven bone where collagen is more disordered. Additionally, an important question is to what extent do novel tissue engineering approaches for treatment of bone and cartilage defects (for instance as a result of injury or degeneration) recapitulate this original intricate nano- to microscale structural relationship between organic and inorganic constituents of these biological fiber systems.

In addition to this, future studies might combine specimen staining with the capability to use multiple backscattered electron detectors simultaneously and at 4 nm voxel size which can allow for a better 3D understanding of the trajectory of mineralization, such as in bone osteoid. Careful segmentation of stained and overall cylindrical collagen type I fibrils from small mineral foci that each have unique electron contrasts when assessed using differently positioned detectors can be used to generate evidence in support of extra- or intra-fibrillar mineralization as being favored initially, or perhaps occurring simultaneously as has been proposed with roles for collagen confinement and specific nucleators which may initiate mineralization outside of the fibrils.

For eggshell, there are many remaining questions regarding the initial mineralization events that occur at the outermost membrane fibers and at organic "mammillary cores". We know

now that this mineralization process occurs through an amorphous phase (89). This thesis reveals the presence of unique crystalline mineral morphologies within the outer membrane fiber mantle and core. How is this mineralization within the fibers initiated as opposed to outside the fibers amongst the other mammillary proteins? Does fiber mineralization occur first and then expand outside into the organic mammillary zone where there is less inhibition – and thus the eventual formation of single crystal calcite? Or, could it conversely be that such widespread mineralization through an amorphous phase in the mammillary zone infiltrates the outer fibers which then form unique crystalline morphology given the presence of other mineralization-regulating proteins and peptides. Careful *in vitro* study combined with high-pressure freezing and preparation for electron microscopy could be a starting point to help reveal some of these more intricate subtleties regarding the native process of biomineralization of this fiber.

Final Conclusions

Recent advances in 3D imaging (including X-ray and electron tomography approaches), image analysis, and cryo-processing techniques for tissues provide a tremendous opportunity to include critical broad and correlative context in studies of biological tissue. While additional alternative techniques with various resolving power that are used for the study of mineralized biological fiber systems can address the degree of mineralization more broadly, or even the degree and orientation of mineral nanocrystals more finely, focused ion beam preparations for SEM backscattered serial-surface-view imaging and for TEM/STEM lamella preparation are of utmost importance in assessing critical relationships between organic biological fiber systems and their inorganic mineral units at the nanoscale and in three dimensions. Despite the laborious and expensive preparation and acquisition, studies of mineralized tissues that do not offer a perspective at this scale may lack the necessary depth to fully understand normal structure-function relationships or understand the complete basis of diseases resulting in musculoskeletal malfunction. The collection of studies in this thesis offers a glimpse into what can be understood with regard to mineralized fibrous biocomposites at this scale and in three dimensions, and it also aims to motivate further studies on how organic fibrous networks interface with mineral in various tissues and organisms.

References

1.   Murshed M, Harmey D, Millan JL, McKee MD, Karsenty G. Unique coexpression in osteoblasts of broadly expressed genes accounts for the spatial restriction of ECM mineralization to bone. Genes Dev. 2005;19(9):1093-104.
2.   Reznikov N, Hoac B, Buss DJ, Addison WN, Barros NMT, McKee MD. Biological stenciling of mineralization in the skeleton: Local enzymatic removal of inhibitors in the extracellular matrix. Bone. 2020;138:115447.
3.   Traub W, Arad T, Weiner S. Origin of mineral crystal growth in collagen fibrils. Matrix. 1992;12(4):251-5.
4.   Landis WJ, Song MJ, Leith A, McEwen L, McEwen BF. Mineral and organic matrix interaction in normally calcifying tendon visualized in three dimensions by high-voltage electron microscopic tomography and graphic image reconstruction. J Struct Biol. 1993;110(1):39-54.
5.   Neuman W, Neuman M. The nature of the mineral phase of bone. Chemical Reviews. 1953;53(1):1-45.
6.   Nylen MU. Mineralization of turkey leg tendon: II. Collagen-mineral relations revealed by electron and x-ray microscopy. Calcification in biological systems. 1960:129-42.
7.   Ascenzi A, Bonucci E, Bocciarelli DS. An Electron Microscope Study of Osteon Calcification. J Ultrastruct Res. 1965;12:287-303.
8.   Landis WJ, Silver FH. The structure and function of normally mineralizing avian tendons. Comparative Biochemistry and Physiology Part A: Molecular & Integrative Physiology. 2002;133(4):1135-57.
9.   Reznikov N, Almany-Magal R, Shahar R, Weiner S. Three-dimensional imaging of collagen fibril organization in rat circumferential lamellar bone using a dual beam electron microscope reveals ordered and disordered sub-lamellar structures. Bone. 2013;52(2):676-83.
10.   Wess TJ. Collagen Fibrillar Structure and Hierarchies. In: Fratzl P, editor. Collagen: Structure and Mechanics. Boston, MA: Springer US; 2008. p. 49-80.
11.   McKee MD, Nanci A. Osteopontin: an interfacial extracellular matrix protein in mineralized tissues. Connect Tissue Res. 1996;35(1-4):197-205.
12.   Staines KA, MacRae VE, Farquharson C. The importance of the SIBLING family of proteins on skeletal mineralisation and bone remodelling. J Endocrinol. 2012;214(3):241-55.
13.   Hulmes DJS. Collagen Diversity, Synthesis and Assembly. In: Fratzl P, editor. Collagen: Structure and Mechanics. Boston, MA: Springer US; 2008. p. 15-47.
14.   Cook KM, Hogg PJ. Post-Translational Control of Protein Function by Disulfide Bond Cleavage. Antioxidants & Redox Signaling. 2012;18(15):1987-2015.
15.   Neville AC. Biology of Fibrous Composites: Development beyond the Cell Membrane. Cambridge: Cambridge University Press; 1993.
16.   Moussian B. Chitin: Structure, Chemistry and Biology. Adv Exp Med Biol. 2019;1142:5-18.
17.   Taylor NG. Cellulose biosynthesis and deposition in higher plants. New Phytologist. 2008;178(2):239-52.
18.   Eder M, Schäffner W, Burgert I, Fratzl P. Wood and the Activity of Dead Tissue. Advanced Materials. 2021;33(28):2001412.
19.   Gibson LJ. The hierarchical structure and mechanics of plant materials. J R Soc Interface. 2012;9(76):2749-66.

20.   Veis A. Mineral-matrix interactions in bone and dentin. J Bone Miner Res. 1993;8 Suppl 2:S493-7.
21.   Berendsen AD, Olsen BR. Bone development. Bone. 2015;80:14-8.
22.   Karsenty G. Chondrogenesis just ain't what it used to be. J Clin Invest. 2001;107(4):405-7.
23.   Hall BK. Cellular interactions during cartilage and bone development. J Craniofac Genet Dev Biol. 1991;11(4):238-50.
24.   Boskey AL. Mineral-matrix interactions in bone and cartilage. Clin Orthop Relat Res. 1992(281):244-74.
25.   Buenzli PR, Sims NA. Quantifying the osteocyte network in the human skeleton. Bone. 2015;75:144-50.
26.   Dallas SL, Bonewald LF. Dynamics of the transition from osteoblast to osteocyte. Ann N Y Acad Sci. 2010;1192:437-43.
27.   Buss DJ, Reznikov N, McKee MD. Crossfibrillar mineral tessellation in normal and Hyp mouse bone as revealed by 3D FIB-SEM microscopy. J Struct Biol. 2020:107603.
28.   Bonivtch AR, Bonewald LF, Nicolella DP. Tissue strain amplification at the osteocyte lacuna: a microstructural finite element analysis. J Biomech. 2007;40(10):2199-206.
29.   Bonewald LF, Johnson ML. Osteocytes, mechanosensing and Wnt signaling. Bone. 2008;42(4):606-15.
30.   Mikolajewicz N, Zimmermann EA, Willie BM, Komarova SV. Mechanically stimulated ATP release from murine bone cells is regulated by a balance of injury and repair. Elife. 2018;7.
31.   Henriksen K, Neutzsky-Wulff AV, Bonewald LF, Karsdal MA. Local communication on and within bone controls bone remodeling. Bone. 2009;44(6):1026-33.
32.   Robling AG, Bonewald LF. The Osteocyte: New Insights. Annu Rev Physiol. 2020;82:485-506.
33.   Boyce BF, Xing L. Functions of RANKL/RANK/OPG in bone modeling and remodeling. Arch Biochem Biophys. 2008;473(2):139-46.
34.   Bonewald LF. The amazing osteocyte. Journal of Bone and Mineral Research. 2011;26(2):229-38.
35.   Reznikov N, Phillips C, Cooke M, Garbout A, Ahmed F, Stevens MM. Functional Adaptation of the Calcaneus in Historical Foot Binding. J Bone Miner Res. 2017;32(9):1915-25.
36.   Almany Magal R, Reznikov N, Shahar R, Weiner S. Three-dimensional structure of minipig fibrolamellar bone: adaptation to axial loading. J Struct Biol. 2014;186(2):253-64.
37.   Wolff J. Das gestetz der transformation der knochem. Verlag von August Hirschwald. 1892.
38.   Biewener AA, Fazzalari NL, Konieczynski DD, Baudinette RV. Adaptive changes in trabecular architecture in relation to functional strain patterns and disuse. Bone. 1996;19(1):1-8.
39.   Felsenthal N, Rubin S, Stern T, Krief S, Pal D, Pryce BA, et al. Development of migrating tendon-bone attachments involves replacement of progenitor populations. Development. 2018;145(24).
40.   Zelzer E, Blitz E, Killian ML, Thomopoulos S. Tendon-to-bone attachment: from development to maturity. Birth Defects Res C Embryo Today. 2014;102(1):101-12.
41.   Blitz E, Sharir A, Akiyama H, Zelzer E. Tendon-bone attachment unit is formed modularly by a distinct pool of Scx- and Sox9-positive progenitors. Development. 2013;140(13):2680-90.

42.   Apostolakos J, Durant TJ, Dwyer CR, Russell RP, Weinreb JH, Alaee F, et al. The enthesis: a review of the tendon-to-bone insertion. Muscles Ligaments Tendons J. 2014;4(3):333-42.

43.   Rufai A, Ralphs JR, Benjamin M. Ultrastructure of fibrocartilages at the insertion of the rat Achilles tendon. J Anat. 1996;189 (Pt 1):185-91.

44.   Rufai A, Ralphs JR, Benjamin M. Structure and histopathology of the insertional region of the human Achilles tendon. J Orthop Res. 1995;13(4):585-93.

45.   Patel S, Caldwell JM, Doty SB, Levine WN, Rodeo S, Soslowsky LJ, et al. Integrating soft and hard tissues via interface tissue engineering. J Orthop Res. 2018;36(4):1069-77.

46.   Bloebaum RD, Kopp DV. Remodeling capacity of calcified fibrocartilage of the hip. Anat Rec A Discov Mol Cell Evol Biol. 2004;279(2):736-9.

47.   Myllyharju J. Intracellular Post-Translational Modifications of Collagens. In: Brinckmann J, Notbohm H, Müller PK, editors. Collagen: Primer in Structure, Processing and Assembly. Berlin, Heidelberg: Springer Berlin Heidelberg; 2005. p. 115-47.

48.   Canty EG, Kadler KE. Procollagen trafficking, processing and fibrillogenesis. J Cell Sci. 2005;118(Pt 7):1341-53.

49.   Fratzl P. Collagen: Structure and Mechanics: Springer US; 2008.

50.   Avery NC, Bailey AJ. Restraining Cross-Links Responsible for the Mechanical Properties of Collagen Fibers: Natural and Artificial. In: Fratzl P, editor. Collagen: Structure and Mechanics. Boston, MA: Springer US; 2008. p. 81-110.

51.   Hodge AJ. Recent studies with the electron microscope on ordered aggregates of the tropocollagen molecules. Aspects of protein structure. 1963:289-300.

52.   Orgel JP, Antipova O, Sagi I, Bitler A, Qiu D, Wang R, et al. Collagen fibril surface displays a constellation of sites capable of promoting fibril assembly, stability, and hemostasis. Connect Tissue Res. 2011;52(1):18-24.

53.   Orgel JP, Irving TC, Miller A, Wess TJ. Microfibrillar structure of type I collagen in situ. Proceedings of the National Academy of Sciences. 2006;103(24):9001-5.

54.   Reznikov N, Bilton M, Lari L, Stevens MM, Kroger R. Fractal-like hierarchical organization of bone begins at the nanoscale. Science. 2018;360(6388).

55.   Reznikov N, Shahar R, Weiner S. Bone hierarchical structure in three dimensions. Acta Biomater. 2014;10(9):3815-26.

56.   Burgert I, Fratzl P. Plants control the properties and actuation of their organs through the orientation of cellulose fibrils in their cell walls. Integrative and Comparative Biology. 2009;49(1):69-79.

57.   Meek KM, Knupp C. Corneal structure and transparency. Prog Retin Eye Res. 2015;49:1-16.

58.   Trelstad RL, Coulombre AJ. Morphogenesis of the collagenous stroma in the chick cornea. J Cell Biol. 1971;50(3):840-58.

59.   Mathew JH, Goosey JD, Söderberg PG, Bergmanson JPG. Lamellar changes in the keratoconic cornea. Acta Ophthalmologica. 2015;93(8):767-73.

60.   Linsenmayer TF, Fitch JM, Gordon MK, Cai CX, Igoe F, Marchant JK, et al. Development and roles of collagenous matrices in the embryonic avian cornea. Prog Retin Eye Res. 1998;17(2):231-65.

61.   Giraud-Guille M-M. Liquid crystallinity in condensed type I collagen solutions: A clue to the packing of collagen in extracellular matrices. Journal of Molecular Biology. 1992;224(3):861-73.

62.   Arias JL, Fernandez MS, Dennis JE, Caplan AI. Collagens of the chicken eggshell membranes. Connect Tissue Res. 1991;26(1-2):37-45.

63.   Leach RM. Biochemistry of the Organic Matrix of the Eggshell1. Poultry Science. 1982;61(10):2040-7.

64.   Ahmed TA, Suso HP, Hincke MT. In-depth comparative analysis of the chicken eggshell membrane proteome. J Proteomics. 2017;155:49-62.

65.   Romanoff AL, Romanoff AJ. The Avian Egg: J. Wiley; 1949.

66.   Hincke MT, Nys Y, Gautron J, Mann K, Rodriguez-Navarro AB, McKee MD. The eggshell: structure, composition and mineralization. Front Biosci (Landmark Ed). 2012;17:1266-80.

67.   McKee TJ, Perlman G, Morris M, Komarova SV. Extracellular matrix composition of connective tissues: a systematic review and meta-analysis. Sci Rep. 2019;9(1):10542.

68.   Boskey AL. Bone composition: relationship to bone fragility and antiosteoporotic drug effects. Bonekey Rep. 2013;2:447.

69.   McKee MD, Nanci A. Osteopontin and the bone remodeling sequence. Colloidal-gold immunocytochemistry of an interfacial extracellular matrix protein. Ann N Y Acad Sci. 1995;760:177-89.

70.   Kawasaki K, Suzuki T, Weiss KM. Genetic basis for the evolution of vertebrate mineralized tissue. Proceedings of the National Academy of Sciences. 2004;101(31):11356-61.

71.   McKee M, Nanci A. Osteopontin at mineralized tissue interfaces in bone, teeth, and osseointegrated implants: ultrastructural distribution and implications for mineralized tissue formation, turnover, and repair. Microscopy research and technique. 1996;33(2):141-64.

72.   Bianco P, Fisher LW, Young MF, Termine JD, Robey PG. Expression and localization of the two small proteoglycans biglycan and decorin in developing human skeletal and non-skeletal tissues. Journal of Histochemistry & Cytochemistry. 1990;38(11):1549-63.

73.   During A, Penel G, Hardouin P. Understanding the local actions of lipids in bone physiology. Progress in Lipid Research. 2015;59:126-46.

74.   Sartori J, Stark H. Tracking tendon fibers to their insertion - a 3D analysis of the Achilles tendon enthesis in mice. Acta Biomater. 2020.

75.   Pękala PA, Henry BM, Ochała A, Kopacz P, Tatoń G, Młyniec A, et al. The twisted structure of the Achilles tendon unraveled: A detailed quantitative and qualitative anatomical investigation. Scandinavian Journal of Medicine & Science in Sports. 2017;27(12):1705-15.

76.   Biewener AA, Roberts TJ. Muscle and tendon contributions to force, work, and elastic energy savings: a comparative perspective. Exerc Sport Sci Rev. 2000;28(3):99-107.

77.   Freedman BR, Gordon JA, Soslowsky LJ. The Achilles tendon: fundamental properties and mechanisms governing healing. Muscles Ligaments Tendons J. 2014;4(2):245-55.

78.   Zou Z, Tang T, Macias-Sanchez E, Sviben S, Landis WJ, Bertinetti L, et al. Three-dimensional structural interrelations between cells, extracellular matrix, and mineral in normally mineralizing avian leg tendon. Proc Natl Acad Sci U S A. 2020;117(25):14102-9.

79.   Ameye L, Aria D, Jepsen K, Oldberg A, Xu T, Young MF. Abnormal collagen fibrils in tendons of biglycan/fibromodulin-deficient mice lead to gait impairment, ectopic ossification, and osteoarthritis. FASEB J. 2002;16(7):673-80.

80.   Kjær M, Magnusson SP. Mechanical Adaptation and Tissue Remodeling. In: Fratzl P, editor. Collagen: Structure and Mechanics. Boston, MA: Springer US; 2008. p. 249-67.

81.   Thomopoulos S, Birman V, Genin G. The Challenge of Attaching Dissimilar Materials in Structural Interfaces and Attachments in Biology. 1 ed. New York: Springer; 2013. p. 3-17.

82. Naveh GRS, Foster JE, Silva Santisteban TM, Yang X, Olsen BR. Nonuniformity in ligaments is a structural strategy for optimizing functionality. Proc Natl Acad Sci U S A. 2018;115(36):9008-13.

83. Golman M, Abraham AC, Kurtaliaj I, Marshall BP, Hu YJ, Schwartz AG, et al. Toughening mechanisms for the attachment of architectured materials: The mechanics of the tendon enthesis. Sci Adv. 2021;7(48):eabi5584.

84. Marinovich R, Soenjaya Y, Wallace GQ, Zuskov A, Dunkman A, Foster BL, et al. The role of bone sialoprotein in the tendon-bone insertion. Matrix Biol. 2016;52-54:325-38.

85. Rossetti L, Kuntz LA, Kunold E, Schock J, Muller KW, Grabmayr H, et al. The microstructure and micromechanics of the tendon-bone insertion. Nat Mater. 2017;16(6):664-70.

86. Hincke MT, Gautron J, Panheleux M, Garcia-Ruiz J, McKee MD, Nys Y. Identification and localization of lysozyme as a component of eggshell membranes and eggshell matrix. Matrix Biol. 2000;19(5):443-53.

87. Lifshitz A, Baker R, Naylor H. The relative importance of chicken egg exterior structures in resisting bacterial penetration. Journal of Food Science. 1964;29(1):94-9.

88. Nys Y, Gautron J, Garcia-Ruiz JM, Hincke MT. Avian eggshell mineralization: biochemical and functional characterization of matrix proteins. Comptes Rendus Palevol. 2004;3(6):549-62.

89. Rodriguez-Navarro AB, Marie P, Nys Y, Hincke MT, Gautron J. Amorphous calcium carbonate controls avian eggshell mineralization: A new paradigm for understanding rapid eggshell calcification. J Struct Biol. 2015;190(3):291-303.

90. Weiner S, Sagi I, Addadi L. Structural biology. Choosing the crystallization path less traveled. Science. 2005;309(5737):1027-8.

91. Termine JD, Posner AS. Amorphous/crystalline interrelationships in bone mineral. Calcif Tissue Res. 1967;1(1):8-23.

92. Weiner S. Biomineralization: a structural perspective. J Struct Biol. 2008;163(3):229-34.

93. Addadi L, Weiner S. Interactions between acidic proteins and crystals: stereochemical requirements in biomineralization. Proc Natl Acad Sci U S A. 1985;82(12):4110-4.

94. Midura RJ, Vasanji A, Su X, Midura SB, Gorski JP. Isolation of calcospherulites from the mineralization front of bone. Cells Tissues Organs. 2009;189(1-4):75-9.

95. Boyde A. Electron microscopy of the mineralizing front. Metab Bone Dis Rel Res. 1980;2:69-78.

96. Steendijk R, Boyde A. Scanning electron microscopic observations on bone from patients with hypophosphataemic (vitamin D resistant) rickets. Calcif Tissue Res. 1973;11(3):242-50.

97. Ayoubi M, van Tol AF, Weinkamer R, Roschger P, Brugger PC, Berzlanovich A, et al. 3D Interrelationship between Osteocyte Network and Forming Mineral during Human Bone Remodeling. Adv Healthc Mater. 2021;10(12):e2100113.

98. Fernandez-Moran H, Engström A. Electron microscopy and X-ray diffraction of bone. Biochimica et biophysica acta. 1957;23:260-4.

99. Imel EA. Enthesopathy, Osteoarthritis, and Mobility in X-linked Hypophosphatemia. J Clin Endocrinol Metab. 2020;105(7).

100. Parashar A, Gourgas O, Lau K, Li J, Muiznieks L, Sharpe S, et al. Elastin calcification in in vitro models and its prevention by MGP's m3pS peptide. J Struct Biol. 2020:107637.

101. Towler OW, Shore EM. BMP signaling and skeletal development in fibrodysplasia ossificans progressiva (FOP). Dev Dyn. 2022;251(1):164-77.

102.   Luo G, Ducy P, McKee MD, Pinero GJ, Loyer E, Behringer RR, et al. Spontaneous calcification of arteries and cartilage in mice lacking matrix GLA protein. Nature. 1997;386(6620):78-81.
103.   Exposito J-Y, Larroux C, Cluzel C, Valcourt U, Lethias C, Degnan BM. Demosponge and Sea Anemone Fibrillar Collagen Diversity Reveals the Early Emergence of A/C Clades and the Maintenance of the Modular Structure of Type V/XI Collagens from Sponge to Human*. Journal of Biological Chemistry. 2008;283(42):28226-35.
104.   Kawasaki K, Weiss KM. Genetic Basis for the Evolution of Vertebrate Mineralized Tissue. Handbook of Biomineralization2007. p. 330-47.
105.   Neuman W. Mechanism of calcification: role of collagen polyphosphates and phosphatascs. Amer J Physiol.200.
106.   Hendricks SB, Hill WL. The Inorganic Constitution of Bone. Science. 1942;96(2489):255-7.
107.   Millan JL, Whyte MP. Alkaline Phosphatase and Hypophosphatasia. Calcif Tissue Int. 2016;98(4):398-416.
108.   Murshed M. Mechanism of Bone Mineralization. Cold Spring Harb Perspect Med. 2018;8(12).
109.   Schäfer C, Jahnen-Dechent W. The Biological and Cellular Role of Fetuin Family Proteins in Biomineralization. Handbook of Biomineralization2007. p. 317-28.
110.   Fleisch H, Bisaz S. Mechanism of calcification: inhibitory role of pyrophosphate. Nature. 1962;195:911.
111.   Karaplis AC, Bai X, Falet JP, Macica CM. Mineralizing enthesopathy is a common feature of renal phosphate-wasting disorders attributed to FGF23 and is exacerbated by standard therapy in hyp mice. Endocrinology. 2012;153(12):5906-17.
112.   Hasegawa T. Ultrastructure and biological function of matrix vesicles in bone mineralization. Histochem Cell Biol. 2018;149(4):289-304.
113.   Lacruz RS. Enamel: Molecular identity of its transepithelial ion transport system. Cell Calcium. 2017;65:1-7.
114.   Fisher L, Torchia D, Fohr B, Young M, Fedarko N. Flexible structures of SIBLING proteins, bone sialoprotein, and osteopontin. Biochemical and biophysical research communications. 2001;280(2):460-5.
115.   Xu Z, Yang Y, Zhao W, Wang Z, Landis WJ, Cui Q, et al. Molecular mechanisms for intrafibrillar collagen mineralization in skeletal tissues. Biomaterials. 2015;39:59-66.
116.   Xu Y, Nudelman F, Eren ED, Wirix MJM, Cantaert B, Nijhuis WH, et al. Intermolecular channels direct crystal orientation in mineralized collagen. Nat Commun. 2020;11(1):5068.
117.   Silver FH, Landis WJ. Deposition of apatite in mineralizing vertebrate extracellular matrices: A model of possible nucleation sites on type I collagen. Connect Tissue Res. 2011;52(3):242-54.
118.   Orgel JP, Miller A, Irving TC, Fischetti RF, Hammersley AP, Wess TJ. The in situ supermolecular structure of type I collagen. Structure. 2001;9(11):1061-9.
119.   Gautron J, Stapane L, Le Roy N, Nys Y, Rodriguez-Navarro AB, Hincke MT. Avian eggshell biomineralization: an update on its structure, mineralogy and protein tool kit. BMC Mol Cell Biol. 2021;22(1):11.
120.   Li N, Niu LN, Qi YP, Yiu CK, Ryou H, Arola DD, et al. Subtleties of biomineralisation revealed by manipulation of the eggshell membrane. Biomaterials. 2011;32(34):8743-52.

121.   Athanasiadou D, Jiang W, Goldbaum D, Saleem A, Basu K, Pacella MS, et al. Nanostructure, osteopontin, and mechanical properties of calcitic avian eggshell. Science Advances. 2018;4(3):eaar3219.

122.   Hoac B, Ostergaard M, Wittig NK, Boukpessi T, Buss DJ, Chaussain C, et al. Genetic Ablation of Osteopontin in Osteomalacic Hyp Mice Partially Rescues the Deficient Mineralization Without Correcting Hypophosphatemia. J Bone Miner Res. 2020.

123.   Boukpessi T, Hoac B, Coyac BR, Leger T, Garcia C, Wicart P, et al. Osteopontin and the dento-osseous pathobiology of X-linked hypophosphatemia. Bone. 2017;95:151-61.

124.   Klosowski MM, Carzaniga R, Abellan P, Ramasse Q, McComb DW, Porter AE, et al. Electron Microscopy Reveals Structural and Chemical Changes at the Nanometer Scale in the Osteogenesis Imperfecta Murine Pathology. ACS Biomater Sci Eng. 2017;3(11):2788-97.

125.   Fratzl-Zelman N, Schmidt I, Roschger P, Roschger A, Glorieux FH, Klaushofer K, et al. Unique micro- and nano-scale mineralization pattern of human osteogenesis imperfecta type VI bone. Bone. 2015;73:233-41.

126.   Rauch F. Material matters: a mechanostat-based perspective on bone development in osteogenesis imperfecta and hypophosphatemic rickets. J Musculoskelet Neuronal Interact. 2006;6(2):142-6.

127.   Gohil A, Imel EA. FGF23 and Associated Disorders of Phosphate Wasting. Pediatr Endocrinol Rev. 2019;17(1):17-34.

128.   Wysolmerski JJ. Parathyroid hormone-related protein: an update. J Clin Endocrinol Metab. 2012;97(9):2947-56.

129.   Matikainen N, Pekkarinen T, Ryhänen EM, Schalin-Jäntti C. Physiology of Calcium Homeostasis: An Overview. Endocrinol Metab Clin North Am. 2021;50(4):575-90.

130.   Torres PAU, De Brauwere DP. Three feedback loops precisely regulating serum phosphate concentration. Kidney International. 2011;80(5):443-5.

131.   Kinoshita S, Kawai M. The FGF23/KLOTHO regulatory network and its roles in human disorders. Vitamins & Hormones. 2016;101:151-74.

132.   Erben RG. Physiological Actions of Fibroblast Growth Factor-23. Front Endocrinol (Lausanne). 2018;9:267.

133.   Blau JE, Collins MT. The PTH-Vitamin D-FGF23 axis. Rev Endocr Metab Disord. 2015;16(2):165-74.

134.   Beck-Nielsen SS, Mughal Z, Haffner D, Nilsson O, Levtchenko E, Ariceta G, et al. FGF23 and its role in X-linked hypophosphatemia-related morbidity. Orphanet J Rare Dis. 2019;14(1):58.

135.   Beck L, Soumounou Y, Martel J, Krishnamurthy G, Gauthier C, Goodyer CG, et al. Pex/PEX tissue distribution and evidence for a deletion in the 3' region of the Pex gene in X-linked hypophosphatemic mice. J Clin Invest. 1997;99(6):1200-9.

136.   Barros NM, Hoac B, Neves RL, Addison WN, Assis DM, Murshed M, et al. Proteolytic processing of osteopontin by PHEX and accumulation of osteopontin fragments in Hyp mouse bone, the murine model of X-linked hypophosphatemia. J Bone Miner Res. 2013;28(3):688-99.

137.   Strom TM, Francis F, Lorenz B, Boddrich A, Econs MJ, Lehrach H, et al. Pex gene deletions in Gy and Hyp mice provide mouse models for X-linked hypophosphatemia. Hum Mol Genet. 1997;6(2):165-71.

138.   Heymann JA, Hayles M, Gestmann I, Giannuzzi LA, Lich B, Subramaniam S. Site-specific 3D imaging of cells and tissues with a dual beam microscope. J Struct Biol. 2006;155(1):63-73.

139.   Narayan K, Subramaniam S. Focused ion beams in biology. Nat Methods. 2015;12(11):1021-31.

140.   Xu CS, Hayworth KJ, Lu Z, Grob P, Hassan AM, García-Cerdán JG, et al. Enhanced FIB-SEM systems for large-volume 3D imaging. eLife. 2017;6:e25916.

141.   Seligman AM, Wasserkrug HL, Hanker JS. A new staining method (OTO) for enhancing contrast of lipid--containing membranes and droplets in osmium tetroxide--fixed tissue with osmiophilic thiocarbohydrazide(TCH). J Cell Biol. 1966;30(2):424-32.

142.   Chissoe WF, Vezey EL, Skvarla JJ. The Use of Osmium-Thiocarbohydrazide for Structural Stabilization and Enhancement of Secondary Electron Images in Scanning Electron Microscopy of Pollen. Grana. 1995;34(5):317-24.

143.   Reznikov N, Buss DJ, Provencher B, McKee MD, Piche N. Deep learning for 3D imaging and image analysis in biomineralization research. J Struct Biol. 2020:107598.

144.   Reznikov N, Steele JAM, Fratzl P, Stevens MM. A materials science vision of extracellular matrix mineralization. Nature Reviews Materials. 2016;1(8).

145.   Addison WN, Azari F, Sorensen ES, Kaartinen MT, McKee MD. Pyrophosphate inhibits mineralization of osteoblast cultures by binding to mineral, up-regulating osteopontin, and inhibiting alkaline phosphatase activity. J Biol Chem. 2007;282(21):15872-83.

146.   Roberts F, Zhu D, Farquharson C, Macrae VE. ENPP1 in the Regulation of Mineralization and Beyond. Trends Biochem Sci. 2019;44(7):616-28.

147.   Orriss IR. Extracellular pyrophosphate: The body's "water softener". Bone. 2020:115243.

148.   Brylka L, Jahnen-Dechent W. The role of fetuin-A in physiological and pathological mineralization. Calcif Tissue Int. 2013;93(4):355-64.

149.   Reznikov N, Hoac B, Buss D, Addison W, Barros N, McKee M. Biological stenciling of mineralization in the skeleton: Local enzymatic removal of inhibitors in the extracellular matrix. Bone. 2020.

150.   Robey P.G. BAL. Extracellular Matrix and Biomineralization of Bone. Primer on the Metabolic Bone Diseases and Disorders of Mineral Metabolism American Society of Bone and Mineral Research 2003. p. 38-46.

151.   Addison WN, Masica DL, Gray JJ, McKee MD. Phosphorylation-dependent inhibition of mineralization by osteopontin ASARM peptides is regulated by PHEX cleavage. J Bone Miner Res. 2010;25(4):695-705.

152.   Hoac B, Nelea V, Jiang W, Kaartinen MT, McKee MD. Mineralization-inhibiting effects of transglutaminase-crosslinked polymeric osteopontin. Bone. 2017;101:37-48.

153.   Yuan Q, Jiang Y, Zhao X, Sato T, Densmore M, Schuler C, et al. Increased osteopontin contributes to inhibition of bone mineralization in FGF23-deficient mice. J Bone Miner Res. 2014;29(3):693-704.

154.   Sorensen ES, Hojrup P, Petersen TE. Posttranslational modifications of bovine osteopontin: identification of twenty-eight phosphorylation and three O-glycosylation sites. Protein Sci. 1995;4(10):2040-9.

155.   Narisawa S, Yadav MC, Millan JL. In vivo overexpression of tissue-nonspecific alkaline phosphatase increases skeletal mineralization and affects the phosphorylation status of osteopontin. J Bone Miner Res. 2013;28(7):1587-98.

156.   McKee MD, Nanci A. Osteopontin at mineralized tissue interfaces in bone, teeth, and osseointegrated implants: ultrastructural distribution and implications for mineralized tissue formation, turnover, and repair. Microsc Res Tech. 1996;33(2):141-64.

157. Scherft JP. The lamina limitans of the organic matrix of calcified cartilage and bone. J Ultrastruct Res. 1972;38(3):318-31.
158. Currey JD. The Mechanical Adaptations of Bones. Princeton, New Jersey: Princeton University Press; 1984.
159. Marino AA, Becker RO, Bachman CH. Dielectric determination of bound water of bone. Phys Med Biol. 1967;12(3):367-78.
160. Timmins PA, Wall JC. Bone water. Calcif Tissue Res. 1977;23(1):1-5.
161. Turov VV, Gun'ko VM, Zarko VI, Leboda R, Jablonski M, Gorzelak M, et al. Weakly and strongly associated nonfreezable water bound in bones. Colloids Surf B Biointerfaces. 2006;48(2):167-75.
162. Nylen MU, Scott DB, M. MV. Mineralization of turkey leg tendon. II. Collagen-mineral relations revealed by electron and X-ray microscopy. . 1960.
163. Weiner S, Traub W. Organization of hydroxyapatite crystals within collagen fibrils. FEBS Lett. 1986;206(2):262-6.
164. Kim D, Lee B, Thomopoulos S, Jun YS. The role of confined collagen geometry in decreasing nucleation energy barriers to intrafibrillar mineralization. Nat Commun. 2018;9(1):962.
165. Landis WJ, Jacquet R. Association of calcium and phosphate ions with collagen in the mineralization of vertebrate tissues. Calcif Tissue Int. 2013;93(4):329-37.
166. McNally EA, Schwarcz HP, Botton GA, Arsenault AL. A model for the ultrastructure of bone based on electron microscopy of ion-milled sections. PLoS One. 2012;7(1):e29258.
167. Boyde A, Jones S. Aspects of Anatomy and Development of Bone. Advances in Organ Biology. 1998;5A:3-44.
168. Schwarcz HP. The ultrastructure of bone as revealed in electron microscopy of ion-milled sections. Semin Cell Dev Biol. 2015;46:44-50.
169. Hu YY, Rawal A, Schmidt-Rohr K. Strongly bound citrate stabilizes the apatite nanocrystals in bone. Proc Natl Acad Sci U S A. 2010;107(52):22425-9.
170. Wang Y, Von Euw S, Fernandes FM, Cassaignon S, Selmane M, Laurent G, et al. Water-mediated structuring of bone apatite. Nat Mater. 2013;12(12):1144-53.
171. Bocciarelli DS. Morphology of crystallites in bone. Calcif Tissue Res. 1970;5(3):261-9.
172. You L, Cowin SC, Schaffler MB, Weinbaum S. A model for strain amplification in the actin cytoskeleton of osteocytes due to fluid drag on pericellular matrix. J Biomech. 2001;34(11):1375-86.
173. Santos A, Bakker AD, Klein-Nulend J. The role of osteocytes in bone mechanotransduction. Osteoporos Int. 2009;20(6):1027-31.
174. McKee MD, Hoac B, Addison WN, Barros NM, Millan JL, Chaussain C. Extracellular matrix mineralization in periodontal tissues: Noncollagenous matrix proteins, enzymes, and relationship to hypophosphatasia and X-linked hypophosphatemia. Periodontol 2000. 2013;63(1):102-22.
175. Addison WN, Nakano Y, Loisel T, Crine P, McKee MD. MEPE-ASARM peptides control extracellular matrix mineralization by binding to hydroxyapatite: an inhibition regulated by PHEX cleavage of ASARM. J Bone Miner Res. 2008;23(10):1638-49.
176. Malick LE, Wilson RB. Modified thiocarbohydrazide procedure for scanning electron microscopy: routine use for normal, pathological, or experimental tissues. Stain Technol. 1975;50(4):265-9.

177.   Reznikov N, Buss D, Provencher B, McKee M, Piche N. Deep learning and 3D imaging in structural biology. Journal of Structural Biology. 2020.
178.   Ohata Y, Ozono K. [Updates on rickets and osteomalacia: guidelines for diagnosis of rickets and osteomalacia]. Clin Calcium. 2013;23(10):1421-8.
179.   Eicher EM, Southard JL, Scriver CR, Glorieux FH. Hypophosphatemia: mouse model for human familial hypophosphatemic (vitamin D-resistant) rickets. Proc Natl Acad Sci U S A. 1976;73(12):4667-71.
180.   McKee MD, Nanci A. Postembedding colloidal-gold immunocytochemistry of noncollagenous extracellular matrix proteins in mineralized tissues. Microsc Res Tech. 1995;31(1):44-62.
181.   Bonucci E, Silvestrini G, Di Grezia R. The ultrastructure of the organic phase associated with the inorganic substance in calcified tissues. Clin Orthop Relat Res. 1988(233):243-61.
182.   Tang T, Wagermaier W, Schuetz R, Wang Q, Eltit F, Fratzl P, et al. Hypermineralization in the femoral neck of the elderly. Acta Biomater. 2019;89:330-42.
183.   Carpenter TO, Shaw NJ, Portale AA, Ward LM, Abrams SA, Pettifor JM. Rickets. Nat Rev Dis Primers. 2017;3:17101.
184.   Zhang C, Zhao Z, Sun Y, Xu L, JiaJue R, Cui L, et al. Clinical and genetic analysis in a large Chinese cohort of patients with X-linked hypophosphatemia. Bone. 2019;121:212-20.
185.   Shanbhogue VV, Hansen S, Folkestad L, Brixen K, Beck-Nielsen SS. Bone geometry, volumetric density, microarchitecture, and estimated bone strength assessed by HR-pQCT in adult patients with hypophosphatemic rickets. J Bone Miner Res. 2015;30(1):176-83.
186.   McKee MD, Nanci A, Landis WJ, Gotoh Y, Gerstenfeld LC, Glimcher MJ. Developmental appearance and ultrastructural immunolocalization of a major 66 kDa phosphoprotein in embryonic and post-natal chicken bone. Anat Rec. 1990;228(1):77-92.
187.   Finean JB, Engstrom A. The low-angle scatter of x-rays from bone tissue. Biochim Biophys Acta. 1953;11(2):178-89.
188.   Beck GR, Jr., Zerler B, Moran E. Phosphate is a specific signal for induction of osteopontin gene expression. Proc Natl Acad Sci U S A. 2000;97(15):8352-7.
189.   Fatherazi S, Matsa-Dunn D, Foster BL, Rutherford RB, Somerman MJ, Presland RB. Phosphate regulates osteopontin gene transcription. J Dent Res. 2009;88(1):39-44.
190.   Bertazzo S, Bertran, C.A., Camilli, J.A. . Morphological Characterization of Femur and Parietal Bone Mineral of Rats at Different Ages. Key Engineering Materials. 2005:309-11.
191.   Midura RJ, Vasanji A, Su X, Wang A, Midura SB, Gorski JP. Calcospherulites isolated from the mineralization front of bone induce the mineralization of type I collagen. Bone. 2007;41(6):1005-16.
192.   Grandfield K, Vuong V, Schwarcz HP. Ultrastructure of Bone: Hierarchical Features from Nanometer to Micrometer Scale Revealed in Focused Ion Beam Sections in the TEM. Calcif Tissue Int. 2018;103(6):606-16.
193.   Shah FAR, K. Palmquist, A. . Transformation of bone mineral morphology: From discrete marquise-shaped motifs to a continuous interwoven mesh. Bone Reports. 2020.
194.   Reznikov N, Shahar R, Weiner S. Three-dimensional structure of human lamellar bone: the presence of two different materials and new insights into the hierarchical organization. Bone. 2014;59:93-104.
195.   Dallas SL, Prideaux M, Bonewald LF. The osteocyte: an endocrine cell ... and more. Endocr Rev. 2013;34(5):658-90.

196.   Kaya S, Basta-Pljakic J, Seref-Ferlengez Z, Majeska RJ, Cardoso L, Bromage TG, et al. Lactation-Induced Changes in the Volume of Osteocyte Lacunar-Canalicular Space Alter Mechanical Properties in Cortical Bone Tissue. J Bone Miner Res. 2017;32(4):688-97.

197.   Hasegawa T, Yamamoto T, Hongo H, Qiu Z, Abe M, Kanesaki T, et al. Three-dimensional ultrastructure of osteocytes assessed by focused ion beam-scanning electron microscopy (FIB-SEM). Histochem Cell Biol. 2018;149(4):423-32.

198.   Boyde A, Hobdell MH. Scanning electron microscopy of primary membrane bone. Z Zellforsch Mikrosk Anat. 1969;99(1):98-108.

199.   Currey JD. Bones : structure and mechanics. Princeton, New Jersey ;: Princeton University Press; 2002. Available from: https://doi.org/10.1515/9781400849505

200.   Dean MN, Mull CG, Gorb SN, Summers AP. Ontogeny of the tessellated skeleton: insight from the skeletal growth of the round stingray Urobatis halleri. J Anat. 2009;215(3):227-39.

201.   Fratzl P, Kolednik O, Fischer FD, Dean MN. The mechanics of tessellations - bioinspired strategies for fracture resistance. Chem Soc Rev. 2016;45(2):252-67.

202.   Achrai B, Wagner HD. The turtle carapace as an optimized multi-scale biological composite armor - A review. J Mech Behav Biomed Mater. 2017;73:50-67.

203.   Chen IH, Kiang JH, Correa V, Lopez MI, Chen PY, McKittrick J, et al. Armadillo armor: mechanical testing and micro-structural evaluation. J Mech Behav Biomed Mater. 2011;4(5):713-22.

204.   Yin Z, Hannard F, Barthelat F. Impact-resistant nacre-like transparent materials. Science. 2019;364(6447):1260-3.

205.   Gao C, Hasseldine BPJ, Li L, Weaver JC, Li Y. Amplifying Strength, Toughness, and Auxeticity via Wavy Sutural Tessellation in Plant Seedcoats. Adv Mater. 2018:e1800579.

206.   Bar-On B, Wagner HD. The emergence of an unusual stiffness profile in hierarchical biological tissues. Acta Biomater. 2013;9(9):8099-109.

207.   Thompson DAW. On Growth and Form1917.

208.   Pettigrew JB. Design in nature as illustrated by spiral and other arrangements in the inorganic and organic kingdoms as exemplified in matter, force, life, growth, &c., especially in crystals, plants, and animals. : Longman, Green, and co., 1908.

209.   Gardner D. James Bell Pettigrew (1832–1908) MD, LLD, FRS, comparative anatomist, physiologist and aerobiologist. Journal of Medical Biography. 2017;25(3):169-78.

210.   Thompson DW. On Growth and Form. 2nd ed. Cambridge: Cambridge University Press; 1942. 1116 p.

211.   Stolpe M, Zimmer K. Der Schwirrflug des Kolibri im Zeitlupenfilm. J Ornithol. 1939;87:136-55.

212.   Cook TA. The Curves of Life Being an Account of Spiral Formations and Their Application to Growth in Nature, to Science and to Art, With Special Reference to the Manuscripts of Leonardo Da Vinci. London: Constable and Company Ltd.; 1914.

213.   Gambaryan PP, Kielan-Jaworowska Z. Sprawling versus parasagittal stance in multituberculate mammals. Acta Palaeontologica Polonica. 1997;42(1):13-44.

214.   Hert J, Fiala P, Petrtyl M. Osteon orientation of the diaphysis of the long bones in man. Bone. 1994;15(3):269-77.

215.   Currey JD. The many adaptations of bone. Journal of Biomechanics. 2003;36(10):1487-95.

216.   Currey JD, Shahar R. Cavities in the compact bone in tetrapods and fish and their effects on mechanical properties. J Struct Biol. 2013;183(2):107-22.

217.   Wagermaier W, Gupta HS, Gourrier A, Burghammer M, Roschger P, Fratzl P. Spiral twisting of fiber orientation inside bone lamellae. Biointerphases. 2006;1(1):1-5.

218.   Gebhardt W. Ueber funktionell wichtige Anordnungsweisen der feineren und grosseren Bauelemente des Wirbeltierknochens.II. Spezieller Teil Der Bau der Haversschen Lamellensysteme und seine funktionelle Bedeutung. Arch Entwickl Mech Org. 1906;20:187-322.

219.   Reznikov N, Almany-Magal R, Shahar R, Weiner S. Three-dimensional imaging of collagen fibril organization in rat circumferential lamellar bone using a dual beam electron microscope reveals ordered and disordered sub-lamellar structures. Bone. 2013;52:676-83.

220.   Reznikov N, Shahar R, Weiner S. Bone hierarchical structure in three dimensions. Acta Biomaterialia. 2014;10(9):3815-2826.

221.   Reznikov N, Chase H, Brumfeld V, Shahar R, Weiner S. The 3D Structure of the collagen fibril network in human trabecular bone: relation to trabecular organization. Bone. 2015;71:189-95.

222.   Reznikov N, Buss DJ, Provencher B, McKee MD, Piche N. Deep learning for 3D imaging and image analysis in biomineralization research. J Struct Biol. 2020;212:107598.

223.   Buss DJ, Reznikov N, McKee MD. Crossfibrillar mineral tessellation in normal and Hyp mouse bone as revealed by 3D FIB-SEM microscopy. J Struct Biol. 2020;212(2):107603.

224.   Binkley DM, Deering J, Yuan H, Gourrier A, Grandfield K. Ellipsoidal mesoscale mineralization pattern in human cortical bone revealed in 3D by plasma focused ion beam serial sectioning. J Struct Biol. 2020;212.

225.   Prockop DJ, Fertala A. The collagen fibril: the almost crystalline structure. J Struct Biol 1998;122:111-8.

226.   Giraud-Guille M-M. Liquid crystallinity in condensed type I collagen solutions. A clue to the packing of collagen in extracellular matrices. Journal of Molecular Biology. 1992;224:861-73.

227.   Orgel JPRO, Irving TC, Miller A, Wess TJ. Microfibrillar structure of type I collagen in situ. PNAS. 2006;103(24):9001-5.

228.   Orgel JPRO, Persikov AV, Antipova O. Variation in the Helical Structure of Native Collagen. PLoS ONE. 2014;9(2).

229.   Bella J, Eaton M, Brodsky B, Berman HM. Crystal and molecular structure of a collagen-like peptide at 1.9 A resolution. Science. 1994;266:75-81.

230.   Kramer RZ, Bella J, Mayville P, Brodsky B, Berman HM. Sequence dependent conformational variations of collagen triple-helical structure. Nat Struct Biol. 1998;6:454-7.

231.   Charvolin J, Sadoc JF. A phyllotactic approach to the structure of collagen fibrils. Biophys Rev Lett. 2011;6:13-27.

232.   Charvolin J, Sadoc JF. About collagen, a tribute to Yves Bouligand. Interface Focus. 2012;2:567-74.

233.   Hulmes DJS, Miller A. Quasi-hexagonal molecular packing in collagen fibrils. Nature. 1979;282(878-880).

234.   Reznikov N, Bilton M, Lari L, Stevens MM, Kroeger R. Fractal-like hierarchical organization of bone begins at the nanoscale. Science. 2018;360:eaao2189.

235.	Landis WJ, Hodgens KJ, Arena J, Song MJ, MacEwen BF. Structural relations between collagen and mineral in bone as determined by high voltage electron microscopic tomography. Microscopy Reasearch and Technique. 1996;33:192-202.
236.	Schwarcz HP, McNally EA, Botton GA. Dark-field transmission electron microscopy of cortical bone reveals details of extrafibrillar crystals. J Struct Biol. 2014;188:240-8.
237.	Boyde A, Jones S. Aspects of anatomy and development of bone. The nm, um and mm hierarchy. Advances in Organ Biology. 1998;5A:3-44.
238.	Robinson R. An electron microscope study of the crystalline inorganic component of bone and its relationship to the organic matrix. J Bone Joint Surg. 1952;34A:389-434.
239.	Zhou C, Zhang X, Ai J, Ji T, Nagai M, Duan Y, et al. Chiral hierarchical structure of bone minerals. Nano Res. 2021;https://doi.org/10.1007/s12274-021-3653-z.
240.	Gould SJ, Lewontin RC. The spandrels of San Marco and the Panglossian paradigm: a critique of the adaptationist programme. Proc R Soc Lond B. 1979;205:581-98.
241.	Sehnal D, Bittrich S, Deshpande M, Svobodová R, Berka K, Bazgier V, et al. Mol* Viewer: modern web app for 3D visualization and analysis of large biomolecular structures. Nucleic Acids Research. 2021;10.1093/nar/gkab314.
242.	Tits A. Attaching soft to hard: A multimodal correlative investigation of the tendon-bone interface: University of Liege; 2023.
243.	Shaw HM, Benjamin M. Structure-function relationships of entheses in relation to mechanical load and exercise. Scand J Med Sci Sports. 2007;17(4):303-15.
244.	Fang F, Sup M, Luzzi A, Ferrer X, Thomopoulos S. Hedgehog signaling underlying tendon and enthesis development and pathology. Matrix Biol. 2022;105:87-103.
245.	Murata H, Nishizono H, Miyoshi M. Postnatal development of structure and arrangement of tendon cells. A scanning and transmission electron microscope study in the rat calcaneal tendon. Okajimas Folia Anat Jpn. 2000;77(2-3):77-86.
246.	Kanazawa T, Gotoh M, Ohta K, Shiba N, Nakamura K. Novel characteristics of normal supraspinatus insertion in rats: an ultrastructural analysis using three-dimensional reconstruction using focused ion beam/scanning electron microscope tomography. Muscles Ligaments Tendons J. 2014;4(2):182-7.
247.	Benjamin M, Ralphs JR. Fibrocartilage in tendons and ligaments--an adaptation to compressive load. J Anat. 1998;193 (Pt 4)(Pt 4):481-94.
248.	Cury DP, Dias FJ, Miglino MA, Watanabe IS. Structural and Ultrastructural Characteristics of Bone-Tendon Junction of the Calcaneal Tendon of Adult and Elderly Wistar Rats. PLoS One. 2016;11(4):e0153568.
249.	Liang G, Katz LD, Insogna KL, Carpenter TO, Macica CM. Survey of the enthesopathy of X-linked hypophosphatemia and its characterization in Hyp mice. Calcif Tissue Int. 2009;85(3):235-46.
250.	Moffat KL, Sun WH, Pena PE, Chahine NO, Doty SB, Ateshian GA, et al. Characterization of the structure-function relationship at the ligament-to-bone interface. Proc Natl Acad Sci U S A. 2008;105(23):7947-52.
251.	Deymier AC, An Y, Boyle JJ, Schwartz AG, Birman V, Genin GM, et al. Micro-mechanical properties of the tendon-to-bone attachment. Acta Biomater. 2017;56:25-35.
252.	Schwartz AG, Pasteris JD, Genin GM, Daulton TL, Thomopoulos S. Mineral distributions at the developing tendon enthesis. PLoS One. 2012;7(11):e48630.

253.   Hu Y, Birman V, Deymier-Black A, Schwartz G, Andrea, Thomopoulos S, Genin M, Guy. Stochastic Interdigitation as a Toughening Mechanism at the Interface between Tendon and Bone. Biophysical Journal. 2015;108(2):431-7.

254.   Zhao L, Thambyah A, Broom ND. A multi-scale structural study of the porcine anterior cruciate ligament tibial enthesis. J Anat. 2014;224(6):624-33.

255.   Derwin KA, Galatz LM, Ratcliffe A, Thomopoulos S. Enthesis Repair: Challenges and Opportunities for Effective Tendon-to-Bone Healing. J Bone Joint Surg Am. 2018;100(16):e109.

256.   Coyac BR, Falgayrac G, Penel G, Schmitt A, Schinke T, Linglart A, et al. Impaired mineral quality in dentin in X-linked hypophosphatemia. Connect Tissue Res. 2018;59(sup1):91-6.

257.   Fratzl-Zelman N, Gamsjaeger S, Blouin S, Kocijan R, Plasenzotti P, Rokidi S, et al. Alterations of bone material properties in adult patients with X-linked hypophosphatemia (XLH). Journal of Structural Biology. 2020;211(3):107556.

258.   Herrou J, Picaud AS, Lassalle L, Pacot L, Chaussain C, Merzoug V, et al. Prevalence of Enthesopathies in Adults With X-linked Hypophosphatemia: Analysis of Risk Factors. J Clin Endocrinol Metab. 2022;107(1):e224-e35.

259.   Steele A, Gonzalez R, Garbalosa JC, Steigbigel K, Grgurich T, Parisi EJ, et al. Osteoarthritis, Osteophytes, and Enthesophytes Affect Biomechanical Function in Adults With X-linked Hypophosphatemia. J Clin Endocrinol Metab. 2020;105(4).

260.   Glorieux FH, Bonewald LF, Harvey NC, van der Meulen MCH. Potential influences on optimizing long-term musculoskeletal health in children and adolescents with X-linked hypophosphatemia (XLH). Orphanet J Rare Dis. 2022;17(1):30.

261.   Faraji-Bellee CA, Cauliez A, Salmon B, Fogel O, Zhukouskaya V, Benoit A, et al. Development of Enthesopathies and Joint Structural Damage in a Murine Model of X-Linked Hypophosphatemia. Front Cell Dev Biol. 2020;8:854.

262.   McKee MD, Buss DJ, Reznikov N. Mineral tessellation in bone and the stenciling principle for extracellular matrix mineralization. J Struct Biol. 2022;214(1):107823.

263.   Buss DJ, Kroger R, McKee MD, Reznikov N. Hierarchical organization of bone in three dimensions: A twist of twists. J Struct Biol X. 2022;6:100057.

264.   Macica CM, Luo J, Tommasini SM. The Enthesopathy of XLH Is a Mechanical Adaptation to Osteomalacia: Biomechanical Evidence from Hyp Mice. Calcif Tissue Int. 2022.

265.   Liu ES, Martins JS, Zhang W, Demay MB. Molecular analysis of enthesopathy in a mouse model of hypophosphatemic rickets. Development. 2018;145(15).

266.   Zimmermann EA, Fiedler IAK, Busse B. Breaking new ground in mineralized tissue: Assessing tissue quality in clinical and laboratory studies. J Mech Behav Biomed Mater. 2021;113:104138.

267.   Wittig NK, Ostergaard M, Palle J, Christensen TEK, Langdahl BL, Rejnmark L, et al. Opportunities for biomineralization research using multiscale computed X-ray tomography as exemplified by bone imaging. J Struct Biol. 2021;214(1):107822.

268.   Weiner S, Raguin E, Shahar R. High resolution 3D structures of mineralized tissues in health and disease. Nat Rev Endocrinol. 2021.

269.   Grunewald TA, Liebi M, Wittig NK, Johannes A, Sikjaer T, Rejnmark L, et al. Mapping the 3D orientation of nanocrystals and nanostructures in human bone: Indications of novel structural features. Sci Adv. 2020;6(24):eaba4171.

270.   Eren ED, Nijhuis WH, van der Weel F, Dede Eren A, Ansari S, Bomans PHH, et al. Multiscale characterization of pathological bone tissue. Microsc Res Tech. 2022;85(2):469-86.

271.   Ichikawa S, Gray AK, Bikorimana E, Econs MJ. Dosage effect of a Phex mutation in a murine model of X-linked hypophosphatemia. Calcif Tissue Int. 2013;93(2):155-62.
272.   Lyon MF. X-chromosome inactivation. Curr Biol. 1999;9(7):R235-7.
273.   Otsu N. A Threshold Selection Method from Gray-Level Histograms. IEEE Transactions on Systems, Man, and Cybernetics. 1979;9(1).
274.   Crameri F, Shephard GE, Heron PJ. The misuse of colour in science communication. Nat Commun. 2020;11(1).
275.   Ecarot B, Desbarats M. 1,25-(OH)2D3 down-regulates expression of Phex, a marker of the mature osteoblast. Endocrinology. 1999;140(3):1192-9.
276.   Deymier-Black AC, Pasteris JD, Genin GM, Thomopoulos S. Allometry of the Tendon Enthesis: Mechanisms of Load Transfer Between Tendon and Bone. J Biomech Eng. 2015;137(11):111005.
277.   Tits A, Ruffoni D. Joining soft tissues to bone: Insights from modeling and simulations. Bone Rep. 2021;14:100742.
278.   Tits A, Plougonven E, Blouin S, Hartmann MA, Kaux JF, Drion P, et al. Local anisotropy in mineralized fibrocartilage and subchondral bone beneath the tendon-bone interface. Sci Rep. 2021;11(1):16534.
279.   Livanov K, Yang L, Nissenbaum A, Wagner HD. Interphase tuning for stronger and tougher composites. Sci Rep. 2016;6:26305.
280.   Weiner S, Nudelman F, Sone E, Zaslansky P, Addadi L. Mineralized biological materials: A perspective on interfaces and interphases designed over millions of years. Biointerphases. 2006;1(2):P12-P4.
281.   Wagermaier W, Klaushofer K, Fratzl P. Fragility of Bone Material Controlled by Internal Interfaces. Calcif Tissue Int. 2015;97(3):201-12.
282.   Micheletti C, Hurley A, Gourrier A, Palmquist A, Tang T, Shah FA, et al. Bone mineral organization at the mesoscale: A review of mineral ellipsoids in bone and at bone interfaces. Acta Biomater. 2022;142:1-13.
283.   Jacob F, Monod J. Genetic regulatory mechanisms in the synthesis of proteins. J Mol Biol. 1961;3:318-56.
284.   Makitie O, Pereira RC, Kaitila I, Turan S, Bastepe M, Laine T, et al. Long-term clinical outcome and carrier phenotype in autosomal recessive hypophosphatemia caused by a novel DMP1 mutation. J Bone Miner Res. 2010;25(10):2165-74.
285.   Rufai A, Benjamin M, Ralphs JR. Development and ageing of phenotypically distinct fibrocartilages associated with the rat Achilles tendon. Anatomy and Embryology. 1992;186(6).
286.   Shaw HM, Vazquez OT, McGonagle D, Bydder G, Santer RM, Benjamin M. Development of the human Achilles tendon enthesis organ. J Anat. 2008;213(6):718-24.
287.   Schmitt D, Zumwalt C, Hamrick MW. The Relationship Between Bone Mechanical Properties and Ground Reaction Forces in Normal and Hypermuscular Mice. J Exp Zool Part A. 2010;313a(6):339-51.
288.   Sullivan D, Pabich A, Enslow R, Roe A, Borchert D, Barr K, et al. Extensive Ossification of the Achilles Tendon with and without Acute Fracture: A Scoping Review. J Clin Med. 2021;10(16).
289.   Oliva F, Via AG, Maffulli N. Physiopathology of intratendinous calcific deposition. BMC Med. 2012;10:95.

290. Binkley DM, Deering J, Yuan H, Gourrier A, Grandfield K. Ellipsoidal mesoscale mineralization pattern in human cortical bone revealed in 3D by plasma focused ion beam serial sectioning. J Struct Biol. 2020;212(2):107615.

291. Raguin E, Rechav K, Shahar R, Weiner S. Focused ion beam-SEM 3D analysis of mineralized osteonal bone: lamellae and cement sheath structures. Acta Biomater. 2021;121:497-513.

292. Shah FA, Ruscsak K, Palmquist A. Transformation of bone mineral morphology: From discrete marquise-shaped motifs to a continuous interwoven mesh. Bone Rep. 2020;13:100283.

293. Giachelli CM. Inducers and inhibitors of biomineralization: lessons from pathological calcification. Orthod Craniofac Res. 2005;8(4):229-31.

294. Sodek J, Ganss B, McKee MD. Osteopontin. Crit Rev Oral Biol Med. 2000;11(3):279-303.

295. Murali SK, Andrukhova O, Clinkenbeard EL, White KE, Erben RG. Excessive Osteocytic Fgf23 Secretion Contributes to Pyrophosphate Accumulation and Mineralization Defect in Hyp Mice. PLoS Biol. 2016;14(4):e1002427.

296. Buck A, Prade VM, Kunzke T, Erben RG, Walch A. Spatial metabolomics reveals upregulation of several pyrophosphate-producing pathways in cortical bone of Hyp mice. JCI Insight. 2022;7(20).

297. Currey J. Structural heterogeneity in bone: good or bad? J Musculoskelet Neuronal Interact. 2005;5(4):317.

298. Tang T, Landis W, Blouin S, Bertinetti L, Hartmann MA, Berzlanovich A, et al. Sub-canalicular nanochannel volume is inversely correlated with calcium content in human cortical bone. J Bone Miner Res. 2022.

299. Tang et. a. A 3D Network of Nanochannels for Possible Ion and Molecule Transit in Mineralizing Bone and Cartilage. Advanced NanoBiomed Research. 2022.

300. Dennis JE, Xiao SQ, Agarwal M, Fink DJ, Heuer AH, Caplan AI. Microstructure of matrix and mineral components of eggshells from White Leghorn chickens (Gallus gallus). J Morphol. 1996;228(3):287-306.

301. Lei C, Wang YH, Zhuang PX, Li YT, Wan QQ, Ma YX, et al. Applications of Cryogenic Electron Microscopy in Biomineralization Research. J Dent Res. 2022;101(5):505-14.

302. Rahn H, Ar A, Paganelli CV. How Bird Eggs Breathe. Scientific American. 1979;240(2):46-55.

303. Rahn H, Paganelli CV, Ar A. Pores and gas exchange of avian eggs: a review. J Exp Zool Suppl. 1987;1:165-72.

304. Riley A, Sturrock CJ, Mooney SJ, Luck MR. Quantification of eggshell microstructure using X-ray micro computed tomography. Br Poult Sci. 2014;55(3):311-20.

305. Tan CK, Chen TW, Chan HL, Ng LS. A scanning and transmission electron microscopic study of the membranes of chicken egg. Histol Histopathol. 1992;7(3):339-45.

306. Bellairs R, Boyde A. Scanning electron microscopy of the shell membranes of the hen's egg. Z Zellforsch Mikrosk Anat. 1969;96(2):237-49.

307. Damaziak K, Marzec A. Analysis of ultrastructure and microstructure of blackbird (Turdus merula) and song thrush (Turdus philomelos) eggshell by scanning electron microscopy and X-ray computed microtomography. Sci Rep. 2022;12(1):11857.

308. Balch, Cooke. A Study of the Composition of Hen's Egg-Shell Membranes. Ann Biol anim Bioch Biophys. 1970;10(Hors-série 2):13-25.

309.   Harris ED, Blount JE, Leach RM, Jr. Localization of lysyl oxidase in hen oviduct: implications in egg shell membrane formation and composition. Science. 1980;208(4439):55-6.
310.   Wong M, Hendrix MJ, von der Mark K, Little C, Stern R. Collagen in the egg shell membranes of the hen. Dev Biol. 1984;104(1):28-36.
311.   Hincke MT, Chien YC, Gerstenfeld LC, McKee MD. Colloidal-gold immunocytochemical localization of osteopontin in avian eggshell gland and eggshell. J Histochem Cytochem. 2008;56(5):467-76.
312.   Le Roy N, Stapane L, Gautron J, Hincke MT. Evolution of the Avian Eggshell Biomineralization Protein Toolkit - New Insights From Multi-Omics. Front Genet. 2021;12:672433.
313.   Bunk MJ, Balloun SL. Structure and relationship of the mammillary core to membrane fibres and initial calcification of the avian Egg Shell. British Poultry Science. 1977;18(5):617-21.
314.   Li Y, Li Y, Liu S, Tang Y, Mo B, Liao H. New zonal structure and transition of the membrane to mammillae in the eggshell of chicken Gallus domesticus. J Struct Biol. 2018;203(2):162-9.
315.   Halgrain M, Georgeault S, Bernardet N, Hincke MT, Rehault-Godbert S. Concomitant Morphological Modifications of the Avian Eggshell, Eggshell Membranes and the Chorioallantoic Membrane During Embryonic Development. Front Physiol. 2022;13:838013.
316.   Chien YC, Hincke MT, McKee MD. Ultrastructure of avian eggshell during resorption following egg fertilization. J Struct Biol. 2009;168(3):527-38.
317.   Athanasiadou D, Jiang W, Goldbaum D, Saleem A, Basu K, Pacella MS, et al. Nanostructure, osteopontin, and mechanical properties of calcitic avian eggshell. Sci Adv. 2018;4(3):eaar3219.
318.   Tyler C, Simkiss K. Studies on egg shells. XII.—Some changes in the shell during incubation. Journal of the Science of Food and Agriculture. 1959;10:611-5.
319.   Örberg J. Relationship between the shell membrane-shell bond and shell deformation in hens' eggs. British Poultry Science. 1990;31(2):249-54.
320.   Liu F, Jiang X, Wang L. Mechanical Design Principles of Avian Eggshells for Survivability arXiv. 2022.
321.   Berrang ME, Cox NA, Frank JF, Buhr RJ. Bacterial Penetration of the Eggshell and Shell Membranes of the Chicken Hatching Egg: A Review. Journal of Applied Poultry Research. 1999;8(4):499-504.
322.   Ray A, Roberts JR, Flavel R, Chousalkar KK. Eggshell penetration by Salmonella Typhimurium in table eggs: Examination of underlying eggshell structures by micro-computed tomography and scanning electron microscopy. Food Research International. 2015;78:34-40.
323.   Park JA, Sohn SH. The Influence of Hen Aging on Eggshell Ultrastructure and Shell Mineral Components. Korean J Food Sci Anim Resour. 2018;38(5):1080-91.
324.   Narushin VG. Egg geometry calculation using the measurements of length and breadth. Poult Sci. 2005;84(3):482-4.
325.   Paganelli CV, Olszowka A, Ar A. The Avian Egg: Surface Area, Volume, and Density. The Condor. 1974;76(3):319-25.
326.   Fratzl P, Weinkamer R. Nature's hierarchical materials. Progress in materials Science. 2007;52(8):1263-334.
327.   Zhou J, Wang S, Nie F, Feng L, Zhu G, Jiang L. Elaborate architecture of the hierarchical hen's eggshell. Nano Research. 2011;4(2):171-9.

328.   Solomon SE. The eggshell: strength, structure and function. Br Poult Sci. 2010;51 Suppl 1:52-9.

329.   Bain MM. Eggshell strength: A relationship between the mechanism of failure and the ultrastructural organisation of the mammillary layer. British Poultry Science. 1992;33(2):303-19.

330.   Gower LB, Odom DJ. Deposition of calcium carbonate films by a polymer-induced liquid-precursor (PILP) process. Journal of Crystal Growth. 2000;210(4):719-34.

331.   Mann S, Weiner S. Biomineralization: structural questions at all length scales. J Struct Biol. 1999;126(3):179-81.

332.   Goldberg HA, Hunter GK. The inhibitory activity of osteopontin on hydroxyapatite formation in vitro. Ann N Y Acad Sci. 1995;760:305-8.

333.   Rodriguez DE, Thula-Mata T, Toro EJ, Yeh YW, Holt C, Holliday LS, et al. Multifunctional role of osteopontin in directing intrafibrillar mineralization of collagen and activation of osteoclasts. Acta Biomater. 2014;10(1):494-507.

334.   Yadav MC, Huesa C, Narisawa S, Hoylaerts MF, Moreau A, Farquharson C, et al. Ablation of Osteopontin Improves the Skeletal Phenotype of Phospho1−/− Mice. Journal of Bone and Mineral Research. 2014;29(11):2369-81.

335.   Portale AA, Carpenter TO, Brandi ML, Briot K, Cheong HI, Cohen-Solal M, et al. Continued Beneficial Effects of Burosumab in Adults with X-Linked Hypophosphatemia: Results from a 24-Week Treatment Continuation Period After a 24-Week Double-Blind Placebo-Controlled Period. Calcif Tissue Int. 2019;105(3):271-84.

336.   Carter DR, Hayes WC. Compact bone fatigue damage: a microscopic examination. Clinical Orthopaedics and Related Research (1976-2007). 1977;127:265-74.

337.   Currey JD. The Mechanical Properties of Bone. Bones. Structure and Mechanics: Princeton University Press; 2002. p. 54-123.

338.   Fratzl P, Gupta HS, Fischer FD, Kolednik O. Hindered Crack Propagation in Materials with Periodically Varying Young's Modulus—Lessons from Biological Materials. Advanced Materials. 2007;19(18):2657-61.

339.   Fantner GE, Oroudjev E, Schitter G, Golde LS, Thurner P, Finch MM, et al. Sacrificial bonds and hidden length: unraveling molecular mesostructures in tough materials. Biophys J. 2006;90(4):1411-8.

340.   Currey J. Sacrificial bonds heal bone. Nature. 2001;414(6865):699-.

341.   Buss DJ, Rechav K, Reznikov N, McKee MD. Mineral tessellation in mouse enthesis fibrocartilage, Achilles tendon, and Hyp calcifying enthesopathy: A shared 3D mineralization pattern. Bone. 2023;174:116818.